# Cure Induced Stress Generation and Viscoelasticity in Polymer Coatings

A DISSERTATION
SUBMITTED TO THE FACULTY OF THE GRADUATE SCHOOL
OF THE UNIVERSITY OF MINNESOTA
BY

Daniel Jeffrey O'Neal

IN PARTIAL FULFILLMENT OF THE REQUIREMENTS
FOR THE DEGREE OF
DOCTOR OF PHILOSOPHY

A. V. McCormick and L. E. Scriven, Advisors

January 2010

## Acknowledgments

Many people helped with my research during my time at the University of Minnesota, generously donating their time, expertise, and effort. Graduate school is a strange mixture of progress and failure, success and frustration, and knowledge and questions. I wish to thank everyone for their help, recognizing that my research would have been much more difficult without you.

First, my advisors Alon McCormick and Skip Scriven. Without your direction, support, and countless research discussions, I would have never finished. I am particularly grateful to have worked under Skip Scriven for as long as I did. I would also like to thank Coating Process Fundamentals Professors Lorraine Francis and Satish Kumar for discussions about coatings, and note that Prof. Kumar's seminars on mathematics and computational issues continued an important tradition for computational research. Professor Victor Barocas was particularly helpful with discussions on computational viscoelasticity.

The Industrial Partnership for Research in Interfacial and Materials Engineering, specifically the Coating Process Fundamentals Program funded my research, allowing me to interact with other engineers in the field and exposing me to new problems and ideas. The Minnesota Supercomputer Institute generously granted our group supercomputer time and had staff assist us when necessary.

Fellow graduate students helped me in ways too numerous to list here. Fluid mechanicists extraordinare Kristianto Tjiptowidjojo and Jae Wook Nam with discussions on finite elements and programming. McCormick group members and 440A inhabitants Chongai Kuang and Ben Richter. Coating Process Fundamentals Researchers Karan Jindal and Christine Cardinal. Shawn Dodds and especially Scott Roberts for countless meetings about computational aspects and research strategies. Also Masano Sugiyama, Janice Boercker, and Scott King for keeping me sane and Giovanni Cocchi for very relevant discussions about computational polymer solidification.

To the staff of the CEMS department and Supercomputer Institute, thank you for keeping the lights on, my advisors informed, and the budgets flowing. Sean Morrissey and Mitch Hoffman at the Center for Outdoor Adventure deserve recognition for letting me share my love of the outdoors with others.

Finally, my family for supporting me half a country away. I could not have done this without years of support and encouragement from you.

## Abstract

Coatings solidified by free-radical polymerization and crosslinking (curing) reactions initiated with ultraviolet (UV) light do so quickly and at room temperature. Low viscosity monomer or oligiomer makes the use of volatile solvent unnecessary, decreasing energy use and making the process more environmentally friendly but photoinitiators can be toxic, limiting certain applications. Stress may be generated by a changing specific volume during cure, and stress-induced defects are undesirable. The goal of this research is to understand stress generation in UV irradiated coatings and to model stress generation and viscoelasticity seen during curing.

Two new mathematical models were created to accomplish viscoelastic stress modeling. The first, a network model, uses a two-dimensional network of one-dimensional elements to replicate deformation in the coating. The second uses continuum momentum conservation and linear viscoelastic equations. Inertial forces can be neglected and a substitution performed, making the solution more rapid and simple with standard finite element methods.

Stress generation in uniformly cured coatings depends on how quickly the specific volume and physical properties change. Reaction kinetics, volume, and stress are calculated simultaneously. Rapid initiation from high initiator concentration or UV light intensity delays volume change, generating more stress because the volume changes with a higher modulus. An optimum curing schedule would insure the actual specific volume and its equilibrium value remain the same.

Inhomogeneities in the substrate or the presence of defects change the stress field. Knowing forces on the coating boundaries suggests defect locations and types. Probing the types of geometries and surface roughnesses seen in different types of coatings shows that restricted deformation increases stress concentrations and surface forces seen. Also, avenues for reducing stress via relaxation are discussed. The two-dimensional stress profiles used in these analyses are not possible to measure experimentally, making computational modeling essential.

The models developed and methodology presented may be extended to other UV cured coatings or to other methods of coating solidification. Process windows of allowable final conversion-stress-energy-time states suggest what tradeoffs must be made to meet constraints.

# Contents

# List of Tables

# List of Figures

# Chapter 1

# Introduction

## 1.1 Polymer coatings

Polymer coatings are important in many different areas of modern science and are applied for several reasons: protection, optical properties, barrier properties, adhesive properties, and to add functionality to surfaces they cover. Coatings are applied as liquids and solidified on the substrate upon which they are coated to create the final layer. The coating process encompasses everything from liquid and substrate preparation to liquid application through solidification and postprocessing. Coated liquid may contain a polymer-solvent solution, a dispersion of particles such as latex, a monomer, oligiomer, or reactive polymer precursor, or a combination of these. Non-polymer molecules or particles may be introduced into the coating formulation for chemical, mechanical, or other reasons.

Solidifying the coated layer may be accomplished in several ways, the method chosen depends on the coating formulation. Solution coatings can be dried by removing volatile solvent, latex dispersions coalesce, compact, and interdiffuse with water removal, polymerization and crosslinking reactions occur in monomer or oligiomers. These chemical reactions can be initiated with ultraviolet (UV) radiation and light sensitive photoinitiators, with high energy electron or $\gamma$ irradiation, or with heat and thermal initiators and are collectively referred to as curing reactions.

This thesis deals with solidification by curing using UV light and photoinitiators that decompose to form radicals upon absorption of light energy. Radicals react with vinyl double bonds, polymerizing monomer in the coating quickly, at room temperature, and without solvent. The absence of solvent increases energy efficiency over dried coatings where elevated temperatures, radiation, or both are applied to hasten the drying process. Photoinitiators, however, can be highly toxic and there is often a finite residual unreacted concentration that remains in the coating after curing, making some UV cured coatings unsuitable for medical or food applications. Common applications of cured coatings include adhesives, photolithography and microelectronics coatings, protective clear-coats, dental restorative materials, contact lenses, optical fiber coatings, and electrical coatings.

UV cured coatings can contain single monomers or mixtures of different types of monomers. Monofunctional monomers cannot form networks, only chains, because there are no junction-forming molecules. Network formation occurs when chains are connected with multiple junctions – *crosslinks*. Multifunctional monomers may be added to coatings of monofunctional monomers to induce network formation, or multifunctional monomers may be polymerized by themselves. During reaction, when the network becomes large enough to span the entire coating, it is said to have passed gelation, the point at which the network percolates the domain and creates essentially one molecule of macroscopic size. Additionally, the glass transition may occur with reaction. The glass transition, or vitrification point, is the temperature where long range molecular motions become hindered and the behavior of the polymer changes, and is usually characterized with a change in the thermal expansion coefficient (Sperling 1986). Physically, less molecular motion serves to greatly increase the elastic modulus and viscosity, which decreases stress relaxation. These physical properties change with polymerization, temperature, and timescale of investigation. The glass transition temperature, $T_g$, is a characteristic of a polymer system. During cure, this polymer system changes with chain growth, crosslinking, and network formation, and $T_g$ changes with monomer conversion. Gelation may occur before vitrification, after it, or either may not occur at all. Cured coatings pass the glass transition when the glass transition

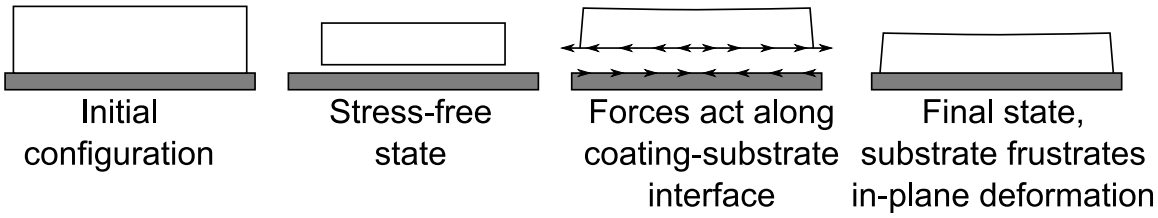


Figure 1.1: Coating volume change, substrate constraints, and forces. Adapted from Tam (1997).

temperature of the curing coating rises above the cure temperature. The relationship between curing, gelation, vitrification, and reaction rate has been discussed in the literature (Enns and Gillham 1983b, Enns and Gillham 1983a, Prime 1997, Sperling 1986, Halley and George 2009).

## 1.2 The Stress-free State and Origins of Stress

During coating solidification, whether by curing or drying, the specific volume of the polymer changes (Hasatani and Itaya 1996, Stansbury et al. 2005, Bowman and Peppas 1991). This change in specific volume induces a deformation in the polymer, commonly referred to as a shrinkage because the final volume is smaller than its initial value. Stress can be generated in the coating if this shrinkage deformation is prevented. Commonly, the shrinkage is frustrated by strong adhesion to a solid substrate and stress is generated in the plane of the coating (Croll 1979a, Sato 1980). Deformation is allowed out of the coating plane, so out-of-plane stress is not generated, however the coating edges are more complicated (Radhakrishnan 2006). Forces are applied on the coating at the coating-substrate interface, and equal and opposite forces act on the substrate, which may deform, leading to curl. Calibrated substrates can be used to measure the stress in relation to deflection of the elastic substrate (Payne et al. 1997).

The change in specific volume and shrinkage deformation seen are manifestations of a change in the *elastic stress-free state* (or simply the *stress-free state*), which is defined to be the material configuration where there is no elastic stress. This configuration can change

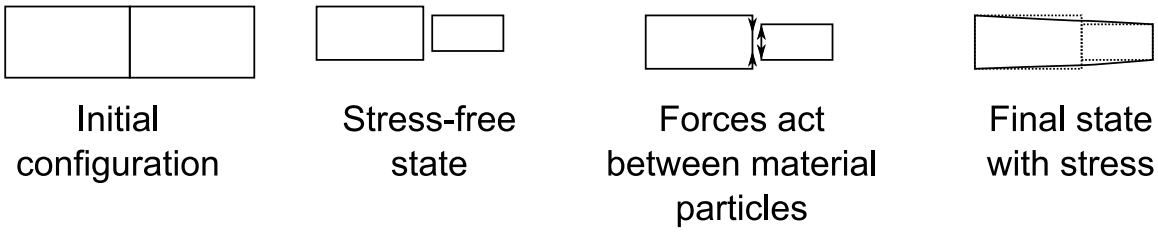


Figure 1.2: Nonuniform stress-free state change, stress due to compatibility between neighboring material particles. Adapted from Tam (1997).

with temperature, extent of reaction, concentration, flow, yielding, and other factors. There actually may be stress in the stress-free state, but only an isotropic, uniform stress such as hydrostatic pressure. Figure 1.1 shows the difference between original, stress-free, and final states as well as where forces act on coatings. Notably, the stress-free state and actual deformation that takes place may not be the same. The difference between these two states is the cause of elastic stress and is deemed *elastic strain*. During coating solidification, the stress-free state changes, as does the actual deformation. Additionally, the stress-free state may not be accessible due to compatibility constraints. Compatibility demands adjacent material particles deform identically, which may make the stress-free state unobtainable. Nonuniformities in coating solidification such as concentration or reaction rate as well as nonuniform geometries may cause this. Figure 1.2 shows how compatibility and nonuniform stress-free states can cause stress.

Stress may only be generated by departure from the stress-free state if there is a nonzero elastic modulus. Fluids will never generate elastic stress, because fluids possess no elastic modulus. Solids and viscoelastic materials, however, may generate elastic stress. Because of this, understanding the progression of the stress-free state, elastic modulus, and any factors affecting these – such as stress relaxation – must be known in time to determine the stress in a coating.

## 1.3 Viscoelasticity

The response of a material based on forces or deformations applied to it depends on the type of material, the location and magnitude of forces or deformations, the geometry, and time. Fluids can support no shear stress in equilibrium (Bird et al. 1960), while some solids can support stresses indefinitely (Sokolnikoff 1956, Malvern 1969). Polymer coatings begin as fluids that may be complex and non-Newtonian – and end as hard, elastic solids. The interim behavior is viscoelastic, which contains characteristics of both viscous fluids and elastic solids: energy storage and recoverable deformation through elastic behavior and energy dissipation through viscous processes (Anseth et al. 1993, Lange et al. 1996, Ernst et al. 2002). The field of viscoelasticity is large, well-developed, and complicated. This section does not attempt to discuss all of viscoelasticity, but introduce some basics that will be necessary in the thesis. The interested reader is directed to treatments of viscoelasticity and rheology, the study and measurement of polymer deformation and flow (Ferry 1970, Malvern 1969, Macosko 1994, Alfrey 1965, Sperling 1986, Bird et al. 1977).

Constitutive equations describe the relationship between stress, deformation, and time mathematically. These equations describe the physical phenomena occurring in the material of interest: deformations of crystalline materials, polymer chains extending, entangling, and relaxing, molecules sliding past one another, and the like in mathematical terms so the response can be determined without experiment. For example, linear (Hookean) elasticity can be described with the following constitutive equation (Sokolnikoff 1956):

$$\boldsymbol{\sigma} = 2G\boldsymbol{\epsilon} + 2G\frac{\nu}{1-2\nu}\left(tr\boldsymbol{\epsilon}\right)\boldsymbol{I} \tag{1.1}$$

where $\boldsymbol{\sigma}$ is the stress tensor, $\boldsymbol{\epsilon}$ is the strain tensor, $G$ is the shear modulus, $\nu$ is Poisson's ratio, $\boldsymbol{I}$ is an identity tensor, and $t$ is time. The modulus and Poisson's ratio are physical properties – they are constants of proportionality – and depend on the material. Poisson's ratio quantifies how deformations are coupled by volume and the shear modulus relates the magnitude of stress to the magnitude of the strain. The strain is a measure of the deforma-

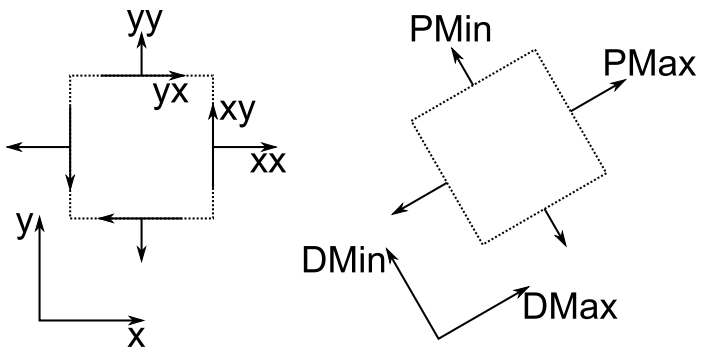


Figure 1.3: Cartesian and principal stresses and directions in two-dimensions.

tion of the material (Malvern 1969). Development of elasticity theory never considered a stress-free state so strain is assumed to be measured from a (non-changing) stress-free state. Equation (1.1) shows that any deformation will generate a stress, which will not change with time unless the strain changes. Upon removal of deformation, the equilibrium configuration is recovered along with the energy supplied for deformation. In contrast, Newton's theory of viscosity for fluids is (Bird et al. 1960):

$$\boldsymbol{\sigma} = 2\mu\frac{\partial\boldsymbol{\epsilon}}{\partial t} + \kappa_b\frac{\mu}{3}\frac{\partial tr\boldsymbol{\epsilon}}{\partial t}\boldsymbol{I} \tag{1.2}$$

where $\mu$ is the shear viscosity, $\kappa_b$ is the bulk viscosity, and $t$ is time. Here, the viscosities are physical properties; $\mu$ relates the magnitude of isochoric strain rate to the stress while $\kappa_b$ relates the volumetric strain rate to the stress. In a fluid, the stress depends on the strain *rate* – the time derivative of the strain – and disappears if motion is ceased. There is no clear definition of the stress-free state, but this does not matter because fluids can not support elastic stress. Upon removal of deformation, the original configuration is not recovered and the energy supplied for deformation is lost through viscous dissipation. The stress-free state changes with the material.

The stress tensor contains information about stresses in every direction in the coating and produces the traction on a surface when the dot product of the stress and surface normal is taken. The tensor is symmetric for mutually perpendicular coordinate systems,

but the components depend on the basis vectors chosen. The principal stresses, however, are invariant of coordinate choice. The principal stresses are defined to be the set of coordinates where shear stresses disappear, only normal stresses remain, and are just a rotation of the original basis set. Principal and their directions are the eigenvalues and eigenvectors of the Cartesian stress tensor. Stresses and directions are shown in Figure 1.3 for two-dimensions.

Viscoelastic behavior falls in between pure elastic and pure viscous behavior, with characteristics from each. While not restricted to polymeric materials (Jeffreys 1929), much work has been performed on the field of viscoelasticity due to and for polymers (Ferry 1970). This is due to the molecular architecture of polymers; long chain molecules with or without branches, crosslinks, and networks move around other polymer molecules in complex ways. Specific molecular motions depend on the polymer, its architecture, and its spatial distribution. This necessitates many constitutive equations to describe viscoelastic phenomena. These will not be reviewed here, but linear viscoelasticity will be since it can be used to model a curing coating's behavior (Anseth et al. 1993, Lange et al. 1996, Ernst et al. 2002). Linear viscoelasticity, like the linear constitutive equations presented above, relates stress, strain, and their time derivatives linearly, and uses similar physical properties. Unfortunately, there are many different ways to mathematically account for the phenomena occurring with linear viscoelasticity, which leads to an unclear relationship between quantities with similar names when used in reference to different constitutive equations (Macosko 1994). Regardless, we will begin with the most common linear viscoelastic constitutive equation, the Maxwell equation, which was originally proposed by J. C. Maxwell for gaseous viscosity, but models viscoelastic behavior well (Maxwell 1867, Ferry 1970). The salient behavior that is captured by this constitutive equation is stress decay – relaxation – over time. Also, at short timescales, elastic behavior is seen while at long timescales, viscous behavior is seen. Viscous flow serves to change the stress-free state, relaxing the stress and reducing the recoverable strain, however the standard mathematical descriptions do not use the stress-free state. Instead, decaying stress and strain,

$$\frac{1}{2G}\frac{\partial \boldsymbol{\sigma}}{\partial t}+\frac{1}{2\mu}\boldsymbol{\sigma}=\frac{\partial \boldsymbol{\epsilon}}{\partial t}+\frac{\nu}{1-2\nu}\frac{\partial\left(tr\left(\boldsymbol{\epsilon}\right)\right)}{\partial t}\boldsymbol{I} \tag{1.3}$$

or decaying modulus,

$$\boldsymbol{\sigma}=\int_{-\infty}^{t} G\left(t-t^{'}\right)\frac{\partial \boldsymbol{\epsilon}(t^{'})}{\partial t^{'}}dt^{'}+K\left(t-t^{'}\right)\frac{\partial tr\left(\boldsymbol{\epsilon}(t^{'})\right)}{\partial t^{'}}dt^{'} \tag{1.4}$$

are used.

## 1.4 Stress Generation During Coating Solidification

The desire to determine the final stress in a coating is not new, and several methods have been developed for different polymer systems and solidification pathways. Even with different ways of determining the final stress, certain information is needed in every model. First, a constitutive equation that describes the stress-deformation behavior and physical properties relating the two. Second, a way to quantify how the stress-free state changes. This is often referred to as a shrinkage or shrinkage strain, but the 'shrinkage' deformation may not occur all the way to the stress-free state. Third, a method to calculate the physical properties and their change with time, and last, the assumption that the coating adheres strongly to its substrate. This section briefly reviews some methods for calculating final stress. It does not discuss measuring stress, which was reviewed by Francis et al. (2002).

Croll's (1979a) work on poly isobutyl methacrylate and polystyrene coatings solidified by drying laid the foundation for subsequent stress modeling. He assumed no stress was generated before the coating solidified by vitrifying; the liquid-solid transition happened instantaneously when $T_g$ rose to the coating temperature. After vitrification, the coating was assumed to be a linear elastic solid. No viscoelasticity was included which made knowing physical property change with time unnecessary. He also assumed a biaxial state of stress in the coating plane and no out-of-plane stress. The change in the stress-free state was determined by the volume at solidification and at the end of drying,

$$\frac{\Delta V}{V} = \frac{\phi_s - \phi_r}{1 - \phi_r}. \tag{1.5}$$

where $V$ is the volume, $\Delta V$ the volume change after solidification, and $\phi_s$ and $\phi_r$ the solidification and residual solvent volume fractions, respectively. The isotropic normal strain after solidification was given by the volume from the lost solvent after solidification,

$$\epsilon = \frac{1}{3}\frac{\Delta V}{V}. \tag{1.6}$$

For a linear elastic material under small displacement, the stress $\sigma$ is given by,

$$\sigma = \frac{E\epsilon}{1 - \nu}, \tag{1.7}$$

where $E$ is Young's modulus and $\nu$ is Poisson's ratio. Combining Equation 1.5 with Equations 1.6 and 1.7 leads to the stress relation,

$$\sigma = \frac{E}{1 - \nu}\frac{\phi_s - \phi_r}{3\,(1 - \phi_r)}. \tag{1.8}$$

This method captures the basics of uniform stress generation (Croll 1979a, Croll 1979b, Croll 1981, Sato 1980).

Tam (1997) and later Lei et al. (2001) developed more sophisticated models for drying coatings that incorporated mass transfer and viscoplasticity in two dimensions (Lei et al. 2002, Lei et al. 2003). These models also assumed no stress built up pre-solidification, pure elastic behavior post-solidification, but included plastic deformation if yielding happened. Plastic yielding changes the stress-free state and lowers the stress.

Several models have been developed to describe stress buildup in cured coatings as well. Thermosets are an especially rich field for stress modeling with cure. Lange et al. (1995) use an integral elasticity constitutive equation,

$$\sigma = \int E d\epsilon \tag{1.9}$$

where the in-plane stress is calculated as an incremental stress-free strain multiplied by an incremental elastic modulus. This treatment allows for changing physical properties with time but does not include viscoelasticity. Ernst et al. (2002) uses an integral linear viscoelastic constitutive equation, like Equation (1.4), and lays out some theory for calculating the decaying modulus based on experimental data using a Boltzmann Superposition of moduli (Ferry 1970). This information is inserted into a two-dimensional model to determine stress profiles during thermoset cure. A similar method is used by Yang et al. (2004). Martin and Adolf (1990) begin with a similar integral constitutive equation to obtain the in-plane stress. Later, Adolf and Martin (1996) couple cure kinetics with an integral constitutive equation that includes volume coupling with a nonzero bulk viscosity. Hossain et al. (2009b) painstakingly derive a new way of expressing Equation (1.4), and model the stress-free state change and physical property buildup. Finally, White and Hahn (1992a) and Meuwissen et al. (2004) use integral viscoelasticity along with kinetics to determine physical properties and stress. Adolf et al. (1998) provides a review of some of the thermoset curing models.

Available models for free-radical photopolymerizations are much more limited than for thermosets. Dauvillier et al. (2001) uses some rudimentary viscoelastic mechanical models along with basic stress-strain data for pulsed measurements, but does not discuss kinetics, predicting stress-free state change, or spatial modeling. Koplin et al. (2009) uses some basic kinetic models with variable physical properties and a viscoelastic model in three-dimensions, but the use of a commercial software package obscures the solution details. Stolov et al. (2000) use an incremental elasticity integration like Equation (1.9) and a simple theory for property buildup with cure.

Accurate stress-free state changes are expected to result from calculating the kinetics and volume simultaneously, and Vaessen (2002) did this for photopolymerizations, though her treatment of stress was not emphasized. Nevertheless, she used simple one-dimensional viscoelastic models and back-calculated the physical property buildup from measured stress. It appears that Rajamani (2005) attempted to build on this model, but the kinetics and physical property buildup assumed are not applicable for photopolymerizations.

## 1.5 Thesis Scope

It is clear that some voids exist in curing stress modeling and understanding, especially for photopolymerizations. Part of this is due to of mathematical simplifications used to make earlier calculations easier, part to later development of kinetic theories for rapid photopolymerizations. Also, correlating experimental data to mathematical models is complicated, difficult, and open to interpretation. Experimentalists and modelers sometimes oversimplify the physical phenomena, especially when volume coupling is involved through a nonzero Poisson's ratio or bulk viscosity, by assuming only one dimension is important. Measuring the volume change upon polymerization may not yield the stress-free state change because of substrate constraints and the neglection of volume coupling.

This thesis aims to fill some voids in the understanding of stress generation during photopolymerization of coatings. First, a more explicit difference between the stress-free state and the shrinkage will be discussed. Second, a viscoelastic model that can be solved in two or three dimensions to account for nonuniformities in reaction or geometry and includes a constitutive equation with volume coupling will be presented. Third, a realistic description of how the stress-free state and physical properties change in time during cure will be developed. Combining these ideas will extend the understanding of stress generation in photopolymerizations. Physical insight gained and calculations performed will allow better design of curing processes.

## 1.6 Thesis Outline

Chapter 2 presents two new mathematical methods for calculating stress and strain in a viscoelastic material. The first method is a network model wherein viscoelastic response is described using a two or three-dimensional network of one-dimensional models. The second method is a continuum model of momentum conservation and linear viscoelasticity. Using a scaling analysis of the forces present during coating solidification, standard numerical differential equation methods, and strain analysis, a new mathematical treatment of the

governing equations is presented that reduces the number of unknowns and allows relaxation analysis. The continuum equations are computed using Galerkin's method with finite element basis functions.

Chapter 3 discusses spatially uniform stress generation in UV cured coatings. Calculation of stresses requires the reaction kinetics to be computed simultaneously and the kinetics of UV initiated multifunctional acrylate photopolymerization are discussed. New methods of calculating the progression of physical properties – the modulus and viscosity – are discussed as well. Buildup of stress and its dependence on polymerization kinetics and the volume of the system are described, as well as methods to alter the final stress. Finally, process windows showing obtainable final states in the coating are discussed.

Chapter 4 discusses how the stress field changes when geometric constraints are imposed and how defects may be brought about in otherwise uniform coatings. Different types, sizes, and distributions of different geometric constraints are included. Stress reduction by nonuniform radiation delivery is also included.

Chapter 5 suggests applications of the stress model presented in this thesis and how it can be extended to other systems. Using the model to optimize coating curing schedules is also included. Finally, avenues for further research that build on this work are presented with an eye for understanding curing processes, stress generation, and the transitions that occur during cure more completely.

# Chapter 2

# Viscoelastic Models

## 2.1 Introduction

Calculating the stress-deformation response of a viscoelastic material is necessary to determine how stress builds up in a curing coating. Standard viscoelastic modeling techniques can not account for time-varying stress-free states, so this chapter introduces two new models capable of accepting a variable stress-free state.

The first builds on network models of Wen (2001) and Rajamani (2005), but adds viscoelastic elements and a variable stress-free state. The next model begins with standard constitutive equations of linear viscoelasticity and rearranges them based on force scaling, equation linearity, and constitutive equation assumptions, producing a new method for solution. Both of these models use constitutive equations common for describing curing coatings, and the limits of the model behave as the limits of the coating, which is applied as a liquid and ends up as an elastic solid.

## 2.2 Introduction to Mechanical Models

Rheologists and viscoelasticians have used mechanical models to illustrate, visualize, and describe processes involved in viscoelastoplastic deformation of real materials. Each mechanical model on its own represents a single simple phenomena; linear elasticity, linear

viscosity, plastic yielding, and changing internal state. Combinations of these simple models are used to reproduce the behavior of complex viscoelastoplastic systems. The way models are combined determine the response of the system to external stimuli, which is matched to the way the real material responds. Because the models are one-dimensional, these external stimuli are slightly altered: stresses become forces and strains (or deformations) become displacements. The goal in using these models is to determine how a material will deform without measuring item, lending some insight into what is happening locally in the material. Sobotka (1984), whose work makes extensive use of mechanical models, states that fundamental relations must be accounted for: stress-strain, stress-strain rate, stress-time, and strain-time. By combining simple models, different types of stress-strain-time behavior can be observed, and by combining the constitutive equations of the models, the stress-strain-time behaviors can be calculated mathematically. Response of mechanical models is chosen to match the 'full' constitutive equations in certain geometries, sometimes more than one model will be appropriate for a single material, usually because the isotropic and deviatoric components of stress and strain behave differently (Bland 1959).

### 2.2.1 Simple One-Dimensional Models

Each one-dimensional model used in the investigation of viscoelastic behavior replicates a single material response, with combinations of models replicating more complicated behavior. One-dimensional models, seen in Table 2.2.1 and Figure 2.1, are the spring, dashpot, stick-yield, and shrinker. Stress is the force in an element and will be given the symbol $\sigma$. Strain is the normalized change in length from the equilibrium or stress-free length of an element, $\varepsilon \equiv \frac{e}{L_o} = \frac{L-L_o}{L_o}$ where $\varepsilon$ is the strain, $e = L - L_o$ is the extension, $L$ is the current length, and $L_o$ is the stress-free length. Each element is bordered by nodes which can be connected to other elements or boundaries.

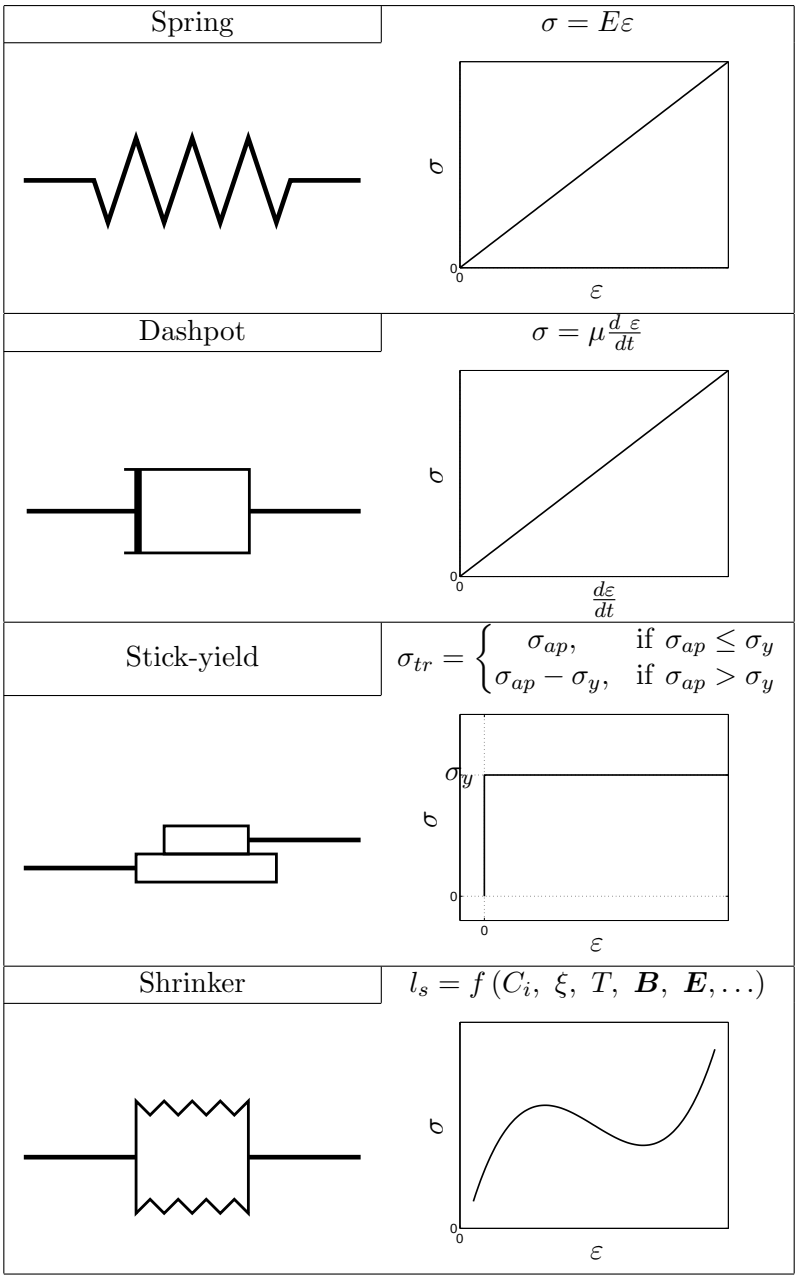


Figure 2.1: One-dimensional elements.

| Element | Represents | Behavior |
|---|---|---|
| Spring | Hookean solid | Elastic |
| Dashpot | Newtonian liquid | Viscous |
| Stick-yield | St. Venant plastic | Plastic yielding, flow, and deformation |
| Shrinker | Ideal solution or internal state | Stress free state |

Table 2.1: One-dimensional elements.

**Spring**

The one-dimensional spring models linear elastic stress-strain behavior. The relationship between stress and strain is linear and the constant of proportionality is the modulus.

$$\sigma = E\varepsilon \tag{2.1}$$

This is Hooke's law when $E$ is the modulus of the spring.

**Dashpot**

The one-dimensional dashpot models viscous flow, as a piston moving in a cylinder of viscous liquid. The relationship between stress and strain *rate* is linear, with viscosity as the constant of proportionality.

$$\sigma = \mu \frac{d\,\varepsilon}{dt} \tag{2.2}$$

This is Newton's law of viscosity for shear deformations. Dashpot strain represents a change in the stress-free state.

**Stick-yield**

The one-dimensional stick-yield models plastic flow, yielding, and deformation.

$$\sigma_{tr} = \begin{cases} \sigma_{ap}, & \text{if } \sigma_{ap} \leq \sigma_y \\ \sigma_{ap} - \sigma_y, & \text{if } \sigma_{ap} > \sigma_y \end{cases} \tag{2.3}$$
$$\frac{d\varepsilon}{dt} = 0, \text{ if } \sigma_{ap} \leq \sigma_y$$

$\sigma_{tr}$ is the transmitted stress, $\sigma_y$ is the yield stress, and $\sigma_{ap}$ is the applied stress. Post-yield deformation of the element represents a change in the stress-free state. The stick-yield behaves as a frictional block on a horizontal surface with identical static and kinetic frictional forces.

**Shrinker**

The one-dimensional shrinker element represents changes in the internal stress-free state of a material. As a coating solidifies, the physical properties of the coating change and the accompanying stress free state changes as a function of those properties. The concentration of chemical species, temperature, extent of reaction, and any applied potential fields such as magnetic or electric determine the stress-free state, though there may be other dependencies such as microstructure, molecular weight, chain entanglement characteristics, or polymer architecture. In an unconstrained system, the change in stress free state results in an isotropic change in volume. The constriction of volume in a solidifying coating has been given the following names based on the cause: *solutostriction* is caused by change in the concentrations of chemical species, *thermostriction* is caused by change in temperature, *chemostriction* is caused by chemical reaction, *electrostriction* is caused by change in polarization or applied electric field, and *magnetostriction* is caused by change in applied magnetic field. One or more of these thermodynamic functions may be active at one time, complicating the stress-free state change in time.

The shrinker element transmits all stress from one end of to the other and is not influenced by stress imposed upon it. The length of the shrinker is a function of the independent variables listed above and since they change with time, the shrinker's length also changes with time. To model real behavior, the shrinker is always combined with spring, dashpot, or stick-yield element. The one-dimensional constitutive equation for a shrinker is

$$l_s = f\left(C_i,\ \xi,\ T,\ \boldsymbol{B},\ \boldsymbol{E}, \ldots\right) \tag{2.4}$$

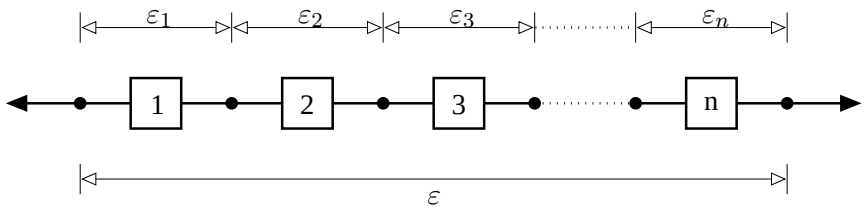


Figure 2.2: Series combination of elements.

Where $l_s$ is the length of the shrinker.

### 2.2.2 Combining Elements

To model multiple properties like elasticity, viscosity, plasticity, and internal state change simultaneously, the one-dimensional elements can be combined in series or parallel. Series combinations attach one model directly to another one in a linear fashion. Each element is free to strain independently, but every element shares the same stress

$$\begin{aligned} \sigma_{series} &= \sigma_1 = \sigma_2 = \ldots = \sigma_n \\ \varepsilon_{series} &= \sum_{i=1}^{n} \varepsilon_i \end{aligned} \tag{2.5}$$

Parallel combinations attach all models to a common end rail. Each element has equal strain, but the overall stress is a sum of the stress of constituent elements.

$$\begin{aligned} \varepsilon_{parallel} &= \varepsilon_1 = \varepsilon_2 = \ldots = \varepsilon_n \\ \sigma_{parallel} &= \sum_{i=1}^{n} \sigma_i \end{aligned} \tag{2.6}$$

Complicated behavior can be approximated by combining models into elements as well as combining elements into larger composite elements.

#### Ideality of Models

It is instructive to think of mechanical models deforming as an aid to understanding stress-strain behavior and relaxation. However, every one-dimensional mechanical model is assumed to be ideal, they have zero mass and do not have to accelerate to a final state, they

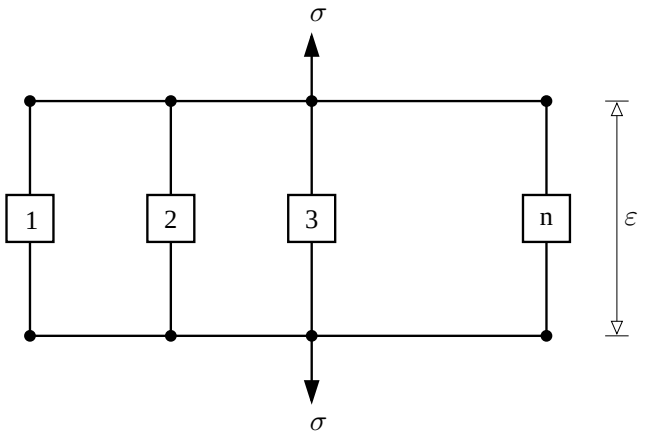


Figure 2.3: Parallel combination of elements.

respond instantly to external stimuli. Connections between models to make elements are rigid and do not allow rotation, while connections between elements to form a network are made with pin joints and allow unhindered rotation.

For models to behave physically, there are some constraints that must be imposed upon them. Departure from the stress-free state is elastic strain, so a shrinker must be in series with a spring. If the stress-free state changes without a corresponding strain, the resulting stress will be elastic. Also, a stick-yield must be in parallel with a spring or dashpot. Since the stick-yield offers no control over post-yield behavior above the support of the yield stress, another element must be included to control the yielding state.

### 2.2.3 Combinations of Elements for Viscoelastic Modeling

The ways of combining models to make elements that approximate real behavior are unbounded. The elements used and method of connection depend on the material to be modeled and range from simple to very complicated. Rheology and viscoelasticity analysis historically has used spring, dashpot, and stick-yield elements to model rheological behavior. The shrinker is a novel element designed for materials with a changing internal state. Elements using the historical rheological models will be presented first, then the introduction of the shrinker will take into account changing stress free state in a series of new elements.

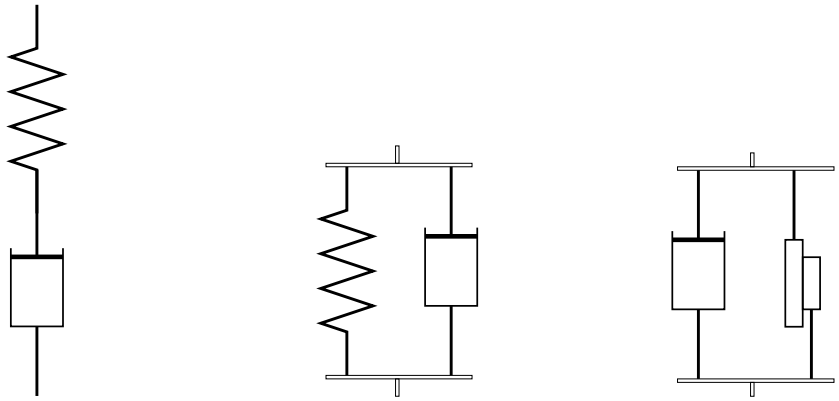

(a) Maxwell element. (b) Voigt element. (c) Bingham plastic element.

Figure 2.4: Two-model elements

**Viscoelastic Maxwell Element**

The simplest viscoelastic element was first proposed by Maxwell (1867) for modeling fluid viscosity and has since been adopted to model viscoelastic behavior. The Maxwell element consists of a spring and dashpot connected in series. The element is both viscous and elastic, but viscous at long times. Stress imposed on the element can relax. The overall strain in each element and can be related to the overall stress and derivative of stress.

This constitutive equation is virtually identical to the Maxwell continuum constitutive equation, Equation (1.3).

$$\frac{d\varepsilon}{dt} = \frac{1}{E}\frac{d\sigma}{dt} + \frac{1}{\mu}\sigma \tag{2.7}$$

**Elastoviscous Voigt Element**

The Voigt or Kelvin element consists of a single spring and dashpot in series. The element represents elastoviscous behavior; it is both viscous and elastic, but elastic at long times. In contrast to the Maxwell element's viscous long-time behavior, stress imposed on the Voigt element cannot relax away.

$$\sigma = E\varepsilon + \mu\frac{d\varepsilon}{dt} \tag{2.8}$$

**Bingham Plastic Element**

The Bingham plastic element represents perfect plasticity and consists of a stick-yield in parallel with a dashpot. The dashpot represents the post-yield viscosity of the element. There is no strain if the applied stress is less than the yield stress.

$$\frac{d\varepsilon}{dt} = \begin{cases} 0, & \text{if } \sigma_{ap} \leq \sigma_y \\ \frac{\sigma_{ap}-\sigma_y}{\mu}, & \text{if } \sigma_{ap} > \sigma_y \end{cases} \tag{2.9}$$

Three and more elements may be combined to model more complicated behavior, but they will not be used in this thesis and are not included here. Sobotka (1984) has an extensive discussion about combining more mechanical models in different ways to duplicate more behaviors.

**Boundary Conditions**

Boundary and initial conditions chosen to solve the differential equations of various combinations of mechanical models depend on the initial state of the material and its physical constraints. For a material that is initially in equilibrium at its stress-free state, initial stress and strain can both be taken to be zero. Also, the position of at least one node is kept fixed, to eliminate strain from solid-body translation. For certain geometries, the position of both nodes may be fixed, and stress can be generated internally without strain.

### 2.2.4 Response of a Viscoelastic Maxwell Element

The response of simple viscoelastic elements to prototypical stimuli can illustrate the behavior these elements are designed to approximate. Step stresses and step strains are limiting cases of the stimuli seen in general, and the response of the Maxwell and Voigt element to these limiting cases is detailed below.

Solving Equation (2.7) to illustrate the behavior for a Maxwell element's response to typical problems can lend some insight to the model. If a step stress is applied, $\sigma = \sigma_o$ for $t > 0$, then

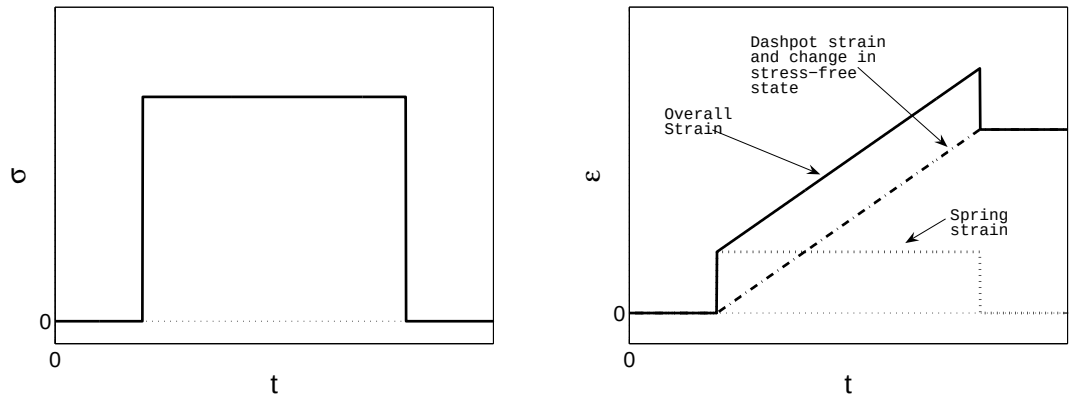


(a) Stress (b) Strain

Figure 2.5: Step stress response of a Maxwell element.

$$\varepsilon = \frac{\sigma_o}{E} + \frac{\sigma_o t}{\mu} \tag{2.10}$$

There is immediate elastic, recoverable deformation followed by viscous flow, commonly called creep. This element exhibits viscous behavior at long times, the applied stress causes constant motion. Figure 2.5 displays the response of the Maxwell element. As the element deforms, the strain in the dashpot represents a changing stress-free state. When the stress is stopped, there is elastic recovery from the spring, but the element has a new, deformed stress-free state.

If a step strain $\varepsilon = \varepsilon_o$ is imposed, the initial stress is purely elastic, with relaxation to a stress-free state at long times to eliminate the stress.

$$\sigma = \varepsilon_o E \ \exp\left[\frac{-E}{\mu} t\right] \tag{2.11}$$

The imposed step strain is immediately all elastic and relaxes away exponentially as time progresses. The ratio of dashpot viscosity to spring modulus is commonly called the relaxation time since it has units of time. This characteristic time signifies the when the stress has dropped to $\frac{1}{e}$ of the original value. As with the step stress, the dashpot deformation represents a change in the stress-free state.

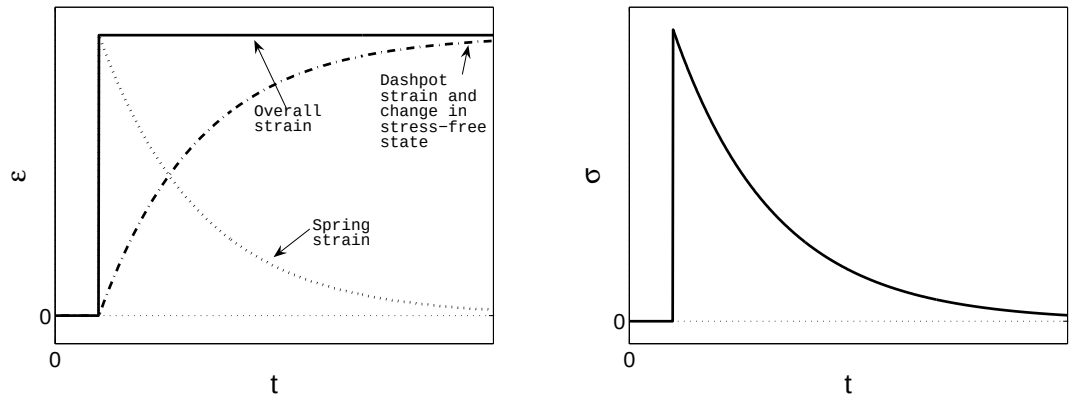


(a) Strain (b) Stress

Figure 2.6: Step strain response of a Maxwell element.

## 2.3 Network Modeling of Viscoelasticity

### 2.3.1 Introduction

Modeling deformation and stress in the interior of a viscoelastic material is complicated. The relationship between deformation and stress generation may be complicated by the introduction of time derivatives, nonuniform physical properties such as modulus, viscosity, or relaxation time, or nonlinear constitutive equations. In general, neither deformation nor stress are known a priori and must be calculated simultaneously. Monomers or oligiomers undergoing polymerization and crosslinking create a complication when domain-spanning networks begin to form, as physical properties change nonuniformly by orders of magnitude.

Network modeling – connecting one-dimensional elements into two or three-dimensional networks – has been used to determine the stress and deformation in materials whose constitutive behavior has been complicated by material discontinuity, internal structures, or viscoelasticity. Networks whose elements form rigid structures are the basis for rigidity percolation modeling (Thorpe 1983, Day et al. 1986). This technique has been used in network elastic solids and polymer networks (Hamlen 1991). Wen (2001) used rigidity percolation modeling in concert with her kinetic gelation model to calculate the macroscopic modulus development with polymer network formation. Her analysis was constructed to

be a simple way to estimate post-percolation modulus development from curing reactions in a polymer coating. This thesis extends this analysis to include calculating stress and deformation of the network from changes in the equilibrium stress-free state.

Bland (1960) states "the microscopic structure of a linear viscoelastic material is mechanically equivalent to a network of linear viscous and elastic elements." It is in this way that linear viscoelastic stress and deformation behavior can be calculated using one-dimensional mechanical models. Also, a "three dimensional viscoelastic material can be approximated by tessellating the material into regular polygons or parallelepipeds of equal size." The edges of the subdivisions are elements and are joined at the vertices by nodes, which are assumed to deform affinely with the rest of the material. Rajamani (2005) used these ideas to see the response of networks of elastic or viscous elements using springs or dashpots, respectively. His work also included hybrid networks which connected different nodes with springs or dashpots in an attempt to duplicate viscoelastic behavior. The procedure for transition from a viscous dashpot to an elastic spring was similar to kinetic gelation work of Wen (2001), and included inserting the springs in a stretched state to model the stress-free state change upon reaction and its subsequent shrinkage of the material. The downside to the Rajamani type of viscoelastic network model is the lack of viscoelastic elements between nodes. Each node has a purely elastic or viscous element joining it to a neighboring node. This restricts the viscoelastic behavior locally. Additionally, as the kinetic gelation continues and more springs appear in the network, the possibility of a rigid elastic sub-networks becomes possible, essentially eliminating viscous behavior entirely, much like the rigid networks of rigidity percolation simulations. Finally, by accounting for stress-free state changes by inserting stressed elastic elements, all stress-free change is quantized in a single event instead of the continuous function it actually is. These downsides warrant additional investigation and improvement in linear viscoelastic network modeling.

One complication in viscoelastic network modeling is at what scale the network behavior matches polymer material behavior. The origins of viscoelasticity in polymers comes

from their macromolecular nature. Large chain molecules must slide past one another, can become entangled in one another, have changeable conformations that pervade large amounts of space, and can be covalently bonded to each other via crosslinking. As chemical curing reactions take place, polymer chains grow, entangle, and transition from monomers to lightly and then highly crosslinked networks.

Clearly, the network model assumes the network spacing is 'big enough.' That is, the nodes are spaced and elements are sized to capture linear viscoelastic behavior in the polymer between nodes. The connections between elements must also be appropriate for polymer behavior which is why freely rotating pin-style joints are chosen over rigid joints commonly used in rigidity percolation modeling. This choice is made because polymer chains are flexible.

This section describes the creation of a new network model of viscoelasticity. In contrast to previous models, the one presented in this thesis includes linear viscoelastic elements between each node. It also includes the use of shrinker elements (as detailed above) to account for the effect of a continuously changing stress-free state. The mathematics is presented in steps, adding one feature at a time to a simple network of spring elastic elements. The geometry in more than one dimension and description of nodal connections is also detailed. For simplicity, the analysis is restricted to two-dimensions, though extension to three-dimensions would be straightforward with the method presented. Drawbacks of network modeling are also discussed.

### 2.3.2 Network of Springs

As a primer to the viscoelastic element, springs are connected between a close packed array of nodes and the elastic response of the system is observed. The formulation takes advantage of the incidence array or matrix, a collection of information about element-node connectivity. The incidence array is often used in modeling electrical circuits containing resistors, capacitors, and inductors. The displacement of every node from its initial position is recorded as the network deforms. This is inconsequential for the pure elastic or

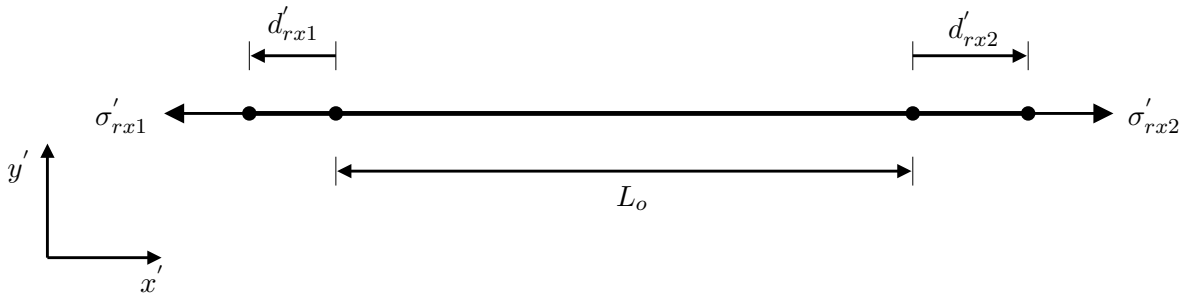


Figure 2.7: One dimensional geometry in the local frame of reference.

viscous case, but presents an interesting challenge when the stress free equilibrium position is changing. The analysis begins in coordinates local to each element.

**Local Coordinates — Basis Vector Method**

The constitutive equation for a spring can be related to the extension,

$$\sigma = E\varepsilon = \frac{E}{L_o}e = \frac{E}{L_o}\Delta d. \tag{2.12}$$

$\sigma$ is the stress in the spring, E is the modulus, $\varepsilon$ is the strain in a direction parallel to the element, $L_o$ is the equilibrium length of the spring, and $e = \Delta d$ is the extension, or net change in displacement parallel to the element. $\sigma > 0$ implies the spring is in tension. In the local frame of reference, there is only one element and two nodes.

Define local variables to element '$r$' with a prime($'$). Local variables are *defined* to have the $x$-axis parallel to the element and the $y$-axis perpendicular. If $\boldsymbol{e'_1}$ and $\boldsymbol{e'_2}$ are the unit vectors in the $x'$ and $y'$ directions, respectively, and the displacement of node j is $d'_{xj}$ in the $x$ direction and $d'_{yj}$ in the $y$ direction, as in Figure 2.7, the displacement can be written as

$$\boldsymbol{d'_j} = d'_{xj}\boldsymbol{e'_1} + d'_{yj}\boldsymbol{e'_2}. \tag{2.13}$$

Subtracting the displacements yields the extensions in the element in each direction, and in vector form,

$$\begin{aligned} \boldsymbol{d}_{\boldsymbol{rx}}^{'} &= d_{x2}^{'}\boldsymbol{e}_{\mathbf{1}}^{'} - d_{x1}^{'}\boldsymbol{e}_{\mathbf{1}}^{'} \\ \boldsymbol{d}_{\boldsymbol{ry}}^{'} &= d_{y2}^{'}\boldsymbol{e}_{\mathbf{2}}^{'} + d_{y1}^{'}\boldsymbol{e}_{\mathbf{2}}^{'} \\ \boldsymbol{\Delta d}_{\boldsymbol{r}}^{'} &= \Delta d_{rx}^{'}\boldsymbol{e}_{\mathbf{1}}^{'} + \Delta d_{ry}^{'}\boldsymbol{e}_{\mathbf{2}}^{'}. \end{aligned} \tag{2.14}$$

Local basis vectors are defined according to the position of the element. Since all of the viscoelastic elements are one dimensional, this assures the extension in any $y^{'}$ direction will be zero. The one dimensional constitutive equation for a spring becomes

$$\boldsymbol{\sigma}_{\boldsymbol{r}}^{'} = \frac{E_r}{L_o}\boldsymbol{e}_{\mathbf{1}}^{'}\ \boldsymbol{e}_{\mathbf{1}}^{'} \cdot \boldsymbol{\Delta d}_{\boldsymbol{r}}^{'} = \boldsymbol{K}_{\boldsymbol{r}}^{'} \cdot \boldsymbol{\Delta d}_{\boldsymbol{r}}^{'}, \tag{2.15}$$

in local coordinates. $\boldsymbol{K}_{\boldsymbol{r}}^{'}$ is the stiffness tensor in element $r$.

**Global Coordinates — Basis Vector Method**

Every element has local coordinates that may be different from other elements in the network. This necessitates a transformation of local coordinates to global ones, as in a laboratory frame of reference. Using global coordinates to measure nodal displacement ensures all elements can use the same set of displacements regardless of the orientation of the element. If $\boldsymbol{e_i}$ are the basis vectors in the global frame and $\alpha_r$ is the rotation angle, as in Figure 2.8, a rotation can be written as

$$\boldsymbol{d_{rj}} = \sum_i \boldsymbol{e}_{\boldsymbol{i}}^{'}\boldsymbol{e_i} \cdot \boldsymbol{d}_{\boldsymbol{rj}}^{'} = \boldsymbol{R_r} \cdot \boldsymbol{d}_{\boldsymbol{rj}}^{'}, \tag{2.16}$$

where $\boldsymbol{R_r} = \boldsymbol{e}_{\mathbf{1}}^{'}\boldsymbol{e_1} + \boldsymbol{e}_{\mathbf{2}}^{'}\boldsymbol{e_2}$ is the rotation dyadic in two dimensions. Similarly,

$$\boldsymbol{\Delta d_r} = \boldsymbol{R_r} \cdot \boldsymbol{\Delta d}_{\boldsymbol{r}}^{'} \tag{2.17}$$

$$\boldsymbol{\sigma_r} = \boldsymbol{R_r} \cdot \boldsymbol{\sigma}_{\boldsymbol{r}}^{'}. \tag{2.18}$$

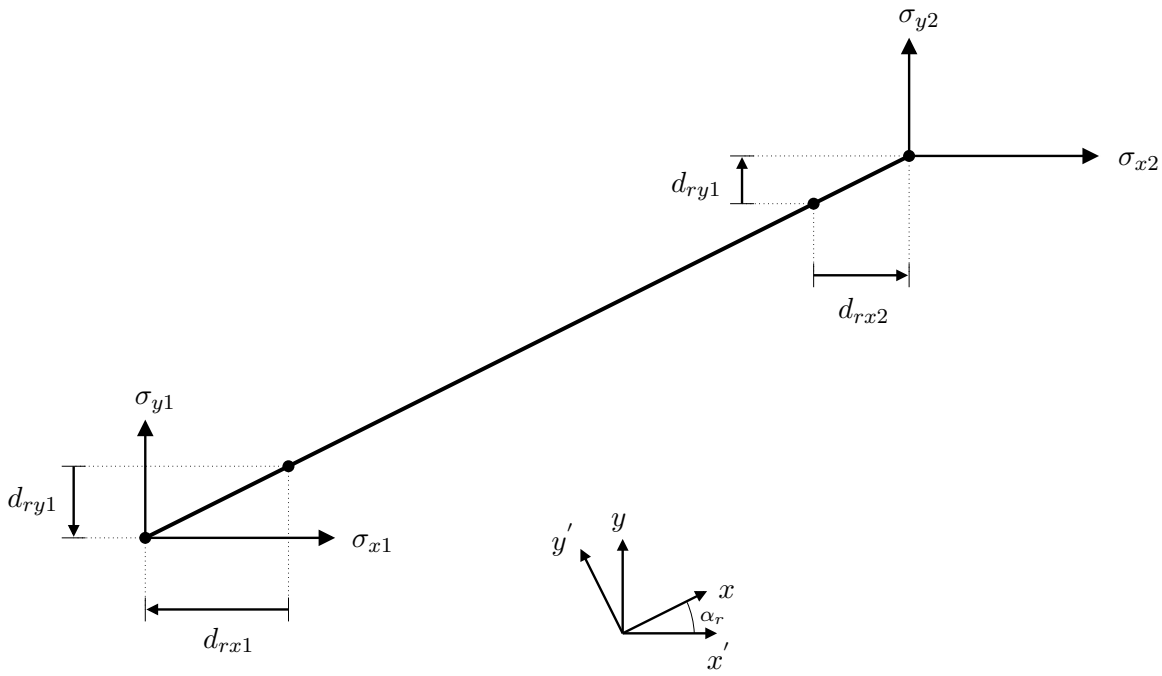


Figure 2.8: Geometry transformation from local to global coordinates.

$\boldsymbol{R}$ is an orthogonal rotation, so $\boldsymbol{R^T} = \boldsymbol{R^{-1}}$ and

$$\boldsymbol{\Delta d_r^{'}} = \boldsymbol{R_r} \cdot \boldsymbol{\Delta d_r} \tag{2.19}$$

$$\boldsymbol{\sigma_r^{'}} = \boldsymbol{R_r} \cdot \boldsymbol{\sigma_r}. \tag{2.20}$$

Substituting to resolve the stress in the element in global coordinates as a function of displacement in global coordinates yields,

$$\boldsymbol{\sigma_r^{'}} = \boldsymbol{K_r^{'}} \cdot \boldsymbol{\Delta d_r^{'}} \tag{2.21}$$

$$\boldsymbol{\sigma_r^{'}} = \boldsymbol{K_r^{'}} \cdot \boldsymbol{R_r^T} \cdot \boldsymbol{\Delta d_r} \tag{2.22}$$

$$\boldsymbol{\sigma_r} = \boldsymbol{R_r} \cdot \boldsymbol{K_r^{'}} \cdot \boldsymbol{R_r^T} \cdot \boldsymbol{\Delta d_r}. \tag{2.23}$$

### Local Coordinates — Matrix and Component Method

Computational mathematics used in network analysis store and manipulate components and matrices instead of basis vectors and tensors to represent stresses, displacements, and rotations. The two methods are equivalent, but the basis vector method is more general and theoretically satisfying while the matrix-component method is closer to computational practice. The displacement of node $j$ in coordinates local to element '$r$' is $\boldsymbol{d'_{rj}} = \begin{bmatrix} d'_{rxj} \\ d'_{ryj} \end{bmatrix}$

The displacement from equilibrium in the $x'$-direction, perpendicular to the element is $\Delta d'_{rx} = d'_{rx2} - d'_{rx1}$. Similarly, in the $y'$-direction, parallel to the element $\Delta d'_{ry} = d'_{ry2} - d'_{ry1} = 0$, since the pin-joints allow no net displacement in the $y'$ direction. The total extension is given by

$$\boldsymbol{\Delta d'_r} = \begin{bmatrix} \Delta d'_{rx} \\ \Delta d'_{ry} \end{bmatrix} = \begin{bmatrix} d'_{rx2} - d'_{rx1} \\ d'_{ry2} - d'_{ry1} \end{bmatrix}, \tag{2.24}$$

and the stress in the element by

$$\boldsymbol{\sigma'_r} = \begin{bmatrix} \sigma'_{rx} \\ \sigma'_{ry} \end{bmatrix} = \begin{bmatrix} \frac{E_r}{L_o} & 0 \\ 0 & 0 \end{bmatrix} \begin{bmatrix} \Delta d'_{rx} \\ \Delta d'_{ry} \end{bmatrix} = \boldsymbol{K'_r}\ \boldsymbol{\Delta d'_r}, \tag{2.25}$$

which is very similar to the stress-displacement relation using the basis vector method, given in Equation (2.15).

### Global Coordinates — Matrix and Component Method

Rotate local coordinates to global ones, as in Equation (2.16), with the rotation matrix. The rotation angle, $\alpha_r$, is the angle global coordinates must be rotated to become parallel to local coordinates in element $r$,

$$\boldsymbol{d_{rj}} = \begin{bmatrix} d_{xrj} \\ d_{yrj} \end{bmatrix} = \begin{bmatrix} \cos(\alpha_r) & -\sin(\alpha_r) \\ \sin(\alpha_r) & \cos(\alpha_r) \end{bmatrix} \begin{bmatrix} d'_{xrj} \\ d'_{yrj} \end{bmatrix} = \boldsymbol{R_r}\ \boldsymbol{d'_{rj}} \tag{2.26}$$

$$\boldsymbol{\Delta d_r} = \boldsymbol{R_r}\ \boldsymbol{\Delta d_r^{'}} \tag{2.27}$$

$$\boldsymbol{\sigma_r} = \boldsymbol{R_r}\ \boldsymbol{\sigma_r^{'}}. \tag{2.28}$$

Because $\boldsymbol{R}$ is an orthogonal matrix, $\boldsymbol{R}^T = \boldsymbol{R}^{-1}$, and

$$\boldsymbol{\sigma_r^{'}} = \boldsymbol{R_r^T}\boldsymbol{\sigma_r} \tag{2.29}$$

$$\boldsymbol{\Delta d_r^{'}} = \boldsymbol{R_r^T}\boldsymbol{\Delta d_r}. \tag{2.30}$$

substituting the rotation into Equation (2.25) yields

$$\boldsymbol{\sigma_r^{'}} = \boldsymbol{K_r^{'}}\ \boldsymbol{\Delta d_r^{'}} \tag{2.31}$$

$$\boldsymbol{\sigma_r^{'}} = \boldsymbol{K_r^{'}}\ \boldsymbol{R_r^T}\ \boldsymbol{\Delta d_r} \tag{2.32}$$

$$\boldsymbol{\sigma_r} = \boldsymbol{R_r}\ \boldsymbol{K_r^{'}}\ \boldsymbol{R_r^T}\boldsymbol{\Delta d_r}. \tag{2.33}$$

**Equality of the Methods**

Any rigid rotation of coordinate axes can be written as

$$\boldsymbol{v} = \sum_i \boldsymbol{e_i}\ \boldsymbol{e_i^{'}} \cdot \boldsymbol{v}^{'} = \boldsymbol{R} \cdot \boldsymbol{v}^{'}, \tag{2.34}$$

and with a basis set $\mathcal{B}$, any general dyadic $\boldsymbol{ab}$ can be decomposed into its basis vectors and components,

$$\boldsymbol{ab} = \mathcal{B}^T \left[ (\boldsymbol{a}) \left( \boldsymbol{b}^T \right) \right] \mathcal{B} = [\boldsymbol{e_1}\ \boldsymbol{e_2}\ \boldsymbol{e_3}] \begin{bmatrix} a_1 \\ a_2 \\ a_3 \end{bmatrix} \begin{bmatrix} b_1 & b_2 & b_3 \end{bmatrix} \begin{bmatrix} \boldsymbol{e_1} \\ \boldsymbol{e_2} \\ \boldsymbol{e_3} \end{bmatrix}$$

$$= [\boldsymbol{e_1}\ \boldsymbol{e_2}\ \boldsymbol{e_3}] \begin{bmatrix} a_1 b_1 & a_1 b_2 & a_1 b_3 \\ a_2 b_1 & a_2 b_2 & a_2 b_3 \\ a_3 b_1 & a_3 b_2 & a_3 b_3 \end{bmatrix} \begin{bmatrix} \boldsymbol{e_1} \\ \boldsymbol{e_2} \\ \boldsymbol{e_3} \end{bmatrix}. \tag{2.35}$$

If the basis set of unit vectors is taken to be the global coordinate vectors, $\mathcal{B} = [\boldsymbol{e_1}\ \boldsymbol{e_2}\ \boldsymbol{e_3}]$, then local vectors to element '$r$' can be written as

$$\begin{aligned} \boldsymbol{e_1'} &= \cos(\alpha_r)\,\boldsymbol{e_1} + \sin(\alpha_r)\,\boldsymbol{e_2} \\ \boldsymbol{e_2'} &= -\sin(\alpha_r)\,\boldsymbol{e_1} + \cos(\alpha_r)\,\boldsymbol{e_2} \\ \boldsymbol{e_3'} &= \boldsymbol{e_3}, \end{aligned} \tag{2.36}$$

and the rotation dyadic around the 3-axis can be represented in the general form as

$$\boldsymbol{R} = \boldsymbol{e_1}\ \boldsymbol{e_1'} + \boldsymbol{e_2}\ \boldsymbol{e_2'} + \boldsymbol{e_3}\ \boldsymbol{e_3'} = [\boldsymbol{e_1}\ \boldsymbol{e_2}\ \boldsymbol{e_3}] \begin{bmatrix} \cos(\alpha_r) & -\sin(\alpha_r) & 0 \\ \sin(\alpha_r) & \cos(\alpha_r) & 0 \\ 0 & 0 & 1 \end{bmatrix} \begin{bmatrix} \boldsymbol{e_1} \\ \boldsymbol{e_2} \\ \boldsymbol{e_3} \end{bmatrix}. \tag{2.37}$$

If the 3-direction is omitted in the two dimensional problem considered here, the rotation dyadic in Equation (2.16) and the rotation matrix in Equation (2.26) are identical.

### Transformation to Network-Wide Variables

The constitutive equations for each element, transformed from the local to global domain, can be combined to form a single constitutive equation for the entire network. Making global

network variables out of the global elemental variables, the global constitutive equation can be written as

$$\boldsymbol{\sigma} = \boldsymbol{R}\ \boldsymbol{K}'\ \boldsymbol{R}^{\boldsymbol{T}}\ \boldsymbol{\Delta d}. \tag{2.38}$$

The global network variables are vectors of vectors or matrices of matrices and are listed in the appendix in chapter A.

**Incidence Matrix and Network Topology**

The network formulation of the viscoelastic problem consists of nodes and elements. Information needs to be provided about the connection between nodes to correctly solve the problem. Elements connect nodes, but each element connects two and only two nodes. The topological information of the network is contained in the incidence matrix or incidence array, which was designed by electrical engineers using nodal analysis to solve current and voltage relationships of large networks of electrical components (Litovski and Zwolinski 1997, Ho et al. 1975, Rushdi 1985, Strang 1986). It has also been used to solve conduction problems in porous media (Pathak 1981). The incidence matrix, $\boldsymbol{C}'$, operates on the idea that elements are directed – they have a beginning and an end. It has rows, each of which represent a network node, and columns, each of which represent a network element. If a node is not connected to an element, there is a 0 entry. If the element leaves a node, there is a +1 entry and if the element enters a node, there is a -1 entry. The directionality of each element is arbitrary and can be assigned based on computational convenience

$$C'_{ij} = \begin{cases} -1 & \text{if element j leaves node i} \\ +1 & \text{if element j enters node i} \\ 0 & \text{otherwise} \end{cases}$$

The network stress-displacement system of equations is not linearly independent to solid body translation or rotation. There must be a reference. This is also apparent in

the fact that the columns of the incidence matrix are not linearly independent, each one must sum to zero. In one dimension, one node must be kept fixed to eliminate solid body translation. In two dimensions, two non-identical nodes must be kept fixed to prevent solid body translation and rotation, and in three dimensions, three non-colinear nodes must be kept fixed to prevent solid body translation and rotation. Establishing reference nodes makes the equation system unique. To assign a node to be a reference, the node corresponding to the reference node is deleted from the matrix, fixing its displacement at zero. In a viscoelastic coating, nodes at the coating-substrate interface strongly adhere to the solid and have zero displacement, so they are chosen to be reference nodes. The new reduced form incidence matrix, $\boldsymbol{C}$, is what remains after removing the reference nodes and is used in all calculations from now on

The incidence array can also be manipulated to extract information about the topology of the network. The node-node incidence array, $\boldsymbol{C}\boldsymbol{C}^T$ represents the connectivity between nodes. Diagonal entries in position $(i, i)$ contain the coordination number of node $i$ – how many other nodes are connected to it. Off-diagonal entries in position $(i, j)$ indicate if nodes $i$ and $j$ are connected. The element-element incidence array, $\boldsymbol{C}^T\boldsymbol{C}$ represents the number of common nodes in elements. Diagonal entries in position $(i, i)$ are all 2, indicating that element $i$ shares 2 nodes with itself – one at each end. Off-diagonal entries in position $(i, j)$ indicate the number of nodes element $i$ and $j$ share – in the network formulation, elements can only share 1 node with other elements.

Since there is only beginning and end to each node, each column must have *only* one -1 entry and +1 entry and the sum of any column must be zero. For example, the incidence matrix for Figure 2.9 is

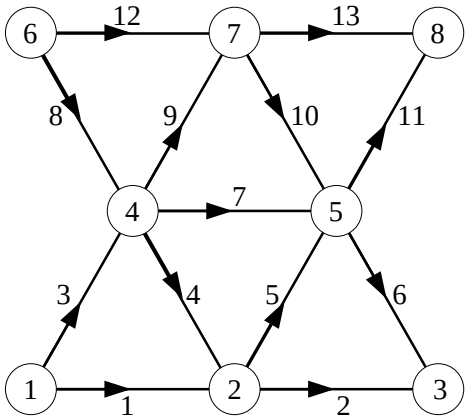


Figure 2.9: Sample Network for Demonstration of Incidence Matrix.

$$\boldsymbol{C}' = \begin{bmatrix} -1 & 0 & -1 & 0 & 0 & 0 & 0 & 0 & 0 & 0 & 0 & 0 & 0 \\ 1 & -1 & 0 & 1 & -1 & 0 & 0 & 0 & 0 & 0 & 0 & 0 & 0 \\ 0 & 1 & 0 & 0 & 0 & 1 & 0 & 0 & 0 & 0 & 0 & 0 & 0 \\ 0 & 0 & 1 & -1 & 0 & 0 & -1 & 1 & -1 & 0 & 0 & 0 & 0 \\ 0 & 0 & 0 & 0 & 1 & -1 & 1 & 0 & 0 & 0 & -1 & 0 & 0 \\ 0 & 0 & 0 & 0 & 0 & 0 & 0 & -1 & 0 & 0 & 0 & -1 & 0 \\ 0 & 0 & 0 & 0 & 0 & 0 & 0 & 0 & 1 & -1 & 0 & 1 & -1 \\ 0 & 0 & 0 & 0 & 0 & 0 & 0 & 0 & 0 & 1 & 1 & 0 & 1 \end{bmatrix}.$$

In reduced form, assuming nodes 1 and 2 are reference nodes, the incidence matrix becomes

$$\boldsymbol{C} = \begin{bmatrix} 0 & 1 & 0 & 0 & 0 & 1 & 0 & 0 & 0 & 0 & 0 & 0 & 0 \\ 0 & 0 & 1 & -1 & 0 & 0 & -1 & 1 & -1 & 0 & 0 & 0 & 0 \\ 0 & 0 & 0 & 0 & 1 & -1 & 1 & 0 & 0 & 0 & -1 & 0 & 0 \\ 0 & 0 & 0 & 0 & 0 & 0 & 0 & -1 & 0 & 0 & 0 & -1 & 0 \\ 0 & 0 & 0 & 0 & 0 & 0 & 0 & 0 & 1 & -1 & 0 & 1 & -1 \\ 0 & 0 & 0 & 0 & 0 & 0 & 0 & 0 & 0 & 1 & 1 & 0 & 1 \end{bmatrix}.$$

### Network-Wide Behavior

The incidence matrix is essential in network deformation analysis since it allows simple calculation of extension in every element and net force on every node. Extension in an element is the difference in the displacements of nodes at each end of the element,

$$\boldsymbol{\Delta d} = \boldsymbol{C^T d}. \tag{2.39}$$

Similarly, the net force on a node is the sum of the stresses from every element connected to the node, plus any forces from external sources, if present.

$$\boldsymbol{C\sigma} = \boldsymbol{f^{external}} \tag{2.40}$$

Equation (2.38), 2.39, and 2.40 can be combined to determine the relationship between external force and nodal displacement in the spring network,

$$\boldsymbol{f^{external}} = \boldsymbol{C\ R\ K'\ R^T\ C^T\ d}. \tag{2.41}$$

### Spring Network Response

A network of springs responds only to external force imposed upon it. The response depends on the modulus of each spring in the network, the network topography, and the external force. Figure 2.10 shows the network response to different stimuli. 2.10 (a) has no boundary conditions other than adherence to the substrate. An external force is imposed upward upon the top row of nodes and the network deforms in response. Force dependence on topology can be seen in the compressive stress in elements oriented horizontally. The vertical external force elongates the network in the vertical direction, causing compressive stress and shrinkage in the horizontal direction. Figure 2.10 (b) has boundary conditions of zero $x$-displacement on vertical boundary nodes imposed by the method described in section 2.3.6. Figure 2.10 (c) has smaller vertical displacement as a result of lower force while (d) has smaller displacement due to larger modulus. The elements bordering the substrate are

stress-free since they cannot move, their springs are always at the equilibrium length.

### 2.3.3 Network of Dashpots

Another prototypical situation preliminary to a viscoelastic network is the viscous network, a network of dashpots only. The stress-strain rate behavior of a dashpot can be related to the extension,

$$\sigma = \mu \frac{d\Delta d}{dt} \tag{2.42}$$

$\sigma$ is the stress in the dashpot, $\mu$ is the viscosity, and $\Delta d$ is the extension parallel to the element. $\sigma > 0$ implies the dashpot is in tension. In the local frame of reference there is only one element and two nodes, and the constitutive equation becomes

$$\boldsymbol{\sigma_r'} = \mu_r \boldsymbol{e_1'}\ \boldsymbol{e_1'} \cdot \frac{d}{dt}\left(\boldsymbol{\Delta d_r'}\right) = \boldsymbol{V_r'} \cdot \frac{d}{dt}\left(\boldsymbol{\Delta d_r'}\right), \tag{2.43}$$

and in global coordinates,

$$\boldsymbol{\sigma_r} = \boldsymbol{R_r} \cdot \boldsymbol{V_r'} \cdot \boldsymbol{R_r^T} \cdot \frac{d}{dt}\left(\boldsymbol{\Delta d_r'}\right). \tag{2.44}$$

The matrix and component method which is to be used for computation, yield

$$\boldsymbol{\sigma_r'} = \begin{bmatrix} \mu & 0 \\ 0 & 0 \end{bmatrix} \frac{d}{dt} \begin{bmatrix} \Delta d_{rx}' \\ \Delta d_{ry}' \end{bmatrix} = \boldsymbol{V_r'}\ \frac{d}{dt}\boldsymbol{\Delta d_r'}, \tag{2.45}$$

and in global coordinates,

$$\boldsymbol{\sigma_r} = \boldsymbol{R_r}\ \boldsymbol{K_r'}\ \boldsymbol{R_r^T} \frac{d}{dt}\boldsymbol{\Delta d_r}. \tag{2.46}$$

Equation (2.46) can describe the behavior of the network with global network variables,

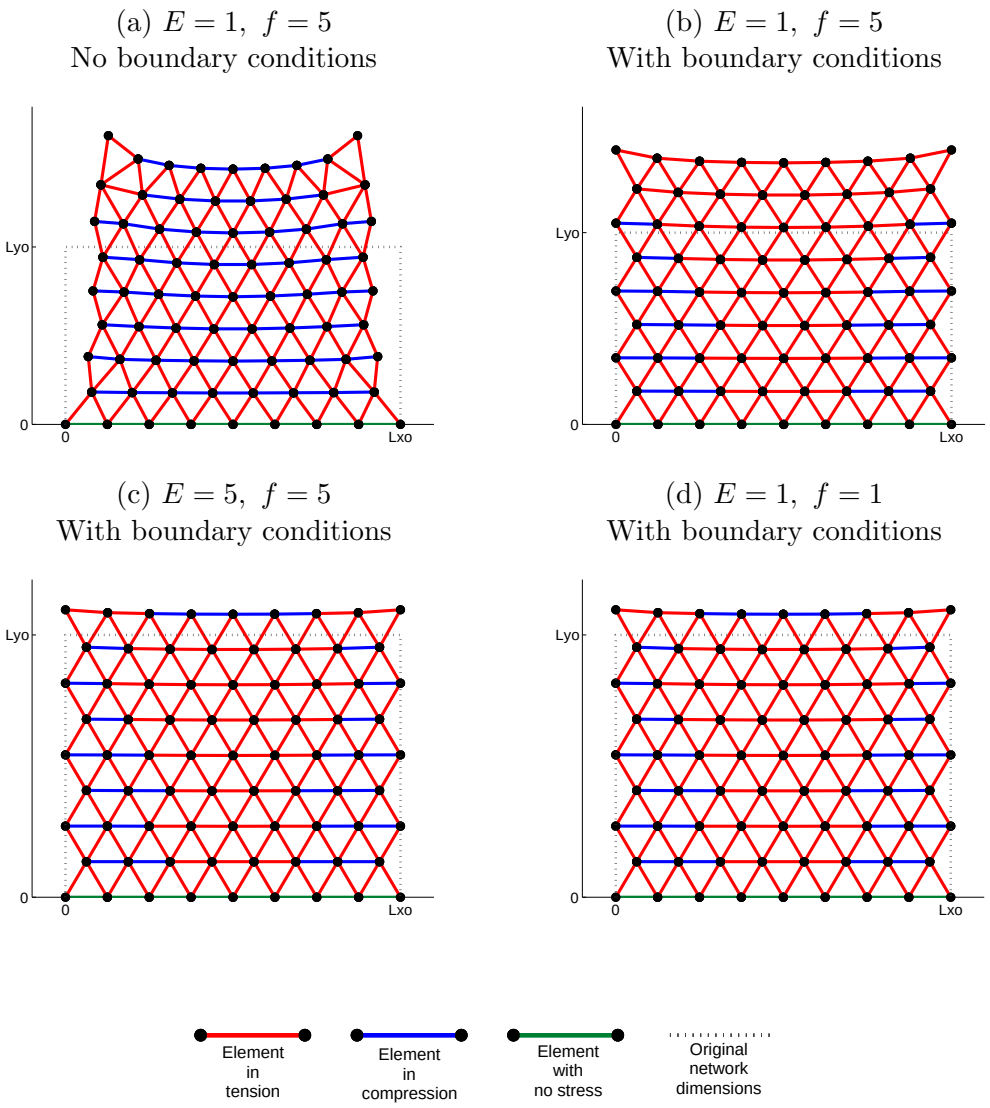


Figure 2.10: Response of a network of springs with various properties – Modulus ($E$) and external force ($f$).

$$\boldsymbol{\sigma} = \boldsymbol{R}\ \boldsymbol{V}'\ \boldsymbol{R}^{\boldsymbol{T}}\ \frac{d}{dt}\boldsymbol{\Delta d} \tag{2.47}$$

$$\boldsymbol{f}^{\boldsymbol{external}} = \boldsymbol{C}\ \boldsymbol{R}\ \boldsymbol{V}'\ \boldsymbol{R}^{\boldsymbol{T}}\ \boldsymbol{C}^{\boldsymbol{T}}\ \frac{d}{dt}\left(\boldsymbol{d}\right). \tag{2.48}$$

**Dashpot Network Response**

A network of dashpots responds only to an external force imposed upon it. The response depends on the viscosity in each dashpot, the magnitude and direction of external force, the network topology, and time. Figure 2.11 shows the network response to an external force. The network is initially in the configuration shown in 2.11 (a). Applying a force initiates movement of the nodes which continues unabated until cessation of the force. Larger forces and smaller viscosities increase deformation rate.

### 2.3.4 Network of Springs with Variable Stress-Free State

The third and final prototypical problem before a viscoelastic network is a network of springs with variable stress-free state. This network consists of nodes connected with a spring and shrinker in series, as in Figure 2.12. The stress in the element is determined solely by the spring and extension in the spring; the shrinker transmits all applied stress and has an extension that does not respond to applied stress. Thus,

$$\begin{aligned} \varepsilon &= \varepsilon_{sp} + \varepsilon_{sh} \\ \varepsilon_{sp} &= \varepsilon - \varepsilon_{sh} \\ \Delta d'_{sp} &= \Delta d' - \Delta d'_{sh}. \end{aligned} \tag{2.49}$$

The stress in the element is determined by the spring alone, so, in local coordinates,

$$\boldsymbol{\sigma}'_{\boldsymbol{r}} = \frac{E_r}{L_o}\boldsymbol{e}'_{\boldsymbol{1}}\ \boldsymbol{e}'_{\boldsymbol{1}} \cdot \left(\boldsymbol{\Delta d}'_{\boldsymbol{r}} - \boldsymbol{\Delta d}'_{\boldsymbol{r,sh}}\right) = \boldsymbol{K}'_{\boldsymbol{r}} \cdot \boldsymbol{\Delta d}'_{\boldsymbol{r}} - \boldsymbol{K}'_{\boldsymbol{r}} \cdot \boldsymbol{\Delta d}'_{\boldsymbol{r,sh}}, \tag{2.50}$$

(a) Initial network configuration

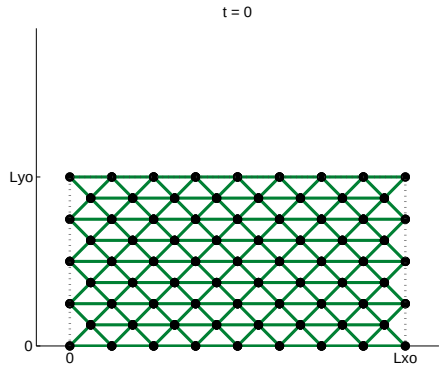


(b) $\mu = 5,\ f = 5$

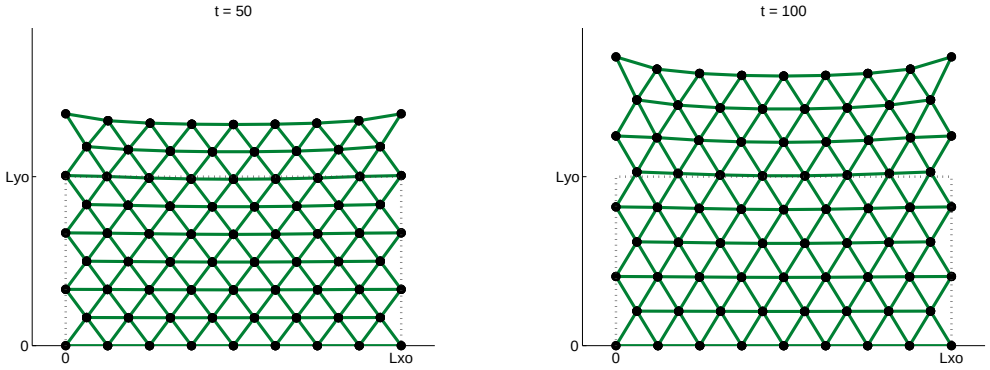


(c) $\mu = 5,\ f = 20$

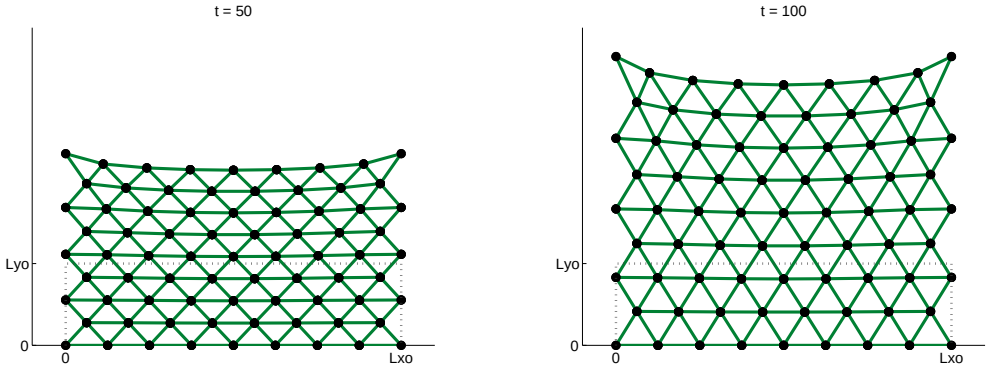


Figure 2.11: Response of a network of dashpots with various properties – Viscosity ($\mu$) and external force ($f$).

Figure 2.12: Spring-shrinker element.

and in matrix notation,

$$\begin{aligned} \boldsymbol{\sigma_r^{'}} &= \begin{bmatrix} \frac{E_r}{L_{or}} & 0 \\ 0 & 0 \end{bmatrix} \left( \begin{bmatrix} \Delta d_{rx}^{'} \\ \Delta d_{ry}^{'} \end{bmatrix} - \begin{bmatrix} \Delta d_{r,sh}^{'} \\ 0 \end{bmatrix} \right) \\ &= \boldsymbol{K_r^{'}\ \Delta d_r^{'} - K_r^{'}\ d_{r,sh}^{'}}. \end{aligned} \tag{2.51}$$

In global network variables,

$$\boldsymbol{\sigma^{'}} = \boldsymbol{R} \tag{2.52}$$

$$tensK^{'}\ \boldsymbol{R^T\ \Delta d - K^{'}\ \Delta d_{sh}} \tag{2.53}$$

$$\boldsymbol{\sigma} = \boldsymbol{R\ K^{'}\ R^T\ \Delta d - RK^{'}\ \Delta d_{sh}} \tag{2.54}$$

$$\boldsymbol{f^{external}} = \boldsymbol{C\ R\ K^{'}\ R^T\ C^T\ d - C\ R\ K^{'}\ \Delta d_{sh}}. \tag{2.55}$$

If the length of the shrinker does not change, $\Delta d_{sh} = 0$, Equation (2.55) reduces to 2.41, the spring only elastic case.

### 2.3.5 Network of Elastoviscous Shrinkage Models

The three-element elastoviscous shrinkage model can be used to model a coating after solidification and before equilibrium concentration, temperature, or extent of reaction have been reached. The three-element elastoviscous shrinker consists of a spring-shrinker combination in parallel with a dashpot. The network response equation is simply the sum of a spring-shrinker and dashpot network.

$$\boldsymbol{f^{external}} = \boldsymbol{C\ R\ K^{'}\ R^T\ C^T\ d + C\ R\ V^{'}\ R^T\ C^T\ \frac{d}{dt}(d) - C\ R\ K^{'}\ \Delta d_{sh}} \tag{2.56}$$

**Elastoviscous Shrinkage Network Response**

A network of elastoviscous shrinkage elements responds to external force as well as change in internal elastic stress-free state. The response depends on the external force, modulus, viscosity, shrinkage, and time. The network in Figure 2.13 was subjected to an instantaneous step shrinkage at $t = 0$. As time progresses and the network deforms toward the new stress-free state, relaxation processes decreases the stress in some elements, slowing the network's movements. When the new stress-free state is reached, motion ceases. The boundary conditions prohibit any relaxation in the in-plane direction, but elements not horizontal can relax to their stress free state.

### 2.3.6 Boundary Conditions

The network formulation of a viscoelastic coating during solidification uses mechanical models to approximate the material response. The end result is a force balance on every node. The only constraints are applied by the reference nodes taken to make the incidence matrix linearly independent. If other boundary conditions are desired, they will have to be applied to the network in another manner.

### 2.3.7 General Boundary Conditions

Boundary conditions are commonplace in the solution of ordinary and partial differential equations, while initial conditions are usually reserved for time-dependent problems. Boundary conditions describe the behavior of the dependent variable or variables at the system boundaries, while initial conditions do so at a reference time. For a general differential equation of space $x, y, z = \boldsymbol{r}$ and time $t$, let there be one dependent variable, $f(\boldsymbol{r}, t)$ for illustration purposes,

$$\mathcal{F}\left(f, \nabla f, \nabla \cdot f, \nabla \cdot \nabla f, \ldots\right) = \mathcal{G}\left(\boldsymbol{r}, t\right),$$

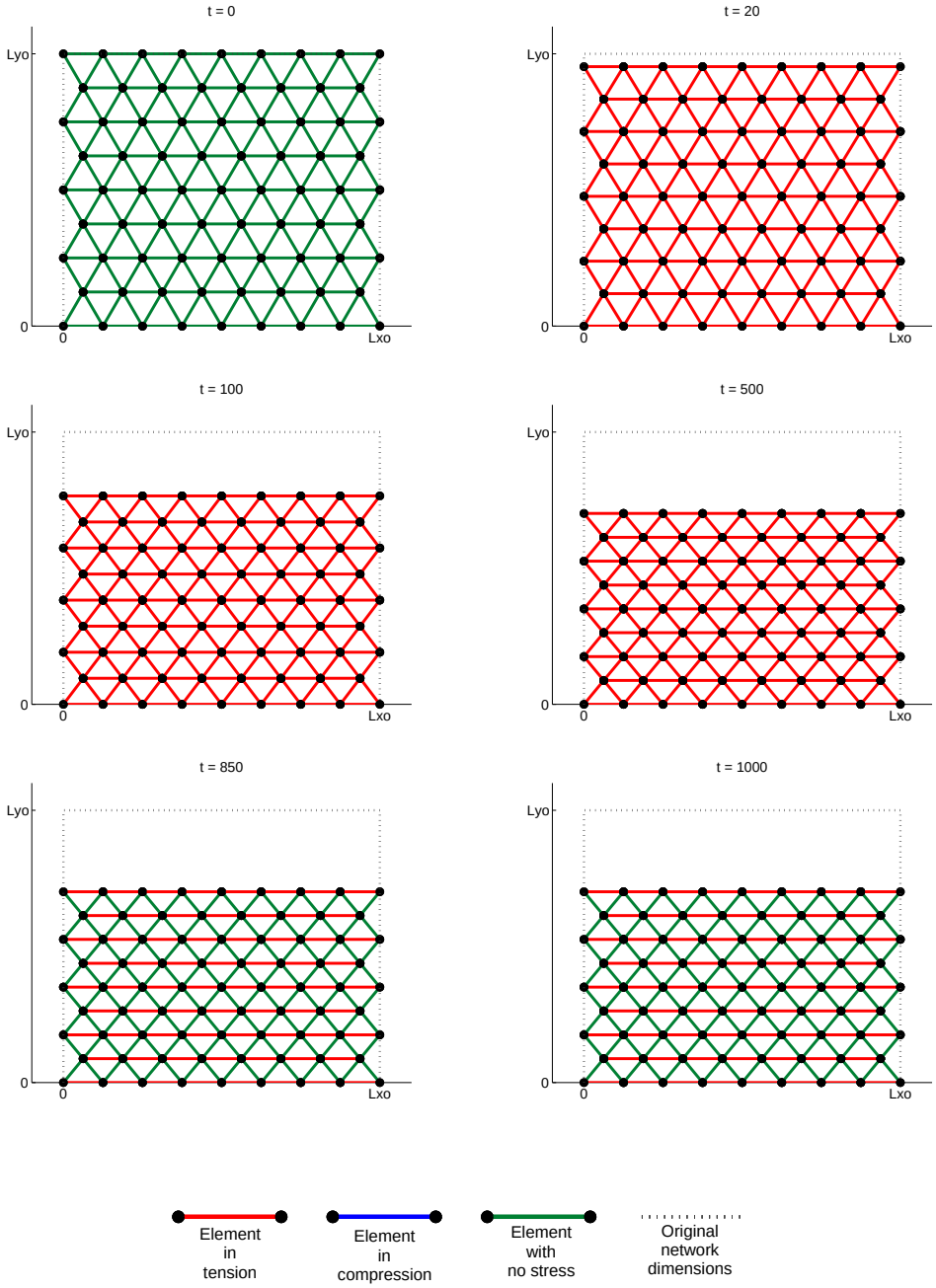


Figure 2.13: Response of a three-element network.

**Neumann**

The Neumann boundary condition sets the value of the dependent variable on the boundary,

$$f = g\left(\boldsymbol{r}, t\right)$$

**Dirichlet**

The Dirichlet boundary condition sets the normal derivative of the dependent variable on the boundary,

$$\frac{\partial f}{\partial n} = \hat{\boldsymbol{n}} \cdot \nabla f = g\left(\boldsymbol{r}, t\right)$$

**Robin**

The Robin boundary condition is the most general of the three types of boundary condition, it relates the dependent variable and its normal derivative on the boundary,

$$\alpha f + \beta \frac{\partial f}{\partial n} = g\left(\boldsymbol{r}, t\right)$$

### 2.3.8 Boundary Conditions In Network Modeling

The network response equation is a system of ordinary differential equations, but the implementation of boundary conditions is unique when network modeling. On the boundary, the displacement and time derivative of displacement (velocity) can be given. Since the network response equation is just a force balance on the nodes, a boundary force is added to enforce the boundary conditions. For example, the displacement of node $i$ is fixed by adding an appropriate boundary force to prevent displacement. The general Robin type boundary condition for node $i$ is

$$\alpha_i d_i + \beta_i \frac{d}{dt}\left(d_i\right) = \gamma_i. \tag{2.57}$$

With this boundary condition, $\alpha_i$, $\beta_i$, or $\gamma_i$ can be functions of time and either $\alpha_i$ or $\beta_i$ should

be zero; setting the displacement *and* velocity of a node results in an overspecified system. Also, every node in the network can have one of these boundary conditions imposed on it, not just the ones on the physical boundary. By setting $\alpha$ or $\beta$ to unity and $\gamma$ to a specified displacement or velocity, the simplest cases of boundary conditions can be decomposed to the following:

$$d_i = d_{fix} \tag{2.58}$$

$$v_i = v_{fix}. \tag{2.59}$$

Since there are two independent dimensions in the network analysis presented here, there can be two independent boundary conditions per node, one in the $x$ and one in the $y$-direction. If every node is assumed to have *both* types of boundary condition, and if the boundary forces from displacement and velocity conditions are $f^{bd,dis}$ and $f^{bd,vel}$ respectively, the network response given in Equation (2.56) can be augmented to nine times its original size by including *both* boundary conditions for each node,

$$\left(\begin{array}{c|cc} \boldsymbol{SP} & \boldsymbol{I} & \boldsymbol{I} \\ \hline \boldsymbol{A} & \mathbf{0} & \mathbf{0} \\ \mathbf{0} & \mathbf{0} & \mathbf{0} \end{array}\right)\left(\begin{array}{c} \boldsymbol{d} \\ \hline \boldsymbol{f^{bd,dis}} \\ \boldsymbol{f^{bd,vel}} \end{array}\right) + \left(\begin{array}{c|cc} \boldsymbol{DP} & \mathbf{0} & \mathbf{0} \\ \hline \mathbf{0} & \mathbf{0} & \mathbf{0} \\ \boldsymbol{B} & \mathbf{0} & \mathbf{0} \end{array}\right)\frac{d}{dt}\left(\begin{array}{c} \boldsymbol{d} \\ \hline \boldsymbol{f^{bd,dis}} \\ \boldsymbol{f^{bd,vel}} \end{array}\right)$$
$$+ \left(\begin{array}{c|cc} \boldsymbol{SH} & \mathbf{0} & \mathbf{0} \\ \hline \mathbf{0} & \mathbf{0} & \mathbf{0} \\ \mathbf{0} & \mathbf{0} & \mathbf{0} \end{array}\right)\left(\begin{array}{c} \boldsymbol{\Delta d_{sh}} \\ \hline \mathbf{0} \\ \mathbf{0} \end{array}\right) = \left(\begin{array}{c} \boldsymbol{f^{external}} \\ \hline \boldsymbol{d^{fix}} \\ \boldsymbol{v^{fix}} \end{array}\right) \tag{2.60}$$

The $\boldsymbol{SP}$, $\boldsymbol{DP}$, and $\boldsymbol{SH}$ entries represent the contributions from springs, dashpots, and shrinkers respectively, in Equation (2.56). $\boldsymbol{A}$ and $\boldsymbol{B}$ represent the $\alpha$ and $\beta$ parameter in equation 2.57 and $\boldsymbol{I}$ is an identity. $\boldsymbol{A}$ is a matrix with $\alpha_i$ entries in the $A(i,i)$ position,

where $\alpha_i = \begin{bmatrix} \alpha_{ix} & 0 \\ 0 & \alpha_{iy} \end{bmatrix}$ and $\boldsymbol{B}$ and $\beta$ are defined similarly. The middle row, below the partition, fixes the nodal displacement and adds the boundary force from displacement constraints to the nodal force balance while the bottom row fixes the nodal velocity and adds the boundary force from velocity constraints to the nodal force balance.

If every node has both displacement and velocity boundary conditions the system is overspecified and has no solution. The solution to this is to 'turn off' any boundary conditions that are not active by setting $\alpha$, $\beta$, and $\gamma$ to zero. The zero entries from inactive boundary conditions make the matrix singular and unsolvable since they introduce rows of zeros. The solution to this problem is to permute the expanded network evolution equation (Equation (2.60)) to place the zeros in the south rows and east columns of matrices and in the south rows of all vectors. The permutation matrix is an amended identity matrix with the ones moved to off-diagonal positions. Pre-multiplication with the permutation matrix interchanges rows while post-multiplication by its transpose interchanges columns. The permutation matrix is constructed by analyzing the $\alpha$ and $\beta$ values for each degree of freedom at each node. The resulting permuted equation is solved disregarding the rows of inactive boundary conditions.

### 2.3.9 Solution of Network Evolution Equation

The augmented, permuted network evolution equation describes the constitutive equations between nodes and their boundary conditions. It is a system of linear differential-algebraic equations (DAEs) because the network evolution equations are a system of ordinary differential equations and the boundary condition equations are a system of algebraic equations. This system of DAEs is solved with a readily available, free DAE solver, DASKR, an improvement on the older code of DASSL (Brenan et al. 1989, Ascher and Petzold 1998, Petzold 1982). DASKR solves DAEs of the form

$$F\left(y, y^{'}, t\right) = 0 \tag{2.61}$$

$$y\left(t_o\right) = y_o \tag{2.62}$$

$$y^{'}\left(t_o\right) = y_o^{'} \tag{2.63}$$

by replacing the derivative with a difference approximation and solving the resulting system for the new solution using Newton's Method.

The system of DAEs is linear, as has been mentioned previously. However, the rotation of local to global coordinates introduces a geometric nonlinearity. After every timestep, DASKR is given an updated stiffness, viscosity, and shrinker matrix with new rotation angles accounted for from motion of the nodes in the previous timestep.

## 2.4 Continuum Modeling of Viscoelasticity

### 2.4.1 Introduction

Continuum models for viscoelasticity assume stress and strain are continuous throughout the calculation domain. An advantage of continuum over network modeling is the availability of well developed constitutive equations designed to match real behavior, especially with the inclusion of volume coupling, which cannot be duplicated with a network model.

Motivation to create this model comes from a desire to calculate viscoelastic stress and deformation in a coating in two-dimensions, but the framework will be presented for a general material. Assumptions will be made based on the conditions encountered during coating solidification, however this method may be applied to other linear viscoelastic systems that satisfy the assumptions laid out in the following section.

### 2.4.2 Governing Equations

#### Equation of Motion

Deformation behavior of a material can be described mathematically with equations describing physical phenomena of the material. An equation of motion enforces the conservation of linear momentum. Linear momentum acts by inertial forces, surface contact forces, forces that act at a distance, and may be accumulated with mass or velocity. The general equation of motion is valid for all materials. A constitutive equation describes the relationship between material deformation and stress in that material. There are many types of constitutive equations, each describe the stress-deformation behavior of a different material.

The differential form of the equation of motion is used here.

$$\frac{\partial\left(\rho \boldsymbol{v}\right)}{\partial t} = -\rho \boldsymbol{v} \cdot \nabla \boldsymbol{v} - \boldsymbol{v} \nabla \cdot \left(\rho \boldsymbol{v}\right) + \nabla \cdot \boldsymbol{\sigma} \tag{2.64}$$

where $\rho$ is the material density, $\boldsymbol{v}$ is the velocity, and $\boldsymbol{\sigma}$ is the state of stress.

Equation (2.64) can be nondimensionalized and scaled to determine which momentum terms are important. This is done because polymer coatings are by nature thin and the small change in the stress-free state create very low velocities in the material. In the equation of motion, $\frac{\partial(\rho \boldsymbol{v})}{\partial t}$ denotes the rate of momentum accumulation, $-\rho \boldsymbol{v} \cdot \nabla \boldsymbol{v} - \boldsymbol{v} \nabla \cdot (\rho \boldsymbol{v})$ denotes momentum influx by convection, and $\nabla \cdot \boldsymbol{\sigma}$ denotes momentum influx by surface forces. Gravitational body forces are ignored. The density of the solidifying medium, $\rho^*$, the velocity of the free surface, $U^*$, a reference shear modulus, $G^*$, the coating thickness, $L^*$, and a process timescale $\tau^*$, are used to define dimensionless variables as follows:

$$\tilde{\rho} = \frac{\rho}{\rho^*} \tag{2.65}$$

$$\tilde{\boldsymbol{v}} = \frac{\boldsymbol{v}}{U^*} \tag{2.66}$$

$$\tilde{\nabla} = \nabla L^* \tag{2.67}$$

$$\tilde{t} = \frac{t}{\tau} \tag{2.68}$$

$$\tilde{\boldsymbol{\sigma}} = \frac{\boldsymbol{\sigma}}{G^*} \tag{2.69}$$

These dimensionless variables are insert into the equation of motion.

$$\frac{\rho^* U^* L}{G^* \tau}\left[\tilde{\rho}\frac{\partial \tilde{\boldsymbol{v}}}{\partial \tilde{t}} + \tilde{\boldsymbol{v}}\frac{\partial \tilde{\rho}}{\partial \tilde{t}}\right] = -\frac{U^{*2}\rho^*}{G^*}\left[\tilde{\rho}\tilde{\boldsymbol{v}}\cdot\tilde{\nabla}\tilde{\boldsymbol{v}} + \tilde{\boldsymbol{v}}\tilde{\nabla}\cdot(\tilde{\rho}\tilde{\boldsymbol{v}})\right] + \tilde{\nabla}\cdot\tilde{\boldsymbol{\sigma}} \tag{2.70}$$

$$\frac{El}{Sr}\left[\tilde{\rho}\frac{\partial \tilde{\boldsymbol{v}}}{\partial \tilde{t}} + \tilde{\boldsymbol{v}}\frac{\partial \tilde{\rho}}{\partial \tilde{t}}\right] = -El\left[\tilde{\rho}\tilde{\boldsymbol{v}}\cdot\tilde{\nabla}\tilde{\boldsymbol{v}} + \tilde{\boldsymbol{v}}\tilde{\nabla}\cdot(\tilde{\rho}\tilde{\boldsymbol{v}})\right] + \tilde{\nabla}\cdot\tilde{\boldsymbol{\sigma}} \tag{2.71}$$

This produces two dimensionless groups, the Elasticity Number $El$, and the Strouhal Number, $Sr$. The Elasticity Number is the ratio of the relative importance of inertial to elastic forces. $El = \frac{\rho^* U^{*2}}{G^*}$. The Strouhal number is a ratio of the process to convective timescales. $Sr = \frac{\tau^* U^*}{L^*}$. This analysis arbitrarily assigns the surface force terms to be $O\left(10^0\right)$. If the Elasticity Number is $O\left(0^{-1}\right)$ or greater, convective forces by inertia are important, and if the ratio of Elasticity Number to Strouhal Number is $O\left(0^{-1}\right)$ or greater, momentum accumulation is important.

Table 2.2 shows the range of parameters typical of a polymer coating solidified by UV curing. The small thickness, high elastic modulus, and low material velocity ensure the Elasticity Number is small while the Strouhal Number can range from small to unity depending on the timescales involved. In any case, the Elasticity Number is small enough to render the inertial force term negligible and the Strouhal Number is not small enough to make momentum accumulation important next to the stress surface force term. Thus, accumulation and inertia can be dropped from the equation of motion. This reduces Equation (2.71) to (2.72) and puts it in a quasi steady-state form. Quasi steady-state means the equation of motion is solved as if every time is at rest in mechanical equilibrium. This is a common way to solve problems of elasticity with low velocities and high moduli (Lei et al. 2002, Adolf et al. 1998, Ernst et al. 2002).

Table 2.2: Scaling parameters and dimensionless groups

| **Parameter** | **Physical Quantity** | **Estimate** |
|---|---|---|
| $\rho^*$ | Density | $1.1\ g/cm^3$ |
| $U^*$ | Material velocity | $1.3 \times 10^{-8} m/s$ |
| $G^*$ | Elastic modulus | $1 \times 10^5 Pa$ |
| $L^*$ | Length (coating thickness) | $50\ \mu m$ |
| $\tau^*$ | Process timescale | $1.8 \times 10^3 s$ |
| **Group** | **Definition** | **Range** |
| Elasticity number | $El = \rho^* U^{2*}/G^*$ | $10^{-11} - 10^8$ |
| Strouhal number | $Sr = \tau^* U^*/L^*$ | $10^{-1} - 10^0$ |

$$\tilde{\nabla} \cdot \tilde{\boldsymbol{\sigma}} = 0 \tag{2.72}$$

Deformations in the polymer are not large because the stress-free state change is small. Therefore, the difference between the Cauchy and Piola-Kirchhoff stress tensors is not significant. These two stress tensors account for forces in relation to the current or to the reference configurations, respectively. $\tilde{\boldsymbol{\sigma}}$ is simply the stress tensor and will be treated as such from this point forward.

### Constitutive Equation and its Manipulation

The constitutive equation describes the specific deformation and stress behavior of a material. Viscoelasticity is included in this solidification model to make the constitutive behavior more complete and to investigate where and when stress relaxation by viscoelastic relaxation is important. The Maxwell equation is selected as the linear viscoelastic equation for several reasons. First, its mathematical form allows stress reduction by relaxation. Second, by choosing physical parameters carefully, Hookean elastic and Newtonian viscous behavior can be captured with the equation, allowing a single constitutive equation to be used throughout solidification. The Hookean elasticity does not match the behavior of polymer coatings at large deformations (Lei 1999), but does for small ones. Finally, the linearity of the constitutive equation allows it to be manipulated in a novel way which allows facile

solution and the quantitative export of relaxation. This analysis is described below. Conceptually, the Maxwell equation behaves as a spring and dashpot in series (as in Section 2.2.3. The three-dimensional version also includes volume coupling by deformation. The differential form of the equation is used here.

$$\frac{1}{2G}\frac{\partial \boldsymbol{\sigma}}{\partial t} + \frac{1}{2\mu}\boldsymbol{\sigma} = \frac{\partial \boldsymbol{\epsilon}}{\partial t} + \frac{\nu}{1-2\nu}\frac{\partial \left(tr\left(\boldsymbol{\epsilon}\right)\right)}{\partial t}\boldsymbol{I} \tag{2.73}$$

$G$ is the shear modulus, $\mu$ is the viscosity, $\boldsymbol{\epsilon}$ is the strain from a reference state, $\nu$ is Poisson's ratio, $tr$ is the trace ($tr\left(\boldsymbol{X}\right) = \boldsymbol{I} : \boldsymbol{X}$) , and $\boldsymbol{I}$ is the identity tensor. The strain is simply a mathematical measure of the deformation of the material. Since the velocity is small, codeformational time derivatives are unnecessary (Bird et al. 1977), in a similar manner to the equality of Cauchy and Piola-Kirchhoff stress tensors.

A benefit of the Maxwell constitutive equation is that the viscous and elastic components of stress and strain in the equation can be separated. Elastic and viscous strains ($\boldsymbol{\epsilon_{EL}},\ \boldsymbol{\epsilon_{V}}$) can be calculated separately and added to obtain the overall strain. Additionally, the elastic and viscous stresses ($\boldsymbol{\sigma_{EL}},\ \boldsymbol{\sigma_{V}}$), which are implicitly may be calculated separately. Either may be used as the stress in the material. To determine the constitutive equations governing elasticity and viscosity, limits are taken where Maxwell's constitutive equation exhibits each behavior.

$$\boldsymbol{\epsilon} = \boldsymbol{\epsilon_{EL}} + \boldsymbol{\epsilon_{V}} \tag{2.74}$$

$$\boldsymbol{\sigma} = \boldsymbol{\sigma_{EL}} = \boldsymbol{\sigma_{V}} \tag{2.75}$$

Liquid behavior is recovered when $G >> \mu$, leading to an equation similar to Newton's law of viscosity for a compressible fluid. The bulk viscosity in Newtonian viscosity ($k_b$) is replaced with a prefactor involving Poisson's ratio and the shear viscosity.

$$\boldsymbol{\sigma_{V}} = 2\mu\frac{\partial \boldsymbol{\epsilon_{V}}}{\partial t} + 2\mu\frac{\nu}{1-2\nu}\frac{\partial tr\boldsymbol{\epsilon}}{\partial t}\boldsymbol{I} \tag{2.76}$$

Solid behavior is recovered when $\mu >> G$. The resulting equation is similar to the time derivative of Hooke's law of elasticity and would integrate to that if the modulus were constant in time.

$$\frac{\partial \boldsymbol{\sigma_{EL}}}{\partial t} = 2G\frac{\partial \boldsymbol{\epsilon_{EL}}}{\partial t} + 2G\frac{\nu}{1-2\nu}\left(\frac{\partial tr\boldsymbol{\epsilon_{EL}}}{\partial t}\right)\boldsymbol{I} \tag{2.77}$$

This separation of deformations has been used in past research to account for different types of deformations (Tam 1997, Lei 1999). Since the material does not deform significantly during cure, quadratic components of strain can be ignored and the small-displacement definition of strain can be used,

$$\boldsymbol{E} = \frac{1}{2}\left(\nabla \boldsymbol{u} + (\nabla \boldsymbol{u})^T + (\nabla \boldsymbol{u})^T \cdot (\nabla \boldsymbol{u})\right) \approx \boldsymbol{\epsilon} = \frac{1}{2}\left(\nabla \boldsymbol{u} + (\nabla \boldsymbol{u})^T\right) \tag{2.78}$$

Where $\boldsymbol{u}$ is a vector of the displacements from an initial state, $\boldsymbol{u} = \begin{bmatrix} u \\ v \end{bmatrix}$ in two-dimensions (Malvern 1969).

**The Stress-free State and its Strain Measure**

Changes in the stress-free state must be quantified to calculate deformations correctly. Any departure from the stress-free state is cause for elastic stress and can be quantified with an elastic strain, $\boldsymbol{\epsilon_{EL}}(t)$. To quantify the stress-free state, which is transient and changes throughout the solidification, define a stress-free strain, $\boldsymbol{\epsilon_{SF}}(t)$, to be the departure of the actual stress-free state from a reference configuration. For the material to have no elastic stress, it must deform to the stress-free configuration, $\boldsymbol{\epsilon}(t) = \boldsymbol{\epsilon_{SF}}(t)$. The obvious choice for a reference state is the initial state before curing begins when the material is stress-free so the initial strain and stress-free strain are both $\mathbf{0}$. The stress-free strain need not be uniform or compatible throughout the coating domain, but for the cases presented here where the specific volume changes, it is isotropic, $\boldsymbol{\epsilon_{SF}} = \beta \boldsymbol{I}$, where $\beta$ is a fraction of the initial specific volume, ie. $\beta = 0.9$ for a 10% 'shrinkage'(Lange et al. 1995). Combining the

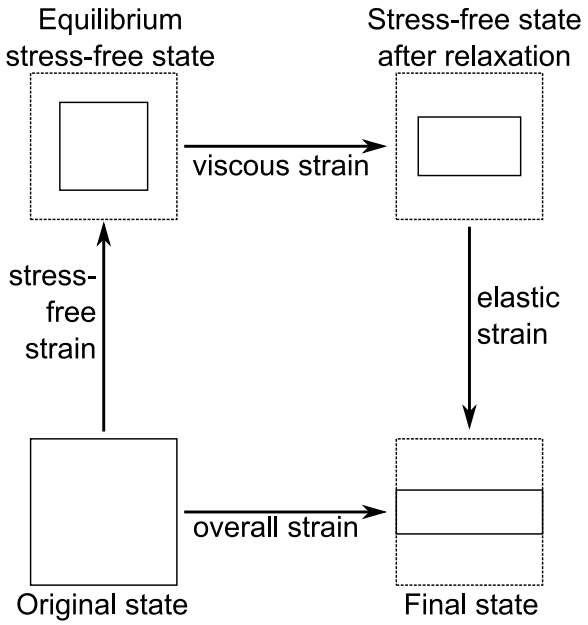


Figure 2.14: Stress-free state change example with strain definitions

stress-free strain with the separated Maxwell constitutive equation and strains, the overall strain is made up of three contributions, one for elastic, one for viscous, and one for changes in the stress-free state.

$$\boldsymbol{\epsilon}(t) = \boldsymbol{\epsilon_{EL}}(t) + \boldsymbol{\epsilon_{V}}(t) + \boldsymbol{\epsilon_{SF}}(t) \tag{2.79}$$

### Time Integration and Governing Equation Manipulation

To calculate the deformation and stress in the material, Equation (2.72) and Equation (2.73) must be solved together. This can be accomplished in a number of ways, one being the solution of stress and strain simultaneously. This formulation is possible and is common when dealing with applications where inertial forces cannot be ignored, however the Babuska-Brezzi condition complicates the mathematics of the numerical formulation (Babuska 1971, Hughes et al. 1986, Franca and Stenberg 1991). The linearity of the Maxwell constitutive equation combined with the quasi steady-state equation of motion can be ex-

ploited to make the mathematics more easily solved with less unknowns. The solution increases from 2 to 5 unknowns in two-dimensions and 3 to 9 in three-dimensions when solved simultaneously instead of with the method presented here. Also, even though more strain unknowns were added in the previous sections, the analysis presented in this section shows how time integration techniques combined with algebraic manipulation reduces these unknowns. This mathematical method is new and has been developed for this thesis to solve these types of viscoelastic problems. From now on, the system will be restricted to two-dimensions, though the same analysis may be performed in three-dimensions as well.

The first step is to calculate the time derivatives of Equations (2.76) and (2.77) with the Implicit Euler method. Using $t$ as the current time and $t - \Delta t$ as time at the previous timestep. This method assumes all variables are known at $t - \Delta t$ since it is the previous timestep.

$$\begin{aligned} \frac{\boldsymbol{\sigma_{EL}}(t) - \boldsymbol{\sigma_{EL}}(t-\Delta t)}{\Delta t} &= 2G(t)\left[\frac{\boldsymbol{\epsilon_{EL}}(t) - \boldsymbol{\epsilon_{EL}}(t-\Delta t)}{\Delta t} + \right. \\ &\left. \frac{\nu(t)}{1-2\nu(t)} tr\left(\frac{\boldsymbol{\epsilon_{EL}}(t) - \boldsymbol{\epsilon_{EL}}(t-\Delta t)}{\Delta t}\right)\boldsymbol{I}\right] \qquad (2.80) \\ \boldsymbol{\sigma_V}(t) &= 2\mu(t)\left[\frac{\boldsymbol{\epsilon_V}(t) - \boldsymbol{\epsilon_V}(t-\Delta t)}{\Delta t}\right. \\ &\left. + \frac{\nu(t)}{1-2\nu(t)} tr\left(\frac{\boldsymbol{\epsilon_V}(t) - \boldsymbol{\epsilon_V}(t-\Delta t)}{\Delta t}\right)\boldsymbol{I}\right] \qquad (2.81) \end{aligned}$$

The elastic and viscous stresses are equal and Equations (2.80) and (2.81) are now rearranged by setting $\boldsymbol{\sigma_{EL}} = \boldsymbol{\sigma_V}$ to determine the viscous strain. The stress and strain tensors are both symmetric, only the unique components will be shown.

$$\epsilon_{V,xx}(t) = \frac{1}{2(G(t)\Delta t+\mu(t))}[2\Delta t G(t)(\epsilon_{SF}(t-\Delta t)-\epsilon_{SF}(t)+ \epsilon_{V,xx}(t-\Delta t)-\epsilon_{xx}(t-\Delta t)+\epsilon_{xx}(t))+2\mu(t)\epsilon_{V,xx}(t-\Delta t) +\Delta t(-\nu\sigma_{xx}(t-\Delta t)+(1-\nu)\sigma_{yy}(t-\Delta t))] \quad (2.82)$$

$$\epsilon_{V,yy}(t) = \frac{1}{2(G(t)\Delta t+\mu(t))}[2\Delta t G(t)(\epsilon_{SF}(t-\Delta t)-\epsilon_{SF}(t)+ \epsilon_{V,yy}(t-\Delta t)-\epsilon_{yy}(t-\Delta t)+\epsilon_{yy}(t))+2\mu(t)\epsilon_{V,yy}(t-\Delta t)+ \Delta t((1-\nu)\sigma_{xx}(t-\Delta t)-\nu\sigma_{yy}(t-\Delta t))] \quad (2.83)$$

$$\epsilon_{V,xy}(t) = \frac{1}{2(G(t)\Delta t+\mu(t))}[2G(t)\Delta t(\epsilon_{V,xy}(t-\Delta t)-\epsilon_{xy}(t-\Delta t)+ \epsilon_{xy}(t))+2\epsilon_{V,xy}(t-\Delta t)+\Delta t\sigma_{xy}(t-\Delta t)] \quad (2.84)$$

With the viscous stress in terms of total and stress-free strain, elastic stress can be calculated without the elastic strain by by rearranging Equation (2.79), ($\boldsymbol{\epsilon_{EL}} = \boldsymbol{\epsilon} - \boldsymbol{\epsilon_V} - \boldsymbol{\epsilon_{SF}}$), inserting the viscous stress into that, and inserting the result into Equation (2.77).

$$\sigma_{xx}(t) = \frac{1}{(1-2\nu(t))(G(t)\Delta t+\mu(t))}[\mu(t)(2G(t)(\epsilon_{SF}(t-\Delta t)- \epsilon_{SF}(t)-\epsilon_{xx}(t-\Delta t)+\nu(t)\epsilon_{xx}(t-\Delta t)+\epsilon_{xx}(t)-\nu(t)\epsilon_{xx}(t)- \nu(t)\epsilon_{yy}(t-\Delta t)+\nu(t)\epsilon_{yy}(t))+(1-2\nu(t))\sigma_{xx}(t-\Delta t))] \quad (2.85)$$

$$\sigma_{yy}(t) = \frac{1}{(1-2\nu(t))(G(t)\Delta t+\mu(t))}[\mu(t)(2G(t)(\epsilon_{SF}(t-\Delta t)- \epsilon_{SF}(t)-\epsilon_{yy}(t-\Delta t)+\nu(t)\epsilon_{yy}(t-\Delta t)+\epsilon_{yy}(t)-\nu(t)\epsilon_{yy}(t)- \nu(t)\epsilon_{xx}(t-\Delta t)+\nu(t)\epsilon_{xx}(t))+(1-2\nu(t))\sigma_{yy}(t-\Delta t))] \quad (2.86)$$

$$\sigma_{xy}(t) = \frac{1}{(G(t)\Delta t+\mu(t))}[\mu(t)(-2G(t)(\epsilon_{xy}(t)-\epsilon_{xy}(t-\Delta t))+ \sigma_{xy}(t-\Delta t))] \quad (2.87)$$

If Equations (2.85) – (2.87) are substituted into Equation (2.72), the equation of motion can be expressed in terms of known stresses and strains at previous timesteps, physical

properties at the current time and the overall strain at the current time. This eliminates stress, viscous strain, and elastic strain, leaving just the deformations that make up the overall strain as unknowns. This analysis is possible because the equation of motion can be solved as a quasi steady-state problem, the Maxwell constitutive equation is linear and can be separated into elastic and viscous components.

One benefit of this analysis is that the strain from viscous relaxation can be calculated and quantitatively output. This is not possible by solving the Maxwell constitutive equation and equation of motion simultaneously. Equations (2.82) – (2.84) show how this is performed. With this technique, the conditions under which viscoelastic relaxation is important, if any, can be determined.

### 2.4.3 Finite Element Formulation

Galerkin's method with Finite Element basis functions (GFEM), a weighted residual method, is used to calculate the unknown displacements of each node. GFEM allows straightforward calculation of spatial derivatives of unknowns, making the strains easy to calculate from displacements. A raw residual is constructed by moving all terms in the equation of motion - the unknown equation - to one side. Weighted residuals are formed by multiplying the raw residual by a weighting function and integrating over the domain.

$$\boldsymbol{R_i} = \iint_A \phi_i\left(x,y\right) \tilde{\nabla} \cdot \tilde{\boldsymbol{\sigma}}\left(x,y\right) dA \tag{2.88}$$

$R_i$ is the weighted residual, $A$ is the area of integration, and $\phi_i\left(x,y\right)\ \ (i = 1, ..., N)$ are the weighting functions, of which there are $N$. There are also $N$ residuals.

The weak form of the residual is obtained by applying the divergence theorem to Equation (2.89) to remove the derivatives of stress.

$$\boldsymbol{R_i} = \oint_{\partial A} \phi_i\left(x,y\right) \boldsymbol{n} \cdot \tilde{\boldsymbol{\sigma}}\left(x,y\right) dS - \iint_A \tilde{\nabla}\phi_i\left(x,y\right) \cdot \tilde{\boldsymbol{\sigma}}\left(x,y\right) dA \tag{2.89}$$

where $\partial A$ is the boundary of the domain and $\boldsymbol{n}$ is the unit outward pointing normal.

The stress can now be removed from the residuals by substituting Equations (2.85) – (2.87) into the weak residual. The residual will now shown in component instead of vector form and the tildes over dimensionless variables will be dropped for clarity, though the variables listed are still dimensionless.

$$\begin{aligned}
\boldsymbol{R_{i,x}}(t) &= \oint_{\partial A} \phi_i \boldsymbol{i}\cdot\boldsymbol{n}\cdot\boldsymbol{\sigma}(x,y)\,dS - \iint_A \frac{\partial\phi_i}{\partial x}\frac{1}{(1-2\nu(t))(G(t)\Delta t+\mu(t))}\left[\mu(t)\right. \\
&\quad (2G(t)(\epsilon_{SF}(t-\Delta t)-\epsilon_{SF}(t)-\epsilon_{xx}(t-\Delta t)+\nu(t)\epsilon_{xx}(t-\Delta t)+\epsilon_{xx}(t) \\
&\quad -\nu(t)\epsilon_{xx}(t)-\nu(t)\epsilon_{yy}(t-\Delta t)+\nu(t)\epsilon_{yy}(t))+(1-2\nu(t))\sigma_{xx}(t-\Delta t))] \\
&\quad +\alpha\frac{\partial\phi_i}{\partial y}\frac{1}{(G(t)\Delta t+\mu(t))}\left[\mu(t)(-2G(t)(\epsilon_{xy}(t)-\epsilon_{xy}(t-\Delta t))+\right. \\
&\quad \left.\sigma_{xy}(t-\Delta t))\right]dA \qquad (2.90) \\
\boldsymbol{R_{i,y}}(t) &= \oint_{\partial A} \phi_i \boldsymbol{j}\cdot\boldsymbol{n}\cdot\boldsymbol{\sigma}(x,y)\,dS - \iint_A \frac{\partial\phi_i}{\partial x}\frac{1}{(G(t)\Delta t+\mu(t))}\left[\mu(t)(-2G(t)\right. \\
&\quad (\epsilon_{xy}(t)-\epsilon_{xy}(t-\Delta t))+\sigma_{xy}(t-\Delta t))]+\alpha\frac{\partial\phi_i}{\partial y} \\
&\quad \frac{1}{(1-2\nu(t))(G(t)\Delta t+\mu(t))}\left[\mu(t)(2G(t)(\epsilon_{SF}(t-\Delta t)-\right. \\
&\quad \epsilon_{SF}(t)-\epsilon_{yy}(t-\Delta t)+\nu(t)\epsilon_{yy}(t-\Delta t)+\epsilon_{yy}(t)-\nu(t)\epsilon_{yy}(t)- \\
&\quad \left.\nu(t)\epsilon_{xx}(t-\Delta t)+\nu(t)\epsilon_{xx}(t))+(1-2\nu(t))\sigma_{yy}(t-\Delta t))\right]dA \qquad (2.91)
\end{aligned}$$

where $\boldsymbol{i}$ and $\boldsymbol{j}$ are unit vectors in the x and y-directions, respectively and $\alpha$ is the aspect ratio that scales the relative lengths in the x and y-directions, $\alpha = \frac{x^*}{y^*}$.

$$
\begin{aligned}
\boldsymbol{R_{i,x}}(t) &= \oint_{\partial A} \phi_i \boldsymbol{i} \cdot \boldsymbol{n} \cdot \boldsymbol{\sigma}(x,y)\, dS - \iint_A \frac{\partial \phi_i}{\partial x} \frac{1}{(1-2\nu(t))(G(t)\Delta t + \mu(t))} [\mu(t) \\
&\quad \left(2G(t)\left(\epsilon_{SF}(t-\Delta t) - \epsilon_{SF}(t) - \epsilon_{xx}(t-\Delta t) + \nu(t)\epsilon_{xx}(t-\Delta t) + \frac{\partial u(t)}{\partial x}\right.\right. \\
&\quad \left.\left. -\nu(t)\frac{\partial u(t)}{\partial x} - \nu(t)\epsilon_{yy}(t-\Delta t) + \nu(t)\frac{\partial v(t)}{\partial y}\right) + (1-2\nu(t)) \right. \\
&\quad \left. \sigma_{xx}(t-\Delta t))\right] + \alpha \frac{\partial \phi_i}{\partial y} \frac{1}{(G(t)\Delta t + \mu(t))} \\
&\quad \left[\mu(t)\left(-2G(t)\left(\frac{1}{2}\left(\alpha\frac{\partial u(t)}{\partial y} + \frac{1}{\alpha}\frac{\partial v(t)}{\partial x}\right) - \epsilon_{xy}(t-\Delta t)\right) + \right.\right. \\
&\quad \left.\left. \sigma_{xy}(t-\Delta t)\right)\right] dA \qquad (2.92) \\
\boldsymbol{R_{i,y}}(t) &= \oint_{\partial A} \phi_i \boldsymbol{j} \cdot \boldsymbol{n} \cdot \boldsymbol{\sigma}(x,y)\, dS - \iint_A \frac{\partial \phi_i}{\partial x} \frac{1}{(G(t)\Delta t + \mu(t))} [\mu(t)(-2G(t) \\
&\quad \left(\frac{1}{2}\left(\alpha\frac{\partial u(t)}{\partial y} + \frac{1}{\alpha}\frac{\partial v(t)}{\partial x}\right) - \epsilon_{xy}(t-\Delta t)\right) + \sigma_{xy}(t-\Delta t)\Big)\Big] + \alpha\frac{\partial \phi_i}{\partial y} \\
&\quad \frac{1}{(1-2\nu(t))(G(t)\Delta t + \mu(t))} [\mu(t)(2G(t)(\epsilon_{SF}(t-\Delta t) - \\
&\quad \epsilon_{SF}(t) - \epsilon_{yy}(t-\Delta t) + \nu(t)\epsilon_{yy}(t-\Delta t) + \frac{\partial v(t)}{\partial y} - \nu(t)\frac{\partial v(t)}{\partial y} - \\
&\quad \left.\nu(t)\epsilon_{xx}(t-\Delta t) + \nu(t)\frac{\partial u(t)}{\partial x}\right) + (1-2\nu(t))\sigma_{yy}(t-\Delta t)\Big)\Big] dA \qquad (2.93)
\end{aligned}
$$

The residuals are now formulated in terms of just two unknowns, the displacements $u$ and $v$ at time $t$. Since there are two equations, these two residuals are sufficient to calculate the displacements. All stresses and strains at $t-\Delta t$ are known, as are the physical parameters at $t$.

### Boundary Conditions

Boundary conditions are necessary to calculate the deformation by specifying stress, displacement, or a combination of the two on the boundary. Boundaries on the substrate are considered rigid and no displacement occurs there. The Dirichlet condition applies:

$$u = v = 0 \qquad (2.94)$$

These Dirichlet boundary conditions are applied *strongly*. That is, the residual for nodes on the boundary are discarded and replaced with an imposition of the Dirichlet condition.

There is no traction at the coating-air interface, the free-surface condition is applied:

$$\boldsymbol{n} \cdot \boldsymbol{\sigma} = \mathbf{0} \tag{2.95}$$

so the boundary integral term in Equations (2.89) – (2.93) is $\mathbf{0}$.

A periodic boundary condition is applied to the edges of the domain where a periodic boundary exists. The periodic boundary is modeled with reflection symmetry instead of translational to provide a unique solution. Reflection symmetry requires no displacement normal to the boundary and no traction parallel to it:

$$\boldsymbol{n} \cdot \boldsymbol{u} = 0 \tag{2.96}$$

$$\boldsymbol{t} \cdot (\boldsymbol{n} \cdot \boldsymbol{\sigma}) = 0 \tag{2.97}$$

$\boldsymbol{n}$ and $\boldsymbol{t}$ are the unit outward pointing normal and unit tangential vectors, respectively. For a vertical boundary, this would enforce $u = 0$ and $\sigma_{yy} = \sigma_{xy} = 0$. These are also imposed strongly. The residuals are discarded and replaced with the appropriate displacement or stress boundary condition.

### Initial Conditions

Initial conditions must be specified at an initial time where solidification calculations are to begin. This choice is important because stresses are calculated as displacements from this initial state, so the definition of the initial configuration determines the strain. Also, the strains must be compatible. Compatibility requires the given initial strains satisfy the constitutive equation and equation of motion. In addition, since the strains were separated into components, they must be compatible with each other and the stress-free strain must be compatible with the elastic stress constitutive equation.

At first, these initial requirements seem daunting but there is a simple choice for initial conditions that satisfies compatibility and the strain definitions. The configuration before any solidification has started is chosen as the initial condition at $t = 0$. The displacements are 0 by definition, $u(0) = v(0) = 0$ which makes $\boldsymbol{\epsilon}(0) = 0$ as well. $\boldsymbol{\epsilon_V}(0)$ is also 0 initially as no viscous relaxation has taken place. The initial configuration is chosen to coincide with the stress-free state, making $\boldsymbol{\epsilon_{SF}}(0) = 0$. Equation (2.79) insures $\boldsymbol{\epsilon_{EL}}(0) = 0$ and the constitutive equations determine $\boldsymbol{\sigma}(0) = 0$. Thus, all compatibility and constitutive relations are trivially satisfied by making all stresses and strains zero at the initial time.

**Finite Element Discretization**

Unknown displacements are discretized into finite element forms constructed of sums of products of domain-spanning basis functions and unknown weighting coefficients. It is these unknown weighting coefficients that are calculated. In the GFEM formulation, the basis functions are the same as the residual weighting functions.

$$u(x, y, t) = \sum_{i=1}^{N} u_i(t)\,\phi_i(x, y) \tag{2.98}$$

$$v(x, y, t) = \sum_{i=1}^{N} v_i(t)\,\phi_i(x, y) \tag{2.99}$$

where the $u_i$ and $v_i$ are the unknown weighting coefficients for displacement in the x and y-direction, respectively. Since the problem is time dependent, the weighting functions change in time while the basis functions remain constant.

The two-dimensional domain is discretized into elements joined by nodes. Each node is associated with a single basis function and two unknowns, one each for $u$ and $v$. The weighting functions are identical to the basis functions, each node is associated with two residuals, which makes the total number of residuals and unknowns the same. Basis functions are bilinear and act locally, spanning up to four elements as is standard for GFEM.

### Solution Method

Residual integrations are carried out using Gaussian Quadrature. The unknown weighting coefficients are calculated using the Newton-Rhapson method. The residual vector is set to zero as a function of the unknown coefficient vector.

$$\boldsymbol{R}(\boldsymbol{U}) = \boldsymbol{0} \tag{2.100}$$

where $\boldsymbol{R}$ is the residual vector,

$$\boldsymbol{R} = \begin{bmatrix} \begin{bmatrix} R_{1,x} \\ R_{1,y} \end{bmatrix} \\ \begin{bmatrix} R_{2,x} \\ R_{2,y} \end{bmatrix} \\ \vdots \\ \begin{bmatrix} R_{N,x} \\ R_{N,y} \end{bmatrix} \end{bmatrix} \tag{2.101}$$

and $\boldsymbol{U}$ is the unknown vector,

$$\boldsymbol{U} = \begin{bmatrix} \begin{bmatrix} u_1 \\ v_1 \end{bmatrix} \\ \begin{bmatrix} u_2 \\ v_2 \end{bmatrix} \\ \vdots \\ \begin{bmatrix} u_N \\ v_N \end{bmatrix} \end{bmatrix} \tag{2.102}$$

Newton-Rhapson is carried out using a Jacobian matrix of partial derivatives to iteratively find the unknowns.

$$\boldsymbol{J} \cdot \delta \boldsymbol{U} = -\boldsymbol{R} \tag{2.103}$$

where $\delta \boldsymbol{U}$ is the solution update,

$$\boldsymbol{U}^{n+1} = \boldsymbol{U}^{n} + \delta \boldsymbol{U} \tag{2.104}$$

and $n$ and $n+1$ are iteration numbers, with $n = 1$ being the initial guess. The formulation presented here is linear so Newton-Rhapson should converge in one iteration. Convergence is defined to be when the $L_2$ norm of the residual or solution update fall below the error criteria of $10^{-8}$. The Jacobian is a matrix of partial derivatives,

$$\boldsymbol{J} = \frac{\partial \boldsymbol{R}}{\partial \boldsymbol{U}} \tag{2.105}$$

$$\boldsymbol{J} = \begin{bmatrix} \begin{bmatrix} \frac{\partial R_{1,x}}{\partial u_1} & \frac{\partial R_{1,x}}{\partial v_1} \\ \frac{\partial R_{1,y}}{\partial u_1} & \frac{\partial R_{1,y}}{\partial v_1} \end{bmatrix} & \begin{bmatrix} \frac{\partial R_{1,x}}{\partial u_2} & \frac{\partial R_{1,x}}{\partial v_2} \\ \frac{\partial R_{1,y}}{\partial u_2} & \frac{\partial R_{1,y}}{\partial v_2} \end{bmatrix} & \cdots & \cdots \\ \begin{bmatrix} \frac{\partial R_{2,x}}{\partial u_1} & \frac{\partial R_{2,x}}{\partial v_1} \\ \frac{\partial R_{2,y}}{\partial u_1} & \frac{\partial R_{2,y}}{\partial v_1} \end{bmatrix} & \begin{bmatrix} \frac{\partial R_{2,x}}{\partial u_2} & \frac{\partial R_{2,x}}{\partial v_2} \\ \frac{\partial R_{2,y}}{\partial u_2} & \frac{\partial R_{2,y}}{\partial v_2} \end{bmatrix} & \ddots & \vdots \\ \vdots & \ddots & \ddots & \begin{bmatrix} \frac{\partial R_{i,x}}{\partial u_j} & \frac{\partial R_{i,x}}{\partial v_j} \\ \frac{\partial R_{i,y}}{\partial u_j} & \frac{\partial R_{i,y}}{\partial v_j} \end{bmatrix} \end{bmatrix} \tag{2.106}$$

**Solution**

The GFEM formulation of strain is solved in the following manner. First, the computational domain is discretized into nodes and elements and the mesh is generated. The strains are initialized to zero and stress is calculated to be zero at the initial time. Time is advanced and the physical properties and stress-free strain are updated at $t = \Delta t$. The overall strain is calculated using the GFEM routine with Gaussian Quadrature and Newton's method. The stress and viscous relaxation strain are determined using the newly calculated strain. Time is advanced to $2\Delta t$, the physical properties and stress-free strain are updated, and the

strain is calculated again, this time using stress calculated during the previous timestep.

### 2.4.4 Numerical verification

Numerical results from the method presented in this paper are compared to analytical solutions of the Maxwell's constitutive equation to show that the methodology presented is sound and that the numerical calculations of stress and deformation match analytical solutions of the same. To do this, numerical experiments were conducted in two-dimensions where deformation was initiated using boundary motion. Calculations were performed in uniaxial and biaxial extension, in shear, and for more general deformations and the physical properties were varied by orders of magnitude in time. The stress and deformation from the numerical solutions must match those from analytical solutions to validate the model. In a coating solidification, the physical properties do change greatly, so the method must work for a wide range of parameters. Throughout the calculations, strains were kept between 1%-10% to guarantee the strain remained within the small-strain limit.

First, the assumption that inertia is small enough to be negligible is tested. In Figure 2.4.4 the relative importance of elastic forces to inertial forces is shown. Inertial forces become important when the ratio of inertial to stress forces becomes $O(1)$. Inertial forces are calculated to be the maximum inertial traction from $\rho \boldsymbol{v}\boldsymbol{v}$ and stress or elastic forces are the maximum stress traction from $\boldsymbol{\sigma}$. These tractions correspond to the largest eigenvalue of the stress tensor. Inertial forces were estimated after solution of the system. In the plot, the elasticity number has been modified from its original definition to account for which process controls the elastic forces. For relaxation times smaller than the process time, as when the elastic modulus is large, the stress reaches a plateau when the viscous strain begins deforming at the same rate as the boundary. In this regime, the stress is controlled by the rate of relaxation $\boldsymbol{\sigma} = \mu \frac{\partial \boldsymbol{\epsilon}}{\partial t}$. When the relaxation time is larger than the process time (small elastic modulus), the stress does not reach its plateau value, the elastic force is controlled by the rate of stress buildup, both the elastic and viscous forces. Thus, the smaller of the elastic ($G$) or viscous ($\mu \frac{\partial \boldsymbol{\epsilon}}{\partial t}$) stress scalings is more important (Macosko 1994). To rectify

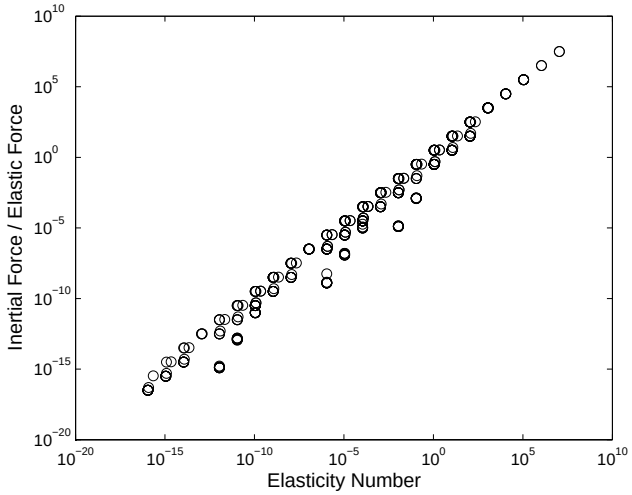


Figure 2.15: Inertia magnitude

this problem of stress scaling, the stress was scaled with the inverse of the elastic or viscous forces to make the smaller contribution more important

$$\tilde{\boldsymbol{\sigma}} = \frac{\boldsymbol{\sigma}}{\frac{1}{\frac{1}{G}+\frac{1}{\mu}\frac{\partial \boldsymbol{\epsilon}}{\partial t}}}$$

Figure 2.4.4 shows that inertial forces only become important as the Elasticity number approaches unity. Thus, for the cases with small Elasticity number, the assumption of a quasi-steady state system is valid.

Comparing stress and strain for the continuum model presented here with those where analytical solutions can be calculated confirmed that this method correctly calculates them. All of the numerical verification calculations will not be presented here, but the stresses and strains matched the analytical solutions over a wide range of physical parameters, deformations, and their time dependence. Figure 2.4.4 shows the stress and strain for a partially fixed domain strained linearly. The stress is in the same direction as the strain, while the calculated strain is perpendicular to that. Figure 2.4.4 shows the stresses for a domain whose boundaries are being oscillated with several superposed sine waves. The

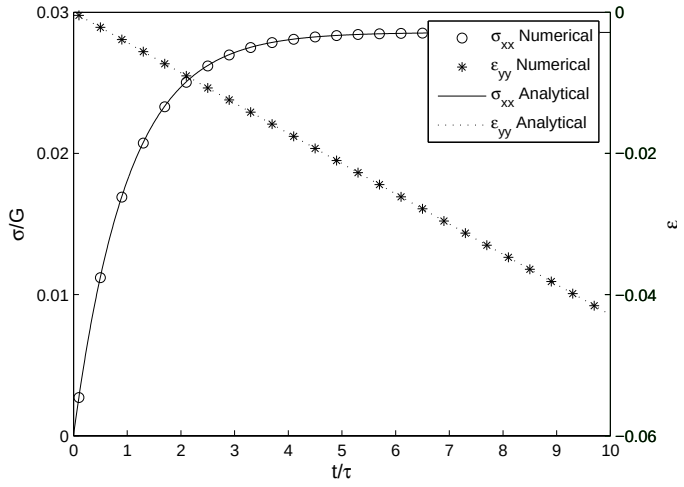


Figure 2.16: Stress and strain for a continuously deforming domain.

physical properties are cyclical as well. This shows that the continuum model presented here correctly solves the stress and can be used in viscoelastic modeling in lieu of the full Maxwell constitutive equation.

## 2.5 Conclusions

This chapter presents two new models for calculating stress and deformation in a viscoelastic material. The first, a network model, used two-dimensional combinations of one-dimensional viscoelastic mechanical models to approximate the behavior of the whole. The second continuum model used Maxwell's linear viscoelastic constitutive equation, scaling out inertial forces.

The network model is easy to implement computationally, and the deformations can be easily seen with nodal movement. The method of network generation, however, presents a problem. Topology will determine how an element can deform based on the other elements it joins at a node. This makes selection of percolating networks extremely important, and forces in every element are dictated by the topology chosen. Also, the network model can not include volume coupling for materials with nonzero Poisson's ratios. Because of this,

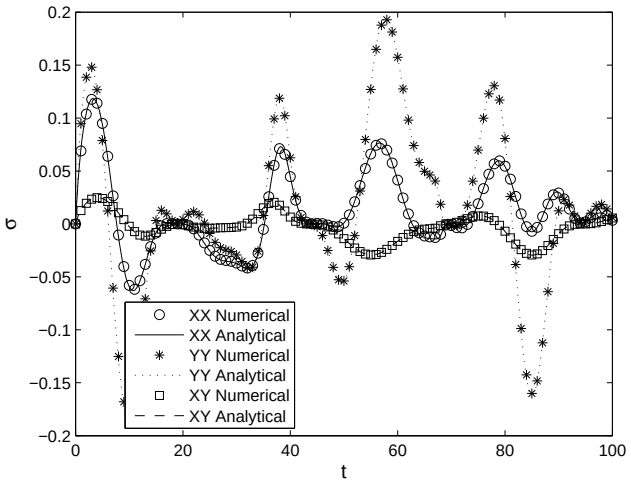


Figure 2.17: Stress for time-dependent property change, general deformation

the network model will not be discussed further.

The continuum model takes advantage of small inertial forces and the linearity of the constitutive equation to decompose strain into its constituents. This allows manipulation of the sets of governing equations, reducing the number of unknowns and making relaxation exportable. Solving these equations is relatively straightforward using standard finite element methods.

# Chapter 3

# Stress Generation During Uniform Cure

## 3.1 Introduction

Coatings solidified uniformly on flat substrates generate stress only in the plane of the coating. Deformation occurs perpendicular to the coating plane, making that direction stress-free. Section 1.4 discussed some models of curing stress generation both in the coating plane and for spatially nonuniform coatings, and how some have been connected to the kinetics of curing. There is, however, a void in UV initiated photopolymerization curing and stress generation understanding. This chapter discusses modeling stress in a commonly used multifunctional acrylate coating and couples, for the first time, the reaction kinetics, stress-free state change, physical properties, and stress. Inclusion of nonequilibrium volume effects that are manifested experimentally as delayed shrinkage helps further the understanding of the origins of stress and how it may be altered by externally manipulable parameters. Also discussed are constraints – imposed by the monomer – on the final state of the coating, and how sets of physically accessible final states can be acquired. Knowledge gained can be used to help design curing schedules to meet process constraints.

Stress in the coating plane in itself is not a coating defect, but may introduce defects

to the coating or substrate. Understanding the physical processes behind stress generation can help reduce defects once they are seen or prevent them from occurring at all.

## 3.2 UV Curing Kinetics

Ultraviolet light initiated free radical polymerizations are used to create solid coatings quickly at room temperature. Surfaces are coated with low molecular weight monomer or oligomer because their viscosity is low enough to coat uniformly. Free radical polymerizations solidify the liquid, which commonly includes multifunctional monomers to create crosslinks. Initiators that decompose upon illumination with UV light are used to generate primary radicals. After initiation, kinetics take over and the state of the polymerizing medium – concentrations, volumes, and temperature of the coating – determine the reaction rates.

### 3.2.1 Free-radical Polymerization

Free-radical polymerization kinetics incorporate generation of radicals, conversion of vinyl double bonds through propagation, radical annihilation by termination, and kinetic radical trapping. The basic reactions are:

**Initiation:**

$$M \xrightarrow{Heat,\text{UV,EB}} R_{1a\cdot} \tag{3.1}$$

**Propagation:**

$$R_{na\cdot} + M \xrightarrow{k_p} R_{(n+1)a\cdot} \tag{3.2}$$

**Radical Trapping or Burying**

$$R_{na\cdot} \xrightarrow{k_b} R_{nb\cdot} \tag{3.3}$$

**Termination:**

$$R_{na\cdot} + R_{ma\cdot} \xrightarrow{k_t} P_{(n+m)} \tag{3.4}$$

$M$ is a monomer molecule, $R_{1a\cdot}$ is a chain initiating radical (a radical monomer), $R_{na\cdot}$ is a radical chain with $n$ repeat units that is active, $R_{nb\cdot}$ is a trapped or buried radical with $n$ repeat units, and $P_n$ is dead polymer incorporating $n$ repeat units. This reaction scheme presented here neglects termination by disproportionation as well as chain transfer reactions, in line with previous work, due to their rare occurrence (Wen and McCormick 2000, Wen 2001, Vaessen 2002, Kurdikar and Peppas 1994a). The initiation step creates a chain initiating radical by one of three main processes; thermal initiators decompose into radicals upon heating, UV initiators decompose into radicals upon irradiation with ultraviolet light, and electron beam systems impinge high energy electrons upon the reaction precursors, knocking off atoms or molecular fragments to create radicals. These primary radicals must then react with a monomer to form chain initiating radicals. The rate of polymerization describes the conversion of monomeric double bonds with rate constant $k_p$, $r_p = k_p [M] [R_{na\cdot}]$. Trapping occurs when active radical become immobile and unavailable for reaction. It is described with the burying rate constant $k_b$, $r_b = k_b [R_{na\cdot}]$. Radicals are only kinetically trapped, they may react after long times but over the reaction times of interest are unreactive (Wen and McCormick 2000). Termination occurs when a radical reacts with another radical instead of a monomer, annihilating the radicals and leaving dead polymer. $k_t$ is the rate constant for the termination rate $r_t = k_t [R_{na\cdot}] [R_{ma\cdot}]$.

We will now go through each reaction step in UV curing one by one. These models for acrylate polymerizations have been well developed to describe the kinetics accurately and match experimental data. Therefore, this will be a brief review of the kinetics with an eye to using them to predict stress generation during cure. The interested reader is directed to the development of the model by Kurdikar and Peppas (1994a), Kurdikar and Peppas (1994b), Bowman and Peppas (1991), Wen and McCormick (2000), and Vaessen (2002). We also restrict our view to UV initiated systems of acrylate monomers from now on because

these are our materials of interest.

Reactions (3.1) – (3.4) seem to suggest that the rate coefficients do not change during the polymerization. In reality, the rate coefficients change by orders of magnitude as polymerization progresses because of changes in *free volume* during the reaction. Free volume is all space not taken up by polymer or solvent molecules. As free volume decreases, the mobility of reactants is drastically reduced, the propagation rate suffers and trapping increases. Reaction rates do depend on reactant concentrations, but the rate coefficient dependence on free volume eclipses this. This should be kept in mind when reading the following section. Duda and Zielinski (1996) present a thorough analysis of free volume, and it is used in the development of this kinetic model as well. Kloosterboer (1988), Decker (1994), Andrzejewska (2001), and Decker (1996) offer reviews of photopolymerization for more information and detail.

### 3.2.2 Initiation

Initiation is not as simple as Equation (3.1). To create a chain initiating radical, the photoinitiator must decompose into primary radicals, one of which must react with a monomer before recombining with its sister radical. The proximity of the two radicals makes recombination important, especially as reaction progresses and mobility decreases (Kurdikar and Peppas 1994b).

**Initiator Dissociation:**

$$A \xrightarrow{\text{UV}} 2R. \tag{3.5}$$

**Addition to Monomer**

$$R. + M \longrightarrow R_{1a}. \tag{3.6}$$

The initiation step is slower than the addition step (Odian 2004), so the rates of initiation can be combined into a single reaction step,

$$r_i = 2\phi I_a \tag{3.7}$$

$\phi$ is the overall quantum efficiency of initiation, the number of initiated chains per photon of UV light absorbed and $I_a$ is the intensity of absorbed light. The factor of 2 comes from two radicals created per dissociation. UV light is generally known in terms of energy per unit area per unit time ($W/dm^2$), so the incident light intensity must be converted to the intensity of absorbed light in ($einstein/dm^2 \cdot s$) (Odian 2004)

$$\text{Rate of incidence of photons} = \frac{\lambda I_0}{N_A hc} \tag{3.8}$$

where $\lambda$ is the wavelength of light, $I_o$ is the incident light intensity, $N_A$ is Avogadro's number, $h$ is Planck's constant, and $c$ is the speed of light.

The quantum efficiency $\phi$ is calculated using the initiator efficiency $f_I$ and the number of initiator dissociations per absorbed photon, $\phi'$

$$\phi = f_I \phi' \tag{3.9}$$

Incident UV light is absorbed by photoinitiators and the absorbed light is quantified using the Beer-Lambert law

$$I_a = \varepsilon_c I_o [A] \tag{3.10}$$

The initiation rate becomes

$$r_i = 2 f_I \phi' \varepsilon_c I_0 [A] \tag{3.11}$$

The initiator efficiency has been determined by Kurdikar and Peppas (1994b). We consider 2,2-dimethoxy-2-phenylacetophenone (DMPA) to be the initiator of choice for UV initiation as Vaessen (2002) did.

$$f_I = \left[1 - \frac{ak_{i,l}}{D_A + ak_{i,l} + a\sqrt{k_{d,r,l}D_A}}\right] \times \left[1 - \frac{a^2 k_{i,l}k_{d,r,l}}{\sqrt{\frac{k}{D_A}} + \sqrt{\frac{k_{d,r,l}}{D_A}}}\left(\frac{1}{D_A + ak_{i,l} + a\sqrt{k_{d,r,l}D_A}}\right)\left(\frac{1}{D_A + ak_{i,l} + a\sqrt{kD_A}}\right)\right] \tag{3.12}$$

where

$$k = k_{p,1}[=] + k_t[R_a\cdot] \tag{3.13}$$

$[=]$ is the concentration of double bonds, $a$ is the radius of the solvent cage around primary radicals, $k_{i,l}$ is the rate constant for radical recombination, $k_{r,d,l}$ is the rate constant for secondary radical decomposition, $k_{p,1}$ is the true rate constant for reaction of a monomer with a primary radical with an unreacted monomer, and $k_{t,1}$ is the true rate constant for reaction of a primary radical with the growing polymer chain.

The concentration of double bonds and monomer is related by the number of double bonds ($n_{db}$) per monomer molecule:

$$[M] = \frac{[=]}{n_{db}} \tag{3.14}$$

The diffusion coefficient of initiator in the polymerizing medium, $D_A$, can be approximated to be twice the radical diffusion coefficient, which is related to the mass fractions of monomer and polymer by Vrentas-Vrentas theory (Vrentas and Vrentas 1991)

$$D_A = 2D_r = 2D_{0,r}\exp\left[-\frac{E_a}{RT}\right]\exp\left[-\frac{\gamma(\omega_1 V_1^* + \omega_2 \xi V_2^*)}{V_{FH}}\right] \tag{3.15}$$

where $D_{0,r}$ is the pre-exponential factor, $E_a$ is the energy per mole that a molecule must possess to overcome attractive forces, $\gamma$ is a volume overlap factor, $\xi$ is solvent to polymer critical jumping volume ratio, $V_1^*$ and $V_2^*$ are monomer and polymer critical hole jumping volume, $\omega_1$ and $\omega_2$ are the monomer and polymer mass fraction, and $V_{FH}$ is the average

hole free volume per gram,

$$V_{FH} = \omega_1 v_m v_{fm} + \omega_2 v_p v_{fp} \delta + V_{FHe} \tag{3.16}$$

$V_{FHe}$ is the excess free volume per gram of mixture, the difference between current and equilibrium free volumes

$$V_{FHe} = v_a - v_\infty \tag{3.17}$$

Mass fractions of monomer and polymer are calculated with total masses of monomer, polymer, and the system,

$$\omega_1 = \frac{m_m}{m_{tot}} \tag{3.18}$$

$$\omega_2 = \frac{m_p}{m_{tot}} \tag{3.19}$$

where the monomer mass is

$$m_m = [M] m w_m \tag{3.20}$$

the polymer mass is

$$m_p = ([M]_0 - [M]) m w_m + ([A]_0 - [A]) m w_A \tag{3.21}$$

and the system mass is

$$m_{tot} = [M]_0 m w_m + [A]_0 m w_A \tag{3.22}$$

### 3.2.3 Propagation

Growing polymer chains become sufficiently immobile after just a few monomer additions that propagation rates depend solely on the monomer's ability to reach the reactive site on

the growing chain and react. This process is discretized into three steps. First, the monomer must translate toward the active radical by diffusion; second, the monomer must align its functional group with the active radical; third, the monomer reacts with the radical. Since this process is sequential, the overall reaction rate constant is determined by the resistances of the individual steps,

$$k_p = \frac{1}{\frac{1}{k_{p,trans}} + \frac{1}{k_{p,seg}}} \tag{3.23}$$

Translational ($k_{p,trans}$) and segmental ($k_{p,seg}$) rate coefficients can be calculated using Smoluchowski rate expressions,

$$k_{p,trans} = 4\pi(R_m + R_r)D_m \tag{3.24}$$

$$k_{p,seg} = 4\pi(R_m + R_r)D_{seg} \tag{3.25}$$

Diffusion coefficients can be calculated using Vrentas-Vrentas theory similar to Equation (3.15)

$$D_m = D_{0,m} \exp\left[-\frac{E_a}{RT}\right] \exp\left[-\frac{\gamma(\omega_1 V_1^* + \omega_2 \xi V_2^*)}{V_{FH}}\right] \tag{3.26}$$

here $D_{0,m}$ is the monomer prefactor. Kurdikar and Peppas (1994a) estimate the segmental diffusion to be

$$D_{seg} = pD_m \tag{3.27}$$

where $p$ is the probability that a monomer's functional group is oriented toward the active radical.

### 3.2.4 Trapping

Radical trapping was introduced by Wen and McCormick (2000) to account for the removal of otherwise active radicals from reactive availability by trapping or burying in immobile regions where monomer can not diffuse to react with the radical in a reasonable amount of time. These low mobilities are caused by a deficiency of $V_{FH}$. Trapping is assumed to be a pseudo-first order reaction with a rate constant dependent on the fractional free volume, $v_f$, and the dimensionless activation volume, $A_b$.

$$k_b = k_{bo} \exp\left[\frac{A_b}{v_f}\right] \tag{3.28}$$

Fractional free volume is detailed in Section 3.2.6 along with the volume change during reaction. In reality, this is not a chemical reaction, the active radical simply remains unreacted. However, the time for a buried radical to react may be quite large so it appropriate to forever remove it from the reaction pool with this pseudo-reaction.

### 3.2.5 Termination

As mentioned in Section 3.2.3, the growing polymer chains quickly become too large to move by translational diffusion. Monomers must diffuse to the reactive sites for reaction to occur. Thus, the motion of radicals in the medium is by reaction-diffusion; the radical moves the distance of two bond lengths per reaction, effectively 'diffusing' each time a reaction takes place. Chain length dependent termination is not considered here. The root mean square displacement per reaction can be calculated by assuming growth as a random coil given the angle between bonds. For $n$ bonds of length $l$,

$$r_{rms} = \sqrt{2nl^2} \tag{3.29}$$

The diffusion coefficient can be determined if the time necessary to move a distance of $r_{rms}$ is known,

$$D_{rp} = \frac{r_{rms}^2}{6t_{rms}} \tag{3.30}$$

Time to complete a single propagation reaction is known from the propagation rate,

$$t_p = \frac{1}{k_p[=]} \tag{3.31}$$

so $t_{rms}$ can be calculated,

$$t_{rms} = \frac{n}{2}t_p = \frac{n}{2}\frac{1}{k_p[=]} \tag{3.32}$$

and the radical reaction-diffusion coefficient is known,

$$D_{rp} = \frac{2}{3}l^2 k_p[=] \tag{3.33}$$

The termination rate coefficient can be determined using Smoluchowski theory as in Section 3.2.3 for the propagation rate coefficient,

$$k_t = 4\pi(R_r + R_r)(D_{rp} + D_{rp}) \tag{3.34}$$

### 3.2.6 Volume Change

Vrentas-Vrentas diffusion theory predicts a strong dependence of species diffusivity on free volume. Experimentally, volume changes are seen to take place after chemical reaction does (Bowman and Peppas 1991). This 'physical aging' or delayed shrinkage (Rajamani 2005) describes the relaxation of the system volume, $v$, to its equilibrium value over time. When the system does not occupy its equilibrium specific volume, excess free volume is created which enhances the diffusivities of reactants, increases reaction rates, and suppresses termination. Bowman and Peppas (1991) developed an analysis to describe the kinetics of relaxation to equilibrium specific volume, $v_\infty$. Specific volume decays toward its equilibrium value at a rate determined by the volume relaxation time, $\tau$,

$$\frac{dv}{dt} = -\frac{1}{\tau}(v - v_\infty) \tag{3.35}$$

$$v_\infty = v_m(1 - \epsilon_v x) \tag{3.36}$$

The conversion of double bonds, $x$ is defined as

$$x = \frac{[=]_0 - [=]}{[=]_0} \tag{3.37}$$

and the volume contraction factor, $\epsilon_v$, is the fractional reduction in volume during reaction

$$\epsilon_v = \frac{v_m - v_p}{v_m} \tag{3.38}$$

The volume relaxation time is given as

$$\tau = \exp\left[C_1 + \frac{C_2}{v_f}\right] \tag{3.39}$$

where $C_1$ and $C_2$ are relaxation time constants and $v_f$ is the fractional free volume which is defined to be

$$v_f = v_{fm}\phi_m + v_{fp}\phi_p + \frac{v_a - v_\infty}{v_\infty} \tag{3.40}$$

where equilibrium fractional free volume of monomer, $v_{fm}$, is

$$v_{fm} = v_{fmg} + \alpha_m(T - T_{gm}) \tag{3.41}$$

and the polymer fractional free volume, $v_{fp}$, is assumed constant because the polymer is below the glass transition temperature. $v_{fmg}$ is the hole free-volume fraction of the monomer at its glass transition temperature, $T_{gm}$.

The fractional free volume in Equation (3.40) depends on the equilibrium free volume of monomer and polymer – the first two terms – as well as excess free volume caused by a

lag of the actual specific volume behind its equilibrium value – the last term. The specific volume takes a time determined by $\tau$ to relax to its equilibrium state, which is what causes delayed volume shrinkage, excess free volume, and enhances propagation rates.

Volume fractions occupied by monomer, $\phi_m$, and polymer, $\phi_p$ can be calculated with their masses and specific volumes along with those of the initiator,

$$\phi_m = \frac{v_m m_m}{v_m m_m + v_p m_p + v_A[A] m w_A} \tag{3.42}$$

$$\phi_p = \frac{v_p m_p}{v_m m_m + v_p m_p + v_A[A] m w_A} \tag{3.43}$$

### 3.2.7 Conservation Equations

The reactions in Section 3.2.1 can now be combined with the reaction rate development in Sections 3.2.2 – 3.2.6 and the stoichiometry of the polymerization. Initiation consumes photoinitiators and creates radicals. Radicals are destroyed through burying and termination, and double bonds are consumed by propagation. The volume of the system changes with equilibrium volume and time.

**Initiator:**

$$\frac{d[A]}{dt} = -\frac{1}{2} r_i = -f_I \phi' I_0 \varepsilon_c [A] \tag{3.44}$$

**Radicals:**

$$\frac{d[R_a\cdot]}{dt} = r_i - r_b - 2r_t = 2 f_I \phi' I_0 \varepsilon_c [A] - k_b [R_a\cdot] - 2k_t [R_a\cdot]^2 \tag{3.45}$$

**Double Bonds:**

$$\frac{d[=]}{dt} = -r_p = -k_p [=][R_a\cdot] \tag{3.46}$$

**Volume Relaxation:**

$$\frac{dv}{dt} = -\frac{1}{\tau}(v - v_\infty) \tag{3.47}$$

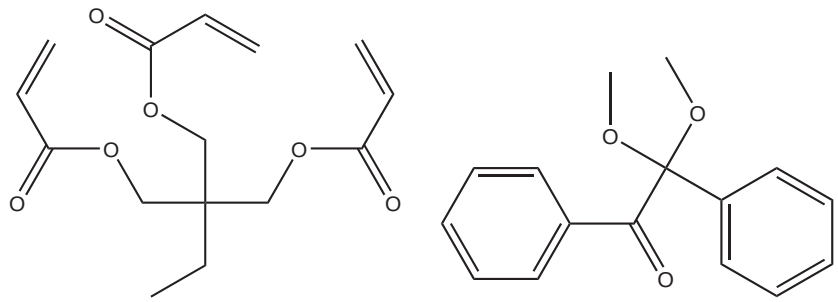

(a) TMPTA (b) DMPA

Figure 3.1: Chemical structures of monomer and photoinitiator.

Parameters necessary to calculate the reaction rates are listed in Table 3.1, which have been shown to closely match the actual kinetics of the photopolymerization (Kurdikar and Peppas 1994a, Wen and McCormick 2000, Bowman and Peppas 1991, Goodner et al. 1997, Vaessen 2002). The monomer considered in this thesis is trimethylolpropane triacrylate (TMPTA), a trifunctional acrylate, and the photoinitiator is 2,2-dimethoxy-2-phenylacetophenone (DMPA). Chemical structures are shown in Figure 3.1. Isothermal curing is also assumed from this point forward, as was done in the kinetic studies.

## 3.3 Uniform Viscoelasticity and Stress Generation

### 3.3.1 Introduction

Stresses generated during chemical curing of polymer coatings can be calculated using information about how the system solidifies and its configuration while doing so. This section describes the calculation of stress and its relaxation using chemical reaction rate information.

Changes taking place during cure are significant enough to transform a layer of liquid to a hard solid, so the physical property buildup must be taken into account in order to calculate an accurate stress at the completion of cure. UV initiation creates reactive free radicals which begin converting functional groups – in this case monomeric double bonds – and turning monomer or oligomer to polymer. If the monomers are multifunctional, the

Table 3.1: Parameters used in the kinetic model of photopolymerization.

| Parameter | Value | Units | Description |
|---|---|---|---|
| $[=]_0$ | 11.12 | mol/L | initial concentration of double bonds |
| $[R_a\cdot]_0$ | 0 | mol/L | initial concentration of active radicals |
| $\lambda$ | 365 | nm | wavelength of incident light |
| $\varepsilon_c$ | 1000 | L/mol-dm | molar absorption coefficient |
| $v_{fp}$ | 0.025 | - | polymer fractional free volume |
| $\alpha_m$ | 0.001 | 1/K | expansion coefficient of monomer |
| $v_{fmg}$ | 0.025 | - | monomer hole free-volume fraction at $T_{gm}$ |
| $v_m$ | 0.9 | $cm^3/g$ | monomer specific volume |
| $v_p$ | 0.8 | $cm^3/g$ | polymer specific volume |
| $v_A$ | 0.9 | $cm^3/g$ | photoinitiator specific volume |
| $C_1$ | 0.5 | - | relaxation time constant |
| $C_2$ | 0.165 | $g/cm^3$ | relaxation time constant |
| $l$ | 0.154 | nm | bond length |
| $a$ | 1 | nm | solvent cage radius around primary radical |
| $R_m$ | 0.3 | nm | monomer reaction radius |
| $R_r$ | 0.15 | nm | radical reaction radius |
| $\phi'$ | 1.0 | - | number of initiators dissociated per photon absorbed |
| $E_a$ | 9253 | cal/mol | energy required to overcome attractive force |
| $T$ | 303 | K | cure temperature |
| $T_{gm}$ | 213 | K | glass transition temperature of monomer |
| $\gamma$ | 0.9 | - | overlap factor for shared free volume |
| $\delta$ | 1.0 | - | crosslink accommodation factor |
| $\xi$ | 0.9 | - | critical volume ratio of jumping units |
| $k_{d,r,l}$ | $10^{11}$ | 1/sec | rate coefficient for decomposition of radical |
| $k_{i,l}$ | 132 | dm/sec | intrinsic rate constant for radical combination |
| $k_{p,1}$ | $10^8$ | L/mol-sec | propagation rate coefficient |
| $p$ | $10^{-4}$ | - | probability of proper double bond orientation |
| $V_1$ | 0.5 | $cm^3/g$ | specific critical hole volume for monomer to jump |
| $V_2$ | 0.9 | $cm^3/g$ | specific critical hole volume for polymer to jump |
| $k_{b0}$ | 7.79 | $10^{-7}$/sec | pre-exponential radical trapping factor |
| $A_b$ | 0.7 | - | dimensionless activation volume of radical trapping |
| $D_{0,m}$ | 0.44 | $dm^2/sec$ | pre-exponential monomer diffusion factor |
| $D_{0,r}$ | 4.40 | $dm^2/sec$ | pre-exponential radical diffusion factor |
| $mw_m$ | 296.32 | g/mol | molecular weight of monomer |
| $mw_A$ | 256.30 | g/mol | molecular weight of initiator |
| $n_{db}$ | 3 | - | number of double bonds per monomer |

polymers may form crosslinks between chains and a network will form. If enough junctions are formed for the network to percolate the entire domain, the coating will have passed gelation. Further reaction may cause the glass-transition temperature, $T_g$, of the coating to rise enough that that the coating will vitrify, though vitrification or gelation may occur in different orders, or not at all, depending on the monomer used and the temperature of the system (Enns and Gillham 1983b, Enns and Gillham 1983a).

During these transitions, the coating that was deposited as a liquid acquires an elastic modulus that rises by orders of magnitude throughout the polymerization (Love and Piguet-Ruinet 2007, Simon et al. 2000). The viscosity, present at the onset of polymerization, rises greatly as well. As the stress-free state changes via acquisition of a new, smaller, specific volume, the coating shrinks in whatever dimensions it can. A stress model that attempts to calculate the final stress needs to account for these changes along with the polymer constitutive behavior, which has been seen to exhibit viscoelasticity (Vaessen et al. 2002).

The combination of polymer solidification and stress calculation is not new and has been carried out for several systems solidifying by curing as well as drying. Elastic and viscoelastic constitutive equations have been used along with different methods of numerical solution. Several will be presented here as an introduction to polymer solidification stress modeling as well as to highlight the differences between previous models and the one developed here.

Tam (1997) developed a elasto-viscoplastic model for drying coatings, which was extended by Lei (1999). The stress in these dried coatings cannot be spatially uniform due to concentration gradients through the coating thickness. Radhakrishnan (2006) accounted for the change in elastic modulus with concentration, which was not done in Tam's (1997) or Lei's (1999) work.

Simple mechanical analogs have been used to model stress generation including viscoelasticity and cure shrinkage in a curing dental restorative (Dauvillier et al. 2001) in order to determine which viscoelastic model is appropriate for the material. Koplin et al. (2009) used similar methods to compare stress generation in different formulations. Integral or incremental step-wise methods have been used by Stolov et al. (2000), Stolov,

Xie, Penelle, Hsu and Stidham (2001), Hossain et al. (2009a), Hossain et al. (2009b), and Wang et al. (2008) to account for shrinkage strain through small steps in time, allowing more simple insertion of changing physical properties. Yang et al. (2004) accounted for rising physical properties and volume effects with reaction with an integral method, in a similar manner to Meuwissen et al. (2004) and Ernst et al. (2002). Curing via thermoset is a widely studied field as well, with several integral viscoelastic constitutive equations that include viscoelasticity along with cure shrinkage (Lange et al. 1995, Ernst et al. 2002, Adolf et al. 1998, Martin and Adolf 1990, Adolf and Martin 1996, White and Hahn 1992a, White and Hahn 1992b, Prasatya et al. 2001) which can be especially important as materials are brought to room temperature from elevated temperatures used for thermal curing.

Work most closely resembling the research in this thesis was carried out by Vaessen (2002) and Rajamani (2005) because they looked at UV cured multifunctional acrylates. Vaessen (2002) was instrumental in unifying the kinetic work in Section 3.2 and she also attempted to use the kinetic information to calculate stress. Inclusion of physical property rise with reaction made the model more physical and allowed her to more closely match measured stress data. Rajamani (2005) used less specific kinetic models and estimated his parameters more significantly. His work does include some parametric studies for different cases of solidification but does not tie the stress generation to a specific system. Both of these methods use simple one-dimensional constitutive equations to relate the stress, strain, and physical properties, which neglects important volume effects.

This section presents a new analysis of linear viscoelasticity as applied to spatially uniform stress generation in the coating. It ties the reaction kinetics shown in Section 3.2 to physical property and stress-free state changes.

### 3.3.2 Linear Viscoelasticity

The analysis of spatially uniform linear viscoelasticity will now be presented. If the coating is evenly applied to a substrate that does not deform, if initial concentrations of reactants are the same everywhere, and if curing reactions occur at the same rates everywhere in

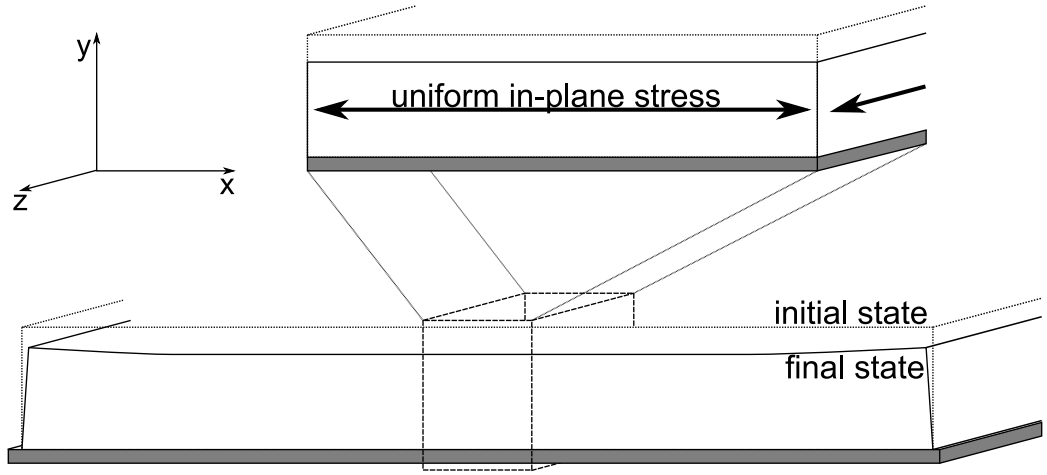


Figure 3.2: Geometry and Cartesian coordinate system for uniform stress generation. x and z-directions are identical.

the coating domain, deformation and stress everywhere will be the same far from the edge. Figure 3.2 shows the geometry of the coating and the Cartesian coordinate axes used in this analysis. The y-direction is out of the coating plane while x and z-directions define the coating plane. Assuming strong adhesion to the substrate, there is no deformation in the coating plane. Out of the coating plane, there is deformation in response to a change in the stress-free state and in-plane stress. Since the in-plane directions are indistinguishable from each other, the stress is biaxial (Lei 1999) and we will only refer to the x-direction from now on. Keep in mind that x and z stress and strain are equivalent.

The constitutive equation for linear viscoelasticity for the curing coating is given by the Maxwell constitutive equation,

$$\frac{1}{2G}\frac{\partial \boldsymbol{\sigma}}{\partial t} + \frac{1}{2\mu}\boldsymbol{\sigma} = \frac{\partial \boldsymbol{\epsilon}}{\partial t} + \frac{\nu}{1-2\nu}\frac{\partial \left(tr\left(\boldsymbol{\epsilon}\right)\right)}{\partial t}\boldsymbol{I} \tag{3.48}$$

To account for a changing stress-free state, the strain is split into viscoelastic, $\boldsymbol{\epsilon_{VE}}$, and stress-free, $\boldsymbol{\epsilon_{SF}}$, strains, similar to Equation (2.79), where $\boldsymbol{\epsilon}$ is the strain from the initial state. Here the initial state is taken to be the uniform liquid film before any polymerization reactions have been initiated. This initial state is stress-free so the initial stress-free strain

is $\mathbf{0}$.

$$\boldsymbol{\epsilon}(t) = \boldsymbol{\epsilon_{VE}}(t) + \boldsymbol{\epsilon_{SF}}(t) \tag{3.49}$$

Due to periodicity and uniformity, there can be no deformation in the x-direction. There can also be no stress in the y-direction from a simple momentum (force) balance. The y normal component of Equation (3.48) is used to determine the out of plane deformation and Equation (3.49) is substituted in,

$$0 = \frac{\partial \epsilon_{yy}}{\partial t} - \frac{\partial \epsilon_{SF}}{\partial t} + \frac{\nu}{1-2\nu}\left(\frac{\partial \epsilon_{yy}}{\partial t} - 3\frac{\partial \epsilon_{SF}}{\partial t}\right) \tag{3.50}$$

$$\frac{\partial \epsilon_{yy}}{\partial t} = \frac{(1+\nu)}{1-\nu}\frac{\partial \epsilon_{SF}}{\partial t} \tag{3.51}$$

This out of plane deformation must be known to calculate the in-plane stress due to the volume coupling in the Maxwell constitutive equation. Equation (3.51) can now be inserted into the x normal component of Equation (3.48) to produce a new constitutive equation for in-plane stress generation.

$$\frac{\partial \sigma_{xx}}{\partial t} = \frac{2G(1+\nu)}{\nu - 1}\frac{\partial \epsilon_{SF}}{\partial t} - \frac{G}{\mu}\frac{\partial \epsilon_{SF}}{\partial t} \tag{3.52}$$

Equation (3.52) has reduced Equation (3.48) to a single unknown, the in-plane stress, from 9 stress-strain unknowns. The shear stresses and strains are not needed because they are 0 everywhere due to uniformity. If there were not spatial uniformity, each of the 3 normal and 3 shear stresses and the 3 displacements would need to be calculated separately.

To determine how important viscous relaxation is, the strain from relaxation can be calculated as in Equation (2.76),

$$\frac{\partial \epsilon_{V,xx}}{\partial t} = \frac{1-2\nu}{2\mu}\sigma_{xx} \tag{3.53}$$

Some analyses of uniform strain ignore the z-direction. This is undesirable because the

second in-plane axis contributes to the overall in-plane stress through the volume coupling term. Ignoring the z-direction would result in an underprediction in $\epsilon_{yy}$ by a factor of $(1+\nu)$, $\sigma_{xx}$ by $(1+\nu)$, and $\epsilon_{V,xx}$ by $\left(\frac{1+\nu}{1-\nu}\right)$.

### 3.3.3 Physical Property Buildup

One of the most difficult aspects of accurately calculating stress with curing reactions is capturing the vast changes that take place as the coating solidifies. This section details the methods used to calculate shrinkage, modulus, and viscosity changes with time as well as how to determine gelation and vitrification.

#### Gelation

Gelation occurs when the macromolecule produced by reactions of multifunctional monomers passes the percolation threshold, essentially creating one molecule spanning the coating from boundary to boundary. Flory (1969) created the first percolation theories based on co-reaction of monofunctional and multifunctional monomers in a step-growth reaction. This theory defines gelation to be when the probability of traveling along the polymer network from junction to junction becomes unity – the percolation threshold will have been passed when this happens. These theories were developed extensively by Macosko and Miller (1976) for different types of monomers and crosslinking reactions (Miller and Macosko 1988, Miller and Macosko 1978, Miller and Macosko 1976, Miller and Macosko 1987, Pearson and Graessley 1978). Free-radical reactions for polymerization and crosslinking were added by Tobita and Hamielec (1989), Zhu et al. (1993), and Luo et al. (1996). Stolov et al.'s (2000) work that modifies the theory of Flory (1969) to be appropriate for UV curable acrylates (Stolov, Xie, Penelle, Hsu and Stidham 2001, Stolov, Xie, Penelle and Hsu 2001). The extended Flory theory is described here. The differences between step growth and chain growth polymerizations make some of the nomenclature somewhat confusing. A vinyl double bond will form two bonds on a growing chain, while a functional group on a typical step-growth polymer – an acid, alcohol, amine, etc. – will only form one. A multifunctional

monomer with $m$ vinyl bonds will have a functionality of $f_{max} = 2m$. For TMPTA, $m = 3$ and $f_{max} = 6$. Define the probability of $n$ vinyl groups having reacted on a monomer by $P_n$

$$P_n = C_m^n P^n (1-P)^{m-n} \tag{3.54}$$

where $P$ is the overall vinyl group conversion and $C_m^n$ are binomial distribution coefficients,

$$C_m^n = \frac{n!}{(n-m)!m!} \tag{3.55}$$

The branching coefficient, $\alpha$ is the probability of traveling from network junction to network junction with 2 or more reacted vinyl groups ($M_{2,3,...}$) along a polymer chain with a single reacted vinyl group($M_1$)

$$\underbrace{M_{2,3,...}}_{\text{Network Junction}} - \underbrace{M_1 - M_1 - M_1 - M_1 - M_1 - M_1}_{\text{j chains between network junctions } 0 \leq j \leq \infty} - \underbrace{M_{2,3,...}}_{\text{Network Junction}} \tag{3.56}$$

This probability is given as

$$\alpha = \left( \sum_{n=2}^{m} P_n \right) \sum_{j=0}^{\infty} P_1^j = \frac{\sum_{n=2}^{m} P_n}{1 - P_1} \tag{3.57}$$

The average number of branches per junction, $f_{av}^{ends}$ is

$$f_{av}^{ends} = \frac{\sum_{n=2}^{m} 2nP_n}{\sum_{n=2}^{m} P_n} \tag{3.58}$$

Gelation occurs when the travel from junction to junction occurs indefinitely,

$$\alpha = \frac{1}{f_{av}^{ends} - 1} \tag{3.59}$$

| Monomer | Vinyl groups | $f_{max}$ | Experimental gelation conversion | Extended Flory gelation conversion |
|---|---|---|---|---|
| TPGDA | 2 | 4 | 35–43 | 41.4 |
| TMPTA | 3 | 6 | 21–25 | 26.8 |
| PETA | 4 | 8 | 14–16 | 20.0 |

Table 3.2: Conversion at gelation for acrylates with 2–4 vinyl groups. Data from Stolov et al. (2000)

Using Equations (3.54) – (3.59), the overall conversion of vinyl bonds at gelation can be determined. Table 3.2 shows the extended Flory analysis closely matches experimental measurements for acrylates with 2–4 vinyl groups.

### Glass Transition

The glass transition is the most single important property of any polymer system. At a temperature below the glass transition temperature ($T_g$) molecular motion is is significantly hindered, stress relaxation is minimal, and the modulus and viscosity are extremely high (Ferry 1970). In fact, Croll (1979a) used the glass transition as the step where coatings became solid, even though they were probably viscoelastic before that. For a given polymer sample, the glass transition is usually approached by changing the temperature of the polymer in relation to a fixed $T_g$. However, during cure, the glass transition changes with reaction. If the polymer sample remains at a constant temperature, vitrification will occur when $T_g$ rises above the curing temperature.

It now becomes necessary to calculate the glass transition temperature as a function of the extent of cure to determine when or if the coating vitrifies. DiBendetto's equation has been used to calculate $T_g$, but mobilities and lattice energies are needed (Pascault and Williams 1990, Perrin et al. 2007, Hale et al. 1991). Couchman (1979) developed an analysis for two-phase polymerizations that will work for the curing of TMPTA if the monomer and polymer are treated as the two phases (Sperling 1986).

| Property | Monomer | Polymer | Units |
|---|---|---|---|
| $\Delta C_p$ | 145.45 | 169.9 | $Jmol^{-1}K^{-1}$ |
| $T_g$ | 213 | 513 | $K$ |

Table 3.3: Constants used in the calculation of $T_g$ with reaction

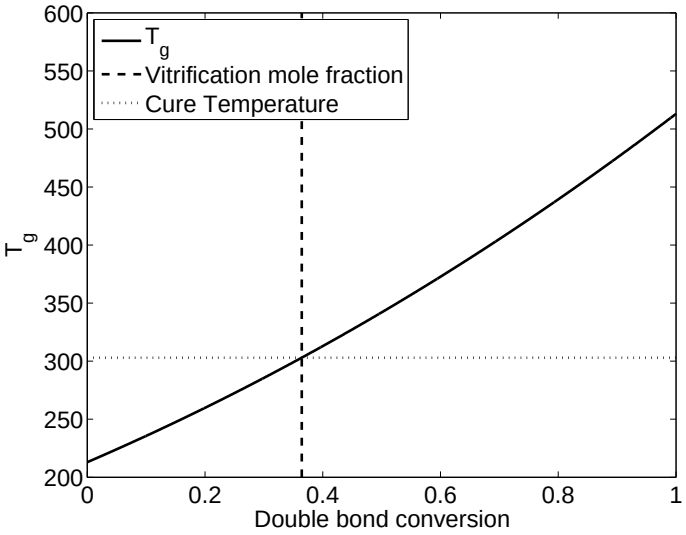


Figure 3.3: Glass transition temperature dependence on monomer conversion. Cure temperature of $30°C$ used. The system has vitrified to the right of the vitrification conversion

$$\ln T_g = \frac{M_1 \Delta C_{p1} \ln T_{g1} + M_2 \Delta C_{p2} \ln T_{g2}}{M_1 \Delta C_{p1} + M_2 \Delta C_{p2}} \tag{3.60}$$

where $T_{gi}$ is the glass transition temperature of the individual components, $\Delta C_{pi}$ is the difference in heat capacity above and below the glass transition temperature, and $M_i$ is the mass fraction per repeat unit. This is identical to the mole fraction due to the repeat unit basis.

The parameters are calculated as follows; $M_i$ is calculated using Equations (3.20) – (3.22). $T_{gi}$ is determined using experimental data in the literature (Anseth et al. 1993, Richter 2007). $\Delta C_{pi}$ is determined using a group contribution theory (van Krevelen 2009). Table 3.3 lists the data used to calculate the vitrification temperature with reaction.

As the glass transition temperature of the polymer rises, the system vitrifies when $T_g$

reaches the temperature of cure (Croll 1979a). Figure 3.3 shows the rise of $T_g$ with double bond conversion increase by reaction. Raising the cure temperature delays vitrification more and more. It is important to point out that this calculation of the glass transition temperature does not take molecular architecture or volume relaxation into account. To what degree the rate of polymerization influences the vitrification temperature and if vitrification alters volume change is still unknown.

### Stress-free State Evolution

Change in the stress-free state is the impetus for deformation and stress generation. It is often called a 'shrinkage' strain due to the decreasing specific volume with reaction (Tam 1997, Lei 1999, Radhakrishnan 2006, Rajamani 2005, Lange et al. 1995). The new stress-free state must be expressed as a strain from the original state,

$$\epsilon_{SF} = \frac{v_{initial} - v}{v_{initial}} \tag{3.61}$$

where $v_{initial}$ is the volume at the onset of polymerization and $v$ is the current volume of the coating. Also, $\boldsymbol{\epsilon_{SF}} = \epsilon_{SF} \cdot \boldsymbol{I}$. Equation (3.52) requires the time derivative of stress-free strain,

$$\frac{\partial \epsilon_{SF}}{\partial t} = \frac{-1}{v_{initial}} \frac{\partial v}{\partial t} \tag{3.62}$$

$\frac{\partial v}{\partial t}$ may be calculated using Equation (3.47).

### Modulus and Viscosity Evolution

The buildup of modulus and viscosity with conversion is the most difficult process to model. Reactions are nonlinear and the properties of the polymer change by such large amounts that small errors in calculation may cause large deviations in the actual and calculated values. Changes are large enough that constructing an instrument capable of measuring properties over the entire range of curing is extremely difficult (Wen 2001). That being said, it is

possible to predict the modulus and viscosity of the curing coating. In fact these changes are becoming important enough to establish a new field, *chemorheology* (May 1982, Murakami and Ono 1979, Halley and George 2009).

Calculation of modulus and viscosity during cure can be performed in a variety of ways. The method of modeling the stress generation determines how the buildup must be represented. The simplest way to model the buildup is to assume one point in time where the coating solidifies and have a step change in modulus or viscosity then. These approaches tend to omit viscoelasticity and use vitrification as the solidification point (Croll 1979a, Prasatya et al. 2001). Lange et al. (1995) used an incremental integral elastic buildup model and an estimate of the integral modulus buildup to model thermoset coatings, similar to Hossain et al. (2009a) (Hossain et al. 2009b). Koplin et al. (2009) uses a simple but elegant method that scales modulus and viscosity with the degree of crosslinking past gelation according to network theory of Vilgis (1989). For viscoelastic modeling using time integrals of spectra of fading moduli, a superposition of Maxwell elements can be used for simultaneous constitutive and modulus modeling (Yang et al. 2004, Adolf and Martin 1996, Simon et al. 2000, Martin and Adolf 1990). A separate viscosity is not needed with these. Similarly, Prony series models have been used for viscoelastic analysis (Meuwissen et al. 2004, Ernst et al. 2000, Ernst et al. 2002). O'Brien et al. (2001) used a relaxation scaling with a viscoelastic constitutive equation. Rajamani (2005) used a WLF-like (Williams et al. 1955) exponential scaling with departure from vitrification conversion. Yousefi et al. (1997) review some WLF scaling arguments for thermoset cure.

For the Maxwell constitutive equation in differential form, a single, time dependent value for modulus and viscosity are needed. This is in contrast to superposition methods that use a series of time decaying moduli. From a physical standpoint, sigmoidal models behave as the real viscosities and moduli of the curing coatings would; they have low initial values that rise and finally plateau. The liquid coating has a low value of modulus that rises due to network formation and gelation and reaches a steady value after vitrifying. The same is true for viscosity, and an extremely high viscosity entirely suppresses relaxation, making the

Maxwell constitutive equation behave as an elastic solid, which the coatings are at the end of cure. Liang and Chandrashekhara (2006) recognized this, as did Vaessen (2002), whose back-calculation of modulus and viscosity from measured stress data is close to real behavior. However, it is Love, Ruinet and Teyssandier's (2008) elegant sigmoidal characterization combined with experimental rheology of UV cured acrylates that describes the modulus and viscosity for the curing coatings the most closely (Love and Piguet-Ruinet 2007, Love, Teyssandier, Sun and Wong 2008). A modified Boltzmann sigmoid is used to describe the property buildup,

$$\ln\left(G\left(x\right)\right) = \ln\left(G_{\infty}\right) + \frac{\ln\left(G_o\right) - \ln\left(G_{\infty}\right)}{1 + \exp\left(\frac{x - x_{Go}}{\Delta x_G}\right)} \tag{3.63}$$

$$\ln\left(\mu\left(x\right)\right) = \ln\left(\mu_{\infty}\right) + \frac{\ln\left(\mu_o\right) - \ln\left(\mu_{\infty}\right)}{1 + \exp\left(\frac{x - x_{\mu o}}{\Delta x_{\mu}}\right)} \tag{3.64}$$

$G_o$ and $\mu_o$ are the modulus and viscosity at 0 conversion, $G_{\infty}$ and $\mu_{\infty}$ are the modulus and viscosity at full conversion, $x_{Go}$ and $x_{\mu o}$ are initiation constants, and $\Delta x_G$ and $\Delta x_{\mu}$ are widths of transition from low to high values of the sigmoid. Using known values for initial viscosity and modulus with the modulus and conversion at gelation and vitrification (from Section 3.3.3), the constants can be evaluated and the modulus and viscosity can be calculated for all conversions. Since the viscosity of TMPTA was not known anywhere except before reaction, a WLF scaling is used (Williams et al. 1955). Relaxation processes scale similarly, so $G$, $\tau$, and $\mu$ should all buildup at the same relative rate. This means $x_{Go} = x_{\mu o}$ and $\Delta x_G = \Delta x_{\mu}$. Glassy modulus and initial viscosity are known by experiment (Vaessen et al. 2002, Sartomer, Inc 2009). Initial modulus is estimated by calculating initial relaxation time and using the known initial modulus, $G_o = \frac{\mu_o}{\tau_o}$. $\tau_o$ is taken from initial stress relaxation experiments in TMPTA (Vaessen et al. 2002). Gelation conversion is known using Table 3.2 and modulus is taken to be that of a typical rubber (Ferry 1970, Sperling 1986). Vitrification modulus is taken to be 90% of the final value and vitrification conversion is obtained using Equation (3.60).

| Parameter | Value | Units |
|---|---|---|
| $G_o$ | $5.0 \cdot 10^3$ | $Pa$ |
| $G_\infty$ | $6.75 \cdot 10^8$ | $Pa$ |
| $\mu_o$ | $1.0 \cdot 10^{-1}$ | $Pa \cdot s$ |
| $\mu_\infty$ | $1.4 \cdot 10^{17}$ | $Pa \cdot s$ |
| $x_o$ | 0.2232 | – |
| $\Delta x$ | 0.02571 | – |

Table 3.4: Parameters for calculating $G$ and $\mu$ with changing conversion using Equations (3.63) and (3.64)

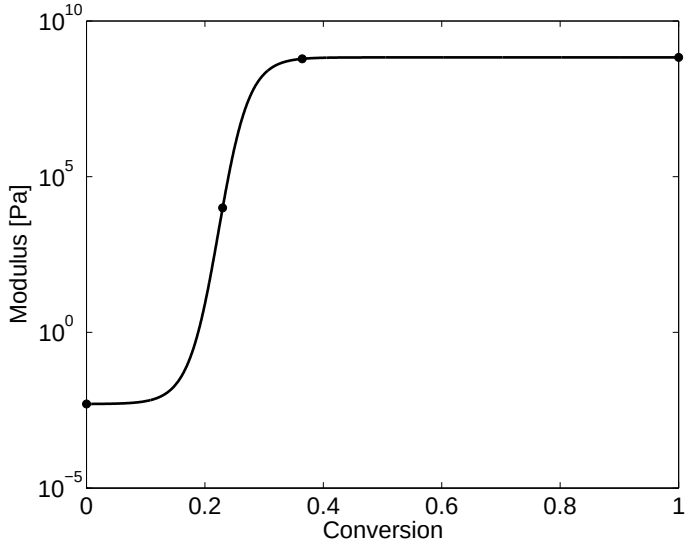


Figure 3.4: Modulus dependence on conversion. Points (•) indicate matching points to calculate parameters in Table 3.4

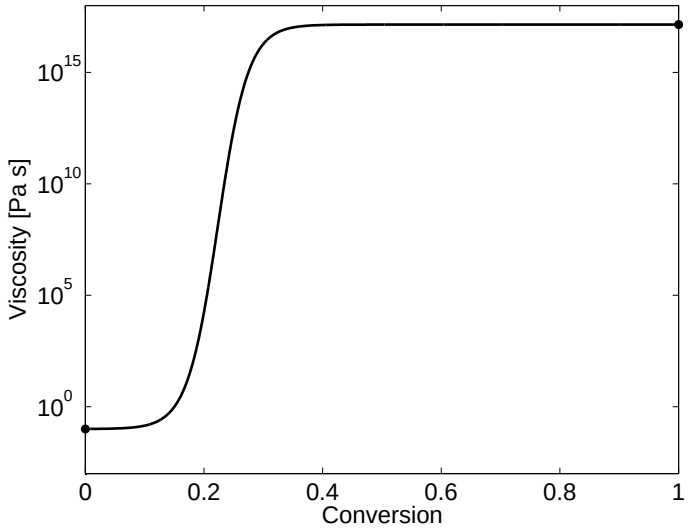


Figure 3.5: Viscosity dependence on conversion. Points (•) indicate matching points to calculate parameters in Table 3.4

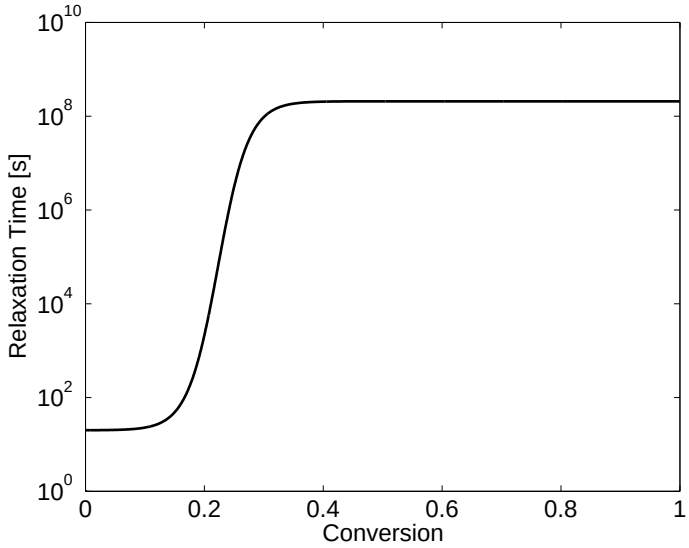


Figure 3.6: Relaxation time dependence on conversion

### Poisson's Ratio

The evolution of Poisson's ratio – which quantifies the severity of volume coupling – is much more difficult to predict than that of the modulus or viscosity. Theoretically, $\nu$ is initially 0 and rises to its final value post-solidification. Assuming $\nu$ remains constant at its final value throughout polymerization has little effect on the final stress and is assumed here, $\nu = 0.35$. This is a common treatment for these types of calculations (Lange et al. 1995)

### Solution

The kinetic species conservation, stress evolution, and relaxation evolution equations are a set of coupled ordinary differential equations with variable coefficients. Specifically, Equations (3.44) – (3.47), (3.52), and (3.53) must be solved together. Initial conditions for initiator concentration must be supplied. Initial concentrations of polymer, active and buried radicals, stress, viscous strain are all zero. Additionally, incident UV light intensity must be supplied as a function of time. This is because the UV light intensity may be altered or turned off during reaction. The equations are solved using the ordinary differential solver `ode15s` in MATLAB (The Mathworks Inc. R2009b).

## 3.4 Results

This section presents results for uniform stress generation by the method of Section 3.3. Controllable parameters include the initial initiator concentration, UV light intensity, and the irradiation time. This section only considers constant UV intensity with sufficient time for the completion of reaction and stress generation. UV intensity will be reported in $\mathrm{W/dm^2}$, the natural units for calculation instead of $\mathrm{W/cm^2}$, $\mathrm{mW/cm^2}$, or $\mu\mathrm{W/cm^2}$, which are reported for experiments. It is not difficult to convert between these units $1\mathrm{W/dm^2} = 10\mathrm{mW/cm^2}$.

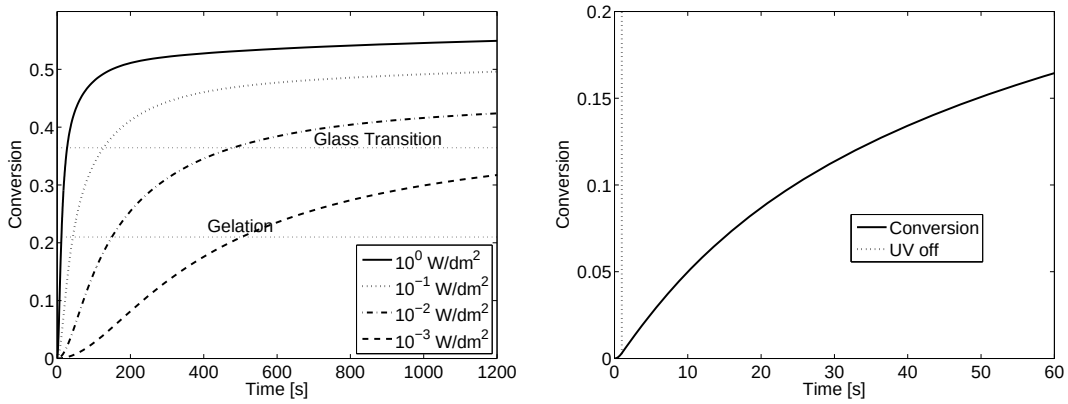


(a) Double bond conversion in time. Continuous UV irradiation

(b) Double bond conversion showing post-cure. UV light is turned off after 1 s. Active radicals continue reacting in the dark. 1.0 W/dm$^2$

Figure 3.7: Double bond conversion. $10^{-2}$ % DMPA.

### 3.4.1 Conversion

Constant UV light intensity limits the control over the reaction rates to initiation of radical chains. This initiation control is not great, increasing photoinitiator concentration will increase initiation, as will increasing UV intensity, however, the fall in the reaction rate caused by falling diffusivities cannot be explicitly controlled. There is only so much control given by changing initiator concentration and UV light intensity. Initiation can be ceased by turning off the UV source, so initiation can be stopped completely at will. This does not stop active radicals created during irradiation from continuing to react. In fact the continued curing after irradiation – post-cure – may cause undesired reaction and stress generation. Figure 3.7(a) shows several conversion profiles in time. Conversion increases with initiator concentration by initiating more reactions. The shape of the curve comes from the kinetics – autoacceleration and autodeceleration (Andrzejewska 2001, Wen and McCormick 2000) – with the plateau caused as mobilities decrease, virtually ceasing propagation. Figure 3.7(b) shows the post-cure phenomena; virtually all conversion comes after the UV light has been turned off.

Detailed studies of the conversion profile, initiation, reaction rate constants, autoacceler-

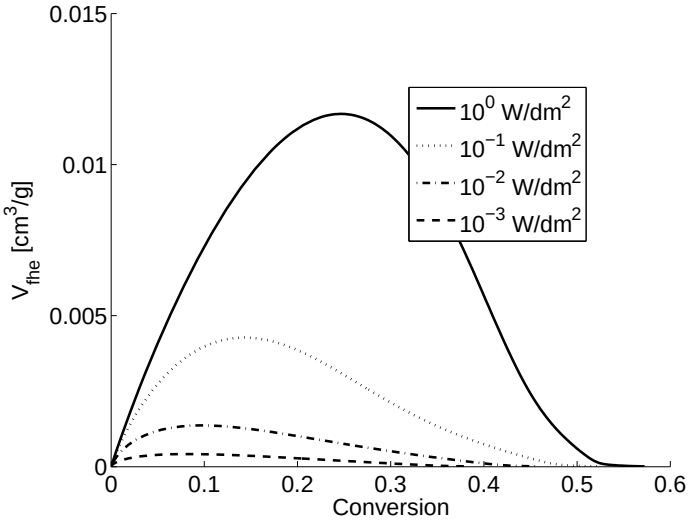


Figure 3.8: Excess free volume with conversion. $10^{-2}$ % DMPA.

ation and autodeceleration, and radical concentrations do not fall in the scope of this thesis. They have been investigated in other sources in detail (Kurdikar and Peppas 1994a, Kurdikar and Peppas 1994b, Wen and McCormick 2000, Vaessen 2002, Bowman and Peppas 1991, Richter 2007).

### 3.4.2 Volume

The specific volume of the polymer system is intimately tied to the reaction rates. In fact, the only way to obtain high conversions in TMPTA polymerizations is to exploit the volume relaxation shown in Equation (3.47) by initiating radicals quickly. Propagation happens faster and to higher conversions with more excess free volume before diffusional limitations cease reactions. Figure 3.8 shows excess free volume with conversion for various incident light intensities. As UV intensity increases, there is more excess free volume leading to higher propagation rates and higher final conversions, which can be seen in Figure 3.7. With faster reactions, $v_\infty$, the equilibrium volume, changes faster. $v$, the actual volume cannot change as fast as $v_\infty$ and lags behind according to Equation (3.47). Figure 3.9 shows that as time progresses and reactions slow down, $v$ has sufficient time to relax to $v_\infty$. This lag in specific

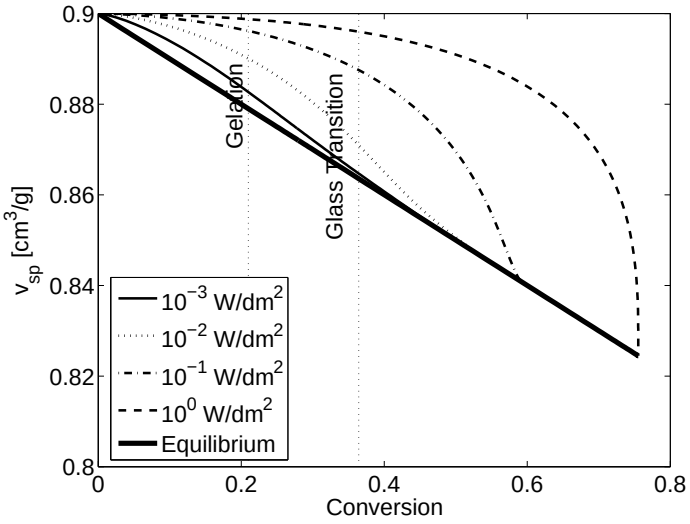


Figure 3.9: Specific volume with conversion for several incident UV intensities. 1 % DMPA.

volume causes measured shrinkages to lag behind the equilibrium value, leading to delayed shrinkage (Rajamani 2005). Faster initiation rates cause longer delays in shrinkage with respect to conversion.

### 3.4.3 Gelation and Vitrification

The onset of gelation or vitrification offer convenient benchmarks of conversion and an insight to stress generation. Gelation is where the polymer truly becomes a solid and is accompanied by an increase in the modulus and relaxation time. Vitrification is similar but the transition past $T_g$ causes a significant rise in the modulus and the relaxation time rises so much as to render relaxation virtually nonexistent. For these reasons, the onset of vitrification is taken to be the point of interest for stress generation due to the significantly higher modulus and relaxation time than the gelation. This selection is logical but somewhat arbitrary; gelation could have been chosen, as could the point at when relaxation time becomes larger than process time, or when the modulus became large enough for stress-induced defects to be seen. The rest of this section will use vitrification to help understand how stress is generated and how changing the process parameters changes the stress buildup.

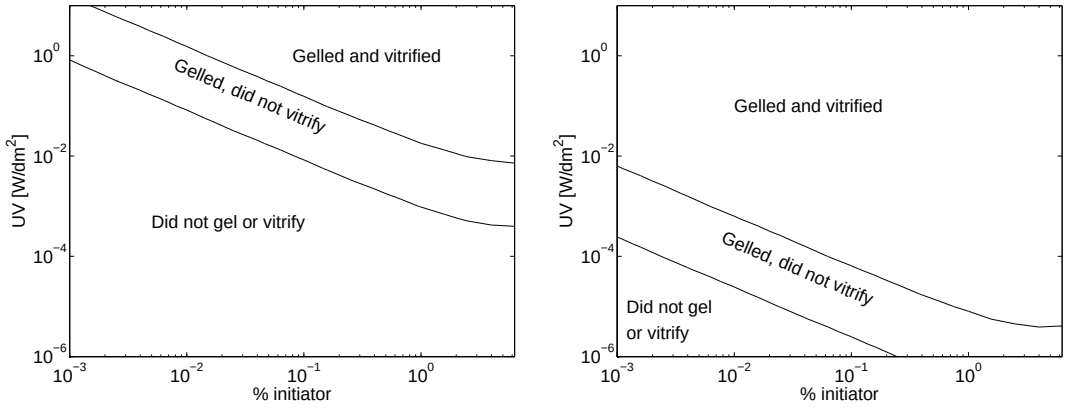


(a) 1 s. irradiation (b) 1 hr. irradiation

Figure 3.10: Gelation and vitrification map for different UV intensities and DMPA concentrations. Regions where gelation and vitrification, gelation but not vitrification, and neither gelation nor vitrification occur are shown.

UV light intensity, initiator concentration, and irradiation time all determine whether the coating will vitrify. If initiation is slow from low UV intensity or initiator concentration, $T_g$ may not be reached, even by increasing the irradiation time. In addition, $T_g$ may be crossed with extremely short irradiation times if the initiation is rapid during irradiation. Figure 3.10 shows regions of vitrification, gelation, and neither for various UV intensities and initiator concentrations. Figure 3.10(a) is only irradiated for 1 s. while Figure 3.10(b) is irradiated for 1 hr. This can be explained with the excess free volume described in Section 3.4.2. For slow initiation, decreasing mobility does not allow propagation to occur even with continued irradiation. For fast initiation, active radicals continue to react long after irradiation has ceased. There is no precise control over the conversion. This has ramifications in stress generation as well and will be described in Section 3.4.5

### 3.4.4 Stress-free state

Delayed volume relaxation also causes the stress-free state to lag behind its equilibrium value. Equation (3.61) shows the stress-free state changes with system volume, so when volume lags behind its equilibrium value, so does the stress-free state. Simply, the coating

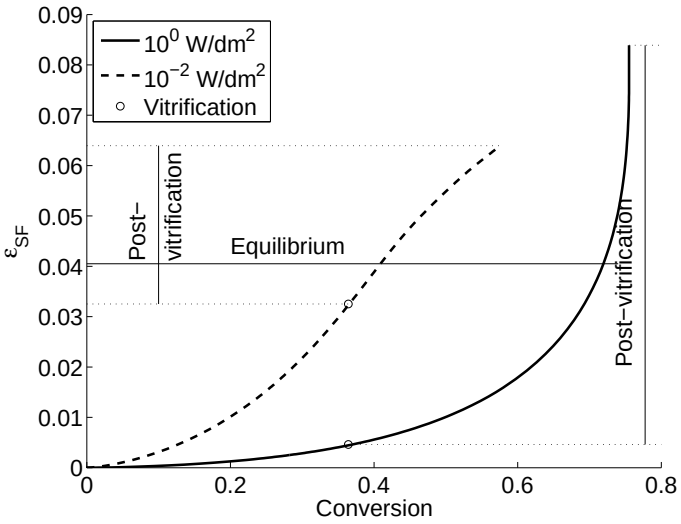


Figure 3.11: Stress-free state evolution with conversion. 1 % DMPA, continuous UV irradiation.

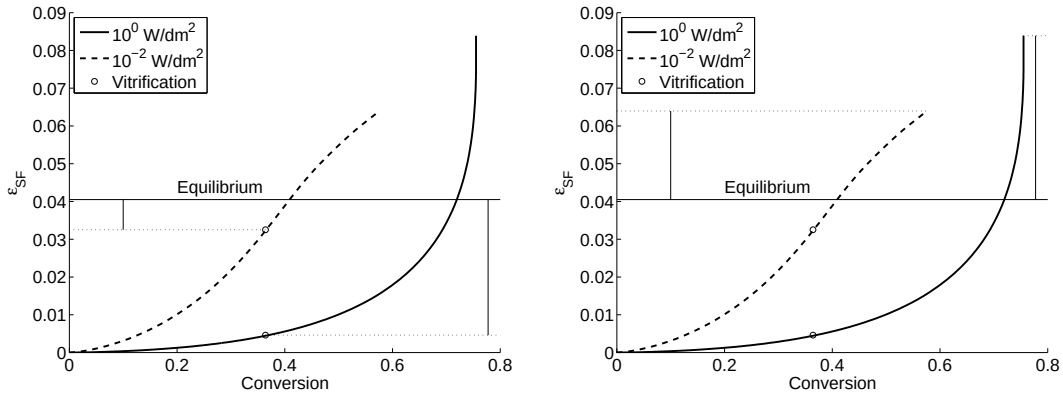


(a) Stress-free strain above $T_g$ caused by vitrification out of equilibrium from fast reactions.

(b) Stress-free strain above $T_g$ caused by continued reaction above the vitrification conversion

Figure 3.12: Strains above $T_g$. 1 % DMPA, continuous UV irradiation.

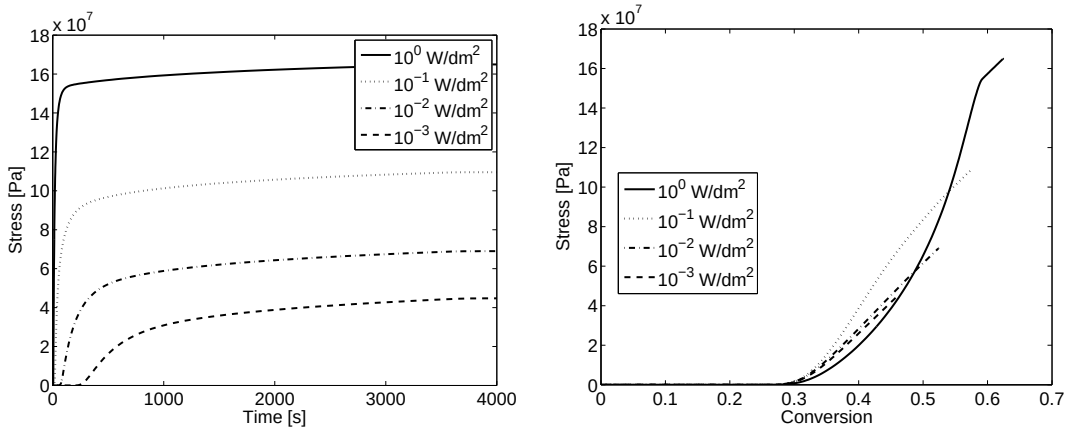


(a) Stress in time

(b) Stress in conversion

Figure 3.13: Stress with time and conversion. $10^{-2}$ % DMPA.

has not shrunk as much as it would like. This lag does not alter the reactions occurring and does not change the conversions at which gelation or vitrification occur in this model. Faster initiation leads to more stress-free state change post vitrification than slower initiation. The modulus and relaxation time are both larger post-vitrification so this stress-free state change causes more stress. Figure 3.11 shows the stress-free state strain and where vitrification occurs. Higher UV intensity causes stress-free state change after vitrification to be larger. There are two reasons for this. First, faster initiations shift the stress-free change to higher conversions, causing stress-free strain above $T_g$ that would be below $T_g$ if equilibrium was maintained at all times. This can be seen in Figure 3.12(a), the higher UV case has much more strain above $T_g$ than the lower UV case. Second, faster initiations increase the overall final conversion which increases the stress-free strain above $T_g$. This strain would occur even if the stress-free state were always in equilibrium. Figure 3.12(b) shows the additional strain above $T_g$ brought about by higher final conversion.

### 3.4.5 Stress

Generation of stress is intimately tied to the reaction kinetics of photopolymerization, the volume relaxation behavior of the polymer, and the physical property buildup. The volume

lag behind equilibrium is especially important in determining the final stress. Section 3.4.4 showed that faster initiations cause more stress-free state change above $T_g$. These strains occur with higher modulus and relaxation times, shown in Equations 3.4 – 3.6. Because of this, higher final stress is expected for faster initiation. Also, as the irradiation time is increased, higher final stress is expected because irradiating the coating for longer time will preserve radical initiation, increasing conversion. Figure 3.13 shows how stress builds up in time as well as with conversion. More quickly initiated polymerizations generate stress faster because they convert and change stress-free state and physical properties faster. When viewed in conversion, however, faster initiated polymerizations generate stress at higher conversions. This is due to the delayed stress-free state change discussed in Section 3.4.4. As the stress-free state reaches its equilibrium value, the stress rises and is the highest for faster initiations. Figures 3.14 – 3.16 show the final stress as functions of UV intensity, DMPA concentration, and irradiation time. Bowman and Peppas (1991) defined the end of reaction to be when the propagation rate falls to $1/100^{\text{th}}$ of its maximum value. This is unacceptable here because stress may continue to develop via delayed stress-free state change long after reactions have ceased. For this reason, the end of stress generation has been defined to be when the rate of stress buildup falls to $1/100^{\text{th}}$ of its maximum value. Some coatings finish generating stress before cessation of irradiation while some continue to generate stress in the dark. This depends on the initiation rate and irradiation time. All data shown was allowed to come to the end of stress generation.

Increasing the initiation rate by raising UV intensity or DMPA concentration raises the final stress for a given irradiation time. This can be seen in Figure 3.14. Similar trends are seen for lower irradiation times, but all stresses are lower. This is a universal feature of this stress model; increasing radical initiation increases final conversion as well as stress. The reason for this is the enhanced mobilities of reactants with excess free volume as was explained in Section 3.4.2. Figure 3.14 also shows that initiator and UV intensity can be traded off. More initiator can be added and the UV light can be turned down or the opposite to reach the same final stress. The figure axes are logarithmic, so the tradeoff is

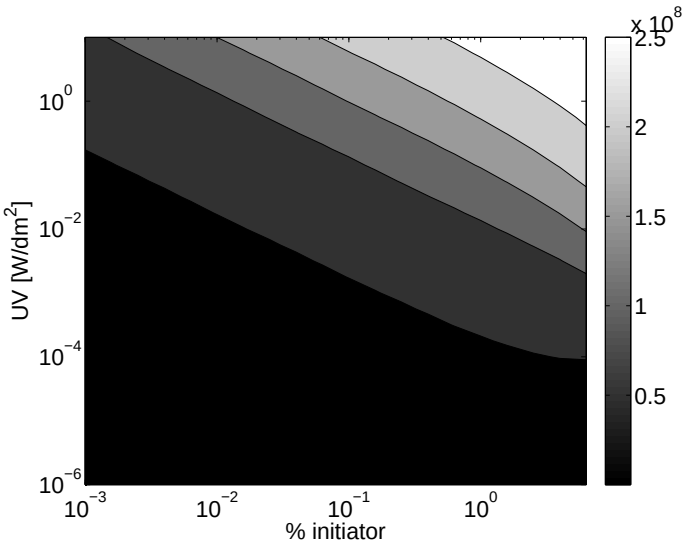


Figure 3.14: Final stress dependence on DMPA concentration and UV intensity. Stress in Pa. 1 hr. irradiation. Final stress defined to be stress after reactions and stress generation cease by reaching $1/100^{\text{th}}$ of their maximum rate.

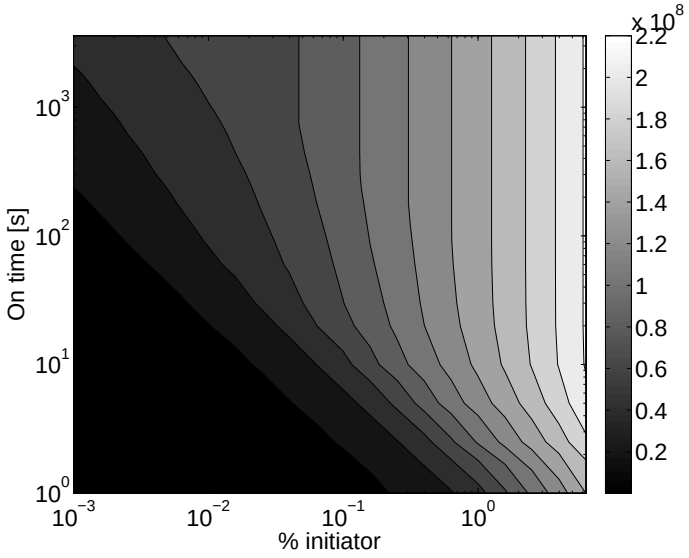


Figure 3.15: Final stress dependence on DMPA concentration and irradiation time. Stress in Pa. 0.1 W/dm$^2$.

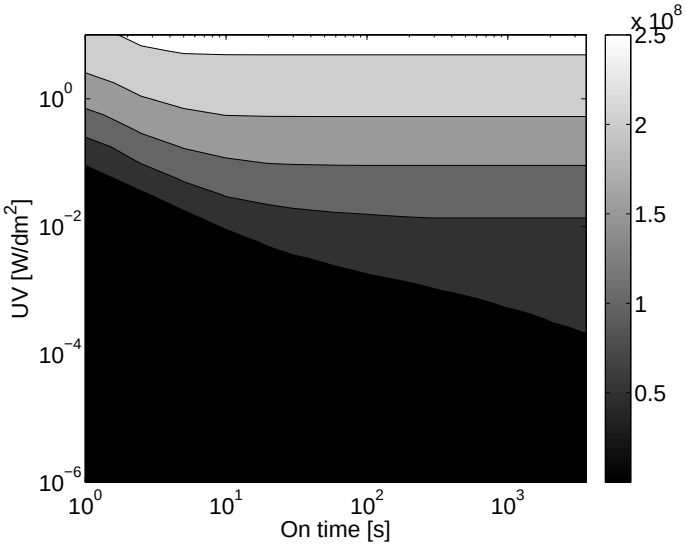


Figure 3.16: Final stress dependence on irradiation time and UV intensity. Stress in Pa. 1 % DMPA.

not constant, but this modeling technique can direct the selection of appropriate alternate curing conditions to obtain the same final state.

Increasing the irradiation time increases stress to a point, after which the stress does not increase with longer irradiation. This can be seen by the vertical contours at the top of Figure 3.15 and the horizontal contours on the right of Figure 3.16. For short irradiation times, lengthening irradiation enhances propagation; what was once slow propagation in the dark with no influx of radicals is now being supplied with active radicals via initiation. As irradiation times get longer and longer, diffusional limitations take over and propagation slows even with continued irradiation. The slowing of propagation also slows stress generation, so all the stress is generated while the light is on. Further increasing the irradiation time does nothing further to the stress, it already has reached its plateau value for a given set of initiator concentration and UV light intensity.

Figure 3.11 suggests that the further from equilibrium volume the actual volume is during vitrification, the higher the stress will be at the end of generation. This is indeed the case. Figure 3.17 shows the stress-free strain before vitrification and Figure 3.18 shows

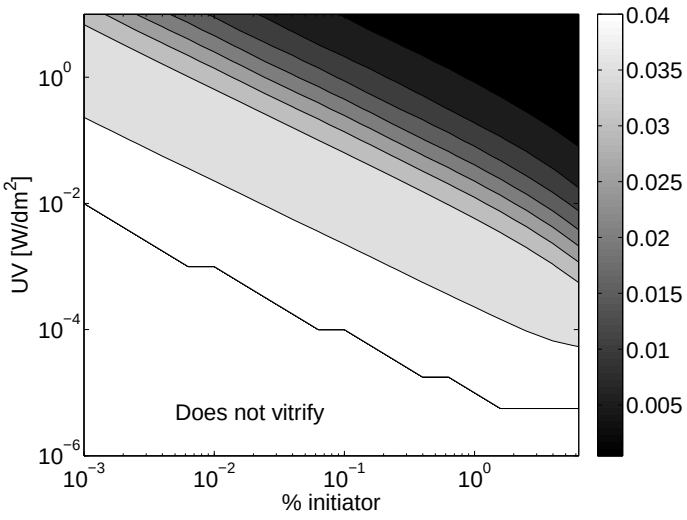


Figure 3.17: Stress-free state change at vitrification dependence on DMPA concentration and UV intensity. 1 hr. irradiation.

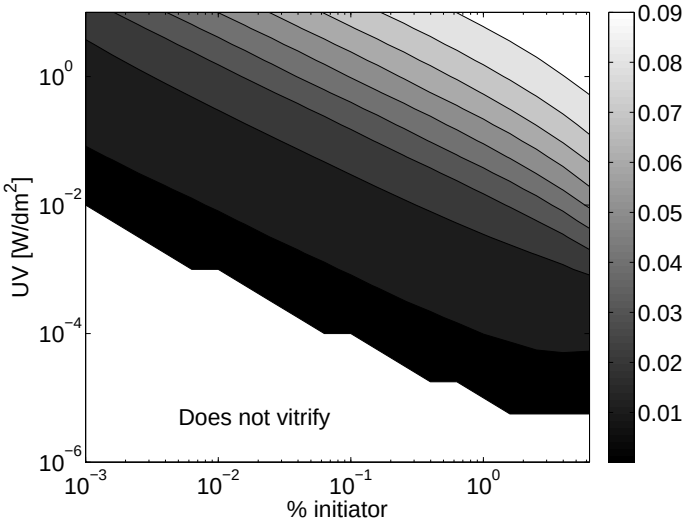


Figure 3.18: Stress-free state change after vitrification dependence on DMPA concentration and UV intensity. 1 hr. irradiation.

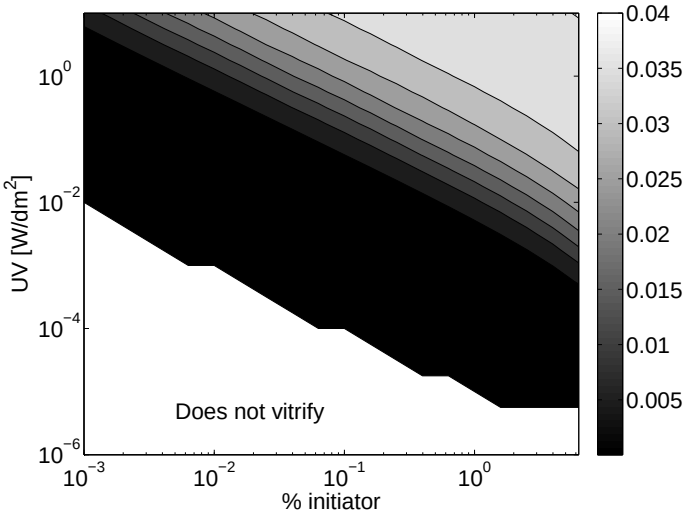


Figure 3.19: Additional stress-free state change after vitrification due to nonequilibrium volume. Dependence on DMPA concentration and UV intensity. 1 hr. irradiation.

it after vitrification. The dependence on UV intensity and initiator concentration is also shown. The stress-free strain after vitrification combines strain caused by nonequilibrium vitrification with strain caused by continued reaction as in Figure 3.11. Figure 3.19 shows the stress-free strain caused just by vitrification out of equilibrium, similarly to Figure 3.12(a). As initiation rate increases with UV and initiator, the reactions happen so fast that volume equilibrium cannot be reached. Eventually equilibrium is reached, however this happens after vitrification; the stress-free strain must occur after $T_g$. This generates more stress because the modulus and relaxation time are higher after $T_g$. Figures 3.20 and 3.21 show the stress at vitrification and the additional stress added after. The stress at vitrification is somewhat deceiving because it seems like faster initiation rates have less stress. It is true that fast initiation generates little stress before vitrification but this is temporary as the stress generated after $T_g$ is much higher; stress is generated at later conversions for faster initiation. The stress maximum in Figure 3.20 is brought about by reacting slowly enough to be close to equilibrium volume at $T_g$ – a large stress-free strain – but not slowly enough for stress relaxation.

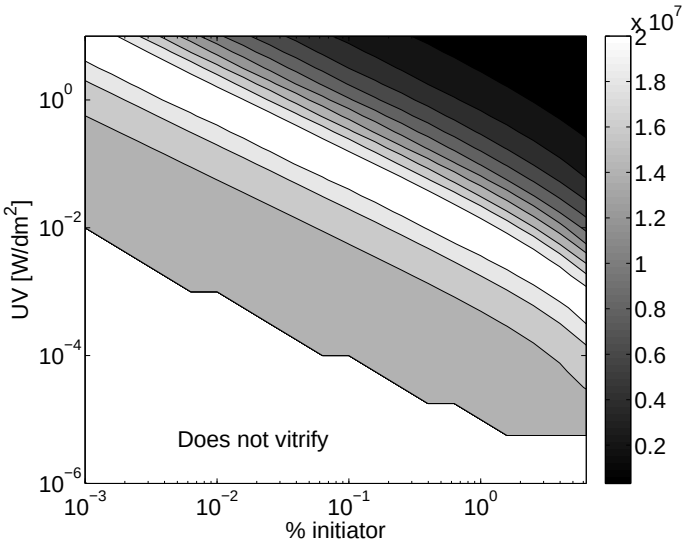


Figure 3.20: Stress at vitrification dependence on DMPA concentration and UV intensity. Stress in Pa. 1 hr. irradiation.

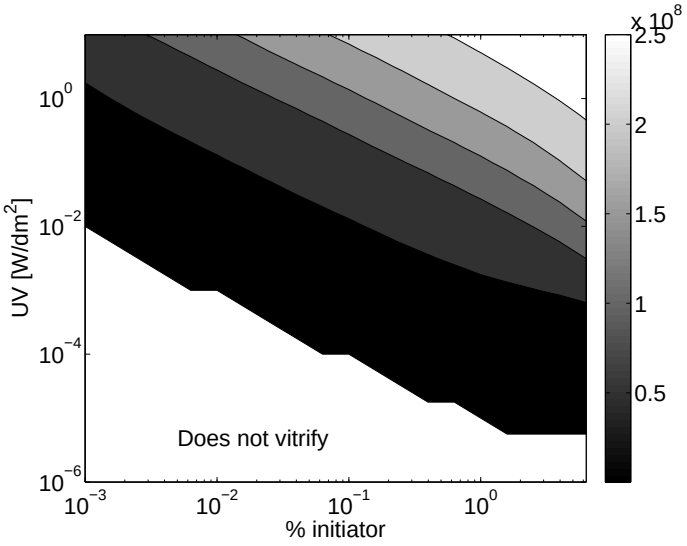


Figure 3.21: Stress after vitrification dependence on DMPA concentration and UV intensity. Stress in Pa. 1 hr. irradiation.

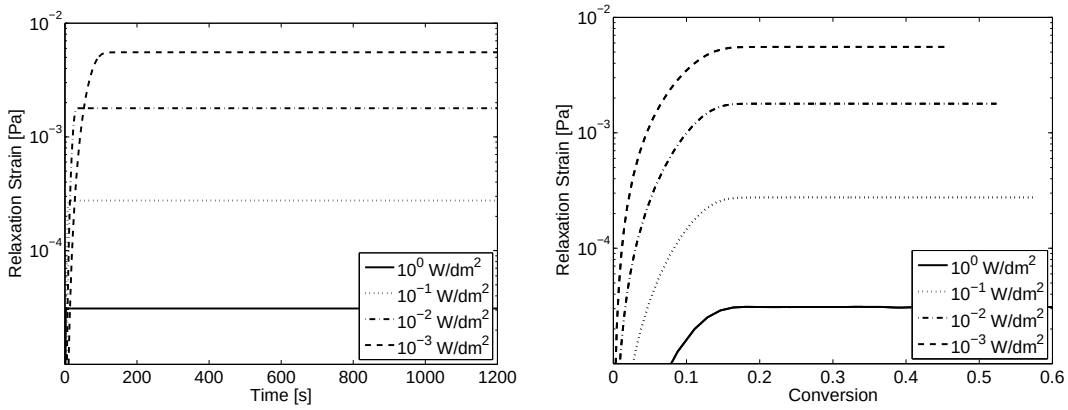


(a) Relaxation strain in time.

(b) Relaxation strain in conversion.

Figure 3.22: Relaxation strain in time and conversion. $10^{-2}$ % DMPA.

### 3.4.6 Relaxation

Relaxation reduces stress and can be quantified by a relaxation strain as described by Equation (3.53). Viscous strain is only a measure of the deformation induced by the relaxation, not a measure of the amount of stress relieved. Figure 3.22 shows how relaxation strain develops in time and with conversion. Figure 3.22(b) shows that relaxation is effectively stopped when a conversion is obtained with a large relaxation time, the relaxation strain reaches a plateau. Figure 3.22(a) shows that the amount of time elapsed before this happens depends on the initiation rate, with slower initiations spending more time with low relaxation times leading to higher overall relaxations.

Figure 3.23 shows the relaxation strain at vitrification and its dependence on UV intensity and initiator concentration. Fast initiation has very small relaxations before vitrification for two reasons. First, they reach vitrification very quickly which does not leave sufficient time for relaxation. Second, the stress obtained between cure initiation and vitrification is not high – shown in Figure 3.20 – so the driving force for stress relaxation is low. Final relaxation and its dependence on UV intensity and initiator concentration is shown in Figure 3.24. Quickly initiated reactions do not relax significantly after vitrification because the relaxation time becomes very high then. Very slowly initiated systems do not relax signifi-

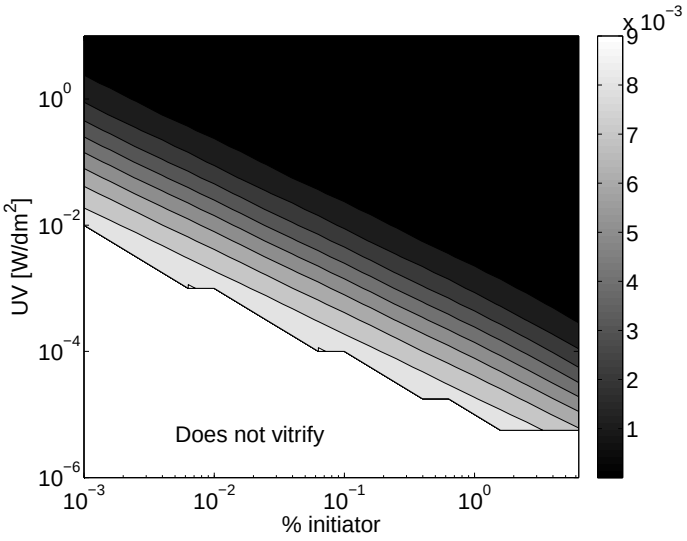


Figure 3.23: Relaxation strain at vitrification dependence on DMPA concentration and UV intensity. 1 hr. irradiation.

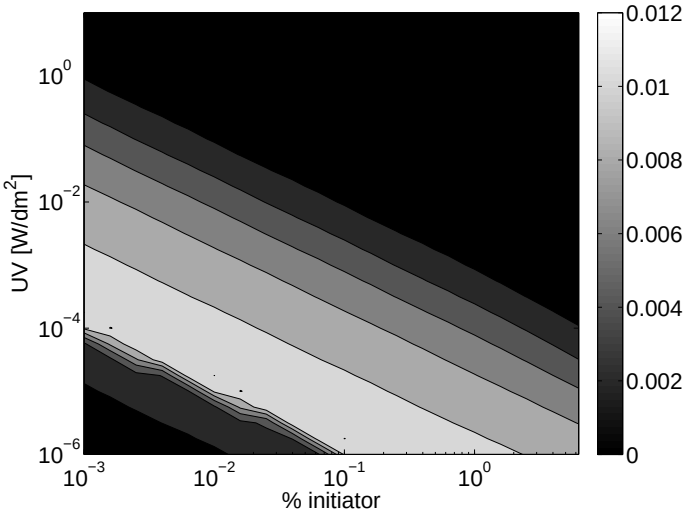


Figure 3.24: Final relaxation strain dependence on DMPA concentration and UV intensity. 1 hr. irradiation.

cantly because the stress and stress-free strains are both low. The maximum in relaxation comes from a combination of longer time to reach $T_g$, higher stress driving force while doing so, and a reasonable relaxation time that is not too high to prevent relaxation.

### 3.4.7 Quantifying Stress Rates

Rates of stress generation and relaxation are quantified by decomposing the strain and rearranging the constitutive equation. This allows the determination of the importance of buildup, relaxation, and the parameters that influence them.

The viscoelastic strain, $\boldsymbol{\epsilon_{VE}}$, is further decomposed into viscous, $\boldsymbol{\epsilon_V}$, and elastic, $\boldsymbol{\epsilon_E}$, strains

$$\boldsymbol{\epsilon}(t) = \boldsymbol{\epsilon_{EL}}(t) + \boldsymbol{\epsilon_V}(t) + \boldsymbol{\epsilon_{SF}}(t) \tag{3.65}$$

Substituting Equation (3.65), (3.53) and (3.51) into Equation (3.52), the rate of stress buildup in the coating plane can be expressed as

$$\frac{\partial \sigma_{xx}}{\partial t} = 2G\left[\frac{-\sigma_{xx}}{2\mu} + \frac{1+\nu}{\nu-1}\frac{\partial \epsilon_{SF}}{\partial t}\right] \tag{3.66}$$

The rates of stress buildup and relaxation are

$$\text{Rate of stress buildup } = \frac{\partial \sigma_{xx,Buildup}}{\partial t} = \frac{2G(1+\nu)}{\nu-1}\frac{\partial \epsilon_{SF}}{\partial t} \tag{3.67}$$

$$\text{Rate of stress relaxation } = \frac{\partial \sigma_{xx,Relaxation}}{\partial t} = \frac{\sigma_{xx}}{\tau} \tag{3.68}$$

where $\tau$ is the viscoelastic stress relaxation time, $\tau = \frac{\mu}{G}$. Integrating Equations (3.67) and (3.68) show the relative importance of stress relaxation to stress buildup. Equation (3.67) shows that stress builds up from a changing stress-free state. The faster the stress-free state changes, the faster stress builds up. Additionally, the larger the modulus, the faster stress builds up. Equation (3.68) shows that stress can only relax if the system is stressed to

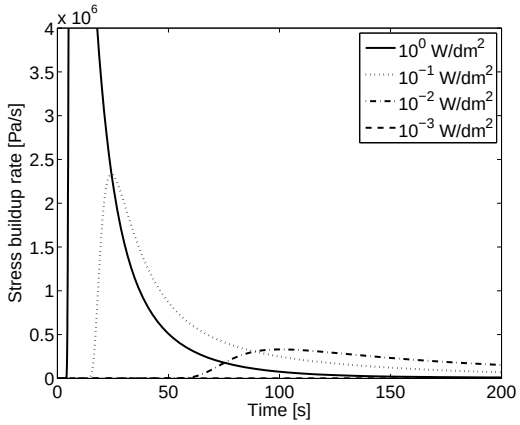


Figure 3.25: Rate of stress buildup in time. 0.1 % DMPA. 1 hr. irradiation.

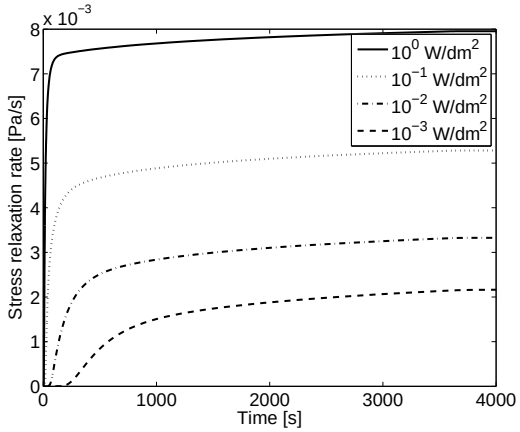


Figure 3.26: Rate of stress relaxation in time. 0.1 % DMPA. 1 hr. irradiation.

some degree. Relaxation happens more quickly for shorter relaxation times and higher the stresses. The total stress at a given time can be calculated by integrating Equation (3.67) and subtracting the integral of Equation (3.68).

Figure 3.25 shows the rate of stress buildup in time for several different values of incident light intensity. The stress rate curves look strikingly similar to the polymerization rate curves that show autoacceleration and autodecelration (Wen and McCormick 2000), however the reasons for a stress buildup rate maxima to occur are different than for a propagation rate maxima. Initial buildup is slow because the modulus is small. As reaction progresses, the modulus begins to get larger. At the same time, the stress-free state begins to change. For fast initiation, delayed stress-free state change causes the stress-free state to change quickly with a large modulus because vitrification has been passed. This causes a high stress buildup rate. For slower initiation, delayed stress-free state change is not as severe. First, some stress-free strain occurs with a smaller modulus before vitrification. Second, the stress-free state can change more slowly because reactions are taking place more slowly. This agrees well with Equation (3.67). The initial delay in stress buildup is caused somewhat by the delay in stress-free state change but moreso by the time taken for the modulus to buildup to a large enough value to cause appreciable stress.

Figure 3.26 shows the rate of stress reduction for the same conditions as Figure 3.25. Stress relaxation rate has monotonically increases. This is due to the increasing stress. Even though the relaxation time increases, the stress increases more during the buildup so stress reduction by relaxation always increases. Figure 3.13(a) shows a monotonically increasing stress for all time for all cases. Stress relaxation is not as important as buildup and hardly reduces the final stress. The relative magnitudes of buildup and relaxation rates show buildup is orders of magnitude more important than relaxation. In fact, Figure 3.27 shows the most stress relaxed is only a few Pa. The maximum in this figure occurs or similar reasons to the maximum in Figure 3.24. Relaxation is not very important for stress reduction, the modulus builds up too quickly and delayed shrinkage exacerbates stress build up after vitrification.

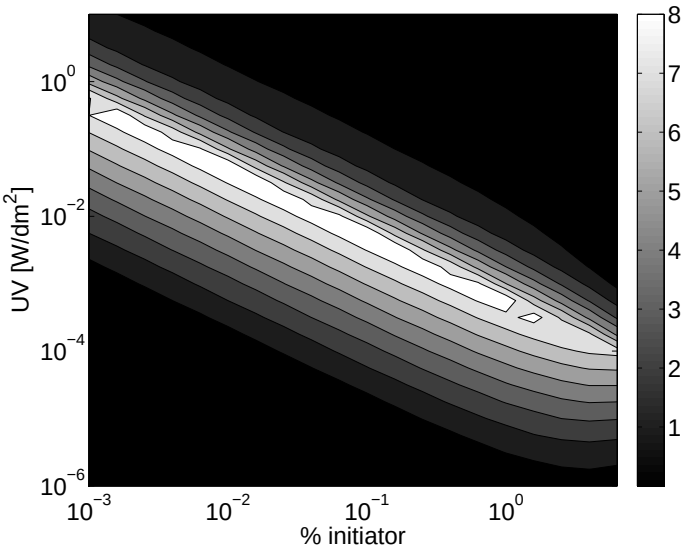


Figure 3.27: Total relaxed stress dependence on DMPA concentration and UV intensity. 1 hr. irradiation. Relaxed stress in Pa.

### 3.4.8 Reducing and Optimizing Stress Generation

Sections 3.4.1 – 3.4.7 detailed the mechanism behind stress generation. Prior to this work there existed no unified explanation of how stress builds up in a curing coating. The combination of coupling kinetics to deformation used in this work combined with the mathematical analysis allowed with a linear constitutive equation allowed the determination of what processes were important (vitrification, modulus increase) and what weren't (relaxation). Engineers designing coating solidification processing schedules desire to have control over the final state of their coating. For coatings that exhibit stress-induced defects it is desirable to reduce the residual stress in the coating. To this end we discuss the process for obtaining the minimum stress in a TMPTA coating initiated with DMPA and UV light. We will place the constraint on the final product that it must have passed $T_g$ to insure it is a hard coating with a high modulus. The process path that produces the lowest stress has three characteristics. First, radicals are initiated slowly enough so the volume remains in its equilibrium state the entire time; there is no delayed stress-free strain, just slow stress-free strain. Second, initiation is ceased early enough so that conversion stops once $T_g$ has been

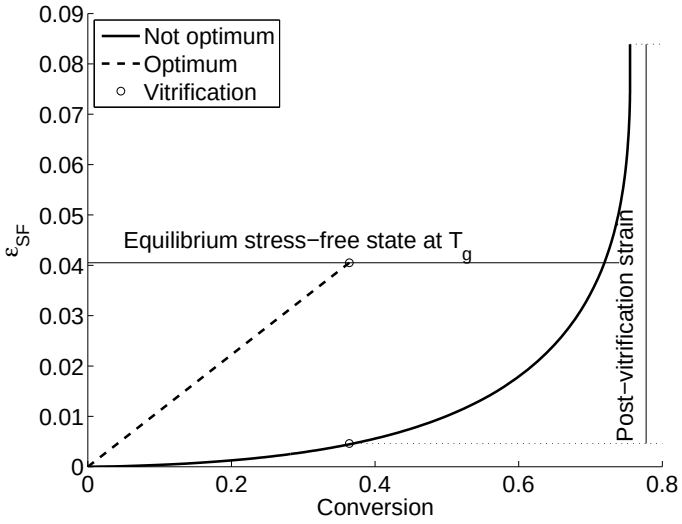


Figure 3.28: Optimum stress-free state change. Fast curing schedule is not optimum due to large strain above $T_g$. Optimum remains in equilibrium and has no strain above $T_g$. Equilibrium stress-free state at $T_g$ shown.

crossed. Third, initiation is sufficiently slow so that relaxation has more time to occur. This last characteristic is somewhat nebulous – the optimum would be to cure infinitely slowly. Infinitely slow curing assures volume is in equilibrium and that the propagation can be ceased at will, however there are two problems. The first is time. Relaxation becomes more important and can reduce the final stress the longer it has to act, but days, weeks, or years are too long to wait. The second problem is energy use. As the propagation rate slows more radicals will end up trapped and more need to be initiated to continue the propagation. Increased trapping reduces the number of double bonds converted per initiator dissociated, requiring more energy to reach the same conversion. The optimum curing schedule can be seen in part in the previous sections. The coating must vitrify and cure slowly enough to remain in equilibrium – no extra stress-free strain past $T_g$ is allowed and it must vitrify – similar to the region of Figure 3.19 with 0 extra strain while out of the non-vitrification region. It must also not react past vitrification conversion – no strain above $T_g$ due to continued reaction – similar to Figure 3.18 with 0 strain. Lastly, it must allow maximum time for relaxation. This can be seen in Figure 3.24. In reality, the maximum time allowed

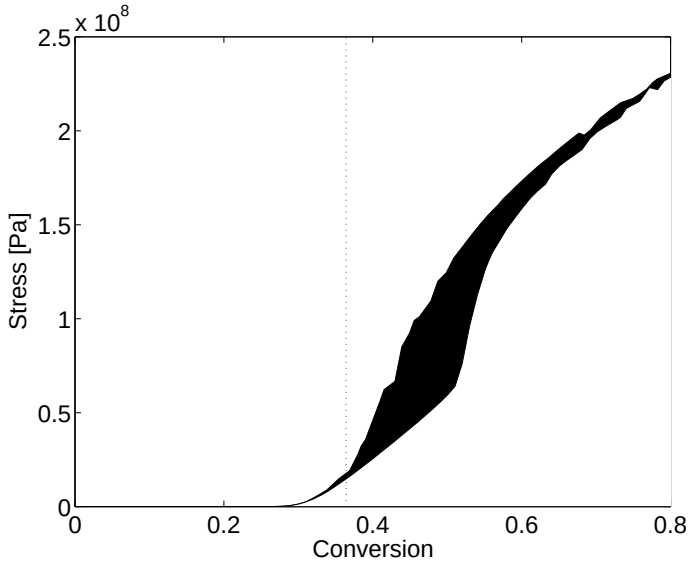


Figure 3.29: Process window showing possible conversion-stress pairs. 1 s. –1 hr irradiation. $10^{-6}$ – $10^{1}$ W/dm$^2$. $10^{-3}$ – $10^{\cdot 8}$ % DMPA. Vitrification indicated by dotted line.

by process conditions or energy use would be acceptable. It is important to note that more than one combination of initiator concentration, UV intensity, and irradiation time may produce the same final stress and conversion.

### 3.4.9 Process Windows

Process windows are the set of attainable final parameters for a system. They are useful in designing processes to see if a desired final state is physically attainable. For coating curing, they may be used to investigate allowable conversions and the resultant stress to see how much freedom is available in stress for a given conversion or vice versa. They present a convenient way to see how the imposition of a constraint will effect the process options. For example, if a coating formulation is found to form stress-related defects at a certain final stress, a constraint could be placed for there to be less stress in the coating. The process window will show the allowable conversions that fall within the stress constraint. Similarly, for a conversion constraint, the process window will show allowable stresses. Ideally the coating could be cured with very little stress in the end. The process window

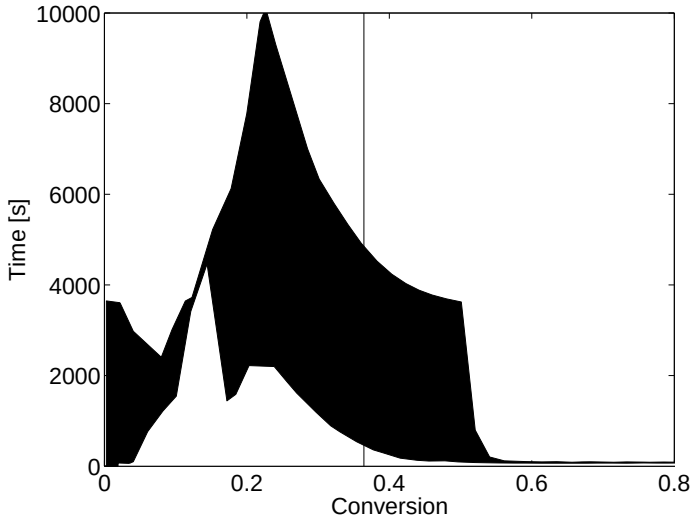


Figure 3.30: Process window showing possible conversion-time pairs. 1 s. –1 hr irradiation. $10^{-6}$ – $10^{1}$ W/dm$^2$. $10^{-3}$ – $10^{\cdot 8}$ % DMPA. Vitrification indicated by line.

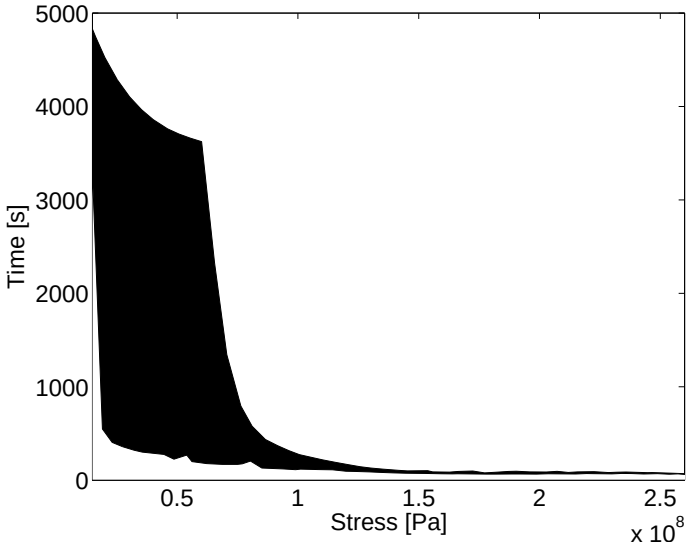


Figure 3.31: Process window showing possible stress-time pairs. 1 s. –1 hr irradiation. $10^{-6}$ – $10^{1}$ W/dm$^2$. $10^{-3}$ – $10^{\cdot 8}$ % DMPA. Only points past the vitrification conversion are shown.

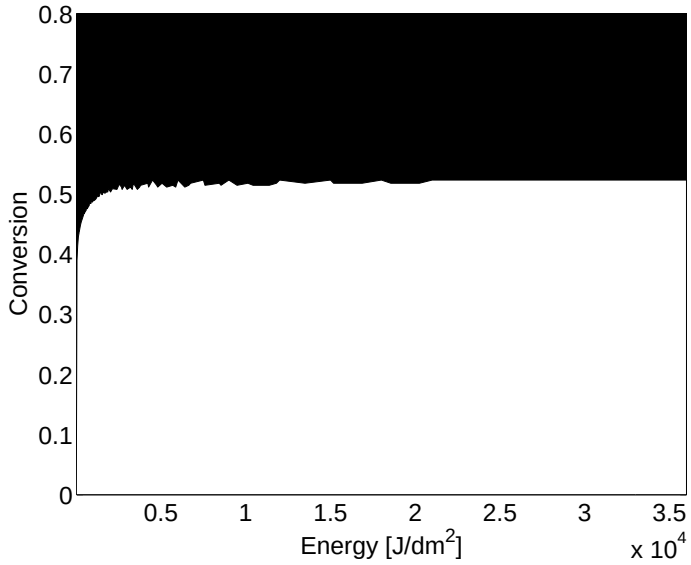


Figure 3.32: Process window showing possible energy-conversion pairs. 1 s. –1 hr irradiation. $10^{-6}$ – $10^{1}$ W/dm$^2$. $10^{-3}$ – $10^{.8}$ % DMPA. Only points past the vitrification conversion are shown.

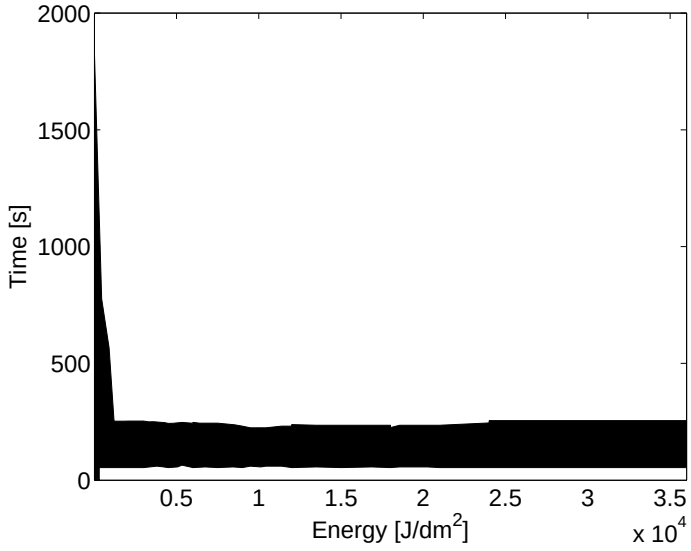


Figure 3.33: Process window showing possible energy-time pairs. 1 s. –1 hr irradiation. $10^{-6}$ – $10^{1}$ W/dm$^2$. $10^{-3}$ – $10^{.8}$ % DMPA. Only points past the vitrification conversion are shown.

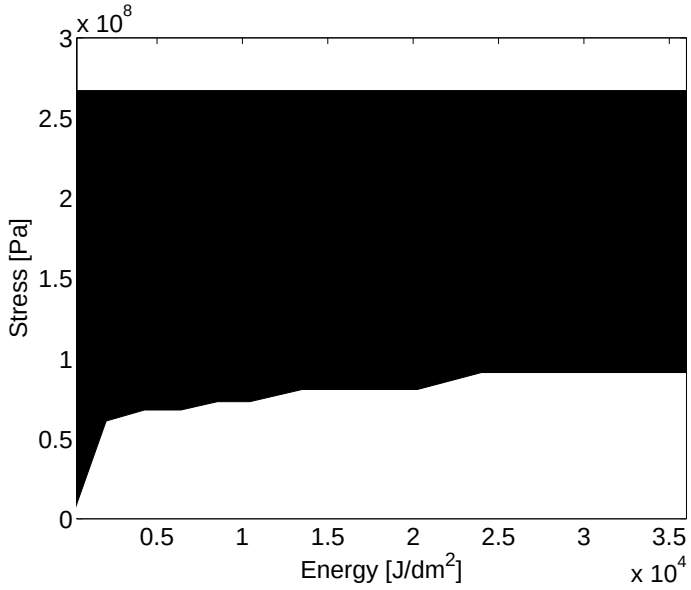


Figure 3.34: Process window showing possible energy-stress pairs. 1 s. –1 hr irradiation. $10^{-6}$ – $10^{1}$ W/dm$^2$. $10^{-3}$ – $10^{.8}$ % DMPA. Only points past the vitrification conversion are shown.

shows this is impossible for realistic values of initiator concentration, UV light intensity and irradiation time. To pass the glass transition, a minimum stress of about $1.0 \cdot 10^7$ Pa is required. Increasing the conversion causes a necessary increase in stress. Figure 3.29 shows the stress-conversion process window for curing TMPTA. It is clear that not all of conversion-stress space is accessible, however there is some freedom allowed. For example, 50 % conversion has a wide range of allowable stresses, from 50 to nearly 150 MPa. The small process window is caused by delayed volume change and physical property buildup. Low conversions all have low stress because the modulus is small. As the conversions start to increase to gelation and vitrification, more stress values may be accessed. This is caused by the onset of delayed volume change and shows how the rate of initiation influences the final stress. Slow reactions in equilibrium will have lower final stress while fast reactions will increase stress. At even higher conversions, the delayed volume change is exacerbated by continued conversion above $T_g$. The highest conversions only allow very small ranges of stress. This is because initiation must be rapid just to reach high conversion. To do this,

vitrification is passed quickly for all sets of parameters and the final stress is nearly the same because virtually all the volume change happens while glassy.

Conversion and stress are the most important final parameters for processing – conversion to insure vitrification has passed and stress to determine if stress-induced defects may be present. Time necessary to reach the end of stress generation is also important in a processing setting, as discussed in Section 3.4.8; it is absent in Figure 3.29. The cost of reducing stress while maintaining the same conversion is longer time until reaction and stress completion. Process windows for completion time with respect to final stress and final conversion are shown in Figures 3.30 – 3.31. The highest conversions occur in relatively short times. This is because very fast initiations are needed to obtain high conversion so propagation happens quickly with greater excess free volume. The dropoff in accessible reaction times just above 50% conversion comes when severe diffusional limitations prohibit continued propagation at slower initation rates. The initial plateau in time from 0–5% is from additioinal irratiation time at the same intensity and initiator concentration. The maximum near 25% comes from delayed volume change. Initially, time increases with conversion as initiation rates increase. The reaction rates are still reasonable here and have not yet been reduced through volume decrease. There comes a point where increasing the initiation rates begins to cause appreciable excess free volume. This excess free volume enhances propagation rates and makes reactions take less time to complete. Figure 3.31 shows possible stress-time pairs for conversions above vitrification. Extremely short times correspond to very fast initiation and finish with the most stress because $T_g$ is passed very quickly. As time rises to between 1000–4000 s., there is a range of possible final stresses. The tradeoff here for lower stress is lower conversion. Remember that these are all vitrified, so a process may be selected to minimize both stress and time, such as the lower left point at 500 s. and 25 MPa. In general, time and stress must be traded off to maintain the same conversion. Lower stress requires reacting closer to the equilibrium volume which demands reactions happen more slowly.

Energy delivery is also important, the total amount of energy delivered may also be a

process constraint from a cost, heat, or environmental standpoint. Taken with the other process constraints, this makes the process window a four parameter set of information for differing process conditions: conversion, stress, time necessary for reaction and stress completion, and total energy delivered. Figures 3.32 – 3.34 show process windows for energy delivery. Similar to the above, several conversions, stresses, and times are accessible for a given amount of delivered energy. The cost for increasing conversion at the same energy is more stress. The cost for decreasing time at the same energy is more stress, less conversion, or both. This is because energy can be maintained by increasing the UV intensity and shortening the irradiation time or the opposite. Increasing the intensity will increase the stress and may increase the conversion. Decreasing the intensity will decrease the stress but may also decrease the conversion. These entire process windows are past vitrification so they will all produce solid glassy coatings.

The dependence on final state in the process window can be seen by overlaying lines of iso-initiator concentration, iso-UV intensity, or iso-reaction time. Figure 3.35 shows this for the stress-time process window. As UV intensity or initiator concentration are increased, The shorter time, higher stress area of the window is accessed. As reaction time increases, so does the stress generation time. The specific location on one iso-line is determined by the value of the other controllable parameters.

### 3.4.10 Stress Trajectories

The rate of stress buildup depends on how fast initiation and propagation happen, and how far away from the equilibrium volume the polymerizing system is. This determines the trajectory of stress with conversion and can be seen in Figure 3.13(b). It may seem that faster initiation can produce lower stress, but the stress generation cannot be stopped along its trajectory, and lower stress is just a temporary condition due to being further from the equilibrium volume. There is no control to stop reactions instantaneously, freezing in low stress and high conversions. Excess free volume can be thought of as a kind of stress-generating inertia which will cause stress later.

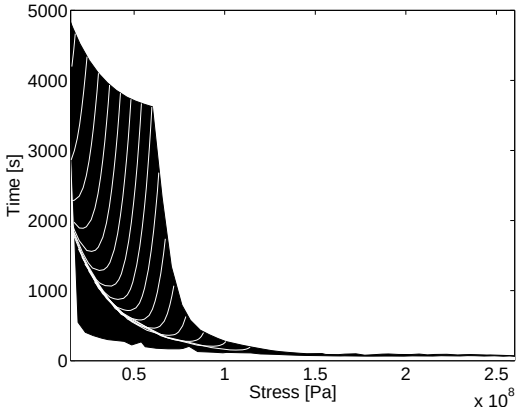


(a) Iso-UV intensity. UV intensity increases to the right and down.

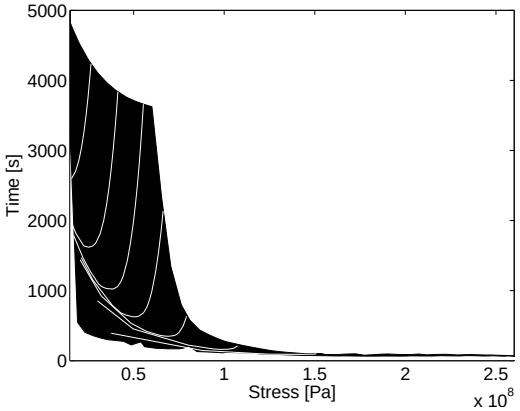


(b) Iso-initiator concentration. Initiator concentration increases to the right and down.

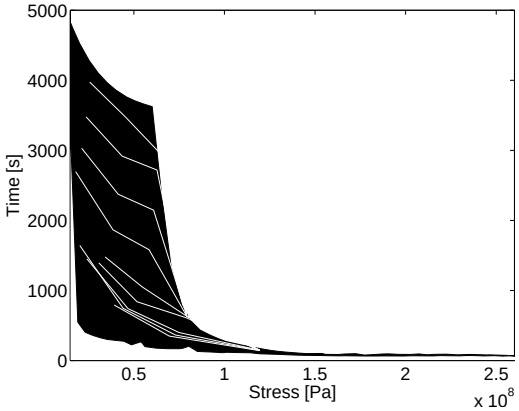


(c) Iso-irradiation time. Irradiation time increases going up.

Figure 3.35: Process window trends: iso-irradiation time, iso-UV irradiation, iso-initiator concentration.

## 3.5 Conclusion

Stress generation in TMPTA initiated by DMPA and UV light depends on the interplay between chemical reactions and volume change. Free volume decrease upon transition from monomer to glassy polymer causes diffusion coefficients to plummet, making reactions slower and slower as the glass transition is approached and passed. Delayed volume change complicates this. Double bond conversion changes the equilibrium specific volume of the curing coating, and the actual specific volume takes a finite amount of time to decay to its equilibrium value. Excess volume created by the mismatch of volumes is taken in the form of free volume, which serves to enhance mobilities of reactive species and increase the reaction rates. Conversions at which gelation, vitrification, and physical property buildup are unchanged by excess volume, and the coating may vitrify far from its equilibrium volume. Modulus, viscosity, and stress relaxation time are quite large above $T_g$, and additional volume change caused by vitrification far from equilibrium serve to greatly increase residual stress in the coating.

Recent experimental work by Schmidt, Schmah, Leterrier and Manson (2007) on 'time-intensity transformation' corroborates the idea of fast reactions generating more stress by non equilibrium vitrification.

This chapter detailed the physical causes of stress and suggested ways to reduce it. Even at equilibrium, stress is generated by stress-free state change (via specific volume) combined with a nonzero modulus. Stress is increased by reaction out of equilibrium. Stress is also increased by continued reaction above the glass transition conversion.

Stress reduction by relaxation is not important for TMPTA coatings. They solidify too quickly and with relaxation times that are too high for appreciable stress relaxation. Virtually all relaxation takes place before vitrification when $\tau$ is somewhat low. Very little relaxation takes place after vitrification, but this is where most of the stress builds up.

Process windows for experimentally accessible sets of input conditions were shown in Section 3.4.9. These show what values of stress, conversion, time to end, and total energy delivered are possible. The kinetics and volume assure that not every area of the parameter

space is accessible. These process windows may be made larger, especially with time-varying UV intensity but this was not considered here.

This chapter presented a new coupling of kinetics, volume, physical properties, and stress that has not been previously investigated. Insight gained here may be used to direct experiments, expand stress development theory, or further explain the origins of stress generation, viscoelasticity, and relaxation during photopolymerization of coatings.

# Chapter 4

# Nonuniformities in Stress Generation

## 4.1 Introduction

Presence of nonuniformities or heterogeneous solidification of a coating can alter reaction kinetics, deformation, and relaxation in a coating, changing the final magnitude and distribution of stress. Understanding how nonuniformities affect the stress can assist with design of coatings and suggest where care must be exercised in coating solidification process design. Chapter 3 only considered spatially uniform stress and relaxation which were oriented in the coating plane. This chapter considers stresses and strains in all directions as a result of nonuniform solidification.

Heterogeneity may arise from any step in the coating process, from preprocessing and substrate preparation, through coating application to solidification and beyond. Initial liquid coatings may not be deposited uniformly, concentrations of reactants may vary spatially, initiating radiation may change through the depth of the coating, the substrate may not be flat, stress-induced defects may occur, among other nonuniformities. This chapter attempts to further understand defect formation by investigating the effects of substrate nonuniformities on otherwise uniform coatings, common defects, and attempts at stress reduction

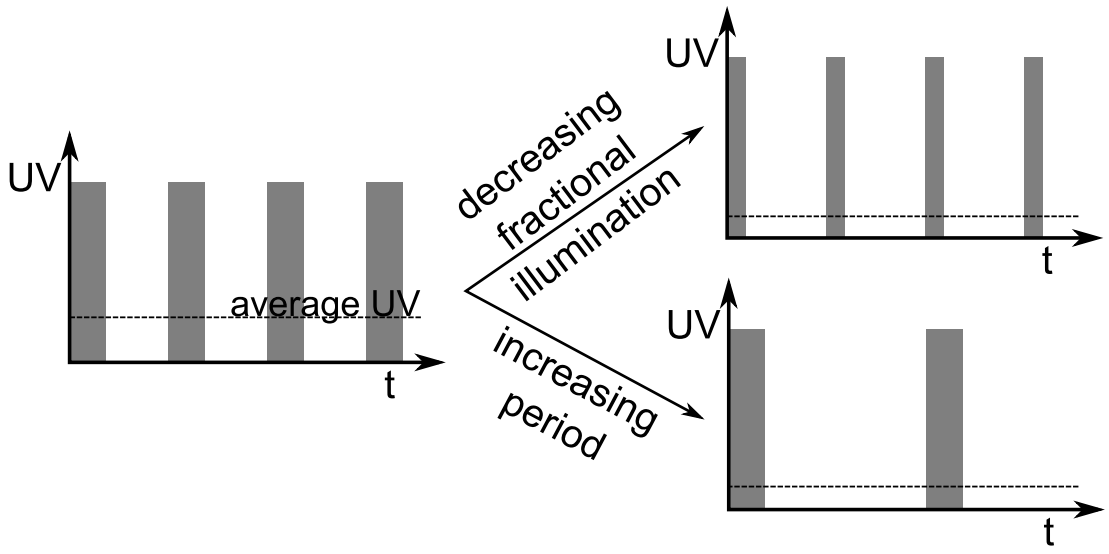


Figure 4.1: UV pulsing characteristics

through process tailoring.

## 4.2 UV Pulsing

Vaessen et al. (2002) investigated the effect of changing the UV light intensity experimentally by cycling irradiation on and off during cure. Her work showed that reducing the period of UV cycling decreased the final stress. Also, dynamic stress measurements showed relaxation during the dark time. This stress relaxation data confirmed the viscoelastic nature of acrylate coatings and allowed our calculation of initial relaxation times used in Section 3.3.3. She proposed that the dark time allowed viscoelastic stress relaxation, slowed the reactions, or both, resulting in lower final stress.

Vaessen's experimental work did not determine the effect of continuing to lower the UV cycle period, the fractional illumination, or the intensity during the irradiation period. Figure 4.1 shows UV–time characteristics and what happens as the period and fractional irradiation change. The average UV rate is also shown; it is the intensity that would deliver energy continuously at the same rate as the pulsed delivery and is the product of fractional irradiation and intensity.

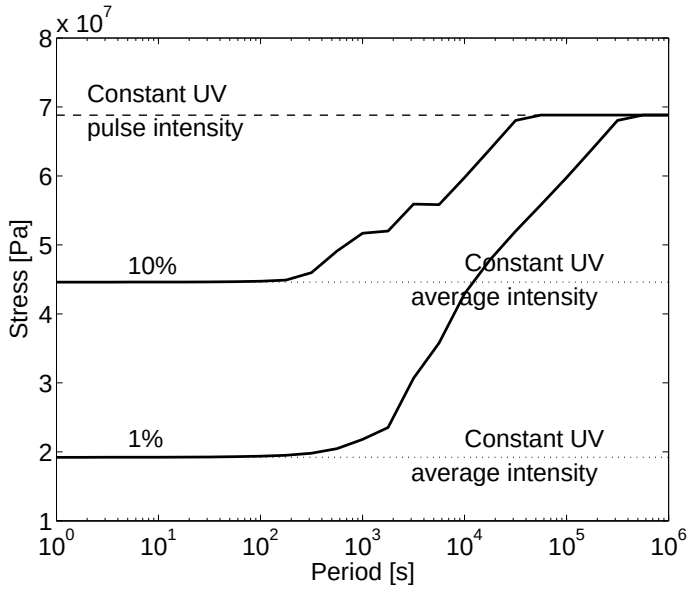


Figure 4.2: Final stress dependence on UV pulse period and fractional illumination

Final stress dependence upon UV pulse period and fractional illumination is shown in Figure 4.2. Two asymptotes are apparent, one at low and one at high period. Two UV intensities are important for these asymptotic values; first is the intensity of pulse irradiation – the intensity when a pulse is 'on' – the second is the average intensity. For long periods, the stress is the same as if continuously irradiated at pulse intensity. Pulses are too long for stress relaxation or reaction suppression; all conversion and stress generation occurs during the first few pulses. Decreasing the period slows reactions which lessens the stress. Further decreasing the period shortens the on and off times such that energy is effectively delivered at the average rate, and stress reaches an asymptote at the average delivery value. Increasing the fractional irradiation increases the stress for all periods up to the maximum intensity asymptote as shown with the 1% and 10% illumination lines. The sharp corners seen in periods between $10^3 - 10^4$ s. arise because pulses are somewhat discrete in time, and one may be cut off at the end.

Stress for pulsed UV irradiation is lower than continuous because dark time reduces the overall reaction rate by initiating no new radicals, keeping the stress-free state closer to

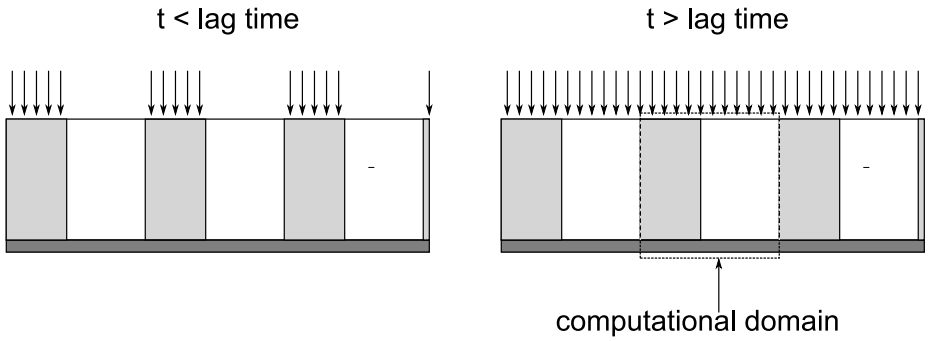


Figure 4.3: Geometry for spatially tailored UV irradiation.

its equilibrium value. Decreasing the period while keeping the same fractional illumination makes the pulses shorter, which keeps the stress-free state even closer to its equilibrium value.

## 4.3 Stress Reduction by Tailored UV Delivery

In addition to stress reduction by changing UV delivery with time, spatially tailored UV delivery has been suggested to reduce stress generation by providing slowly cured regions (Rajamani 2005). These regions act as relaxation sources with smaller relaxation times, allowing stresses in adjacent regions to relax. Figure 4.3 shows the geometry for this. Changing the relative 'stripe' width and how far it lags behind the first initiated regions will determine the extent of allowed relaxation.

The nonuniform delivery of UV light means concentrations of reactants will not be uniform in the coating. If reactions happen slowly with respect to mass-transfer, then the effects of diffusion must be considered simultaneously with reaction. To know if this is the case, the relative importances of reaction and diffusion must be determined before calculating the stress and relaxation in the coating. The Damköhler number is used for this; it is the ratio of diffusion to reaction times,

$$Da = \frac{t_{\text{diffusion}}}{t_{\text{reaction}}} = \frac{k_p[=]L^2}{D_m} \tag{4.1}$$

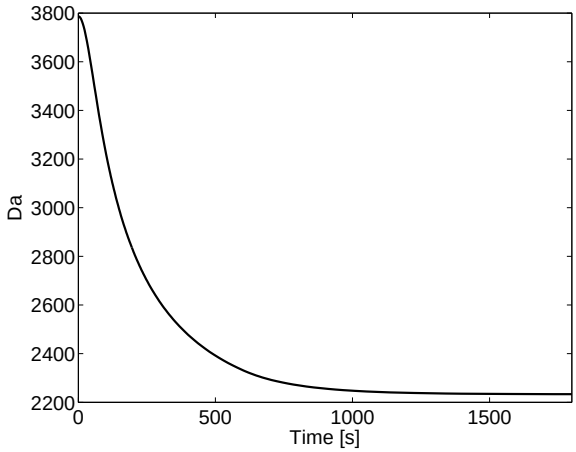


Figure 4.4: Damköhler number as a function of time for a 50 $\mu m$ diffusion length.

where $k_p$ is the propagation rate coefficient, [=] is the concentration of double bonds, and $D_m$ is the monomer diffusion coefficient. $L$ is the characteristic diffusion length, which is not clear perpendicular to the coating thickness. The half-width of the late-cured stripe is chosen here because diffusion over this length renders the stripes ineffective for inducing relaxation. Figure 4.4 shows the Damköhler number with time as curing progresses for a coating initiated with 0.01 % DMPA at 0.01 W/dm$^2$ for 10 min with a characteristic diffusion length of 50 $\mu m$. For all time, the Damköhler number is large; reactions occur much faster than diffusion and mass transfer can be ignored. Even for small diffusion lengths, $Da$ is still large enough to neglect mass transfer; for $L = 1\ \mu m,\ Da > 22$.

Figure 4.5 shows the stress and relaxation components for a typical UV striped coating, with reactions in half of the coating lagging behind the other half. Principal stresses are not shown because they are virtually equal to the in-plane and out-of-plane stresses. In-plane stress is relatively uniform and close to its value without UV striping, but relaxation does lower it a bit. In-plane relaxation is larger where initiation was delayed. Out-of-plane stress is generated, and there is a region of compressive stress. This comes from the mismatch in shrinkage times; the later cured region is stressed and deformed by the earlier cured region and begins to relax. When the later cured region reacts, it deforms downward, placing the adjacent region in compression, generating the out-of-plane stress and relaxation.

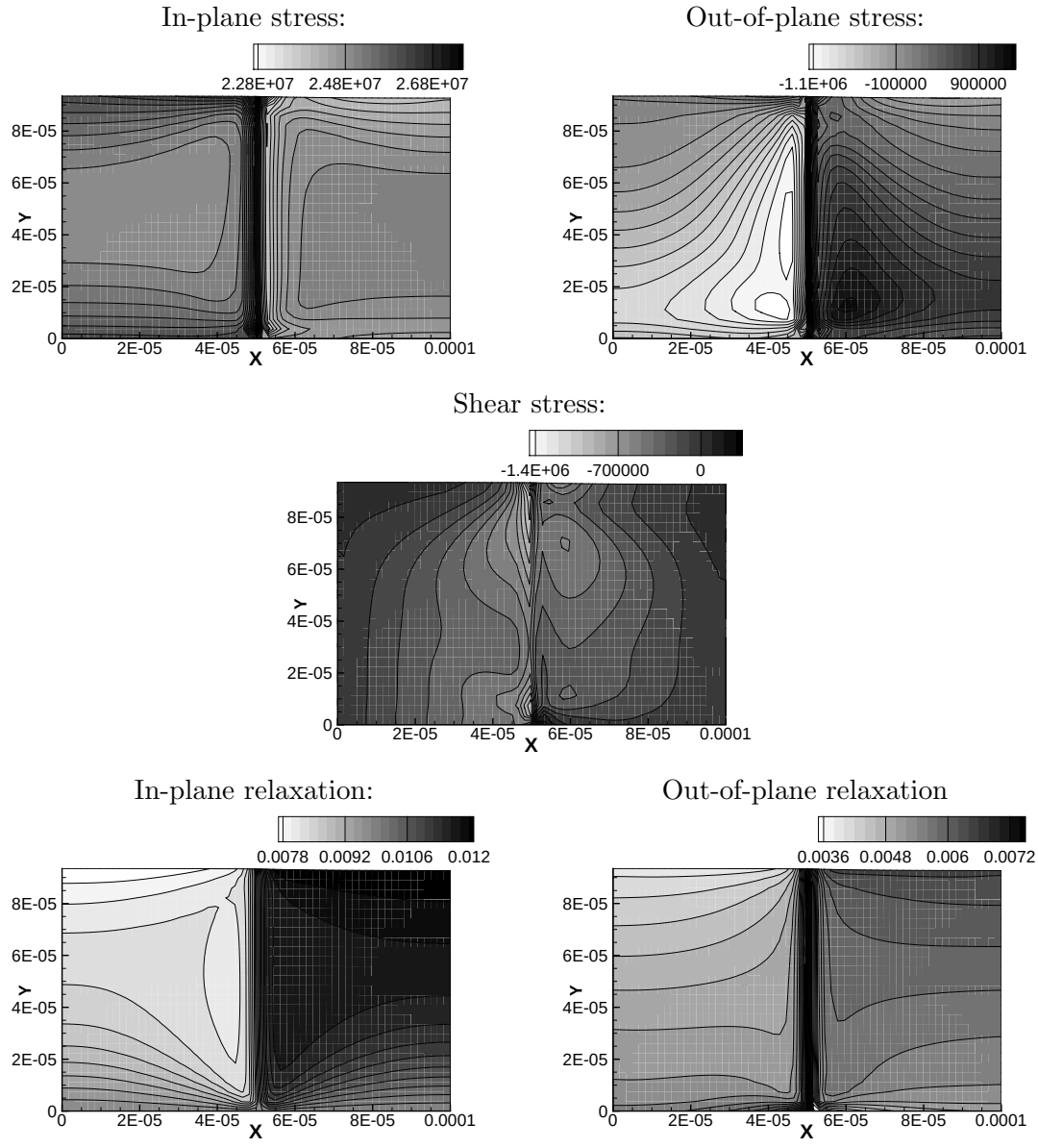


Figure 4.5: Stripe stress components for a 50 $\mu m$ stripe in a 100 $\mu m$ coating. Stripe spacing is 100 $\mu m$

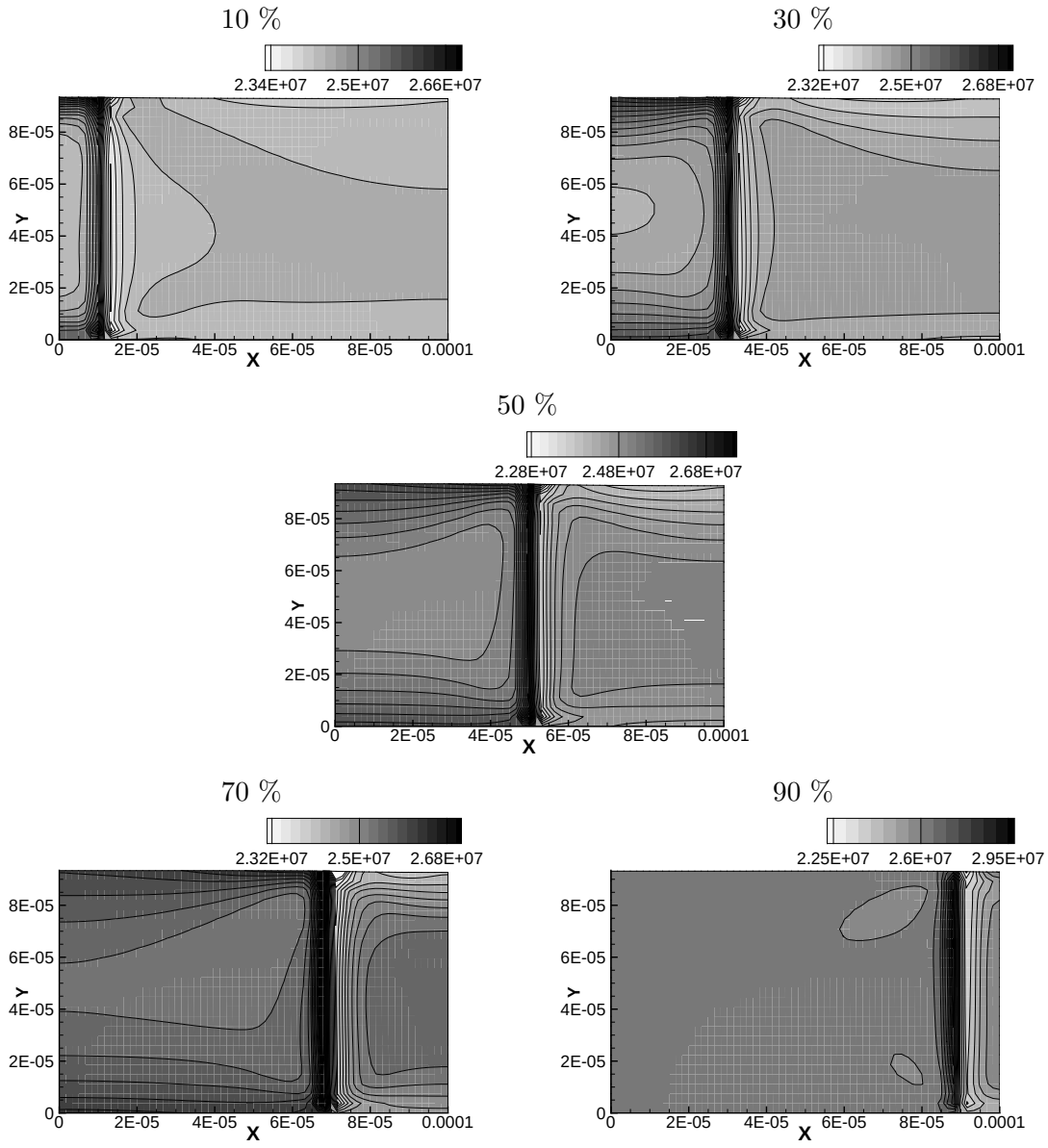


Figure 4.6: In-plane stripe stress dependence on earlier cured stripe width.

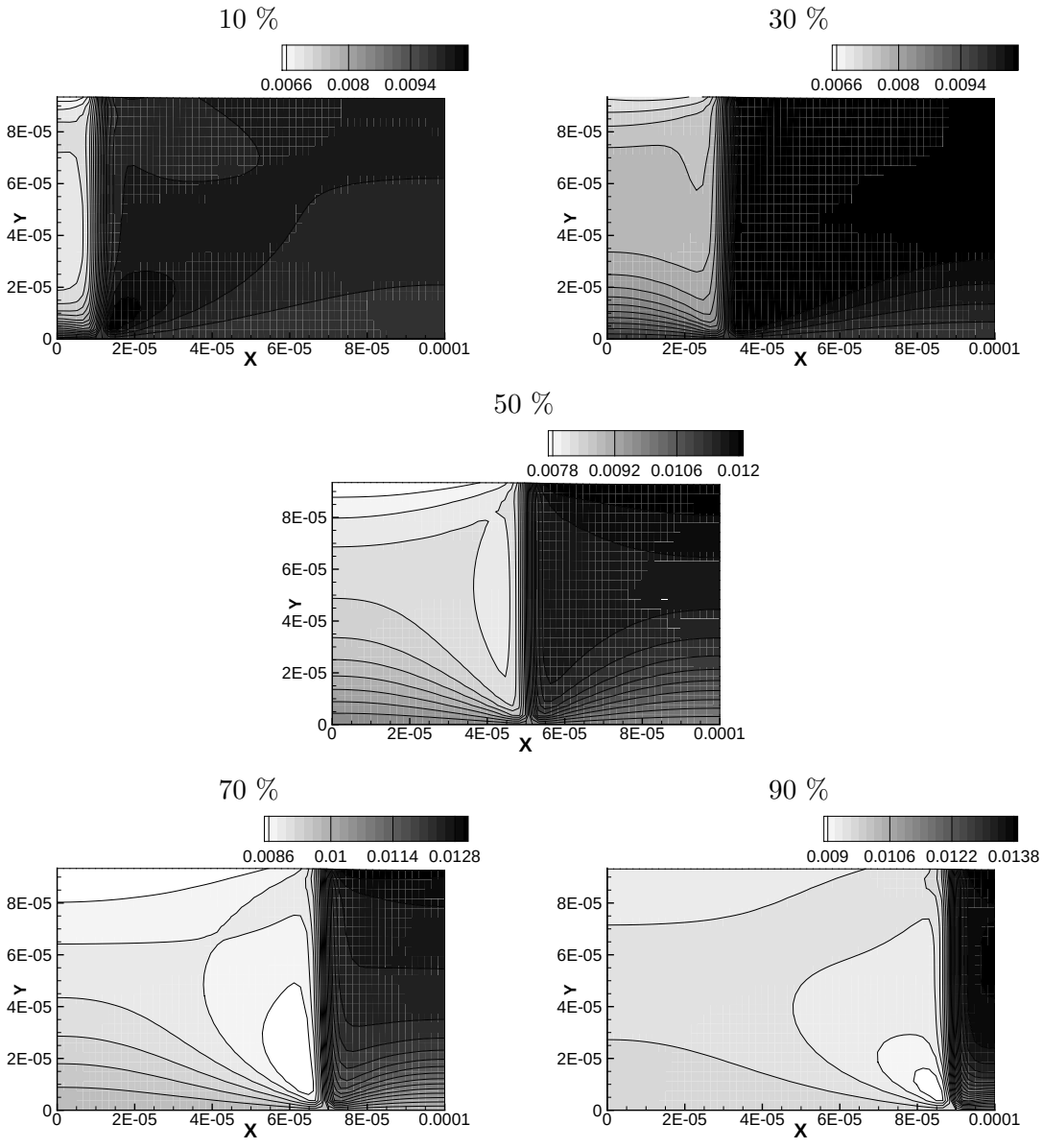


Figure 4.7: In-plane stripe relaxation dependence on earlier cured stripe width.

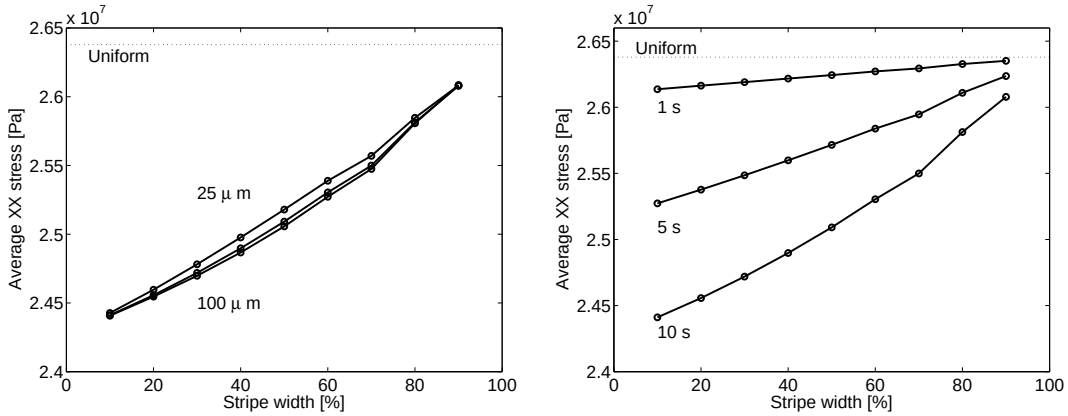


(a) Dependence on coating thickness.

(b) Dependence on lag time.

Figure 4.8: Average in-plane stress dependence on early cured stripe width, coating thickness, and lag time.

As the width of the earlier cured stripe gets larger, less later cured material is available for deformation or relaxation. Figure 4.6 shows how the in-plane stress changes with stripe width. The region of low stress gets smaller and the region of high stress gets larger with increasing stripe width. Figure 4.7 shows that the regions of high relaxation get smaller with increasing stripe width as well. This can be seen in the average stress in the coating, shown in Figure 4.8(a), where larger stripes have higher average stresses, approaching the stress for coatings without stripes. Increasing the lag time between early and late initiations allows more time for relaxation, decreasing the average stress and is shown in Figure 4.8(b). The average relaxation shown in Figure 4.9 obeys the same trend for increasing lag time, and the increase in relaxation in thicker coatings is more pronounced because the constraint of the substrate is further away. The effect of increased relaxation on stress reduction is very slight, however. As the stripes get wider, however, an average relaxation maximum appears. This is simply a manifestation of the greater area of early initiated stripe and the smaller relaxation that goes along with it.

Stress can be reduced with the use of spatially tailored UV delivery. Regions not being cured that are adjacent to regions that are curing allow relaxation, with larger uncured regions lowering average stress the most. Section 3.4.6 showed that relaxation was not

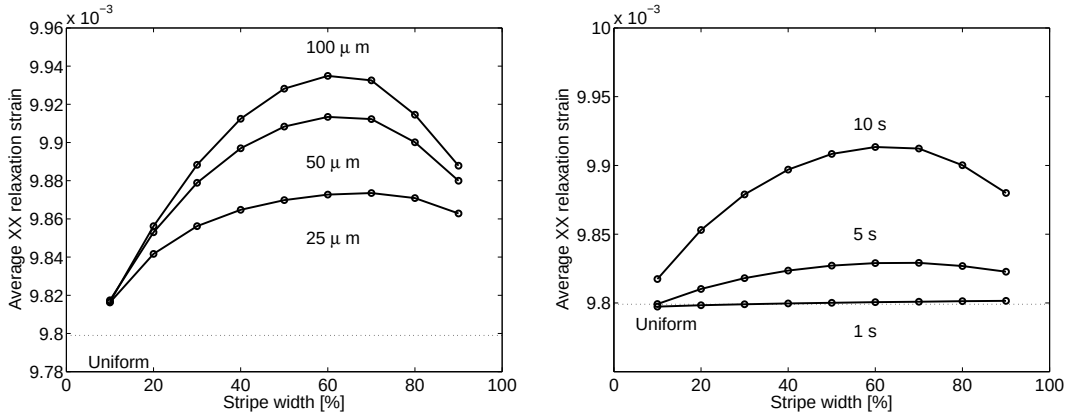


(a) Dependence on coating thickness.

(b) Dependence on lag time.

Figure 4.9: Average in-plane relaxation strain dependence on early cured stripe width, coating thickness, and lag time.

important for uniformly cured coatings, but it is important here because of the disparity in relaxation times of adjacent regions.

## 4.4 Topography

Solidification of a coating deposited onto a substrate with a deliberate topography presents problems not present in a uniform coating. The topography adds more coating-substrate interface where no deformation can occur. These additional deformation constraints influence the final stress and its distribution in two-dimensions, introducing nonuniformities which may increase defect formation.

Topography may be introduced to the substrate for several reasons. Examples include photolithography and microelectronics processing, planarizing coatings over patterned substrates, air channels for adhesives, and electronic protection. These applications produce well-defined surface profiles upon which an initially uniform coating is deposited. Lei et al. (2002) investigated similar configurations for coatings solidified by drying (Lei 1999). For dried coatings, there is no way to decouple the geometry and the solidification, mass-transfer in the coating controls drying, however for the UV cured coatings considered here, the effect

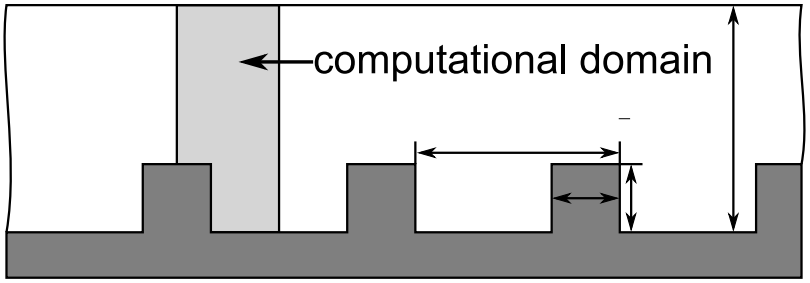


Figure 4.10: Substrate topography, coating thickness, and topographic periodicity.

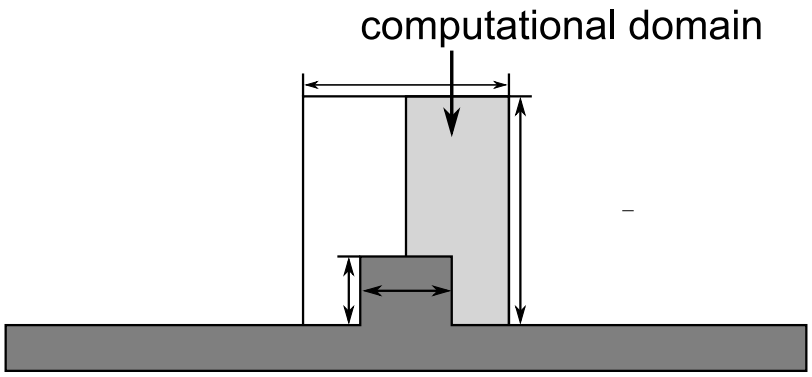


Figure 4.11: Substrate topography, coating thickness, and topographic periodicity for single step topography.

of adding topography to a substrate undergoing otherwise uniform curing will be investigated.

Lei et al.'s (2002) work showed concentration and stress profiles for coatings over topography. Bornside (1990) also investigated single steps of topography. Their work not investigate the influence of topography height, thickness, or coating thickness nor did they investigate possible defect sources. This section details these influences.

Two different configurations will be explored. First, spatially repeating topography with a continuous coating deposited over it. The geometry of this case is shown in Figure 4.10. The topographic step ranges from 10–90% of the domain width and height. The second case considers a single topographic step with a discrete coating just over the step, as shown in Figure 4.11. Coating thickness, domain periodicity, and step fractional size are

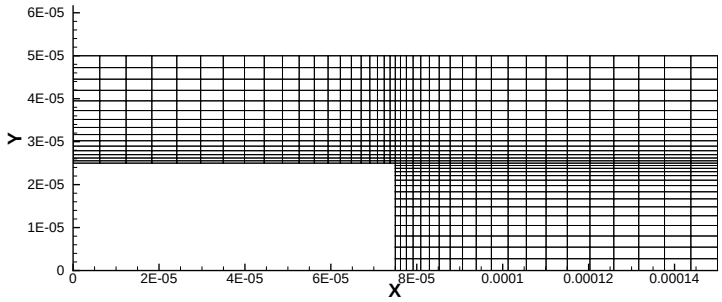


Figure 4.12: Mesh for topography cases. Elements concentrated near the corner. This case has a 50% wide and 50% tall step in a 50 $\mu m$ thick coating with 150 $\mu m$ periodicity.

similar to the first case. These geometries assume perfectly square corners on the substrate and on the coating for the second case where an edge exists. The goal of this study is to determine the influence of the substrate on the final stress, so the kinetics were kept identical for all geometries by keeping the input parameters the same; a temperature of 30 °C, DMPA concentration of 0.01%, and UV intensity of 0.01W/dm$^2$ for 10 min are used.

The topography, especially the corner of the step, presents a new constraint on allowed deformation. Because of this, the finite element mesh was concentrated near the corner to capture large gradients in stress or deformation there. Mesh for a typical geometry can be seen in Figure 4.12.

### 4.4.1 Periodic Step Topography

Final stress profiles and deformation after post-cure are shown for a typical periodic step geometry in Figure 4.13. There are several characteristics that should be be addressed. First, there is a stress maximum tangential to the top surface of the coating above the step corner. The magnitude of this maximum is larger than the uniform in-plane stress. Second, the shear (XY), out-of-plane (YY), and minor principal stresses are nonzero, which is not the case for uniform curing. Third, there is a coating thickness variation caused by the presence of the step; the coating was initially flat. Lastly, the in-plane stress in the valley between steps is larger than the uniform in-plane stress.

**Stress Maximum at Coating Surface**

The presence of a stress maximum on the top surface of the coating may be an indicator of the location of a defect formation such as a crack. The degree to which stress is increased over uniform topography is dependent on the coating thickness, the step periodicity, and the step width and height in the coating.

For a given coating thickness, periodic spacing, and step width, the magnitude of maximum stress is always increased by increasing the step height. Figure 4.14 shows the change in the in-plane stress profile with increasing step height. Taller steps create a larger mismatch between the thick and thin coating regions and compatibility between these regions prevents the thick coating from deforming as much as it would if unconstrained. Additionally, adhesion to the side of the step does not allow deformation there, but it is allowed at the midpoint of the valley at the periodic boundary. The corner becomes a pivot point around which the coating attempts to rotate, concentrating stress on the coating surface and is shown in Figure 4.16. For all step widths, increasing the step height increases the maximum surface stress.

Surface stress is also increased by making the step narrower. Wide steps create narrow valleys, whose deformations are more highly constrained by the close presence of step walls. The walls prevent the thick coating from deforming toward the substrate, making the mismatch between thick and thin coatings matter less. Figure 4.15 shows how the stress profiles change with step width, as valleys get narrower, stress concentration is decreased. Very narrow step widths also increase the stress on the surface, but only for taller steps. This happens when deformation toward the valley is prevented by deformation on the opposite side of the same step deforming toward its adjacent valley – the step can 'feel' its other side. The top of the step is being stretched out by the two valleys next to it. In these cases the stress maximum at the coating surface resides at the midpoint of the step. Wide steps to not exhibit this phenomena because they are far enough apart so deformation from one corner does not interfere with deformation of another. Maximum surface stress for wide steps is directly above the step corner. The stress location can be seen in Figures

In-plane stress:

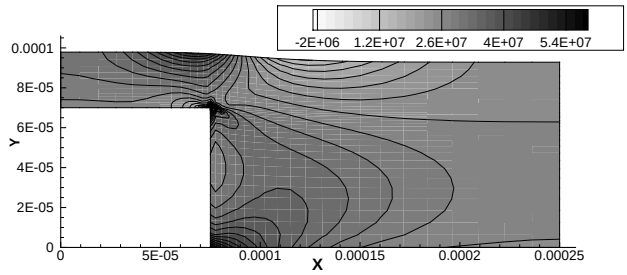


Out-of-plane stress:

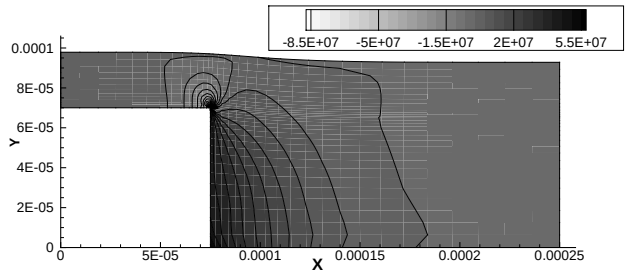


Shear stress:

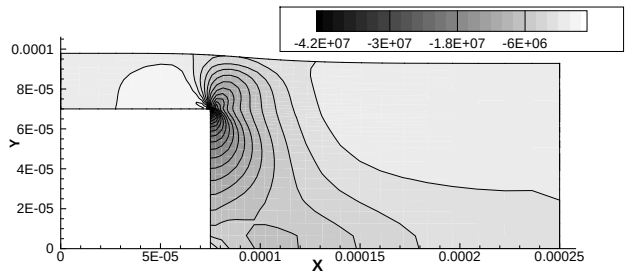


Major principal stress:

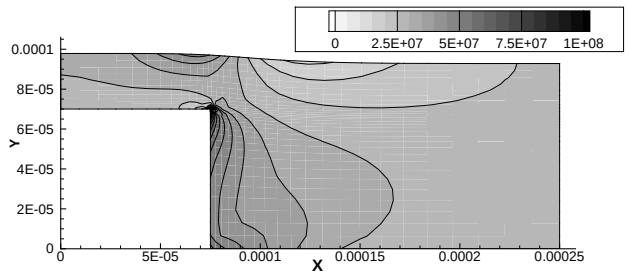


Minor principal stress:

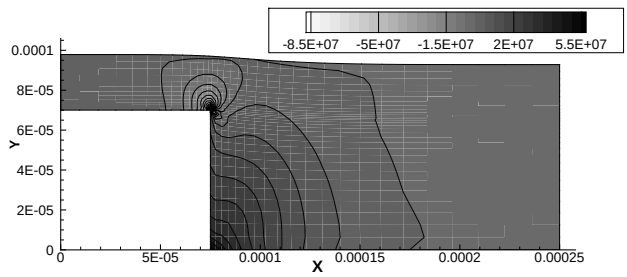


Figure 4.13: Repeating topography stress components. Coating thickness $100\mu m$, step width 30% and height 70% of domain. $250\mu m$ periodicity.

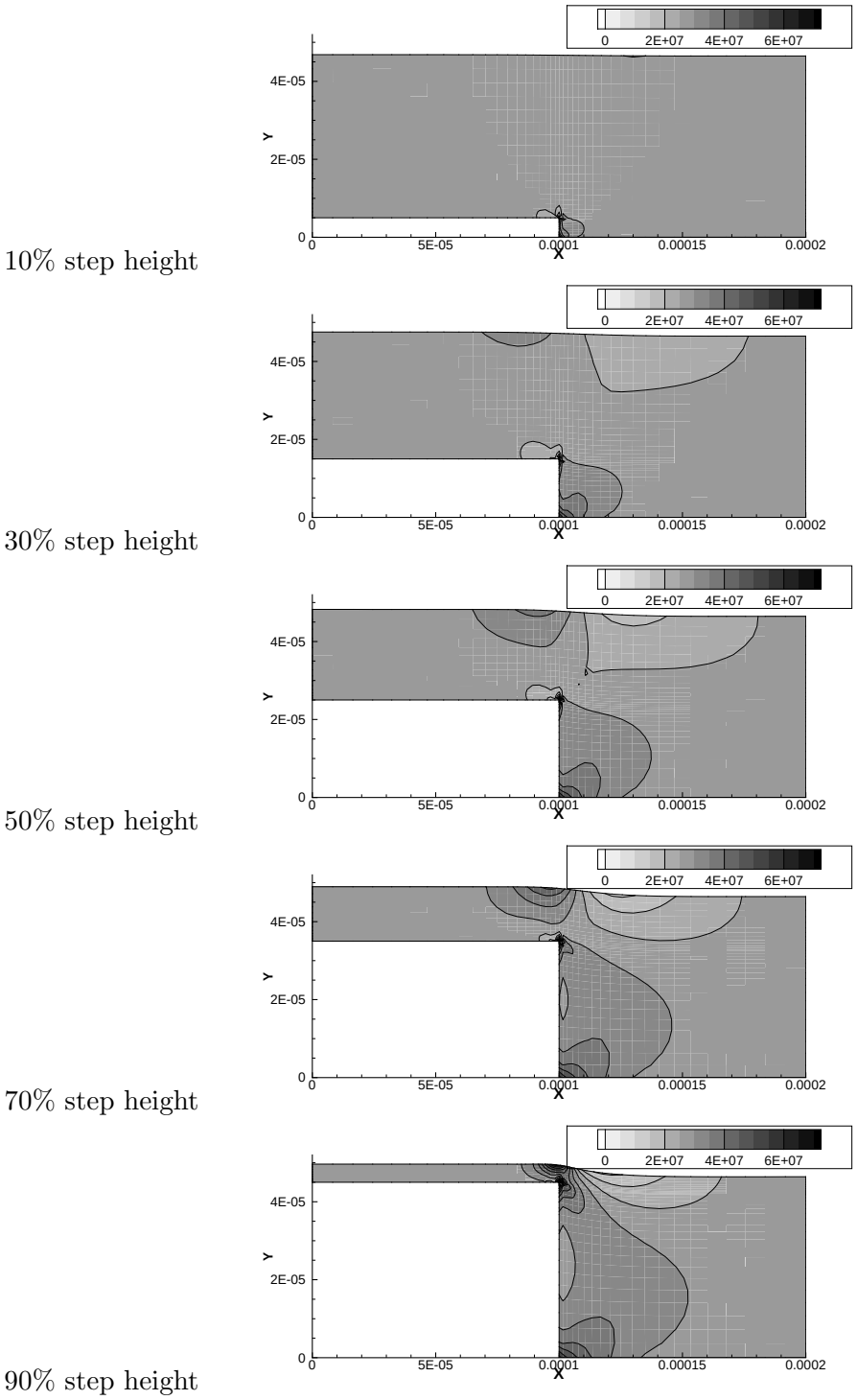


Figure 4.14: In-plane stress profile dependence on step height. Coating thickness $50\mu m$, step width 50% and height 10–90% of domain. $200\mu m$ periodicity.

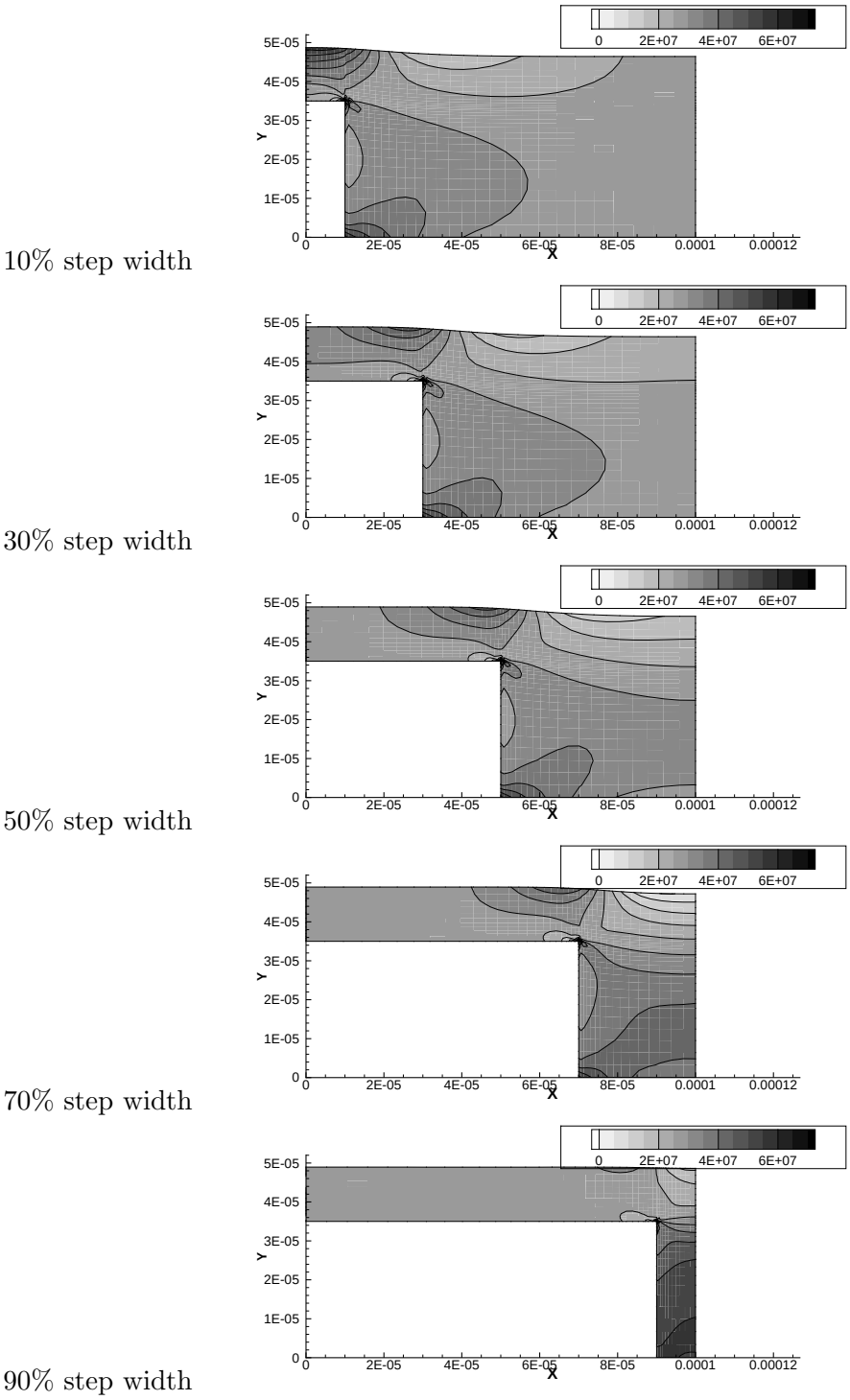


10% step width

30% step width

50% step width

70% step width

90% step width

Figure 4.15: In-plane stress profile dependence on step width. Coating thickness $50\mu m$, step width 10–90% and height 70% of domain. $100\mu m$ periodicity.

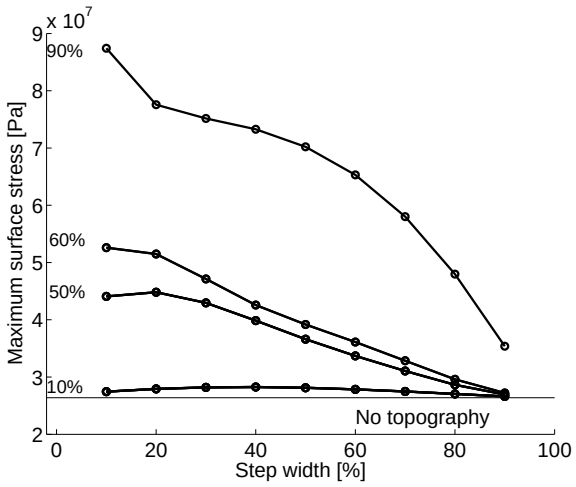


Figure 4.16: Maximum stress on coating surface dependence on step dimensions. Coating thickness $50\mu m$, $50\mu m$ periodicity.

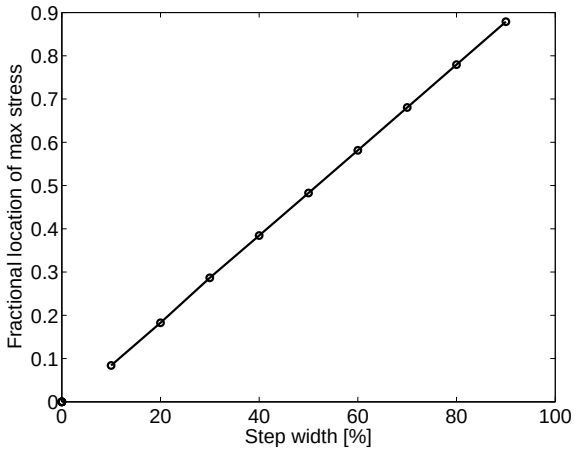


Figure 4.17: Fractional location of maximum on coating surface dependence on step dimensions

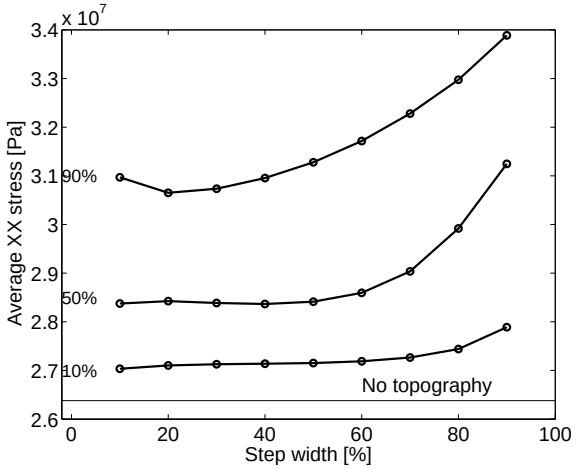


Figure 4.18: Average in-plane stress dependence on step dimensions. Coating thickness $50\mu m$, $100\mu m$ periodicity.

4.17 and 4.16. For all step heights, decreasing the step width increases the stress, albeit very minimally for short steps. As the step gets narrower, tall steps have a sharper increase in stress near the narrowest point. This corresponds to when the step can 'feel' both sides. Shorter steps do not exhibit this upturn in stress during narrowing, but a reduction because the steps are smaller.

Stress concentrations on the coating surface are caused by competing deformation between two adjacent coating regions: the region filling the valley between steps and the region on top of the step. To decrease the maximum stress on the surface, deformation of the plateau coating must be increased and deformation of the valley coating must be decreased. Plateau deformation may be increased with thicker coatings, wider steps, and shorter steps. Valley deformation may be decreased with narrower valleys, shorter valleys, and shorter steps. This insight may be used to tailor coating formulations or geometries to reduce defects seen as a result of topography.

### Average In-plane Stress

The average in-plane stress is a measure of how much stress could be measured macroscopically or contribute to long-range defects like curling. Here the stress averaged over the

area is considered. Figure 4.18 shows how the step geometry changes the average stress. For a given step width, taller steps always increase the stress. Like the maximum surface stress, this is because the valley becomes more constrained and cannot deform toward the substrate. Volume coupling increases the in-plane stress for these deep valleys. Additionally, increasing the step width increases the stress for a given step height because narrower valleys are more constrained than wide ones. Volume coupling exacerbates this. An exception to this is for tall, narrow steps where increasing the width initially decreases the stress. This is a result of the two step corners interacting with each other. Once the step becomes wide enough that the corners do not interact, this effect disappears. In all cases, the in-plane stress with topography is higher than that without topography.

### Final Coating Profile

Mismatch between the thin and thick coatings causes regions with different final equilibrium heights to be attached to each other. This creates a final coating profile that is rippled, with high regions above steps and low regions over valleys. The peak to trough distance is largest for wider valleys – they can deform more easily – and higher steps – equilibrium height mismatch is greater. Thus, narrow valleys and shorter steps should be selected for a flatter final coating.

### Substrate Forces

The appearance of tangential stress on the substrate, absent for curing without topography, may indicate locations for substrate defects like peeling or delamination. The directions of both principal stresses on the surface indicates the direction of force while the magnitudes of both the major or minor principal stresses may be significant. Figure 4.19 shows the magnitude and location of the major principal stresses. Far from the corner, principal stresses are parallel, oriented with the substrate, similar to coatings without topography. Close to the corner and all along the step wall, principal stresses are large and act away from the substrate. The net effect is a force away from the corner, indicating that the corner

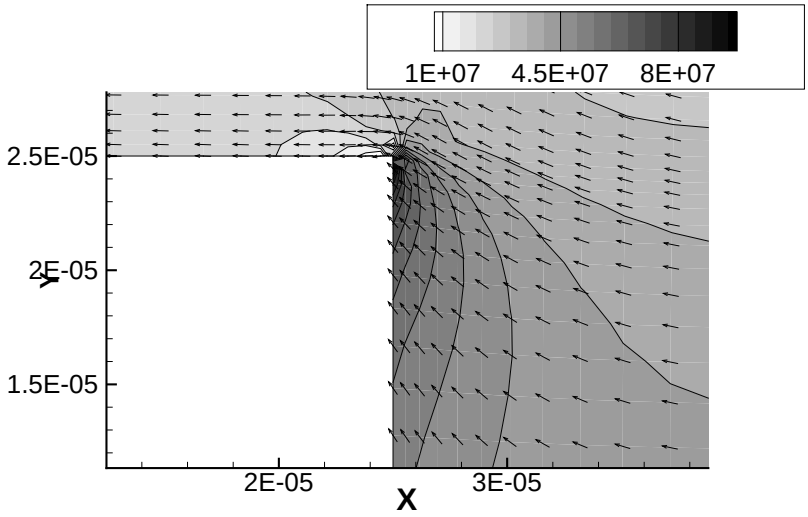


Figure 4.19: Magnitude and direction of major principal stress. Coating thickness $50\mu m$, $50\mu m$ periodicity, with a 50% wide and 50% tall step. Area around step corner enlarged.

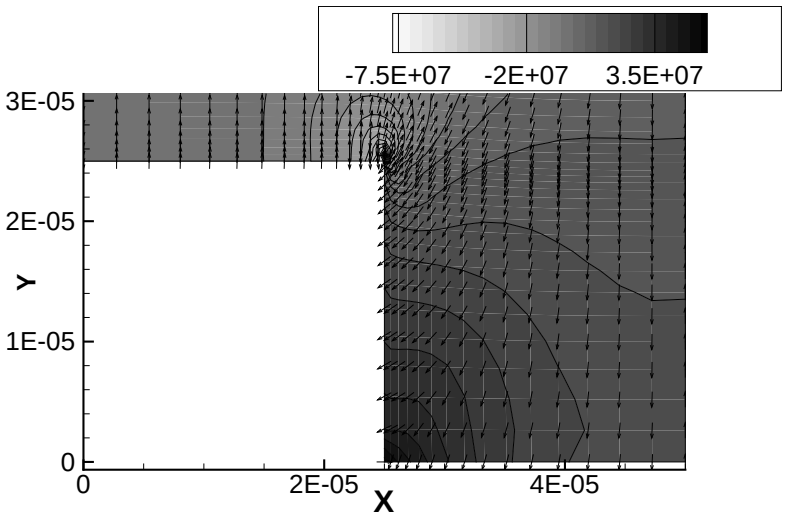


Figure 4.20: Magnitude and direction of minor principal stress. Coating thickness $50\mu m$, $50\mu m$ periodicity, with a 50% wide and 50% tall step. Area around step corner enlarged.

is a likely defect formation location. Minor principal stresses are also significant and can be seen in Figure 4.20. While their magnitude is smaller than major stresses, the forces still may be significant. Because they act perpendicularly to major stresses, the net force is away from the bottom of the substrate and top of the step and is especially pronounced at the bottom corner of the step. These indicate possible defect location – delamination on top of the step and on its bottom corner.

### 4.4.2 Single Step Topography

#### Stress Maximum at Coating Surface

In contrast to Section 4.4.1 with repeating topography, coating a just single step leaves edges that are free to deform, which significantly influences the final stress seen in the coating. Figure 4.21 shows the stress profile in the single step coating.

The stress maximum at the coating surface seen so clearly for repeating steps is not so apparent with just a single step. Figure 4.22 shows the stress profiles as the step height increases. For tall steps, there is a well-defined maximum at the surface, however, for shorter steps, the maximum at the surface encompasses the entire central region above the step and is not localized directly above the corner. The reason for this is the presence of the edge and its ability to deform – repeating steps could not deform at the symmetry plane due to the presence of another step. Deformation at the edge softens the result of coating thickness mismatch at the step edge. Even so, the step wall and bottom substrate still constrain the thick coating, which causes the maximum when step thickness becomes large.

Stress release by edge deformation is also seen by varying the step width. Figure 4.23 shows the in-plane stress for varying step widths. Thin steps have a more localized stress maximum at the surface, which gets wider as the step does. This can be explained similarly to the step height. In the absence of a repeating step, the deep coating region is only constrained by the step wall and bottom substrate. This constraint is largest when the bottom substrate is largest – when the step is smallest.

The combined effects of step height and width are shown in Figure 4.24. Stress maxima

In-plane stress:

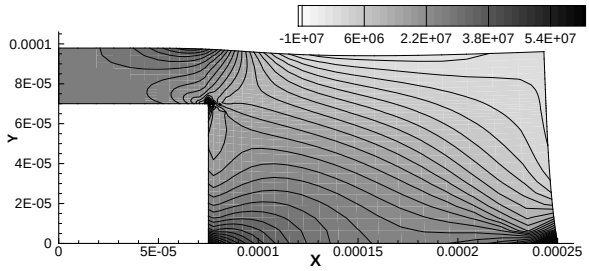


Out-of-plane stress:

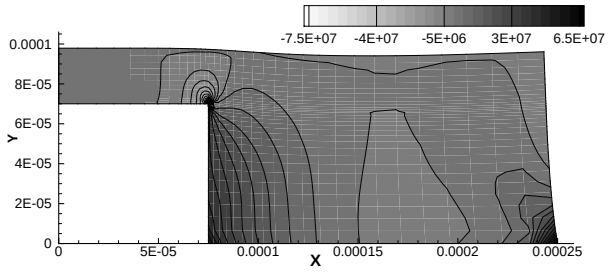


Shear stress:

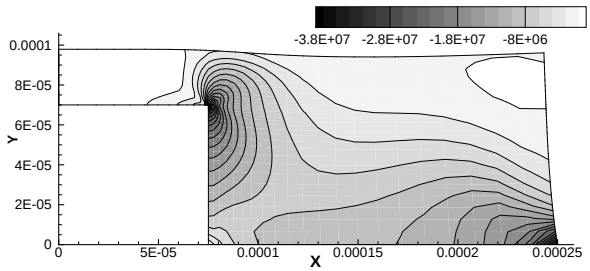


Major principal stress:

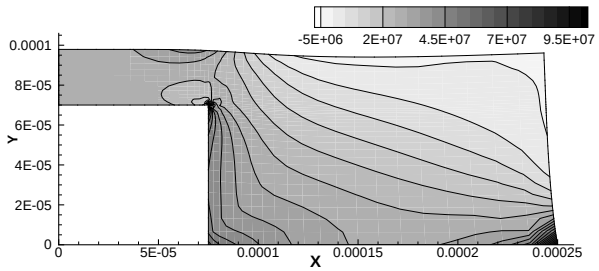


Minor principal stress:

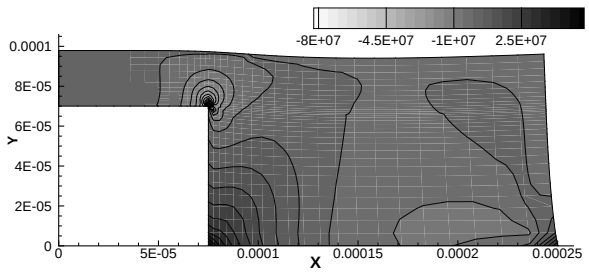


Figure 4.21: Single topography stress components. Coating thickness $100\mu m$, step width 30% and height 70% of domain. $250\mu m$ periodicity.

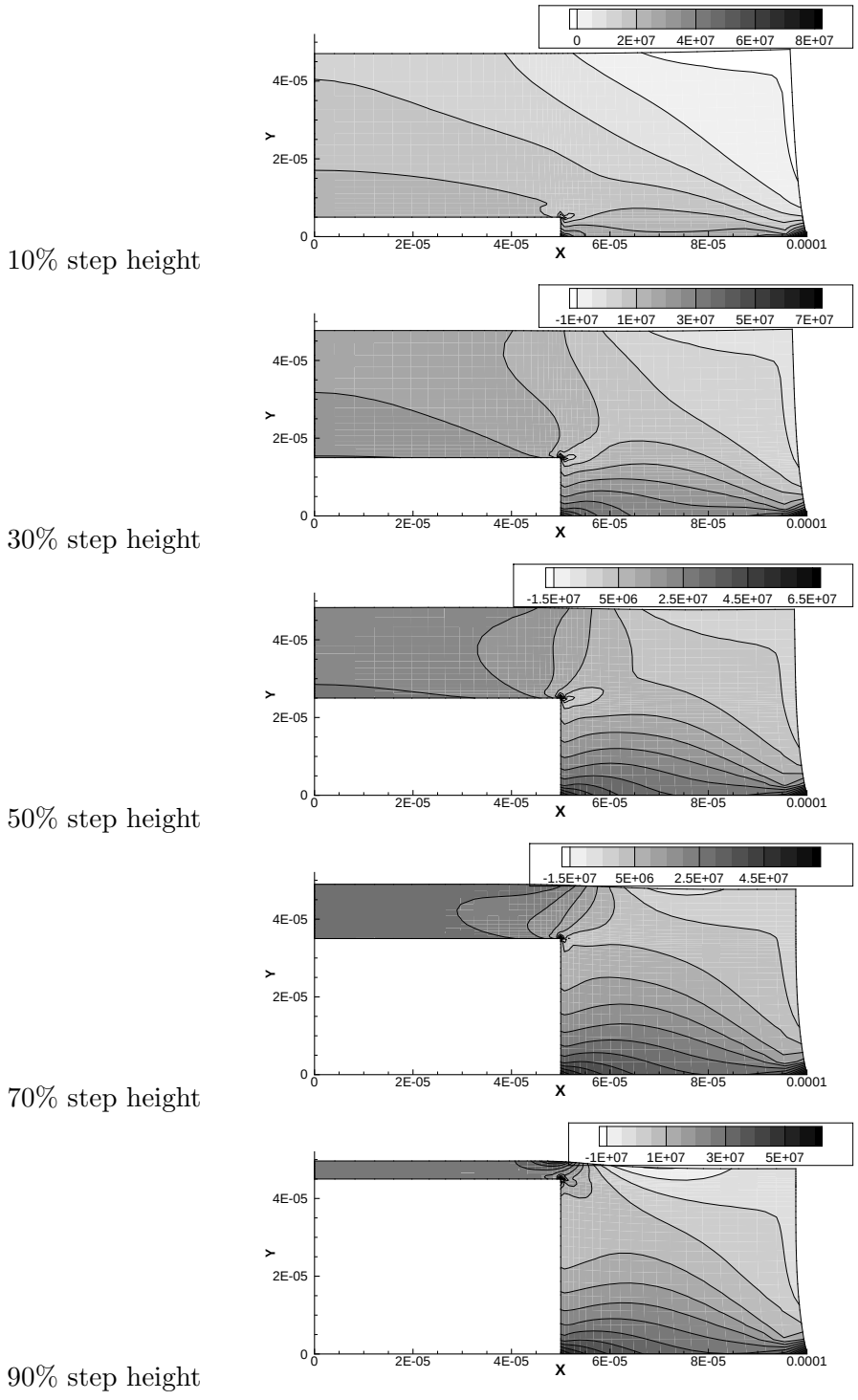


Figure 4.22: In-plane stress profile dependence on step height. Coating thickness $50\mu m$, step width 50% and height 10–90% of domain. $100\mu m$ periodicity.

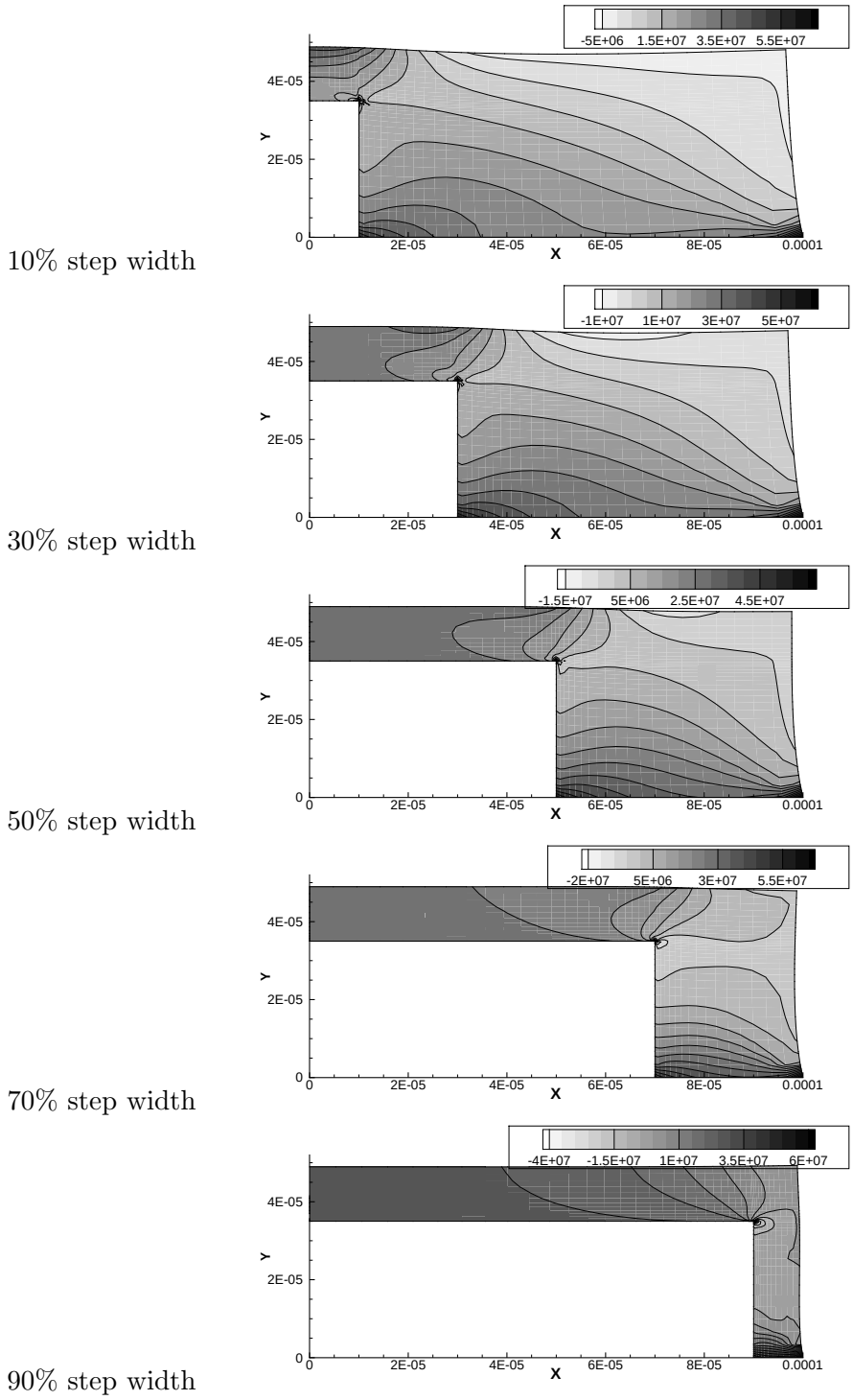


Figure 4.23: In-plane stress profile dependence on step width. Coating thickness $50\mu m$, step width 10–90% and height 70% of domain. $100\mu m$ periodicity.

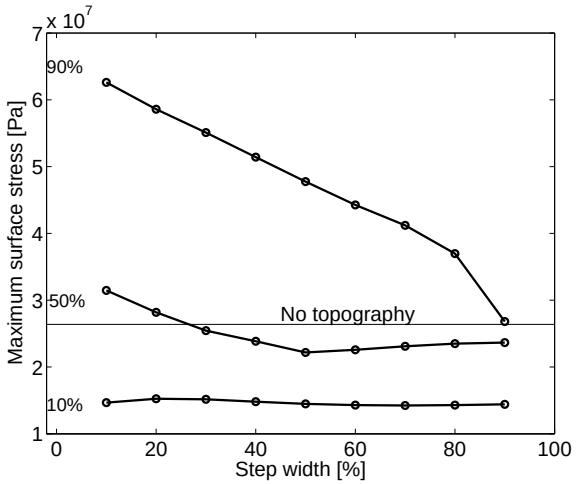


Figure 4.24: Maximum stress on coating surface dependence on step dimensions. Coating thickness $50\mu m$, $100\mu m$ periodicity.

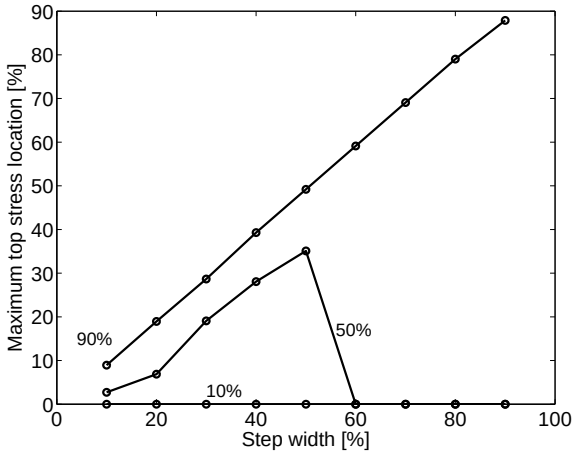


Figure 4.25: Maximum stress on coating surface location dependence on step dimensions. Coating thickness $50\mu m$, $100\mu m$ periodicity.

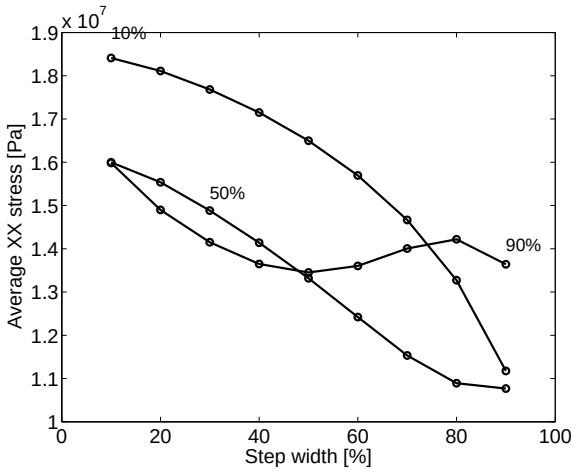


Figure 4.26: Average in-plane stress dependence on step dimensions. Coating thickness $50\mu m$, $100\mu m$ periodicity. Uniform stress of $2.7 \times 10^7$ is off the scale of this plot.

are only seen where the combined constraint from step walls and bottom substrates are large. Short steps never have enough step wall to provide constraints to increase the stress. Medium steps only become significant when the bottom substrate width becomes large – when the step becomes small – this explains the upturn in maximum stress with decreasing step width. High steps are always significant and become more so as bottom substrate becomes larger with decreasing step width. This explains the large slope of the 90% high step. In contrast to repeating topography, the ability of coating edges to deform in can significantly decrease the stress below the level of a uniform coating. This is supported by the location of the stress maximum; figure 4.25 shows how the step dimensions change the stress maximum location. For cases where the step wall and substrate bottom are not large enough to constrain the deep coating, the maximum occurs at the periodic boundary ($x = 0$) whereas when the stress maximum increases, its location is above the step, with a slight offset for shorter steps.

### Average In-plane Stress

The average in-plane stress over a single step is quite different than over repeating steps. Figure 4.26 shows how the average stress depends on step geometry. Unlike repeating steps,

the major factor in stress reduction is deformation of the edge. For a short step, increasing the width always decreases the stress because the edge deforms toward the middle of the step, causing a low stress region over the step. This can be seen in the extending low stress regions over the step in Figure 4.23. For a tall step, initial widening has the same effect, however, as the step gets wider, the thin coating above the step can no longer feel the influence of the deforming edge and becomes virtually uniform. This uniform stress is higher than the stress relieved by edge deformation. This can be seen in Figure 4.22. Even with these increases, the stress relieved by edge deformation makes the average stress in all cases lower than the uniform in-plane stress.

**Final Coating Profile**

Coating a single step places regions with different final equilibrium heights to be attached to each other, just like coating multiple steps, however deformation at the edges reduces the stress there. Volume coupling causes less stressed regions to be thicker in directions perpendicular to the stress. This means unlike repeating steps, the middle of single step valleys can increase in thickness. This can be seen in Figures 4.22 and 4.23. Figure 4.22 shows that for large mismatch – tall steps – shrinkage dominates and the edge is low. For short steps, low stress dominates and the edge is high. Also, Figure 4.23 shows that wide valleys have a more pronounced thickness change than narrow ones. If a uniformly flat surface is desired, a tall step with narrow valley is the optimum.

**Substrate Forces**

Tangential stresses on the substrate for coatings over a single step are not as pronounced for those over repeating steps. Figures 4.27 and 4.28 show the principal stresses and the directions in which they act. The large stress pulling away from the corner is absent, but the stresses pulling up on the top of the step and away from the bottom step corner are still present. Also present is a significant stress at the coating edge on the substrate that is not seen for repeating steps and may be a defect location for delamination.

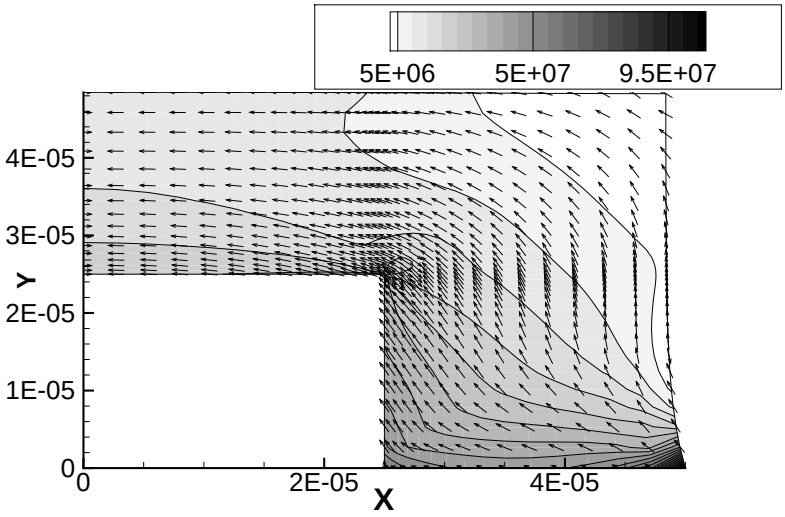


Figure 4.27: Magnitude and direction of major principal stress. Coating thickness $50\mu m$, $50\mu m$ periodicity, with a 50% wide and 50% tall step.

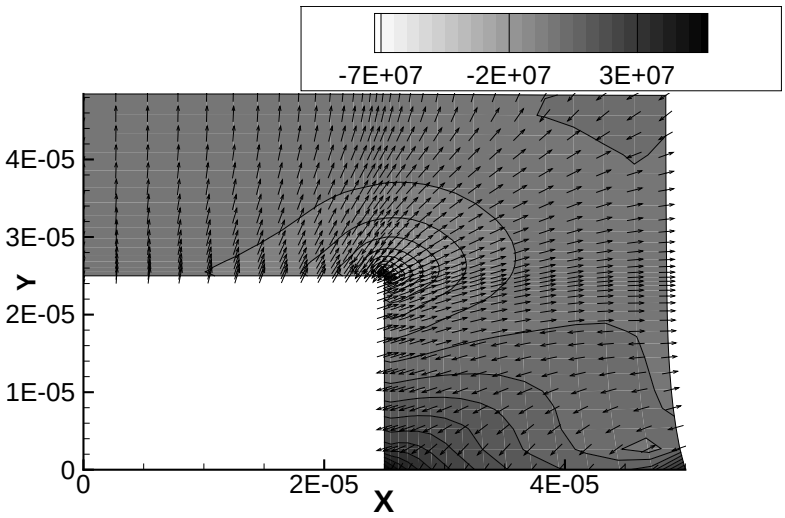


Figure 4.28: Magnitude and direction of minor principal stress. Coating thickness $50\mu m$, $50\mu m$ periodicity, with a 50% wide and 50% tall step.

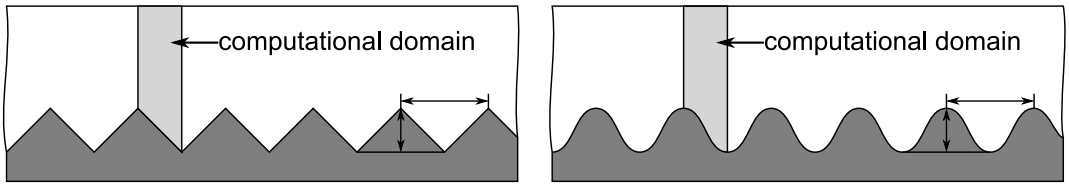


(a) Sawtooth roughness (b) Sinusoidal wave roughness

Figure 4.29: Roughness geometries.

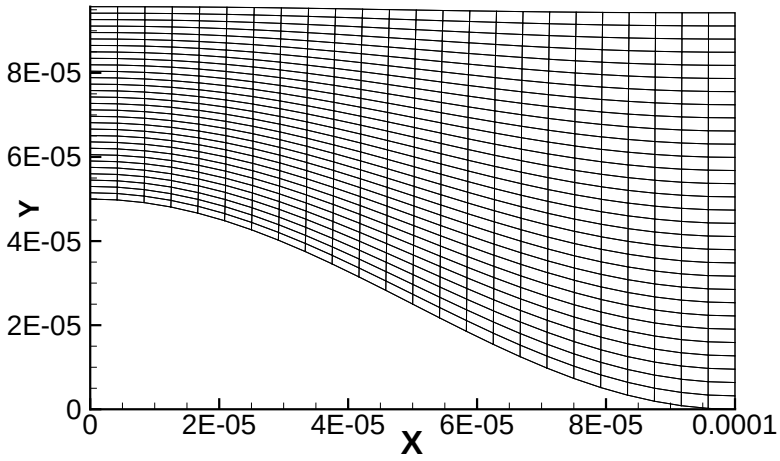


Figure 4.30: Mesh for wave roughness. This case has a 50% tall wave in a 100 $\mu m$ thick coating with 100 $\mu m$ periodicity.

## 4.5 Roughness

Coating over a substrate with surface roughness may alter the final stress profile and coating thickness. Roughness is modeled as two surface pattern extremes; first, straight sides for a sawtooth-type roughness (Figure 4.29(a)), second, a sinusoid for a wave-type roughness (Figure 4.29(b)). The mesh for a wave roughness is shown in Figure 4.30. Computations were run varying wave and sawtooth height from 10–90% of the coating thickness, for periodicities of 25–250$\mu m$, and for 25–100$\mu m$ thick coatings.

Stress profiles for a typical wave roughness are shown in Figure 4.31. There is a maxi-

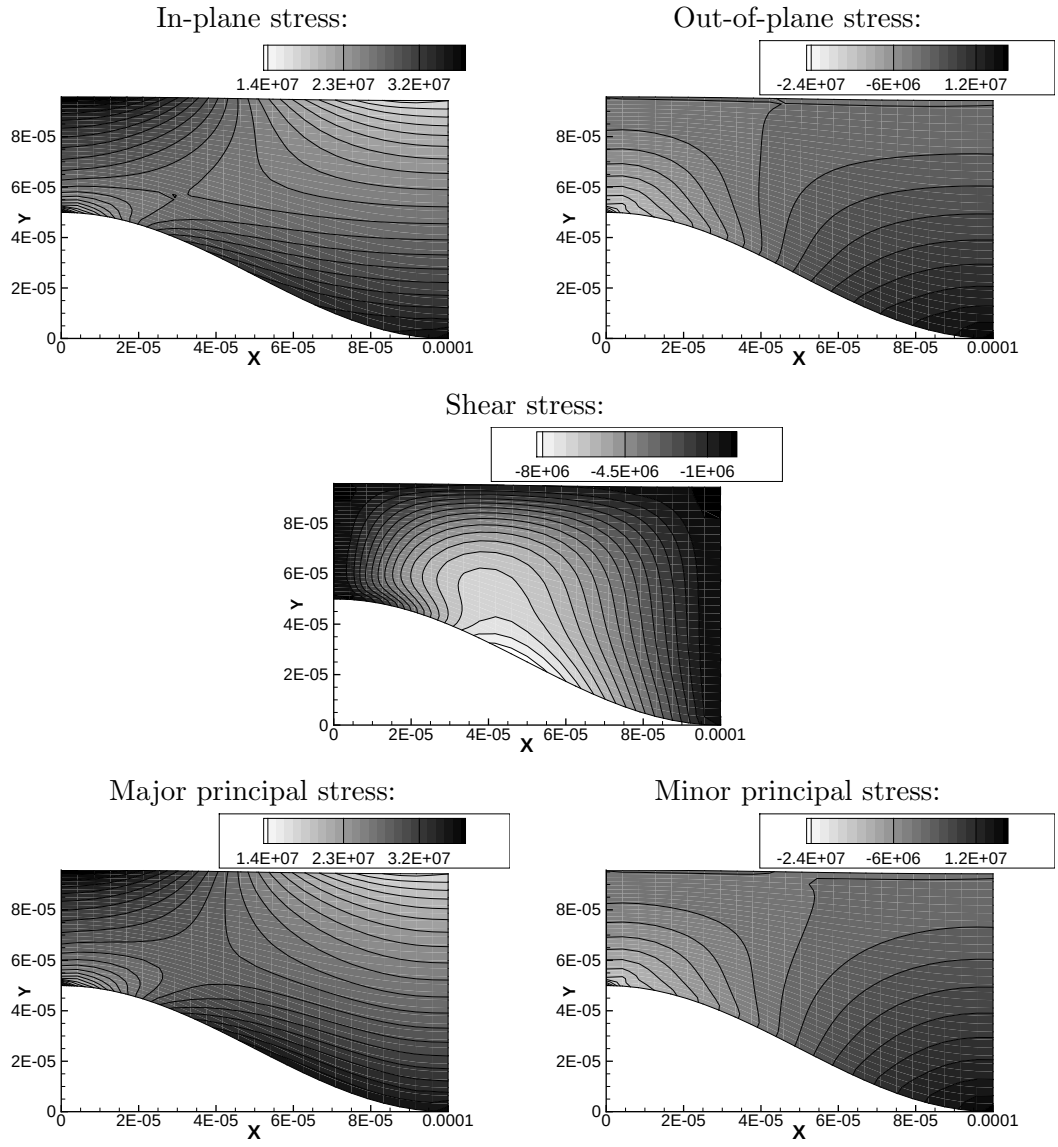


Figure 4.31: Wave topography stress components. Coating thickness $100\mu m$, step height 50%. $100\mu m$ periodicity.

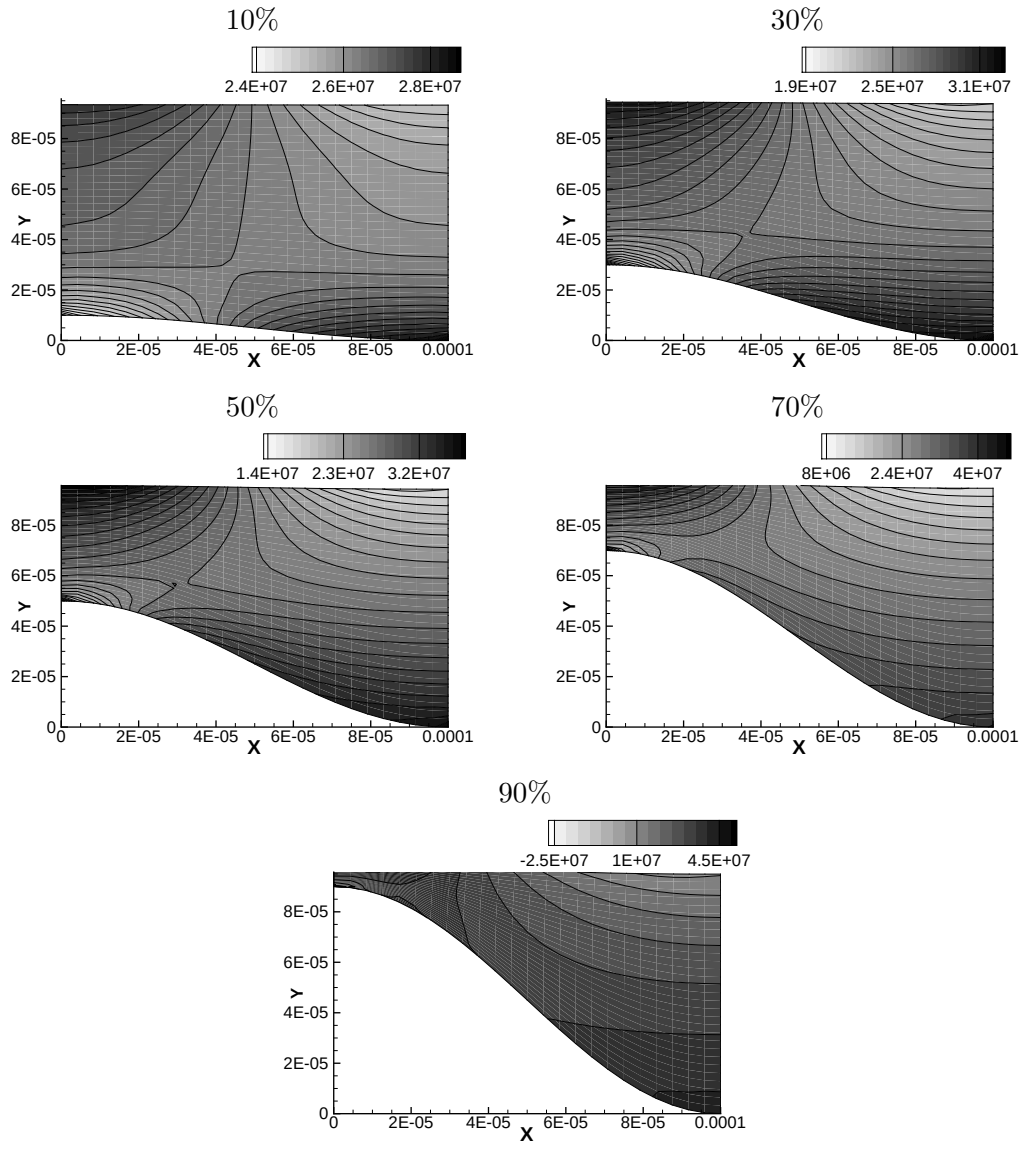


Figure 4.32: In-plane stress dependence on roughness height. Coating thickness $100\mu m$, step height 50%. $100\mu m$ periodicity.

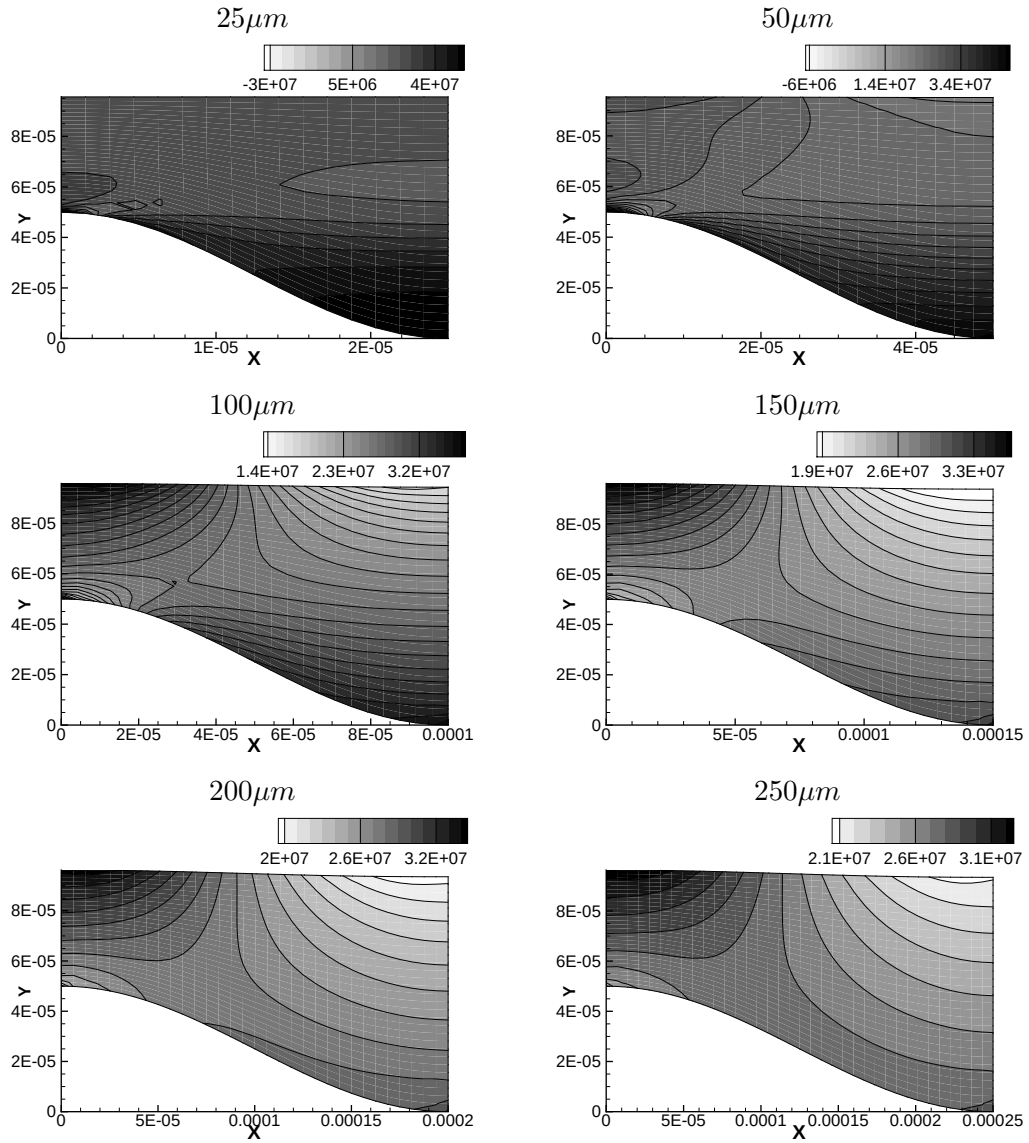


Figure 4.33: In-plane stress dependence on roughness width. Coating thickness $100\mu m$, step height 50%. 25–$250\mu m$ width.

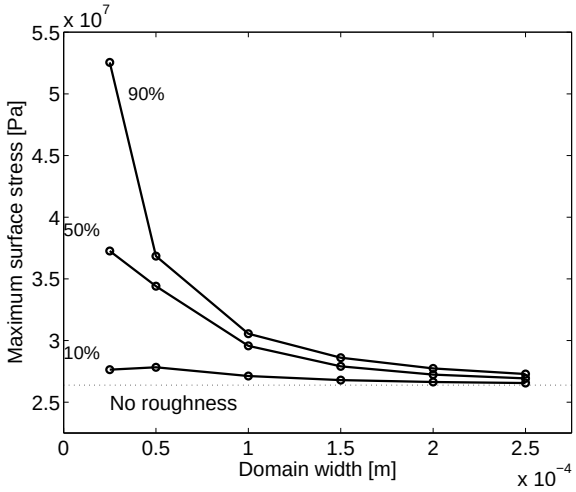


Figure 4.34: Maximum stress on coating surface dependence on wave-roughness height and width. Coating thickness $100\mu m$.

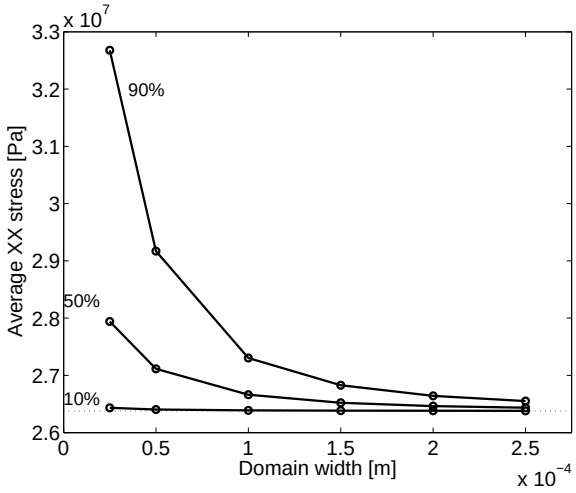


Figure 4.35: Average in-plane stress dependence on wave-roughness height and width. Coating thickness $100\mu m$.

mum in-plane stress above the wave peak, much like the topography cases, however, because the substrate height changes more gradually, the maximum always occurs directly above the wave peak at the periodic boundary. The reasons for the stress concentration at the coating surface are similar to step topography; roughness constrains the deformation of the deeper coating. Figure 4.34 shows the maximum stress dependence on peak height and periodicity (half-wavelength). Increasing constraints on deformation for a given wave width by increasing the height always increases the surface stress, as does shortening the wavelength. These effects on the stress profile are shown in Figure 4.32 and 4.33. These maxima may be defect locations. Additionally, raising and narrowing the roughness increases the average in-plane stress as shown in Figure 4.35. Short waves barely raise the average stress above the uniform levels, while taller waves become important as they get closer together.

Stress profiles for a sawtooth surface roughness are shown in Figure 4.36. There is also a stress concentration at the coating surface, and its dependence on the height and width of the sawtooth is similar to that on the wave and shown with Figure 4.39. The average in-plane stress and its dependence on sawtooth height and width are shown in Figure 4.40. The trends are the same as the wave roughness, but the average stress is lower. The shape of the roughness causes this; steeper walls constrain the thicker regions of coating more tightly, magnifying the mismatch between thin and thick coating. This is shown in Figure 4.40.

## 4.6 Cracking

Cracks form when the stress in a coating is larger than a fracture criteria. This is described in detail in fracture mechanics literature. The analysis in this section is not designed to predict formation and propagation of cracks in time, however, it attempts to show deviations from a uniform stress profile and deformations as a result of crack formation. Tam (1997) and Lei (1999) investigated similar crack influence on stress for coatings solidified by drying but did not determine how crack spacing, coating thickness, or crack depth affected the

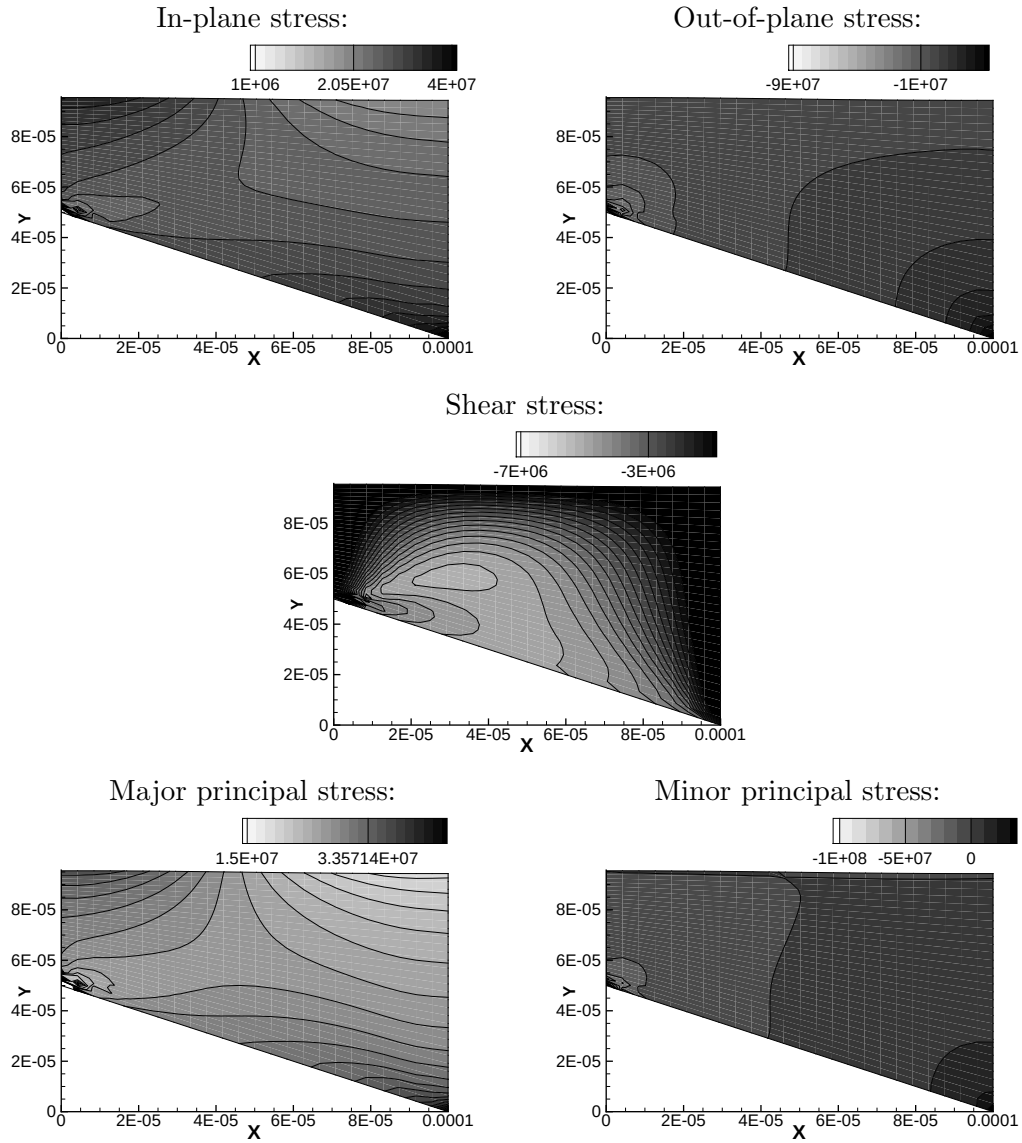


Figure 4.36: Sawtooth topography stress components. Coating thickness $100\mu m$, step height 50%. $100\mu m$ periodicity.

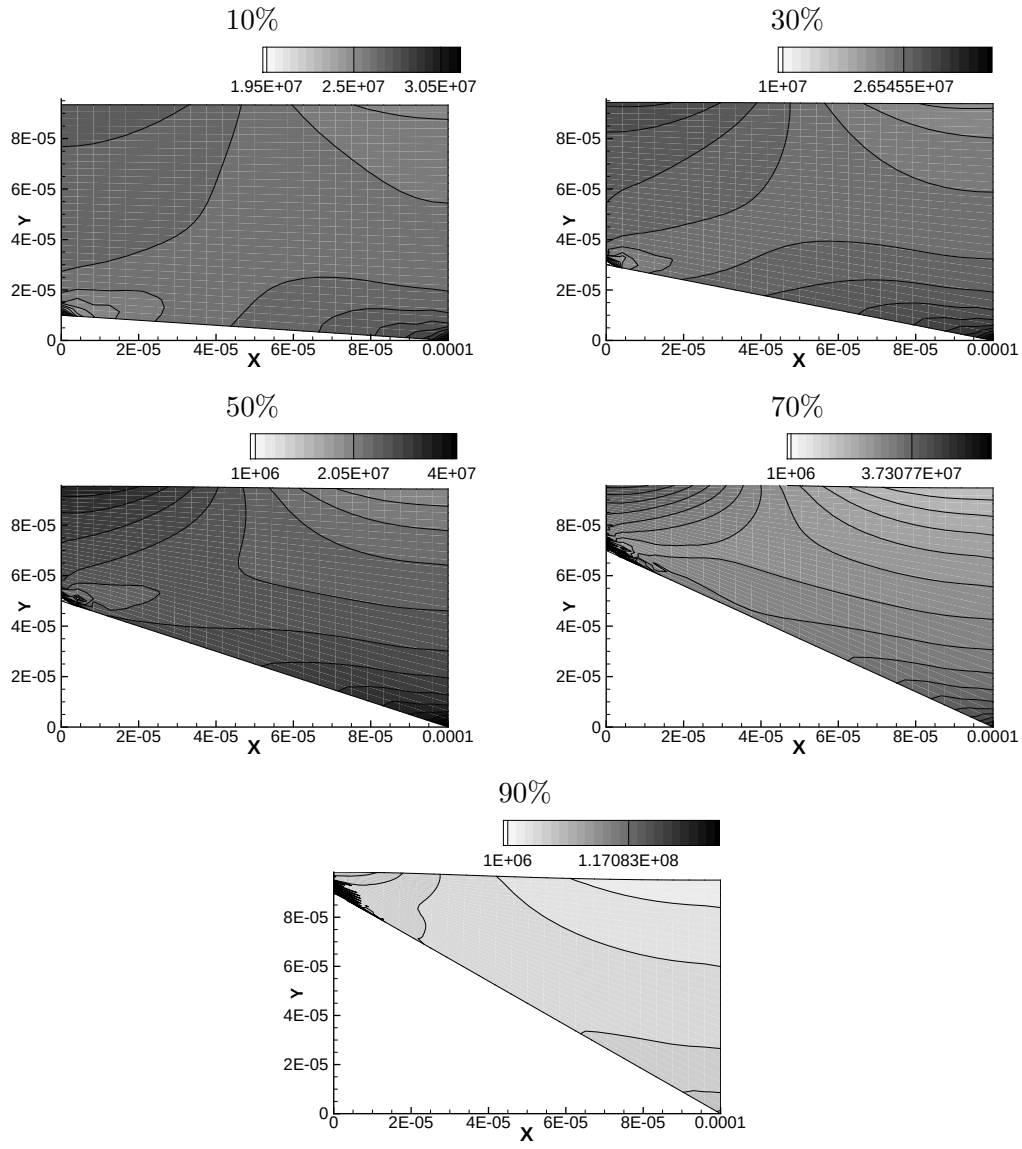


Figure 4.37: In-plane stress dependence on roughness height. Coating thickness $100\mu m$, step height 50%. $100\mu m$ periodicity.

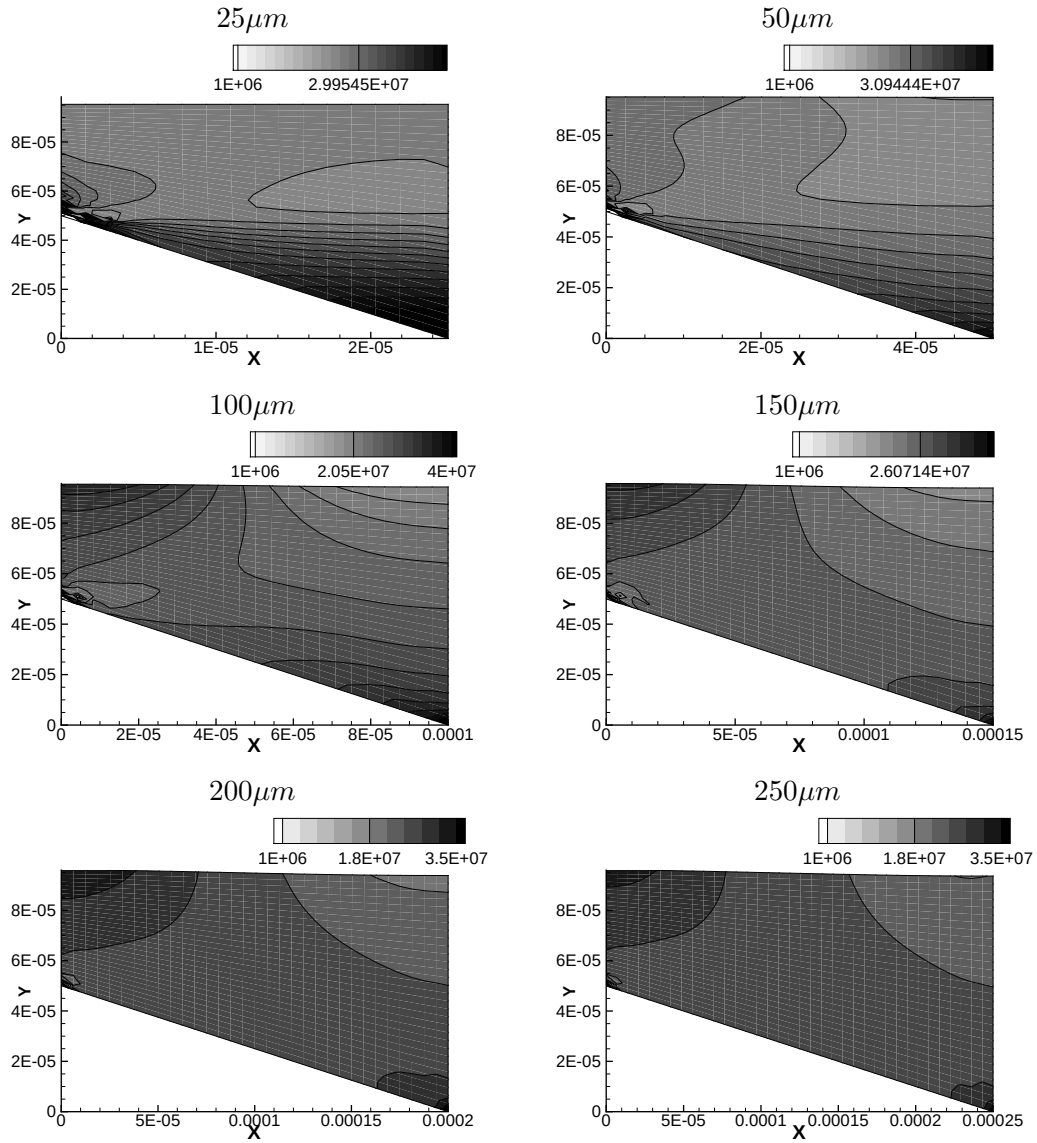


Figure 4.38: In-plane stress dependence on roughness width. Coating thickness $100\mu m$, step height 50%. 25–$250\mu m$ width.

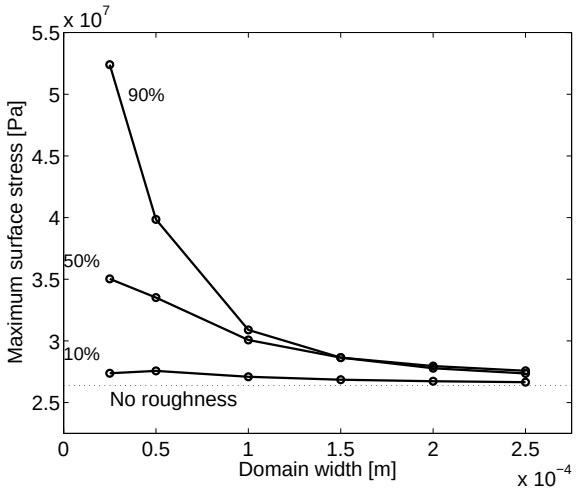


Figure 4.39: Maximum stress on coating surface dependence on sawtooth-roughness height and width. Coating thickness $100\mu m$.

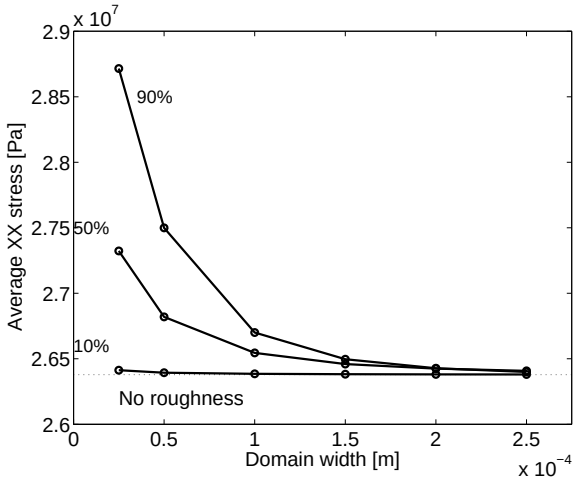


Figure 4.40: Average in-plane stress dependence on sawtooth-roughness height and width. Coating thickness $100\mu m$.

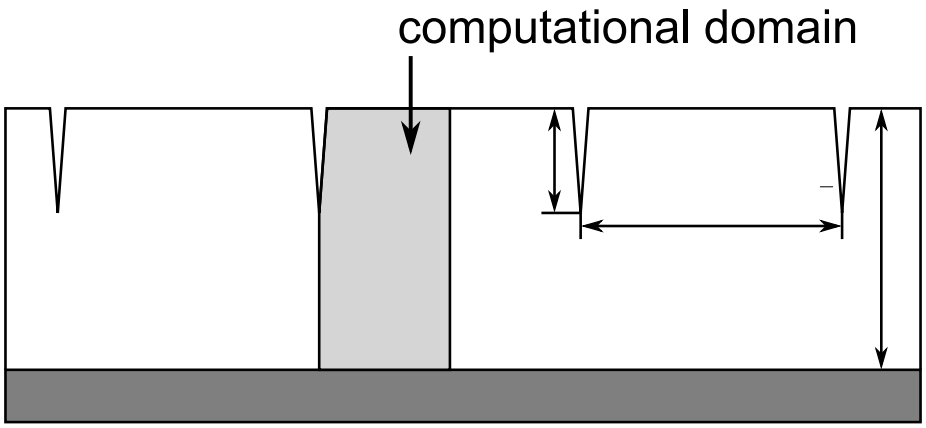


Figure 4.41: Crack Geometry. d is the crack depth, s is the crack spacing.

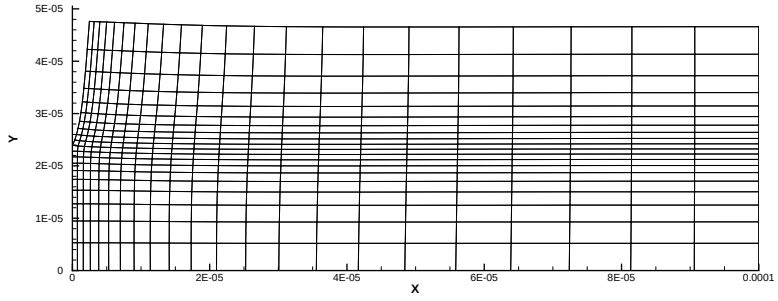


Figure 4.42: Typical mesh used in crack stress calculations post-deformation. Elements are concentrated near the crack tip. $50\mu m$ coating thickness, $100\mu m$ crack spacing, 50% crack depth.

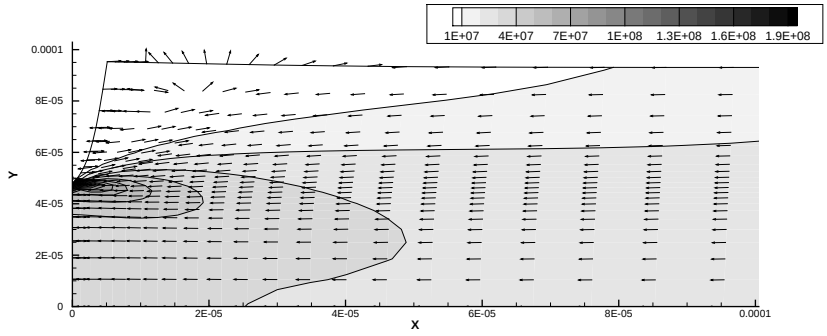


Figure 4.43: Major principal stresses and directions in a cracked coating. $50\mu m$ crack in a $100\mu m$ coating. Crack spacing is $250\mu m$. The entire computational domain is not shown.

final stress. It is expected that stresses become the highest and most nonuniform near the crack tip, so elements in the mesh will be concentrated there. Figure 4.42 shows a typical mesh for crack calculation.

Reaction and stress-free state change drive deformation, and the inclusion of a crack creates more free surfaces not constrained by a substrate or by compatibility. The unconstrained regions directly adjacent to the crack deform in reaction to stress-free state change as well as stress in adjacent regions of the coating. Stress in these regions is much lower due to this ability to deform. In the uniformly cured coating with no cracks, stress is generated in the coating plane only. The principal maximum stress is the in-plane stress and is oriented along the coating plane. In contrast, the cracked coating has in-plane, out-of-plane, and shear stress, and the principal stresses are not oriented with the coating plane everywhere. Figure 4.44 shows the in-plane (XX), out-of-plane (YY), shear (XY), and principal stresses for a $50\mu m$ crack in a $100\mu m$ coating. The crack spacing is $250\mu m$. Close to the crack, in-plane stress is increased, and out-of-plane and shear stress both become nonzero. Far from the crack, stress approach those of the uniform case – solely in-plane. Major principal stress is large near the crack tip but approaches the uniform in-plane stress far from the crack. Far from the crack, it also becomes oriented in the direction of the coating plane. Figure 4.43 shows the major principal stress and its direction. Principal stresses on the top surface of the coating adjacent to the crack – pointing upward – are balanced

In-plane stress:

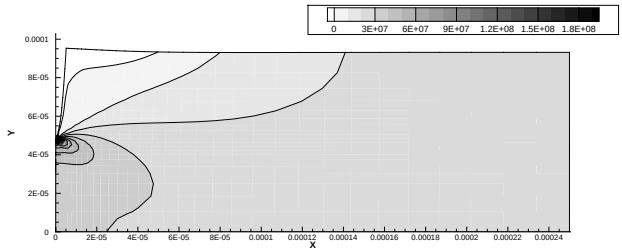


Out-of-plane stress:

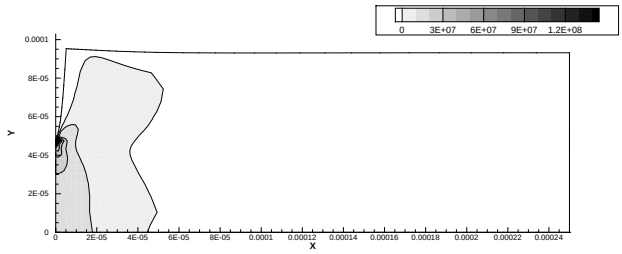


Shear stress:

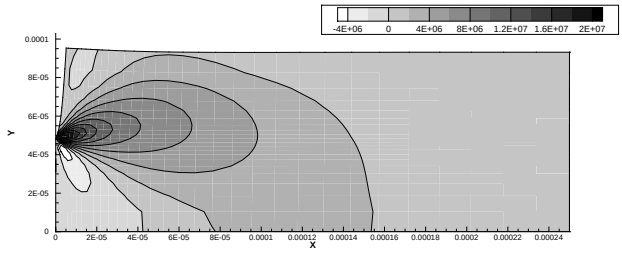


Major principal stress:

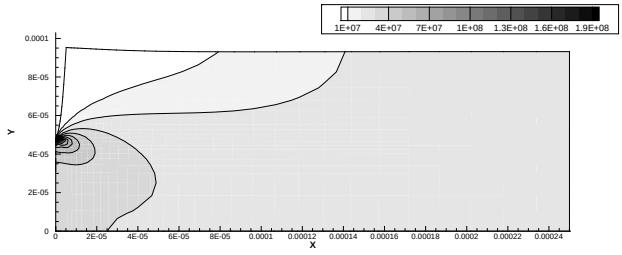


Minor principal stress:

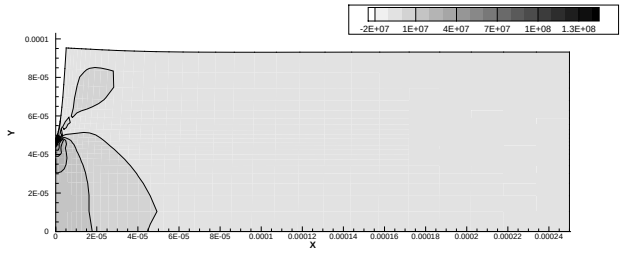


Figure 4.44: Crack stress components for a $50\mu m$ crack in a $100\mu m$ coating. Crack spacing is $250\mu m$

by perpendicular minor principal stresses to satisfy the boundary condition of no normal traction on the surface.

Deformation constraints are released as the crack depth changes. That is, without being bound to the adjacent coating, more and more deformation happens as cracks deepen and it happens in a direction to reduce stress. Coatings with deeper cracks have less stress. Figure 4.45 shows the in-plane stress profile and how it changes with crack depth for a $100\mu m$ coating with $250\mu m$ periodicity. As the crack gets deeper, minimum stress occurs over larger and larger areas. Figure 4.48 shows how the average in-plane stress changes with crack depth for the same geometry as well as thinner coatings. Average in-plane stress is related to the stress that would be measured macroscopically and decreases with increasing crack depth. Similar trends with crack depth are seen with cracks spaced more closely together and are shown in Figure 4.49.

The distance between cracks influences the ability to deform just as the crack depth does. Cracks spaced far apart have a region of essentially uniformly cured and stressed coating between them. This pseudo-uniform coating region cannot 'feel' the crack's presence. As the cracks get closer together, this uniform region disappears and region between the cracks above the crack tip becomes less stressed. This is due to the ability to deform, narrowing the region between cracks. Figure 4.46 shows how the in-plane stress profile changes with crack spacing. Note how the lowest stress region immediately adjacent to the crack is enlarged as cracks move closer together.

The crack depth and crack spacing determine the shape at the end of curing. The top surface of the coating is not flat, but is thicker at the crack. This is from volume coupling due to Poisson's ratio. More highly stressed regions far from the cracks cause out-of-plane deformation. As stress decreases toward the crack, the out-of-plane deformation is not as severe and the thickness increases.

For a given fractional crack depth, changing the coating thickness changes the available amount of material unconstrained and available for deformation to reduce stress. As coatings get thicker, more material becomes available and more stress is relieved through

10% depth:

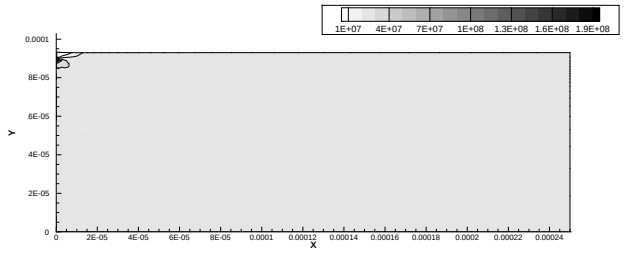


30% depth:

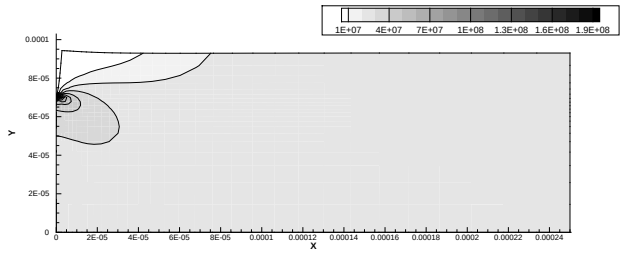


50% depth:

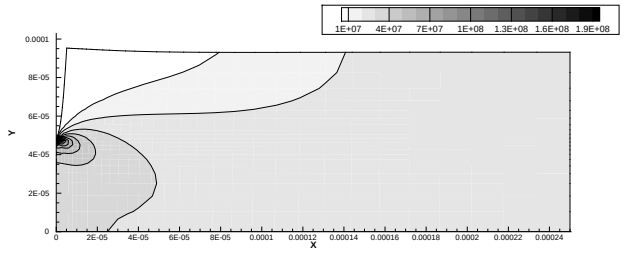


70% depth:

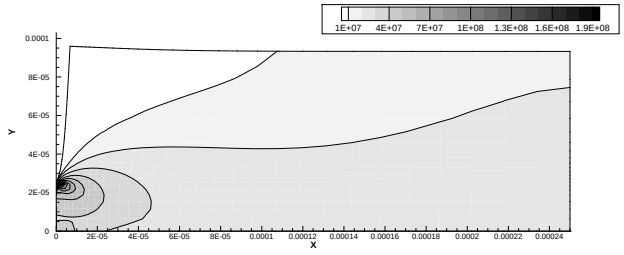


90% depth:

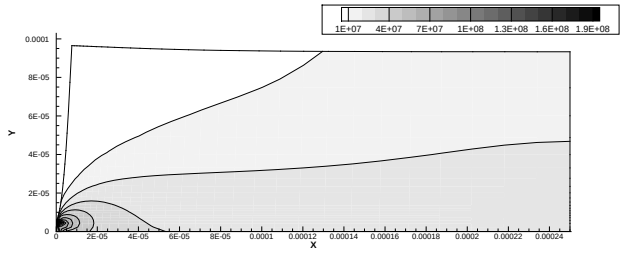


Figure 4.45: In-plane stress profile dependence on crack depth. $100\mu m$ thick coating, $250\mu m$ crack spacing. Crack depth 10–90% of coating thickness.

$25\mu m$ spacing:

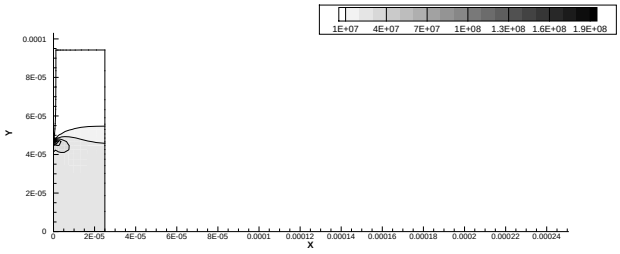


$50\mu m$ spacing:

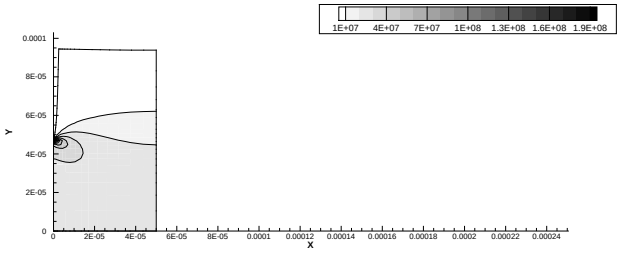


$150\mu m$ spacing:

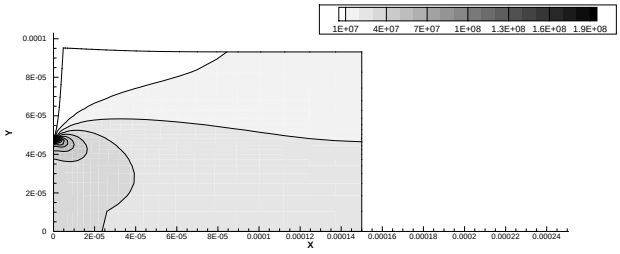


$250\mu m$ spacing:

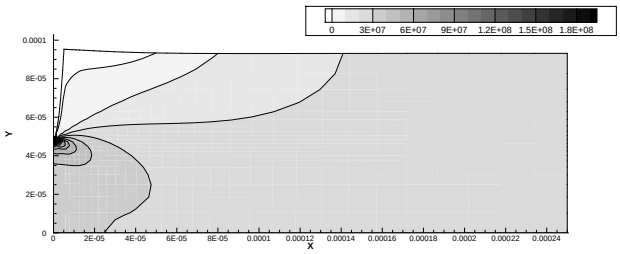


Figure 4.46: In-plane stress profile dependence on crack spacing. $100\mu m$ thick coating, 25–$250\mu m$ crack spacing. Crack depth 50% of coating thickness.

$25\mu m$ coating:

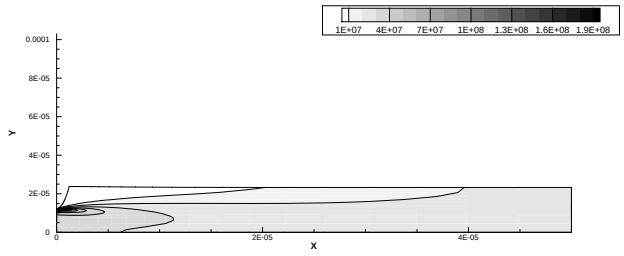


$50\mu m$ coating:

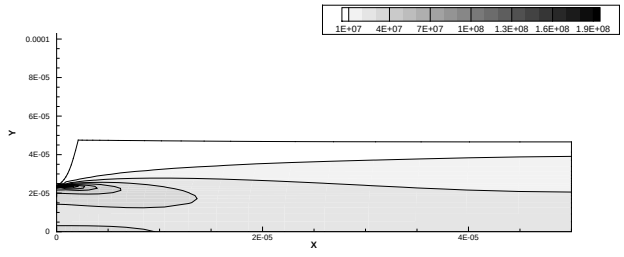


$100\mu m$ coating:

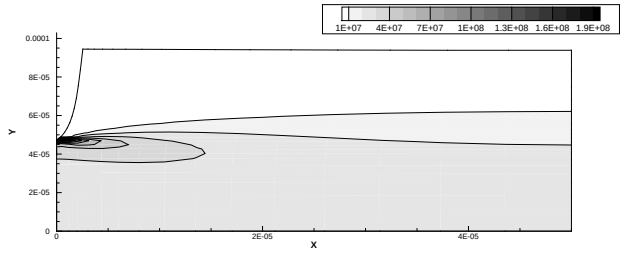


Figure 4.47: Major principal stress profile dependence on coating thickness. 25–$100\mu m$ thick coating, $50\mu m$ crack spacing. Crack depth 50% of coating thickness.

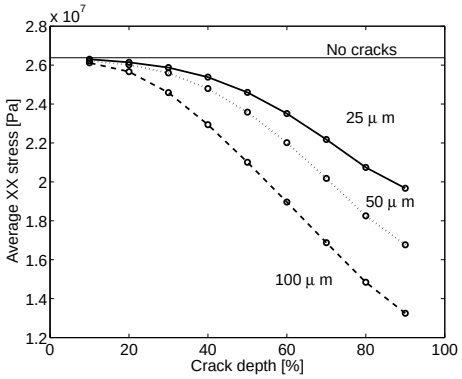


Figure 4.48: Average in-plane stress for cracked coatings with varying thickness. Crack spacing $100\mu m$. Stress for uniform case without cracks shown. Coating thicknesses of 25, 50, and $100\mu m$ shown.

deformation. Figure 4.47 shows the major principal stress profile dependence on coating thickness for 25–$100\mu m$ coatings with 50% deep cracks and $100\mu m$ crack spacing. As coating thickness increases, the uniform region between cracks gets smaller and the area with the smallest stress increases.

The average in-plane stress is a measure of how much stress is present in the coating and how much would be measured macroscopically. Figures 4.45–4.47 showed how the crack depth, crack spacing, and coating thickness affected the stress profile in the cracked coating. More material available for deformation causes lower stress; the material deforms in a direction to reduce stress. More material is available for deformation with deeper cracks, thicker coatings, and more closely spaced cracks. Figures 4.48 and4.49 show the average in-plane stress for varying coating thicknesses, crack thicknesses, and crack depths; the stress is lower when more deformation can occur. Every case with a crack has less stress than the uniform coating without cracks.

## 4.7 Delamination

Delamination occurs when the coating separates from its substrate, usually near an edge. It can occur as a result of poor adhesion between coating and substrate, or a high out-of-plane

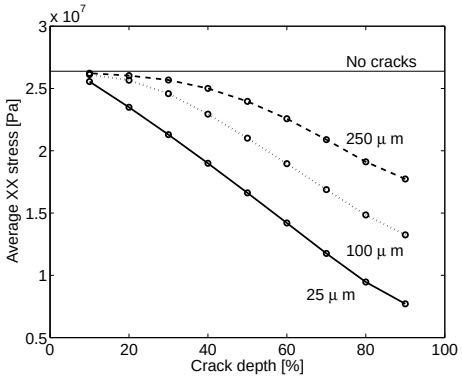


Figure 4.49: Average in-plane stress for cracked coatings with varying crack spacings. Crack spacing $25 - 250\mu m$. Stress for uniform case without cracks shown. Coating thicknesses $100\mu m$.

stress near the edge. This analysis does not attempt to predict delamination with time, rather the influence of delamination width and coating thickness on the stress field.

Stress profiles for all components of stress are shown in Figure 4.50. All components of stress are minimized outside of the delamination because deformation can occur somewhat freely there. Stress is concentrated at the initial point of substrate adhesion, which indicates that more delamination may take place to relieve this stress. Out-of-plane stress is compressive on the surface just on the inside of the adhesion. Also, the delaminated region separates from the substrate, curling up near the edge. The reasons for these come from the geometric constraints and boundary conditions of adhesion. The stress-free state change makes the entire coating want to shrink, but it cannot where it adheres to the substrate. Removing adhesion outside of the delamination makes deformation possible there, which is why there is virtually no stress in that region. The top of the coating shrinks, deforming the edge around the adhesion point with it – this causes the coating curl and out-of plane stress. Figure 4.51 shows how the in-plane stress changes as the delamination gets wider; the low-stress region grows with delamination growth, as does a compressive in-plane stress which arises where the coating curves upward. This curve only happens locally around the delamination tip, the coating is flat outside of that, evidenced by the straight top and bottom coating surfaces far from the tip. Inside the tip, stresses become uniform and ori-

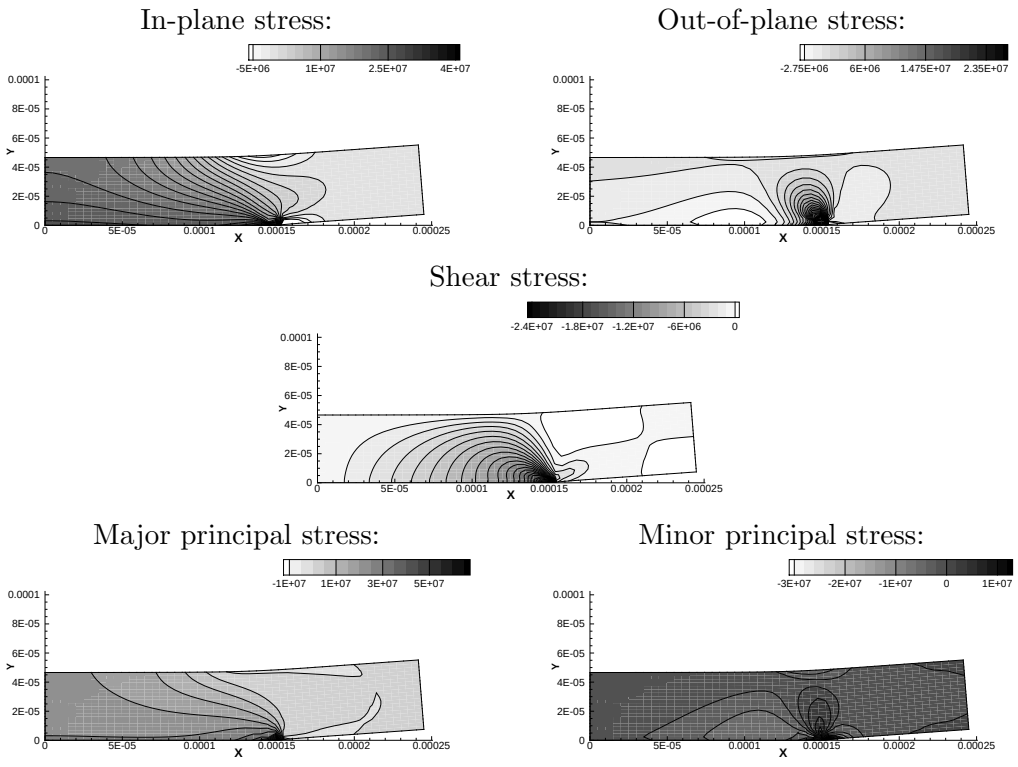


Figure 4.50: Delamination stress components. Coating thickness $50\mu m$, delamination width 40%. $250\mu m$ periodicity.

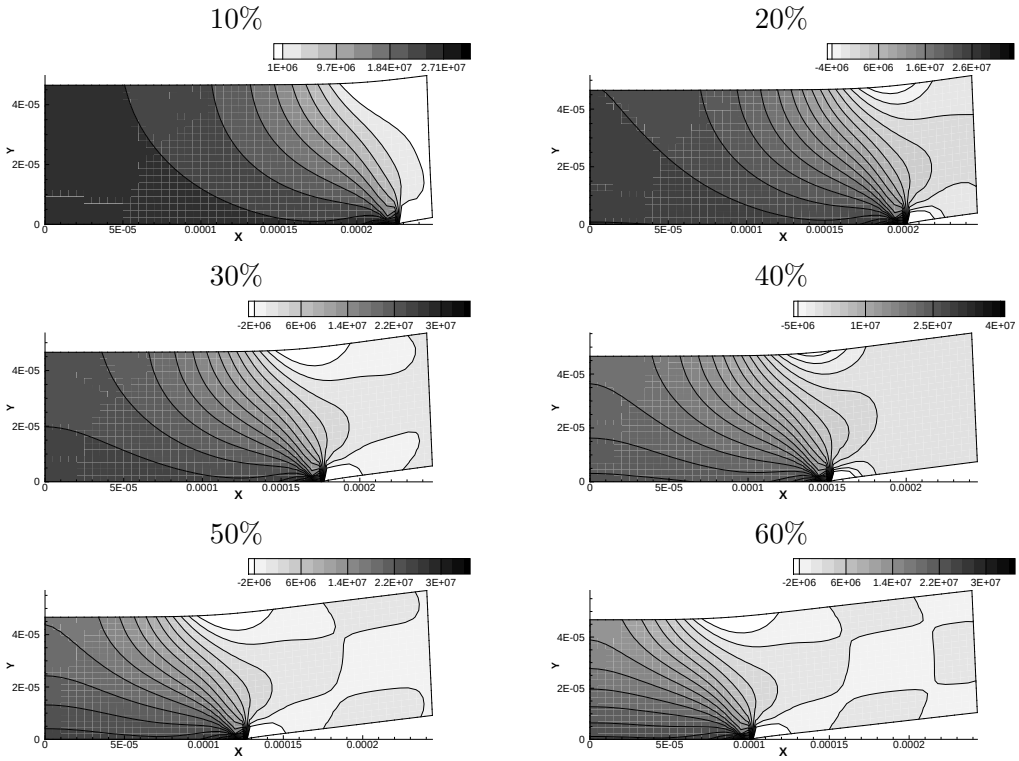


Figure 4.51: In-plane stress dependence on delamination width height. Coating thickness $50\mu m$, delamination width 10–60%. $250\mu m$ periodicity.

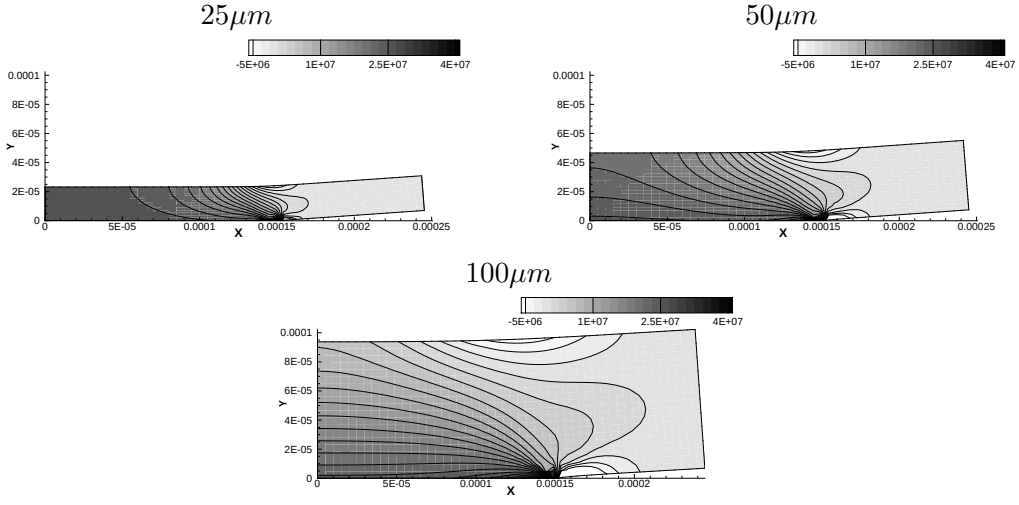


Figure 4.52: In-plane stress dependence on coating thickness. Coating thickness 25–100$\mu m$, delamination width 40%. $250\mu m$ periodicity.

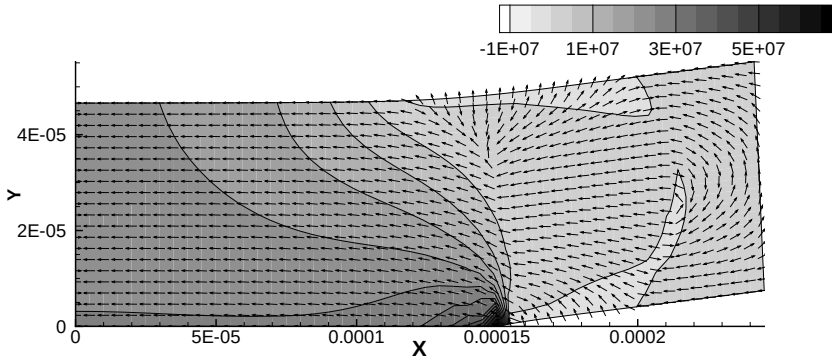


(a) Major principal stresses.

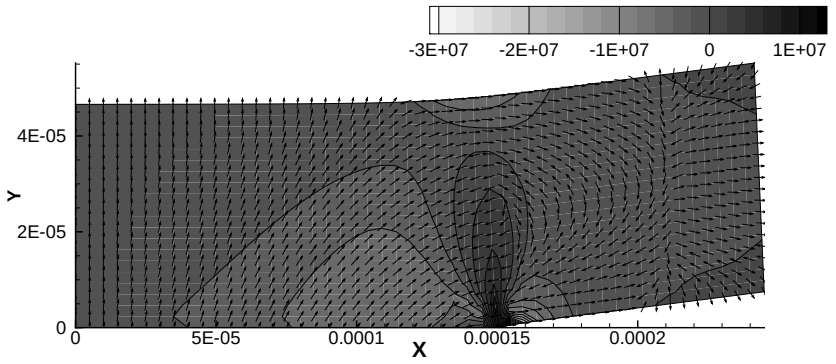


(b) Minor principal stresses.

Figure 4.53: Principal stresses and directions in a delaminated coating. $100\mu m$ wide delamination in a $50\mu m$ thick coating. Domain width is $250\mu m$.

ented in the coating plane. This can be seen in Figure 4.53, where the principal stresses become oriented toward the periodic boundary. Figure 4.53 also shows that the maximum principal stresses, both major and minor, occur at the delamination tip and act in a direction pulling away from the substrate. Coating thickness influence on stress profile is shown in Figure 4.52. The in-plane stress is decreased near the top of the coating inside of the delamination and increased where the coating curves because more deformation can occur in thicker coatings. This is also shown in Figure 4.54, where thicker coatings have lower average stresses for the same delamination width. In addition, deformation is increased with wider delamination regions, and these coatings have lower stress too.

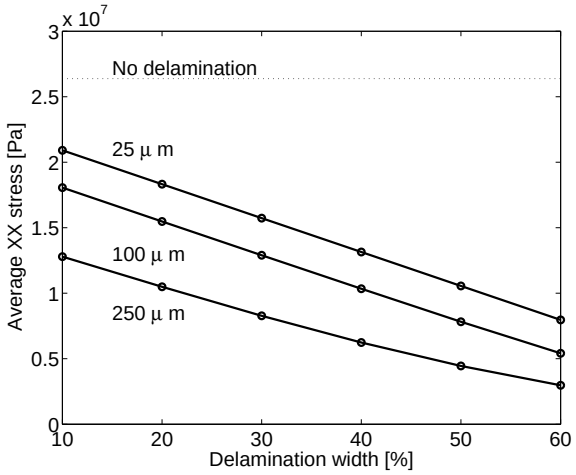


Figure 4.54: Average in-plane stress dependence on dependence on fractional delamination and coating thickness. Domain width $250\mu m$.

## 4.8 Conclusion

Spatially nonuniform stress generation in TMPTA coatings initiated with DMPA and UV light was discussed in this chapter. Introduction of a substrate with topography or surface nonuniformities changed the stress field for otherwise uniform coatings. These new stress distributions point to possible mechanisms of defect formation; stress concentrations on the coating surface, traction away from the substrate, and increased average stress may all create defects. Stress effects of normal defects – cracking and delamination – were also included. In addition, stress reduction by nonuniform UV light delivery was discussed, both in time and space.

A common theme through all of these nonuniformities is the limitation or release of deformation constraints. More constrained coatings – those with larger substrate restrictions, smaller defects, or smaller lag regions – have higher stress because deformation is not allowed in a direction that releases stress. Relaxation can become important only if curing is not uniform, chapter 3 discussed how minimal relaxation is for uniform cure.

Trends predicted by altering the substrate geometry or UV distribution can be used to adjust coating or substrate to change stress or eliminate defects. Computational modeling

is necessary because measurement of the stress distribution in two or three-dimensions is not possible experimentally.

# Chapter 5

# Concluding Remarks

## 5.1 Recapitulation

This thesis discusses viscoelasticity and stress generation during the solidification of polymer coatings by ultraviolet light initiated free-radical polymerization. Polymer coatings are important for protection, optical, mechanical, or other properties.

The objectives of this research were threefold: to create models suitable for determining the stress, deformation, and relaxation in linear viscoelastic coatings, to determine the physical processes responsible for stress buildup in uniformly cured coatings, and to examine the effect of nonuniformities on otherwise uniform coatings.

Chapter 2 presented two new models for viscoelasticity. The first came from the network modeling of Rajamani (2005), but the network model presented here added viscoelastic network elements as well as the ability to change the network stress-free state independently of the elements and in time. Unfortunately, this model has drawbacks, mostly with the representation of a continuum material with discrete elements. The way in which elements are connected has a significant impact in the force in each element and in how elements deform with time. Also, average properties like stress and relaxation are difficult to quantify with the network model. Nonetheless, this model is easy to implement and may be appropriate for simple overall deformation calculations.

Chapter 2 also laid the framework for a new mathematical analysis of a continuum model of linear viscoelasticity. This breakdown is useful because, unlike most standard treatments of viscoelasticity, the driving force for stress and deformation is a change in the stress-free state. The use of a linear viscoelastic constitutive equation which could be separated into its constituent pieces, the scaling of inertia out of the problem, and the decomposition of strain into stress-free, viscous relaxation, and elastic components allowed standard ordinary differential equation methods to be applied. With some mathematical substitutions for time derivatives, the unknown stress could be calculated, reduced to a function of the unknown strain, and removed as an unknown from the system, reducing the total number of unknowns and computational time. The subsequent equations for strain are solved using Galkerin's method with Finite Element basis functions.

Chapter 3 discussed stress generation during uniform cure of a TMPTA coating initiated with UV light and DMPA. Stress generation and relaxation was calculated using a uniform version of the method developed in Chapter 2. The use of free-radical reaction kinetics of polymerization and volume change was necessary to determine how the stress-free state and physical properties changed with time. This coupling of kinetics, volume, and physical properties with stress generation produces results that should more closely match the actual physical properties, and, to our knowledge, is the first time delayed volume change and stress modeling have been combined for photopolymerizations. It turns out that the delayed volume change is very important in determining the final stress, as has been shown experimentally (Schmidt, Schmah, Leterrier and Manson 2007). Computational analysis of stress generation allows more thorough analysis of the stress, using information not available experimentally. This is how relaxation was deemed not very important and how process windows were constructed.

Finally, Chapter 4 discussed final stress profiles and how they are influenced by coating nonuniformities such as substrate geometry, roughness, defects, and nonuniform radiation delivery. Geometry places constraints on how easily deformation can occur, more constraints increase the stress. Stress field development can suggest where defects are likely to occur

as well as what stress would be measured macroscopically.

Stress modeling is important because the two or three-dimensional state of stress cannot be measured experimentally. The micro-distribution of stress can only, at least at with present experimental techniques, be determined throughout in the coating through numerical calculation.

## 5.2 Applications

Concepts developed in this thesis can be applied to the design of curing processes for the TMPTA system presented or to other coating systems. Understanding physical processes behind experimentally observed phenomena can direct further experiments and suggest limitations for process parameters and desired constraints. In addition, the mathematical models developed for viscoelastic coatings can be applied to non-coating viscoelastic materials where deformation-stress information is desired. Property buildup theory can be extended to other curing systems. This mathematical formulation can, unlike previous models, output relaxation information, which may be important to know for different materials.

Chapter 3 discussed combining mature theory for modeling reaction kinetics, diffusion, and monomer conversion with linear viscoelastic modeling of uniform deformation and stress generation for photopolymerizations. The inseparable connection between specific volume, stress-free state, reaction kinetics, and stress was discussed. Understanding the evolution of the stress-free state in combination with buildup of physical properties like the viscosity and modulus is essential to understanding how to control final stress in the coating. The physical properties depend on polymer growth, crosslinking, and network formation in the coating, which in turn depends on double bond conversion through the reaction kinetics. The evolution of the stress-free state depends on the specific volume of the system, which may not be its equilibrium value and itself depends on reaction and volume relaxation kinetics. Viscoelastic stress relaxation is present, but for realistic curing rates is small

enough to be inconsequential. Longer, slower curing schedules do relax enough stress to be meaningful, but the time necessary borders on ridiculous.

In all of these processes, the only controllable parameters by the user, whether experimental or computational, are the initial photoinitiator concentration, the incident UV light intensity, and the UV radiation time. Temperature may also be manipulated, with higher temperatures increasing free volume and the reactions that depend on it, but these effects were not considered in this thesis. Higher temperatures may also delay the glass transition and play a role in the final stress as well. Only the initiation of active radicals may be specifically influenced by these controllable parameters, their behavior once initiated is dictated by the current state of the coating – the concentrations of radicals and double bonds as well as the free volume – which in turn depends on the reaction history and starting point. There is no direct control of propagation, volume change, trapping, or termination. While photoinitiator concentration may not be altered after reactions begin, the UV light intensity and its dependence on time are easily changed to better control kinetics through selective initiation of active radicals. In fact, tailoring the UV intensity in time may be the best method if more control over reaction is desired. These ideas are already being applied to electron beam cured coatings through the use of pulsing (Richter 2007) and were investigated for UV stress reduction (Vaessen et al. 2002). The mathematical framework laid out in Chapter 3 can be used to predict how changing the radiation delivery in time will effect the stress generation, and as such can be used to screen possible radiation schemes. This framework has already been used in Section 3.4.9 to construct process windows showing physically obtainable final states for conversion, stress, time, and total energy required for constant radiation delivery in time. These process windows show what concessions must be made to meet certain constraints, which stem from the interplay between controllable parameters, reaction initiation, and the volume-property-stress buildup relation. Fast initiation and reaction propagate quickly, causing excess free volume, more strain above $T_g$, and higher stress. Slow constant initiation is not as energy efficient late in polymerization where recombination of photoinitiator and radical trapping are increased, it also takes longer.

Designing a time-dependent irradiation scheme can be treated as an optimization problem with multiple possibilities for constraints: irradiation time, stress generation time, conversion, energy requirements, stress. Virtually infinite freedom to change the UV intensity with time is possible, within equipment constraints. White and Hahn (1993) and Lim et al. (2002) discuss different methods for cure tailoring to reduce final stress.

In addition to the effect of changing the initiation conditions, the uniform stress model can be used to determine differences between coating formulations. Replacing photoinitiator may change the efficiency of primary chain creation, cascading all the way through propagation and volume change to stress. Replacing the monomer may change the reaction kinetics, their relationship with free volume, the equilibrium volume, and how the physical properties build up, all of which have an impact on the final stress and conversion.

Chapter 4 discussed the effects nonuniformities have on the stress. This information can be used for insight as to why defects may occur as well as suggest remedies for these defects. In general, stress increase arises from constraints on deformation brought about by substrate geometry or the coating surface. The more tightly placed the constraints are, the greater the influence on stress; narrower topography, sharper corners, and taller features all increase stress. Thicker coatings decrease stress by increasing distance between the coating surface and the geometric constraints. This information can be used to alter substrates or coating thicknesses where defects are seen in order to eliminate those defects. It can also be used, with application of suitable kinetics, volume, and stress, to determine how changing the coating formulation will change the stress for the same geometry. Perhaps process designers could change the coating formulation instead of the geometry.

## 5.3 Further Research

The work in this thesis brought together ideas from diffusion-limited reaction kinetics, delayed volume and stress-free state change, physical property buildup, and linear viscoelasticity. We contributed understanding on how stress is developed in ultraviolet cured coatings,

but more research can be performed. This section discusses avenues for further research in the area of stress generation with radiation cure.

### 5.3.1 Heterogeneous Reaction Kinetics

Section 3.2 introduced spatially uniform concentrations of reactants and isothermal curing. These assumptions could be relaxed by including spatial nonuniformities from both internal and external sources. Internal sources of nonuniformities include heat and mass transfer within the computational domain. Goodner and Bowman (2002) did this for photopolymerizations but used simplified kinetics that did not include volume relaxation. Calculations could include concentrations of initiator, monomer, polymer, active radicals, temperature, and volume along with stress and deformation information. Spatial concentrations will change with mass transfer by diffusion, generation and consumption by reaction, and slightly with concentration due to volume change. Temperature will change with latent heat of reaction, absorption of incident UV radiation, heat conduction inside the coating, and conduction and convection at the coating boundaries. There is no transport of volume, so the volume will only depend on the local volume history and its relaxation to equilibrium, and the 'transport' of stress and deformation are described in Section 2.4 with momentum conservation.

An external source of nonuniformity formation is attenuation of UV light through the depth of the coating by photobleaching initiators or other reactants that absorb the light. This change in incident light will alter primary radical initiation and therefore reactant concentrations, volume, and stress. Long et al. (2009) detail computations of photomechanics and the attenuation of UV light within their polymer sample. Another external source of nonuniformities comes from oxygen inhibition of reactions. Oxygen is a radical scavenger and, if the atmosphere around the coating is not purposely inerted, can diffuse into the top of the coating where it destroys active radicals, creating a depletion zone whose dimensions depend on mass-transfer characteristics in the coating. Lovestead et al.'s (2003) computational work includes oxygen inhibition from atmospheric sources.

The once uniform set of

Ambitious computational modelers may also wish to investigate the influence of more tight spatial control over reactions using two-color single-photon initiation and inhibition as described in Scott et al. (2009). Two photosensitive compounds, each of which responds to a single, independent wavelength, are inserted into the coating before polymerization. One is a photoinitiator, the other an inhibitor. Targeted delivery of incident light creates initiating zones and inhibition zones with spatial control. This technique may be used to customize reaction kinetics to avoid stress generation where it would otherwise build up with uniform radiation delivery.

### 5.3.2 Chemorheology

Physical property – viscosity and modulus – buildup is important to calculate the magnitude of stress and importance of relaxation. Love, Ruinet and Teyssandier's (2008) Boltzmann sigmoidal analysis of buildup does not mention the effect of changing the rate of polymerization. Further work could be done understanding how properties change more thoroughly. The complication for free-radical polymerizations is that their network theory is more difficult to analyze because they create long chains instead of bigger and bigger molecules like step-growth systems. Free-radical network theory is not as well developed as step-growth network theory (Miller and Macosko 1976), even though molecule growth, entanglement, gelation, and vitrification happen in both systems. Additionally, the point where the glass transition is crossed must be further investigated, especially if that point changes with reaction rate as it does with the rate of temperature change in DSC experiments. Schmidt, Leterrier, Schmah, Manson, James, Gustavsson and Svensson (2007) proposed a change in specific volume with incident light intensity, but only after $T_g$ is crossed. Hale et al. (1991) discuss the glass transition in the scope of curing.

### 5.3.3 Defect Modeling

Adding stress-induced defect formation theory to the kinetic, volume, stress, and deformation model would increase the ability to predict the initiation and propagation of defects in time and make the model more comprehensive for defect formation. This theory includes initiation of cracks and their expansion once initiated as well as adhesion to the substrate, delamination, and the propagation of delamination fronts. The impetus for formation and progression of these defects is stress; whether tensile stress at the surface for cracks or normal stress at the substrate for delamination. Adding defect formation criteria will determine when stress profiles like the ones seen in Chapter 4 will initiate a defect and how it will grow. Kim and Nairn (2000) shows crack theory from a fracture mechanics standpoint for polymer coatings. Deformation constraints are released when a defect forms, and the stress-deformation model will determine the resultant effect on the stress field in the coating.

# Bibliography


Adolf, D. B., Martin, J. E., Chambers, R. S. and Guess, T. R. 1998 Stress During Thermoset Cure. *Journal of Materials Research* **13** 530–550.

Adolf, D. and Martin, J. E. 1996 Calculation of Stresses in Crosslinking Polymers. *Journal of Composite Materials* **30** [No. 1] 13–34.

Alfrey, T. 1965 *Mechanical Behavior of High Polymers*. Interscience Publishers,.

Andrzejewska, E. 2001 Photopolymerization kinetics of multifunctional monomers. *Progress in Polymer Science* **26** [No. 4] 605–665.

Anseth, K. S., Bowman, C. N. and Peppas, N. A. 1993 Dynamic mechanical studies of the glass transition temperature of photopolymerized multifunctional acrylates. *Polymer Bulletin* **31** [No. 2] 229–233.

Aris, R. 1962 *Vectors, Tensors, and the Basic Equations of Fluid Mechanics*. Oxford University Press,.

Ascher, U. M. and Petzold, L. R. 1998 *Computer Methods for Ordinary Differential Equations and Differential-Algebraic Equations*. SIAM,.

Babuska, I. 1971 Error-bounds for finite element method. *Numerische Mathematik* **16** [No. 4] 322–333.

Basu, S. K. 2005 *Wrinkling of Solidifying Polymeric Coatings*. PhD thesis University of Minnesota.

Bird, R. B., Armstrong, R. C. and Hassager, O. 1977 *Dynamics of Polymeric Liquids*. John Wiley & Sons,.

Bird, R., Stewart, W. and Lightfoot, E. 1960 *Transport Phenomena*. John Wiley & Sons,.

Bland, D. R. 1959 On the Foundations of Linear Isotropic Visco-Elasticity. *Proceedings of the Royal Society of London, Series A, Mathematical and Physical Sciences* **250** 524–549.

Bland, D. R. 1960 *The Theory of Linear Viscoelasticity*. Pergamon Press,.

Bornside, D. E. 1990 Mechanism for the Local Planarization of Microscopically Rough Surfaces by Drying Thin Films of Spin-Coated Polymer/Solvent Solutions. *J. Electrochem. Soc.* **137** [No. 8] 2589–2595.

Bowman, C. N. and Peppas, N. A. 1991 Coupling of kinetics and volume relaxation during polymerizations of multiacrylates and multimethacrylates. *Macromolecules* **24** [No. 8] 1914–1920.

Brenan, K. E., Campbell, S. L. and Petzold, L. R. 1989 *Numerical Solution of Initial-Value Differential-Algebraic Equations*. Elsevier Science Publishing,.

Callister, W. D. 2003 *Materials Science and Engineering, An Introduction*. John Wiley & Sons,.

Christensen, R. M. 1982 *Theory of Viscoelasticity, An Introduction*. Academic Press,.

Christodoulou, K., Lightfoot, E. and Powell, R. 1998 Model of stress-induced defect formation in drying polymer films. *AIChE Journal* **44** [No. 7] 1484 – 1498.

Couchman, P. R. 1979 The effect of molecular weight on glass-transition temperatures (compositional variation of glass-transition temperatures 3). *J. Appl. Phys.* **50** [No. 10] 6043–6046.

Croll, S. G. 1978 Internal Stress In A Solvent-Cast Thermoplastic Coating. *Journal of Coatings Technology* **50** [No. 638] 33 – 38.

Croll, S. G. 1979a The origin of residual internal stress in solvent-cast thermoplastic coatings. *Journal of Applied Polymer Science* **23** [No. 3] 847–858.

Croll, S. G. 1979b Residual Stress In A Solventless Amine-Cured Epoxy Coating. *Journal of Coatings Technology* **51** [No. 659] 49 – 55.

Croll, S. G. 1981 Residual Strain Due To Solvent Loss From A Crosslinked Coating. *Journal of Coatings Technology* **53** [No. 672] 85 – 92.

Dauvillier, B. S., Hbsch, P. F., Aarnts, M. P. and Feilzer, A. J. 2001 Modeling of viscoelastic behavior of dental chemically activated resin composites during curing. *Journal of Biomedical Materials Research* **58** [No. 1] 16–26.

Day, A. R., Tremblay, R. R. and Tremblay, A. M. 1986 Rigid Backbones: A New Geometry for Percolation. *Physical Review Letters* **56** 2501–2504.

Decker, C. 1994 Photoinitiated Curing of Multifunctional Monomers. *Acta Polymer* **45** 333–347.

Decker, C. 1996 Photoinitiated crosslinking polymerisation. *Progress in Polymer Science* **21** [No. 4] 593–650.

de Gennes, P. G. 1971 Reptation of a Polymer Chain in the Presence of Fixed Obstacles. *Journal of Chemical Physics* **55** 572–579.

de Gennes, P. G. 1983 Entangled Polymers. *Physics Today* **36** 33–39.

Duda, J. L. and Zielinski, J. M. 1996 Free-volume Theory. In P. Negoi ed., *Diffusion in Polymers* 143–171 Marcel-Dekker, Inc,.

Eirich, F. R. 1956 *Rheology Theory and Applications*. Academic Press,.

Enns, J. B. and Gillham, J. K. 1983a Effect Of The Extent Of Cure On The Modulus, Glass Transition, Water Absorbtion, And Density Of An Amine-Cured Epoxy. *Journal of Applied Polymer Science* **28** [No. 9] 2831 – 2846.

Enns, J. B. and Gillham, J. K. 1983b Time-Temperature-Transformation (TTT) Cure Diagram: Modeling The Cure Behavior Of Thermosets. *Journal of Applied Polymer Science* **28** [No. 8] 2567 – 2591.

Ernst, L. J., van 't Hof, C., Yang, D. G., Kiasat, M. S., Zhang, G. Q., Bressers, H. J. L., Caers, J. F. J., den Boer, A. W. J. and Janssen, J. 2002 Mechanical Modeling and Characterization of the Curing Process of Underfill Materials. *J. Electron. Packag.* **124** [No. 2] 97–105.

Ernst, L., van't Hof, C., Yang, D., Kiasat, M., Zhang, G., Bressers, H., Caers, J., den Boer, A. and Janssen, J. 2000 Determination of visco-elastic properties during the curing process of underfill materials. In *Electronic Components and Technology Conference, 2000. 2000 Proceedings. 50th* 1070–1077.

Ferry, J. D. 1970 *Viscoelastic Properties of Polymers*. John Wiley And Sons,.

Findley, W. N., Lai, J. S. and Onaran, K. 1976 *Creep and Relaxation of Nonlinear Viscoelastic Materials*. North-Holland,.

Flory, P. J. 1969 *Principles of Polymer Chemistry*. Cornell University Press,.

Franca, L. P. and Stenberg, R. 1991 Error Analysis of Some Galerkin Least-squares Methods For the Elasticity Equations. *Siam Journal On Numerical Analysis* **28** [No. 6] 1680–1697.

Francis, L. F., McCormick, A. V., Vaessen, D. M. and Payne, J. A. 2002 Development and measurement of stress in polymer coatings. *Journal of Materials Science* **37** 4717–4731.

Gao, J. and Penlidis, A. 1996 A comprehensive simulator/database package for reviewing free-radical homopolymerizations. *Journal of Macromolecular Science-reviews In Macromolecular Chemistry and Physics* **C36** [No. 2] 199–404.

Goodner, M. D. and Bowman, C. N. 2002 Development of a comprehensive free radical photopolymerization model incorporating heat and mass transfer effects in thick films. *Chemical Engineering Science* **57** [No. 5] 887–900.

Goodner, M. D., Lee, H. R. and Bowman, C. N. 1997 Method for Determining the Kinetic Parameters in Diffusion-Controlled Free-Radical Homopolymerizations. *Industrial & Engineering Chemistry Research* **36** [No. 4] 1247–1252.

Hale, A., Macosko, C. W. and Bair, H. E. 1991 Glass transition temperature as a function of conversion in thermosetting polymers. *Macromolecules* **24** [No. 9] 2610–2621.

Halley, P. J. and George, G. A. 2009 *Chemorheology of Polymers: From Fundamental Principles to Reactive Processing*. Cambridge University Press,.

Hamlen, R. C. 1991 *Paper Structure, Mechanics, and Permeability: Computer-Aided Modeling*. PhD thesis University of Minnesota.

Hasatani, M. and Itaya, Y. 1996 Drying-induced strain and stress: A review. *Drying Technology* **14** [No. 5] 1011–1040.

Hiemenz, P. C. and Lodge, T. P. 2007 *Polymer Chemistry*. 2 edition CRC Press,.

Ho, C.-W., Ruehli, A. E. and Brennan, P. A. 1975 Modified Nodal Approach To Network Analysis. *IEEE Transactions on Circuits and Systems* **22** 504 – 509.

Hossain, M., Possart, G. and Steinmann, P. 2009a A finite strain framework for the simulation of polymer curing. Part I: elasticity. *Computational Mechanics* **44** [No. 5] 621–630.

Hossain, M., Possart, G. and Steinmann, P. 2009b A small-strain model to simulate the curing of thermosets. *Computational Mechanics* **43** [No. 6] 769–779.

Hughes, T. J. R., Franca, L. P. and Balestra, M. 1986 A New Finite-element Formulation For Computational Fluid-dynamics .5. Circumventing the Babuska-brezzi Condition - A Stable Petrov-galerkin Formulation of the Stokes Problem Accommodating Equal-order Interpolations. *Computer Methods In Applied Mechanics and Engineering* **59** [No. 1] 85–99.

Jeffreys, H. 1929 *The Earth*. Cambridge University Press,.

Kim, S.-R. and Nairn, J. A. 2000 Fracture mechanics analysis of coating/substrate systems: Part I: Analysis of tensile and bending experiments. *Engineering Fracture Mechanics* **65** [No. 5] 573–593.

Kloosterboer, J. G. 1988 Network formation by chain crosslinking photopolymerization and its applications in electronics. *Advances in Polymer Science* **84** 1–61.

Koplin, C., Jaeger, R. and Hahn, P. 2009 A material model for internal stress of dental composites caused by the curing process. *Dental Materials* **25** [No. 3] 331–338.

Kurdikar, D. L. and Peppas, N. A. 1994a A Kinetic Model for Diffusion-Controlled Bulk Crosslinking Photopolymerizations. *Macromolecules* **27** [No. 15] 4084–4092.

Kurdikar, D. L. and Peppas, N. A. 1994b Method of determination of initiator efficiency: application to UV polymerizations using 2,2-dimethoxy-2-phenylacetophenone. *Macromolecules* **27** [No. 3] 733–738.

Lange, J., Manson, J. A. E. and Hult, A. 1996 Build-up of structure and viscoelastic properties in epoxy and acrylate resins cured below their ultimate glass transition temperature. *Polymer* **37** [No. 26] 5859–5868.

Lange, J., Toll, S., Manson, J. A. and Hult, A. 1995 Residual stress build-up in thermoset films cured above their ultimate glass transition temperature. *Polymer* **36** 3135–3141.

Lei, H. 1999 *Flow, Deformation, Stress and Failure in Solidifying Coatings*. PhD thesis University of Minnesota.

Lei, H., Francis, L. F., Gerberich, W. W. and Scriven, L. E. 2002 Stress Development in Drying Coatings After Solidification. *AIChE Journal* **48** 437–451.

Lei, H., Francis, L. F., Gerberich, W. W. and Scriven, L. E. 2003 Stress development in drying fibers and spheres. *Journal of Applied Polymer Science* **90** [No. 14] 3934–3944.

Lei, H., Payne, J. A., McCormick, A. V., Francis, L. F., Gerberich, W. W. and Scriven, L. E. 2001 Stress Development in Drying Coatings. *Journal of Applied Polymer Science* **81** 1000–1013.

Liang, G. and Chandrashekhara, K. 2006 Cure kinetics and rheology characterization of soy-based epoxy resin system. *Journal of Applied Polymer Science* **102** [No. 4] 3168–3180.

Lim, B. S., Ferracane, J. L., Sakaguchi, R. L. and Condon, J. R. 2002 Reduction of polymerization contraction stress for dental composites by two-step light-activation. *Dental Materials* **18** [No. 6] 436–444.

Litovski, V. and Zwolinski, M. 1997 *VLSI Circuit Simulation and Optimization*. Chapman & Hall,.

Long, K. N., Scott, T. F., Jerry Qi, H., Bowman, C. N. and Dunn, M. L. 2009 Photomechanics of light-activated polymers. *Journal of the Mechanics and Physics of Solids* **57** [No. 7] 1103–1121.

Love, B. J. and Piguet-Ruinet, F. 2007 Analyzing the dynamic chemorheology of curing resins: Extraction of model parameters associated with cure advancement. *Journal of Applied Polymer Science* **106** [No. 6] 3605–3609.

Love, B. J., Ruinet, F. P. and Teyssandier, F. 2008 Chemorheology of photopolymerizable acrylates using a modified Boltzmann sigmoidal model. *Journal of Polymer Science Part B: Polymer Physics* **46** [No. 21] 2319–2325.

Love, B. J., Teyssandier, F., Sun, Y. Y. and Wong, C. P. 2008 Sigmoidal Chemorheological Models of Chip-Underfill Materials Offer Alternative Predictions of Combined Cure and Flow. *Macromolecular Materials and Engineering* **293** [No. 10] 832–835.

Lovestead, T. M., O'Brien, A. K. and Bowman, C. N. 2003 Models of multivinyl free radical photopolymerization kinetics. *Journal of Photochemistry and Photobiology A-chemistry* **159** [No. 2] 135–143.

Luo, Y., Weng, Z., Huang, Z. and Pan, Z. 1996 The combined statistical and kinetic modeling of gel/sol partition in free-radical copolymerization of vinyl/divinyl monomers. *Journal of Polymer Science Part B: Polymer Physics* **34** [No. 1] 65–73.

Macosko, C. W. 1994 *Rheology Principles, Measurements, and Applications*. Wiley-VCH,.

Macosko, C. W. and Miller, D. R. 1976 A New Derivation of Average Molecular Weights of Nonlinear Polymers. *Macromolecules* **9** [No. 2] 199–206.

Malvern, L. E. 1969 *Introduction to the Mechanics of a Continuous Medium*. Pretence Hall,.

Martin, J. E. and Adolf, D. 1990 Constitutive equation for cure-induced stresses in a viscoelastic material. *Macromolecules* **23** [No. 23] 5014–5019.

Maxwell, J. C. 1867 On the Dynamical Theory of Gases. *Philosophical Transactions of the Royal Society of London* **157** 49–88.

May, C. A. ed. 1982 *Chemorheology of Thermosetting Polymers*. Vol. 227 of *ACS Symposium Series*.

Meuwissen, M. H. H., de Boer, H. A., Steijvers, H. L. A. H., Schreurs, P. J. G. and Geers, M. G. D. 2004 Residual stresses in microelectronics induced by thermoset packaging materials during cure. *Microelectronics Reliability* **44** [No. 12] 1985–1994.

Miller, D. R. and Macosko, C. W. 1976 A New Derivation of Post Gel Properties of Network Polymers. *Macromolecules* **9** [No. 2] 206–211.

Miller, D. R. and Macosko, C. W. 1978 Average Property Relations for Nonlinear Polymerization with Unequal Reactivity. *Macromolecules* **11** [No. 4] 656–662.

Miller, D. R. and Macosko, C. W. 1987 Molecular Weigh Relations for Crosslinking of Chains with Length and Site Distribution. *Journal of Polymer Science: Part B: Polymer Physics* **25** 2441–2469.

Miller, D. R. and Macosko, C. W. 1988 Network parameters for crosslinking of chains with length and site distribution. *Journal of Polymer Science Part B: Polymer Physics* **26** [No. 1] 1–54.

Miller, D. R., Valles, E. M. and Macosko, C. W. 1979 Calculation of molecular parameters for stepwise polyfunctional polymerization. *Polymer Engineering & Science* **19** [No. 4] 272–283.

Murakami, K. and Ono, K. 1979 *Chemorheology of Polymers*. Elsevier,.

O'Brien, D. J., Mather, P. T. and White, S. 2001 Viscoelastic Properties of an Epoxy Resin during Cure. *Journal of Composite Materials* **35** [No. 10] 883–904.

Odian, G. 2004 *Principles of Polymerization*. Wiley Interscience,.

Oldroyd, J. G. 1950 On the Formulation of Rheological Equations of State. *Proceedings of the Royal Society of London, Series A, Mathematical and Physical Sciences* **200** 523–541.

Pascault, J. P. and Williams, R. J. J. 1990 Glass transition temperature versus conversion relationships for thermosetting polymers. *Journal of Polymer Science Part B: Polymer Physics* **28** [No. 1] 85–95.

Pathak, P. 1981 *Porous Media: Structure, Strength, and Transport*. PhD thesis University of Minnesota.

Payne, J. A., McCormick, A. V. and Francis, L. F. 1997 In situ stress measurement apparatus for liquid applied coatings. *Rev. Sci. Instrum.* **68** 4564–4568.

Pearson, D. S. and Graessley, W. W. 1978 The Structure of Rubber Networks with Multifunctional Junctions. *Macromolecules* **11** [No. 3] 528–533.

Perrin, F., Nguyen, T. M. H. and Vernet, J. 2007 Chemico-diffusion kinetics and TTT cure diagrams of DGEBA-DGEBF/amine resins cured with phenol catalysts. *European Polymer Journal* **43** [No. 12] 5107–5120.

Petzold, L. 1982 Differential/Algebraic Equations are not ODE's. *SIAM J. Sci. Stat. Comput.* **3** [No. 3] 367–384.

Prasatya, P., McKenna, G. B. and Simon, S. L. 2001 A Viscoelastic Model for Predicting Isotropic Residual Stresses in Thermosetting Materials: Effects of Processing Parameters. *Journal of Composite Materials* **35** [No. 10] 826–848.

Prime, R. 1997 Thermosets. In E. Turi ed., *Thermal Characterisation of Polymeric Materials* 2 edition Academic Press,.

Radhakrishnan, H. 2006 *Solidification By Drying: Effect of Non-uniformities*. PhD thesis University of Minnesota.

Rajamani, V. 2005 *Shrinkage, Viscoelasticity, and Stress Development in Curing Coatings*. PhD thesis University of Minnesota.

Reiner, M. 1969 *Deformation, Strain, and Flow*. H. K. Lewis & Co,.

Richter, K. B. 2007 *Pulsed Electron Beam Curing of Coatings*. PhD thesis University of Minnesota.

Rosen, S. L. 1971 *Fundamental Principles of Polymeric Materials for Practicing Engineers*. Barnes & Noble,.

Rushdi, A. M. 1985 Development Of Modified Nodal Analysis Into A Pedagogical Tool. *IEEE Transactions on Education* **E-28** [No. 1] 17 – 25.

Sartomer, Inc 2009 Application Bulletin 4001: Ethoxylated TMPTA Monomers: Properties and Performance. *Technical report* Sartomer, Inc.

Sato, K. 1980 The internal stress of coating films. *Progress in Organic Coatings* **8** [No. 2] 143–160.

Schmidt, L. E., Leterrier, Y., Schmah, D., Manson, J. A. E., James, D., Gustavsson, E. and Svensson, L. S. 2007 Conversion analysis of acrylated hyperbranched polymers UV-cured below their ultimate glass transition temperature. *Journal of Applied Polymer Science* **104** [No. 4] 2366–2376.

Schmidt, L. E., Leterrier, Y., Vesin, J. M., Wilhelm, M. and Manson, J. A. E. 2005 Photorheology of fast UV-curing multifunctional acrylates. *Macromolecular Materials and Engineering* **290** [No. 11] 1115–1124.

Schmidt, L. E., Schmah, D., Leterrier, Y. and Manson, J. A. E. 2007 Time-intensity transformation and internal stress in UV-curable hyperbranched acrylates. *Rheologica Acta* **46** [No. 5] 693–701.

Scott, T. F., Kowalski, B. A., Sullivan, A. C., Bowman, C. N. and McLeod, R. R. 2009 Two-Color Single-Photon Photoinitiation and Photoinhibition for Subdiffraction Photolithography. *Science* **324** [No. 5929] 913–917.

Simon, S. L., Mckenna, G. B. and Sindt, O. 2000 Modeling the evolution of the dynamic mechanical properties of a commercial epoxy during cure after gelation. *Journal of Applied Polymer Science* **76** [No. 4] 495–508.

Sobotka, Z. 1984 *Rheology of Materials and Engineering Systems*. Elsevier,.

Sokolnikoff, I. S. 1956 *Mathematical Theory of Elasticity*. Robert E. Krieger Publishing Company,.

Sperling, L. H. 1986 *Introduction to Physical Polymer Science*. John Wiley & Sons,.

Stansbury, J. W., Trujillo-Lemon, M., Lu, H., Ding, X. Z., Lin, Y. and Ge, J. H. 2005 Conversion-dependent shrinkage stress and strain in dental resins and composites. *Dental Materials* **21** [No. 1] 56–67.

Stolov, A., Xie, T., Penelle, J. and Hsu, S. 2000 Simultaneous Measurement of Polymerization Kinetics and Stress Development in Radiation-Cured Coatings: A New Experimental Approach and Relationship between the Degree of Conversion and Stress. *Macromolecules* **33** [No. 19] 6970–6976.

Stolov, A., Xie, T., Penelle, J. and Hsu, S. 2001 Stress Buildup in Ultraviolet-Cured Coatings: Sample Thickness Dependence. *Macromolecules* **34** [No. 9] 2865–2869.

Stolov, A., Xie, T., Penelle, J., Hsu, S. and Stidham, H. 2001 An analysis of photopolymerization kinetics and stress development in multifunctional acrylate coatings. *Polymer Engineering & Science* **41** [No. 2] 314–328.

Strang, G. 1986 *Introduction to Applied Mathematics*. Wellesley-Cambridge Press,.

Tam, S. Y. 1997 *Stress Effects in Drying Coatings*. PhD thesis University of Minnesota.

Tam, S. Y., Scriven, L. E. and Stolarski, H. K. 1995 Stress Effects in Drying Polymer Films. *Materials Research Society Symposium Proceedngs* **356** 547–552.

The Mathworks Inc. R2009b MATLAB.

Thorpe, M. F. 1983 Continuous Deformations in Random Networks. *Journal of Non-Crystalline Solids* **57** 335–370.

Timoshenko, S. P. and Goodier, J. N. 1970 *Theory of Elasticity*. McGraw-Hill,.

Tobita, H. and Hamielec, A. E. 1989 Modeling of network formation in free radical polymerization. *Macromolecules* **22** [No. 7] 3098–3105.

Vaessen, D. M. 2002 *Stress and Structure Development in Polymeric Coatings*. PhD thesis University of Minnesota.

Vaessen, D. M., Ngantung, F. A., Palacio, M. L. B., Francis, L. F. and McCormick, A. V. 2002 Effect of lamp cycling on conversion and stress development in ultraviolet-cured acrylate coatings. *Journal of Applied Polymer Science* **84** [No. 14] 2784–2793.

van Krevelen, D. W. 2009 *Properties of Polymers*. 4 edition Elsevier,.

Vilgis, T. A. 1989 Polymer Reactions: Polymer Networks. In *Comprehensive Polymer Science: The Synthesis, Characterization, Reactions, and Applications of Polymers* Pergammon Press,.

Vrentas, J. S. and Vrentas, C. M. 1991 Solvent self-diffusion in crosslinked polymers. *Journal of Applied Polymer Science* **42** [No. 7] 1931–1937.

Wang, Y., Han, B. and Bar-Cohen, A. 2008 Simultaneous Measurement of Effective Chemical Shrinkage and Modulus Evolution During Polymerization. In *Electronic Components and Technology Conference*.

Wen, M. 2001 *Designing Ultraviolet Curing of Multifunctional (Meth)acrylate Hard Coats*. PhD thesis University of Minnesota.

Wen, M. and McCormick, A. V. 2000 A kinetic model for radical trapping in photopolymerization of multifunctional monomers. *Macromolecules* **33** [No. 25] 9247–9254.

White, S. and Hahn, H. 1992a Process Modeling of Composite Materials: Residual Stress Development during Cure. Part I. Model Formulation. *Journal of Composite Materials* **26** [No. 16] 2402–2422.

White, S. and Hahn, H. 1992b Process Modeling of Composite Materials: Residual Stress Development during Cure. Part I. Model Formulation. *Journal of Composite Materials* **26** [No. 16] 2402–2422.

White, S. R. and Hahn, H. T. 1993 Cure Cycle Optimization For the Reduction of Processing-induced Residual-stresses In Composite-materials. *Journal of Composite Materials* **27** [No. 14] 1352–1378.

Williams, M. L., Landel, R. F. and Ferry, J. D. 1955 The Temperature Dependence of Relaxation Mechanisms in Amorphous Polymers and Other Glass-forming Liquids. *Journal of the American Chemical Society* **77** [No. 14] 3701–3707.

Yang, D., Jansen, K., Wang, L., Ernst, L., Zhang, G., Bressers, H. and Fan, X. 2004 Micromechanical modeling of stress evolution induced during cure in a particle-filled electronic packaging polymer. *Components and Packaging Technologies, IEEE Transactions on* **27** [No. 4] 676–683.

Yousefi, A., Lafleur, P. G. and Gauvin, R. 1997 Kinetic studies of thermoset cure reactions: A review. *Polymer Composites* **18** [No. 2] 157–168.

Zhu, S. and Hamielec, A. E. 1992 Influence of cross-link density distribution on network formation in free-radical copolymerization of vinyl/divinyl monomers. *Macromolecules* **25** [No. 20] 5457–5464.

Zhu, S., Hamielec, A. E. and Pelton, R. H. 1993 Modelling of crosslinking and cyclization in free-radical copolymerization of vinyl/divinyl monomers. *Die Makromolekulare Chemie, Theory and Simulations* **2** [No. 4] 587–604.

# Appendix A

# Appendix

## A.1 Global Network Variables

To solve the network evolution equation, the physical properties of modulus, rest length, and viscosity as well as the displacement of each node and stress in each element must be kept track of. Each vector is really a vector of vectors as each matrix is a matrix of matrices since the stress and displacement in each dimension are kept track of separately.
Stress

$$\boldsymbol{\sigma} = \begin{bmatrix} \boldsymbol{\sigma_1} \\ \boldsymbol{\sigma_2} \\ \vdots \\ \boldsymbol{\sigma_{NE}} \end{bmatrix} = \begin{bmatrix} \begin{bmatrix} \sigma_{x1} \\ \sigma_{y1} \end{bmatrix} \\ \begin{bmatrix} \sigma_{x2} \\ \sigma_{y2} \end{bmatrix} \\ \vdots \\ \begin{bmatrix} \sigma_{xNE} \\ \sigma_{yNE} \end{bmatrix} \end{bmatrix} \tag{A.1}$$

Extension

$$\boldsymbol{\Delta d} = \begin{bmatrix} \boldsymbol{\Delta d_1} \\ \boldsymbol{\Delta d_2} \\ \vdots \\ \boldsymbol{\Delta d_{NE}} \end{bmatrix} = \begin{bmatrix} \begin{bmatrix} \Delta d_{x1} \\ \Delta d_{y1} \end{bmatrix} \\ \begin{bmatrix} \Delta d_{x2} \\ \Delta d_{y2} \end{bmatrix} \\ \vdots \\ \begin{bmatrix} \Delta d_{xNE} \\ \Delta d_{yNE} \end{bmatrix} \end{bmatrix} \tag{A.2}$$

Shrinker Extension

$$\boldsymbol{\Delta d_{sh}} = \begin{bmatrix} \boldsymbol{\Delta d_{sh,1}} \\ \boldsymbol{\Delta d_{sh,2}} \\ \vdots \\ \boldsymbol{\Delta d_{sh,NE}} \end{bmatrix} = \begin{bmatrix} \begin{bmatrix} \Delta d_{sh,x1} \\ \Delta d_{sh,y1} \end{bmatrix} \\ \begin{bmatrix} \Delta d_{sh,x2} \\ \Delta d_{sh,y2} \end{bmatrix} \\ \vdots \\ \begin{bmatrix} \Delta d_{sh,xNE} \\ \Delta d_{sh,yNE} \end{bmatrix} \end{bmatrix} \tag{A.3}$$

Stiffness

$$\begin{aligned} \boldsymbol{K'} &= \begin{bmatrix} \boldsymbol{K_1'} & \boldsymbol{0} & \boldsymbol{0} & \boldsymbol{0} \\ \boldsymbol{0} & \boldsymbol{K_2'} & \boldsymbol{0} & \boldsymbol{0} \\ \vdots & & \ddots & \vdots \\ \boldsymbol{0} & \boldsymbol{0} & \boldsymbol{0} & \boldsymbol{K_{NE}'} \end{bmatrix} \\ &= \begin{bmatrix} \begin{bmatrix} \frac{E_1}{L_o} & 0 \\ 0 & 0 \end{bmatrix} & \begin{bmatrix} 0 & 0 \\ 0 & 0 \end{bmatrix} & \begin{bmatrix} 0 & 0 \\ 0 & 0 \end{bmatrix} & \begin{bmatrix} 0 & 0 \\ 0 & 0 \end{bmatrix} \\ \begin{bmatrix} 0 & 0 \\ 0 & 0 \end{bmatrix} & \begin{bmatrix} \frac{E_2}{L_o} & 0 \\ 0 & 0 \end{bmatrix} & \begin{bmatrix} 0 & 0 \\ 0 & 0 \end{bmatrix} & \begin{bmatrix} 0 & 0 \\ 0 & 0 \end{bmatrix} \\ \vdots & & \ddots & \vdots \\ \begin{bmatrix} 0 & 0 \\ 0 & 0 \end{bmatrix} & \begin{bmatrix} 0 & 0 \\ 0 & 0 \end{bmatrix} & \begin{bmatrix} 0 & 0 \\ 0 & 0 \end{bmatrix} & \begin{bmatrix} \frac{E_{NE}}{L_o} & 0 \\ 0 & 0 \end{bmatrix} \end{bmatrix} \end{aligned} \tag{A.4}$$

Viscosity

$$\begin{aligned} \boldsymbol{V'} &= \begin{bmatrix} \boldsymbol{V_1'} & \boldsymbol{0} & \boldsymbol{0} & \boldsymbol{0} \\ \boldsymbol{0} & \boldsymbol{V_2'} & \boldsymbol{0} & \boldsymbol{0} \\ \vdots & & \ddots & \vdots \\ \boldsymbol{0} & \boldsymbol{0} & \boldsymbol{0} & \boldsymbol{V_{NE}'} \end{bmatrix} \\ &= \begin{bmatrix} \begin{bmatrix} \mu_1 & 0 \\ 0 & 0 \end{bmatrix} & \begin{bmatrix} 0 & 0 \\ 0 & 0 \end{bmatrix} & \begin{bmatrix} 0 & 0 \\ 0 & 0 \end{bmatrix} & \begin{bmatrix} 0 & 0 \\ 0 & 0 \end{bmatrix} \\ \begin{bmatrix} 0 & 0 \\ 0 & 0 \end{bmatrix} & \begin{bmatrix} \mu_2 & 0 \\ 0 & 0 \end{bmatrix} & \begin{bmatrix} 0 & 0 \\ 0 & 0 \end{bmatrix} & \begin{bmatrix} 0 & 0 \\ 0 & 0 \end{bmatrix} \\ \vdots & & \ddots & \vdots \\ \begin{bmatrix} 0 & 0 \\ 0 & 0 \end{bmatrix} & \begin{bmatrix} 0 & 0 \\ 0 & 0 \end{bmatrix} & \begin{bmatrix} 0 & 0 \\ 0 & 0 \end{bmatrix} & \begin{bmatrix} \mu_{NE} & 0 \\ 0 & 0 \end{bmatrix} \end{bmatrix} \end{aligned} \tag{A.5}$$

Rotation

$$
\begin{aligned}
\boldsymbol{R} &= \begin{bmatrix} \boldsymbol{R_1} & \mathbf{0} & \mathbf{0} & \mathbf{0} \\ \mathbf{0} & \boldsymbol{R_2} & \mathbf{0} & \mathbf{0} \\ \vdots & & \ddots & \vdots \\ \mathbf{0} & \mathbf{0} & \mathbf{0} & \boldsymbol{R_{NE}} \end{bmatrix} \\
&= \begin{bmatrix} \begin{bmatrix} \cos(\alpha_1) & -\sin(\alpha_1) \\ \sin(\alpha_1) & \cos(\alpha_1) \end{bmatrix} & \begin{bmatrix} 0 & 0 \\ 0 & 0 \end{bmatrix} & \begin{bmatrix} 0 & 0 \\ 0 & 0 \end{bmatrix} \\ \vdots & \ddots & \vdots \\ \begin{bmatrix} 0 & 0 \\ 0 & 0 \end{bmatrix} & \begin{bmatrix} 0 & 0 \\ 0 & 0 \end{bmatrix} & \begin{bmatrix} \cos(\alpha_{NE}) & -\sin(\alpha_{NE}) \\ \sin(\alpha_{NE}) & \cos(\alpha_{NE}) \end{bmatrix} \end{bmatrix}
\end{aligned}
\tag{A.6}
$$